Fall 2010

Nonlinear analysis of pile driving and ground vibrations in saturated cohesive soils using the finite element method

Mehmet Serdar Serdaroglu
University of Iowa

NONLINEAR ANALYSIS OF PILE DRIVING AND GROUND VIBRATIONS IN SATURATED COHESIVE SOILS USING THE FINITE ELEMENT METHOD

by

Mehmet Serdar Serdaroglu

An Abstract

Of a thesis submitted in partial fulfillment
of the requirements for the Doctor of
Philosophy degree in Civil and Environmental Engineering
in the Graduate College of
The University of Iowa

December 2010

Thesis Supervisor: Professor M. Asghar Bhatti

ABSTRACT

In urban areas, vibrations generated by pile driving often affect the neighboring properties vulnerable to ground shaking. These vibrations may cause damage to surrounding structures either by shaking the ground or by causing settlement of the soil beneath foundations in the proximity of pile driving. It is important to distinguish between the conditions under which the vibrations will cause damage and those under which vibrations are tolerable. The numerical studies on the analysis of pile driving have mostly focused on assessing the driving efficiency and the bearing capacity of dynamically loaded piles. A limited number of studies included the study of ground vibrations due to pile driving and its effects on adjacent structures. However, the factors affecting the ground vibrations in soils such as the nonlinear constitutive behavior of soil, soil-pile interaction and penetration depth of the pile have not been clearly identified.

The objective of this research is to implement a numerical method to simulate dynamic loading of a single pile, and study the factors influencing the stress wave propagation in the soil surrounding the pile. The thesis is comprised of two main analyses: (1) the static analysis of a pile in which the phenomenon of static consolidation is studied, and (2) the dynamic analysis of a pile in which pile driving and ground vibrations are studied.

In the static analysis, the load capacity of a single pile is investigated. The results from the finite element method are compared with widely recognized theoretical methods. The theoretical methods that are used to estimate the end bearing capacities are: (1) General Formula, (2) Vesic's Method, (3) Janbu's Method, (4) Meyerhof's Method, and (5) Coyle & Castello's Method. The estimation of skin friction resistance (shaft capacity) of single piles is performed using the (1) Alpha method, (2) Beta method, and (3) Lambda method. Two numerical applications are performed to predict the load capacity of single piles in normally consolidated clays. It is observed that the model with

no slippage at the interface predicts almost twice as much load capacity as the model with interface. In regards with the end bearing capacities, Coyle & Castello's method is found to be most conservative followed by the finite element method, the Janbu's method, the Meyerhof's method, and finally the Vesic's method. In respect to skin friction resistance, the finite element is found to be the most conservative method, followed by the Beta, the Lambda, and the Alpha method.

In the dynamic analysis, the amplitudes of ground vibrations are investigated based on the variation of: (1) the soil type, (2) the pile embedment length and (3) the released hammer energy. In the first analysis, five types of soils – loose and dense sands and, soft, medium stiff, and stiff clays – are modeled. The highest vibration amplitude is calculated for the loose sand with a peak particle velocity (PPV) of 10.0 mm/s followed by the dense sand with a PPV of around 4.0 mm/s. Among the clay types, the vibrations are higher for the stiffer clay in the near field, which is 9 m (half a pile length) or less away from the pile. In the second analysis, three different embedment lengths – full, half, and quarter pile length – are modeled. It is found that the quarter embedded piles produce greater vibration amplitudes as compared to the half and fully embedded piles. Larger amplitudes of vibrations are encountered on the ground surface for shorter pile embedment lengths. In the third analysis, three different impact forces consisting of 2,000 kN (F), 6,000 kN (3F) and 10,000 kN (5F) are applied on the pile head. It is concluded that increase in hammer energy causes increase in the peak particle velocities.

Abstract Approved: _____
Thesis Supervisor

_____
Title and Department

_____
Date

NONLINEAR ANALYSIS OF PILE DRIVING AND GROUND VIBRATIONS IN SATURATED COHESIVE SOILS USING THE FINITE ELEMENT METHOD

by

Mehmet Serdar Serdaroglu

A thesis submitted in partial fulfillment
of the requirements for the Doctor of
Philosophy degree in Civil and Environmental Engineering
in the Graduate College of
The University of Iowa

December 2010

Thesis Supervisor: Professor M. Asghar Bhatti

Graduate College
The University of Iowa
Iowa City, Iowa

CERTIFICATE OF APPROVAL

_____

PH.D. THESIS

_____

This is to certify that the Ph.D. thesis of

Mehmet Serdar Serdaroglu

has been approved by the Examining Committee
for the thesis requirement for the Doctor of Philosophy
degree in Civil and Environmental Engineering at the December 2010
graduation.

Thesis Committee: _____
M. Asghar Bhatti, Thesis Supervisor

_____
Colby C. Swan

_____
Sharif Rahman

_____
Salam Rahmatalla

_____
Jia Lu

To my beloved parents

ACKNOWLEDGEMENTS

I would like to express my deepest appreciation to Professor M. Asghar Bhatti for his continuous guidance and encouragement throughout the development of this dissertation. He has always been an excellent teacher and advisor to me. I am extremely grateful for his patience and constant support.

I would like to thank to Professor Colby C. Swan for taking genuine interest in my thesis by providing thoughtful feedback. I acquired great knowledge from him. I am grateful for his contributions to my thesis.

I am grateful to all of the staff members in the Department of Civil and Environmental Engineering for their administrative assistance and friendly support.

I would like to thank to my colleagues in my office for being supportive and patient with me.

I am grateful to my dear friend Kendra R. Glider who provided me a quite study environment during Summer 2010. I was delighted to have her genuine friendship and generous support.

I would like to express my special gratitude to my beloved sister Emine Ilknur Serdaroglu and my dear brothers Mehmet Sertac Serdaroglu and Mehmet Serkan Serdaroglu who consistently provided me tremendous moral support and encouragement throughout my graduate studies.

Finally, my deepest gratitude goes to my beloved parents, Salih and Cemile Serdaroglu, who sacrificed so much for me to pursue a higher education in the United States. I am deeply grateful for their exceptional moral and financial support throughout my entire education life.

ABSTRACT

In urban areas, vibrations generated by pile driving often affect the neighboring properties vulnerable to ground shaking. These vibrations may cause damage to surrounding structures either by shaking the ground or by causing settlement of the soil beneath foundations in the proximity of pile driving. It is important to distinguish between the conditions under which the vibrations will cause damage and those under which vibrations are tolerable. The numerical studies on the analysis of pile driving have mostly focused on assessing the driving efficiency and the bearing capacity of dynamically loaded piles. A limited number of studies included the study of ground vibrations due to pile driving and its effects on adjacent structures. However, the factors affecting the ground vibrations in soils such as the nonlinear constitutive behavior of soil, soil-pile interaction and penetration depth of the pile have not been clearly identified.

The objective of this research is to implement a numerical method to simulate dynamic loading of a single pile, and study the factors influencing the stress wave propagation in the soil surrounding the pile. The thesis is comprised of two main analyses: (1) the static analysis of a pile in which the phenomenon of static consolidation is studied, and (2) the dynamic analysis of a pile in which pile driving and ground vibrations are studied.

In the static analysis, the load capacity of a single pile is investigated. The results from the finite element method are compared with widely recognized theoretical methods. The theoretical methods that are used to estimate the end bearing capacities are: (1) General Formula, (2) Vesic's Method, (3) Janbu's Method, (4) Meyerhof's Method, and (5) Coyle & Castello's Method. The estimation of skin friction resistance (shaft capacity) of single piles is performed using the (1) Alpha method, (2) Beta method, and (3) Lambda method. Two numerical applications are performed to predict the load capacity of single piles in normally consolidated clays. It is observed that the model with

no slippage at the interface predicts almost twice as much load capacity as the model with interface. In regards with the end bearing capacities, Coyle & Castello's method is found to be most conservative followed by the finite element method, the Janbu's method, the Meyerhof's method, and finally the Vesic's method. In respect to skin friction resistance, the finite element is found to be the most conservative method, followed by the Beta, the Lambda, and the Alpha method.

In the dynamic analysis, the amplitudes of ground vibrations are investigated based on the variation of: (1) the soil type, (2) the pile embedment length and (3) the released hammer energy. In the first analysis, five types of soils – loose and dense sands and, soft, medium stiff, and stiff clays – are modeled. The highest vibration amplitude is calculated for the loose sand with a peak particle velocity (PPV) of 10.0 mm/s followed by the dense sand with a PPV of around 4.0 mm/s. Among the clay types, the vibrations are higher for the stiffer clay in the near field, which is 9 m (half a pile length) or less away from the pile. In the second analysis, three different embedment lengths – full, half, and quarter pile length – are modeled. It is found that the quarter-embedded piles produce greater vibration amplitudes as compared to the half and fully embedded piles. Larger amplitudes of vibrations are encountered on the ground surface for shorter pile embedment lengths. In the third analysis, three different impact forces consisting of 2,000 kN (F), 6,000 kN (3F) and 10,000 kN (5F) are applied on the pile head. It is concluded that increase in hammer energy causes increase in the peak particle velocities.

TABLE OF CONTENTS

LIST OF TABLES

LIST OF FIGURES

CHAPTER 1

INTRODUCTION

1.1 Background and Motivation

Piles are used to support the foundations of buildings, bridges, and other structures where the use of shallow foundations would be risky due to excessive settlement, potential scour effects or future environmental conditions (Poulos, et al., 1980). Piles are installed with either an impact or a vibratory hammer. Impact pile driving is an effective method of installing piles into the ground. When implementing this method, a hammer is dropped on the pile head advancing the pile into the ground by repetitive blows until the pile toe reaches the desired depth. The installation of a precast concrete pile with an impact pile driver is shown in Figure 1.1.

The use of piles is a common practice, because of numerous reasons, most importantly: (1) recently developed powerful hammers have the capability of installing piles in a short period; (2) highly efficient hammers significantly increase the bearing capacity of driven piles; and (3) dynamic testing methods are reliable for the estimation of pile capacities. Although these advantages make pile driving a widely accepted practice, the vibrations generated by pile driving cause disturbance in the neighborhood.

Pile driving generates vibrations in the ground, and occasionally these vibrations can damage structures or disturb people in the proximity of pile driving. It is necessary to take pre-cautionary measures prior to pile installation to avoid physical damage from vibrations. The availability of reliable and accurate vibration records prior to the pile driving operation would give a significant advantage to the designer to choose an appropriate type of pile and hammer. The prediction of pile driving vibrations with high precision is thus critical to prevent damage to the adjacent structures.

Figure 1.1 Installation of a precast concrete pile by an air hammer.

1.2 Problem Statement

The pile driving vibrations in the ground create issues particularly in urban areas such as unwanted noise, environmental disturbance, and potential hazard for the neighboring properties due to the vibrations generated by pile driving. Many case studies have shown that ground vibrations due to pile driving often cause damage to the adjacent structures that are vulnerable to ground shaking (Skipp, 1998; Dowding, 1999; Woods, et al., 2004 and; Kim, et al., 2000). The damage due to pile driving occurs either directly or via settlement of soil beneath foundations in the proximity of pile driving operations.

The potential damage to the adjacent structures can be prevented by conducting pre-construction surveys, monitoring and controlling the vibrations on site, and predicting the anticipated vibrations prior to pile driving (Dowding, 1999). Understanding the conditions under which those vibrations will cause damage is important to avoid

excessive vibrations and damage claims. Thus, development of numerical methods that predict ground vibrations prior to pile driving becomes essential.

Previous studies on the analysis of pile driving have mostly focused on assessing the drivability, the bearing capacity, and driving efficiency of piles (Smith, 1960; Mabsout, et al., 1995 and; Liyanapathirana, et al., 2001). Only a limited number of research studies have focused on ground vibrations due to pile driving and their effects on adjacent structures (Ramshaw et al., 1996 and; Masoumi et al., 2007 & 2008). Although the numerical models predicted ground vibrations consistent with the experimental data, they have not taken into account the essential soil and source parameters such as the nonlinear constitutive behavior of soil, friction between the pile and the soil, variation of pile penetration depth.

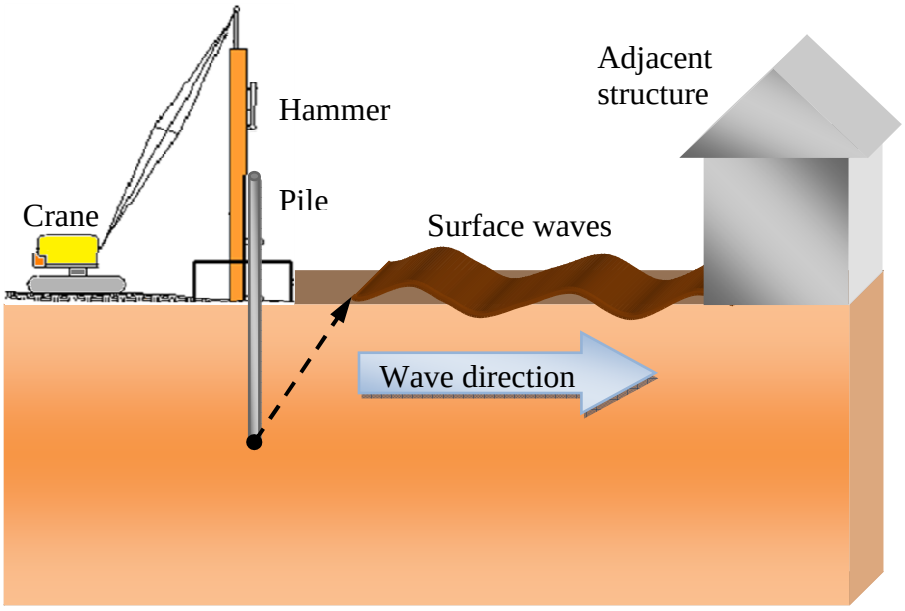

Figure 1.2 Generation of surface waves due to impact pile driving.

1.3 Objectives and Scope

The scope of this thesis is divided into three major areas as follows: (1) The development of coupled soil displacement- pore pressure equations using the finite element method that includes the derivation of finite element equations for static and dynamic analysis of soils using the u/p formulation; (2) the analysis of static pile capacity using the finite element method. The commercial finite element package ABAQUS is used for this analysis. The effect of soil-pile friction is investigated. The analysis is conducted with one layered and three layered homogenous cohesive soils; (3) the analysis of dynamically loaded single pile and stress wave propagation in cohesive soils. This part of the research includes simulation of pile driving with a single hammer blow and ground vibrations generated by pile driving. A finite element model with special boundary conditions is particularly developed for this research. The variation of important design parameters such as soil strength, pile penetration depth and the applied hammer energy are investigated using this model.

There are two main objectives in this study. The first objective of this research is to evaluate the static pile capacity formulas for end bearing and skin friction resistance using the finite method. The conventional pile capacity formulas are compared with the finite element method to determine the limitations of the formulas for cohesive soils. The second objective of this research is to study the effect of soil and vibration source parameters on the stress wave propagation in soils due to impact pile driving to gain a deeper understanding of how pile driving induces ground vibrations. The soil and vibration source parameters studied in this thesis are: (1) soil strength, (2) pile penetration depth and (3) the applied hammer energy.

A comprehensive finite element (FE) method is developed to simulate dynamic loading of a single pile and stress wave propagation in cohesive soils. A coupled pore pressure/displacement formulation is used to model cohesive soils. The Coulomb's contact algorithm is used to include friction between the pile and the soil. The peak

particle velocities on the ground surface are computed with varying soil and pile parameters. The amplitude of the surface waves are compared with varying soil properties, pile penetration depths and hammer energies. Finally, the finite element results are compared with empirical methods.

1.4 Thesis Organization

This thesis consists of eight chapters. In the first chapter, the use of piles and the ground vibrations due to pile driving are introduced followed by the objectives and scope, and the organization of this thesis. In the second chapter, the studies consisting pile driving induced ground vibrations, mechanics of wave propagation in soils, and damage criteria due to pile driving are reviewed. In the third chapter, a coupled pore-pressure/displacement finite element formulation based on Biot's poroelasticity theory is derived followed by the implementation of this model on a steady-state soil consolidation problem. In the fourth chapter, transient analysis of soil consolidation problem is discussed with numerical applications. In the fifth chapter, soil constitutive models that are used in this study are explained. In the sixth chapter, static loading of a single pile is modeled using linear elastic and elastoplastic behavior of soils. The results are compared with the results of the empirical methods. In the seventh chapter, dynamic loading of a single pile is simulated using the finite element method. The amplitudes of ground vibrations from pile driving are computed in the near and far fields. A parametric study is conducted based on varying soil properties, pile penetration depth and hammer energy. Finally, in the eighth chapter, the results of this study are discussed along with the recommendations for future work.

CHAPTER 2

LITERATURE REVIEW

2.1 Introduction

This chapter reviews the literature for wave propagation in soils due to impact pile driving and vibration induced settlements of the cohesionless soils. It consists of three main sections followed by a summary section. The first section describes the fundamentals of ground vibrations and their propagation in soils, followed by the vibration acceptance levels for human perception and nearby structures. The literature is then reviewed for the empirical relations which estimate the amplitudes of the vibrations, and the most widely used empirical relations are presented. In the second section, five case histories that reveal the vibration induced settlements from impact pile driving are described. In the third section, recent numerical studies within the last decade that are conducted on the finite element analysis of pile driving and wave propagation are described. Finally, the chapter is summarized and the conclusions are presented.

2.2 Fundamentals of Ground Vibrations

2.2.1 Ground Vibrations Due to Pile Driving

When a pile hammer hits the pile, energy travels down the pile losing some energy due to friction along the soil-pile interface and some due to compression by penetration at the pile tip while the remaining energy of the blow on the pile causes a stress wave to propagate in the surrounding ground. The amplitude of this energy depends on many factors such as type of hammer, type of pile and soil classification. As the bearing capacity of piles is composed of skin friction and end bearing, the wave generation in pile is similar such that the waves are generated by two mechanisms: shear waves (S-waves) along the shaft and compressive waves or primary waves (P-waves) at the pile tip as shown in Figure 2.1. Shear waves are generated along the pile skin by

relative motion between the pile and the surrounding soil. As the compressive waves in the pile travels down the pile, the shear waves propagate out from the pile on a conical wave front as shown in Figure 2.1.

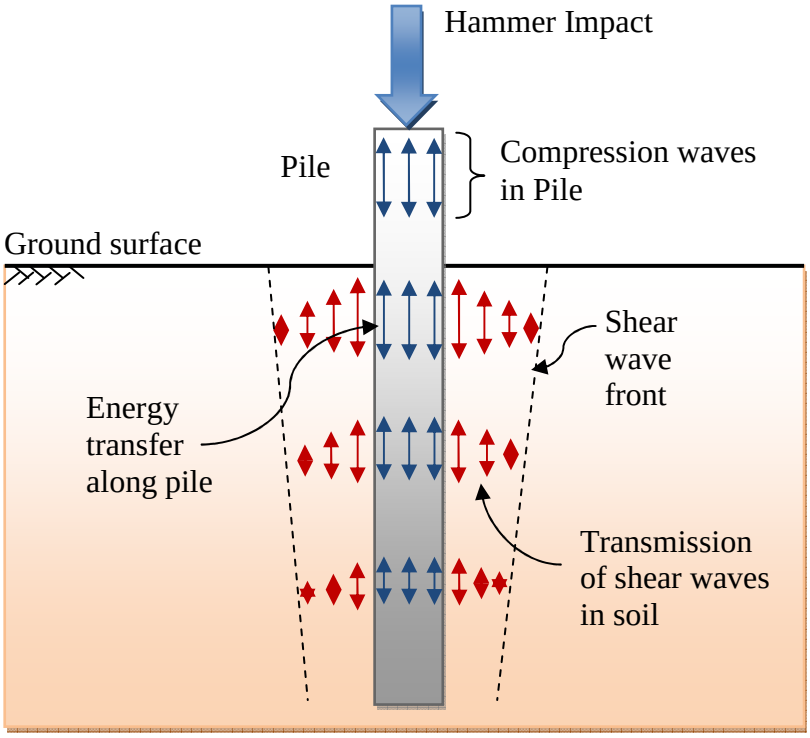

Figure 2.1 Generation of compressive and shear waves during impact pile driving.

The velocities of compressive and shear waves are controlled by the elastic properties of the media in which they travel. The wave velocities can be expressed for P-wave, C_p and S-wave, C_s as follows:

$$C_P = \sqrt{\frac{\lambda + 2\mu}{\rho}} \tag{2.1}$$

$$C_S = \sqrt{\frac{\mu}{\rho}} \tag{2.2}$$

where λ, μ are Lamé's constants, ρ is the mass density of ground, E is the Young's modulus and ν is the Poisson's ratio.

The compression wave velocity in the pile is usually ten or more times the shear wave velocity in the soil, thus the conical wave front emanating from the pile can be assumed cylindrical. The surface of the cone is known as the wave front. It is the leading edge of increase in stress caused by the interaction between the skin of the pile and the soil. The transmission of compression and shear-waves in the soil are schematically shown in Figure 2.2.

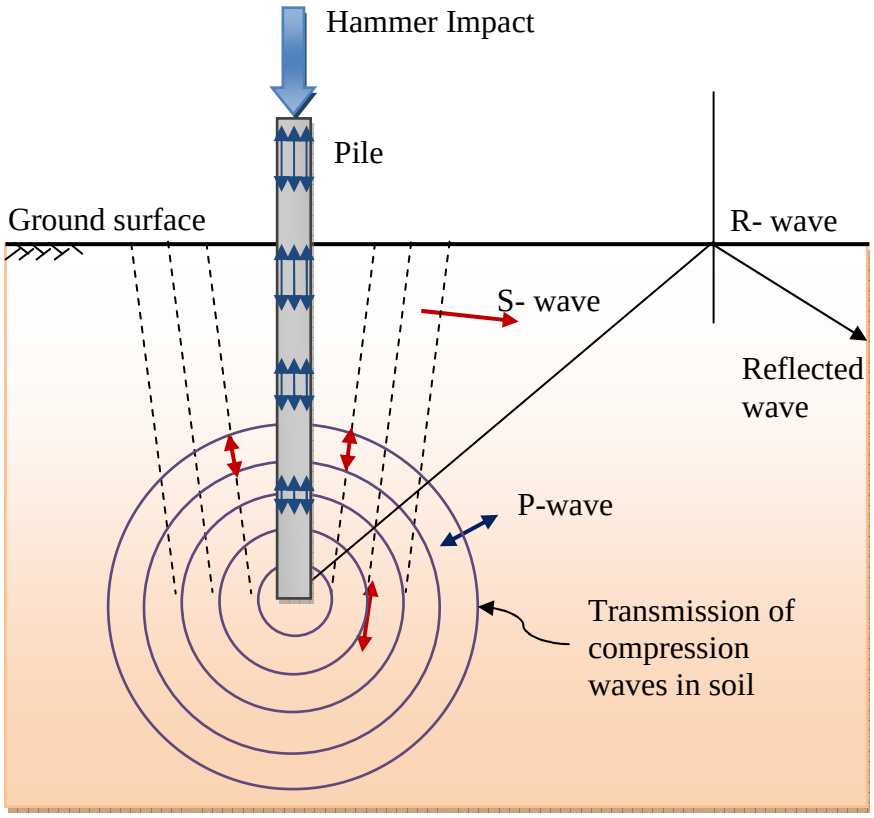

Figure 2.2 Emanating of stress waves from a driven pile at the pile tip.

When the P-wave and S-wave encounter the ground surface, part of their energy is converted to surface waves namely Rayleigh waves, and part is reflected back as reflected P-and S-waves. The deformation pattern of the basic body waves and the Rayleigh wave traveling to the right are shown in Figure 2.3. In the top body, the motion of the primary wave (*P*-wave) is shown where a minute particle of the material is in the direction of wave travel. In the middle body, the travel of the secondary wave (*S*-wave) is shown where the particle motion is in the plane perpendicular to the direction of wave travel. In the bottom body, travel of the Rayleigh wave (surface wave) is shown. The Rayleigh wave shown in Figure 2.3 is a complex combination of vertical and horizontal motion depending on the depth of below the ground surface and Poisson's ratio.

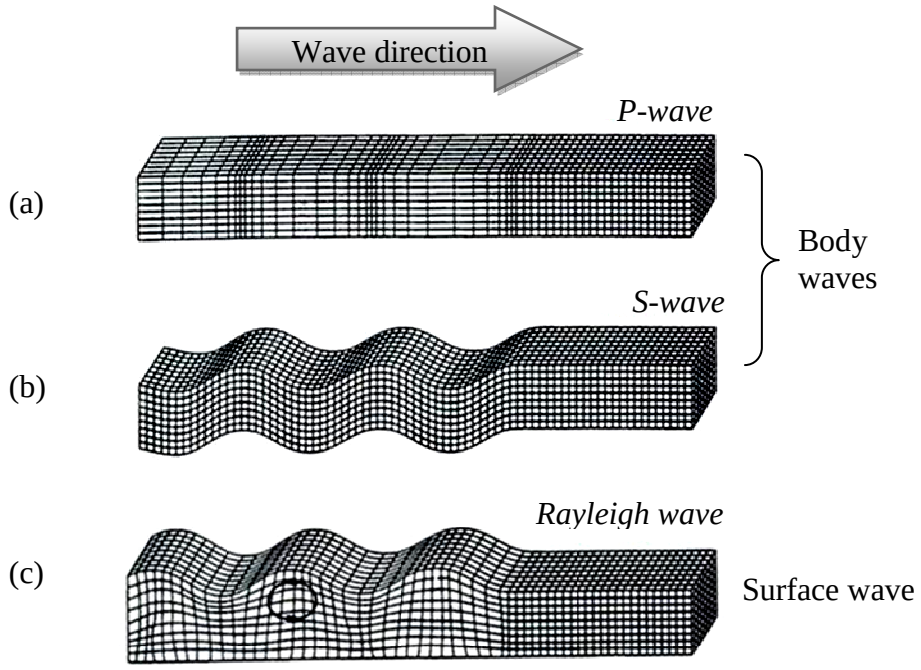

Figure 2.3 Three types of body waves traveling in a continuum media: (a) Primary wave; (b) Secondary wave and; (c) Rayleigh wave.

The newly created Rayleigh waves then travel along the ground surface. Thus, some locations on the ground surface will experience three different types of waves: P-waves, S-waves and Rayleigh waves. These waves transmit energy to the ground surrounding a pile that are potentially damaging to the neighboring structures. The amplitude of this energy associated with each wave depends on many factors, including the pile penetration depth, energy delivered on the pile head, uniformity of the ground and hardness of the ground.

2.2.2 Vibration Damage Criteria

The vibration damage criteria and standards were originally set by the U.S. Bureau of Mines based on the studies of numerous researchers including Nichols et al. (1971), Langefors et al. (1973) and, Edwards et al. (1980). These researchers have correlated the peak particle velocities (PPV) of the ground vibrations with the vibration/blast damage criteria. The amplitudes of these ground vibrations could either be as low as barely noticeable to persons or as high as damaging the neighboring structures and/or equipment. The vibration acceptance levels were set based on (1) human perception; (2) structural damage and; (3) equipment sensitivity.

Pile driving induced ground vibrations can disturb persons and the animals such as birds and fish that live near vibration sources. The human response to transient vibration is summarized in Table 2.1 after Wiss (1974). Ground vibrations can cause damage to the surrounding structures and substructures such as pipelines depending on the maximum amplitude of the vibrations. There are several vibration damage criteria in the literature. Chae (1978) has proposed building vibration criteria for the residential structures based on age and condition as shown in Table 2.2. The impact of construction vibrations induced by different type of sources is also assessed by Dowding (1996). The vibration criteria addressing structural damage based on the type of the structure is shown in Table 2.3. The American Association of State Highway and Transportation Officials

(AASHTO, 1990) also specify the maximum vibration levels for preventing damage to structures from construction or maintenance activities. Table 2.4 summarizes the AASHTO maximum levels.

Table 2.1 Human response to transient vibration

Peak particle velocity, mm/s (in/s)	Human Response
51(2.0)	Severe
23 (0.9)	Strongly perceptible
6 (0.24)	Distinctly perceptible
0.9 (0.035)	Barely perceptible

Table 2.2 Chae building vibration criteria

Category	PPV (Single Blast) mm/s (in/s)	PPV (Repeated Blast) mm/s (in/s)
Buildings of Substantial Construction	100 (4)	50 (2)
Residential, New construction	50 (2)	25 (1)
Residential, Poor Condition	25 (1)	12.5 (0.5)
Residential, Very Poor Condition	12.5 (0.5)	-

Table 2.3 Dowding vibration criteria for structures

Category	Limiting Peak Particle Velocity mm/s (in/s)
Industrial Buildings	50 (2)
Residential	12.5 (0.5)
Residential, New construction	25 (1)
Historic Buildings	12.5 (0.5)
Bridges	50 (2)

Table 2.4 Maximum vibration levels for preventing damage

Category	Particle Velocity mm/s (in/s)
Historic sites or other critical locations	2.5 (0.1)
Residential buildings, plastered walls	5.0-7.5 (0.2-0.3)
Residential buildings in good repair with gypsum board walls	10-12.5 (0.4-0.5)
Engineered structures, without plaster	25-37.5 (1.0-1.5)

The operation of equipment for research, microelectronics manufacturing, medical diagnostics, and vibration sensitive high-tech devices can be adversely affected by vibration. The criteria for designing facilities to house vibration sensitive equipment have been developed by the Institute of Environmental Services. The bandwidth associated with these criteria is the one-third octave band, for which the bandwidth is 23 percent of the center frequency of each band. The generic vibration criteria that relate the one-third-octave root mean square (rms) velocities with the criterion curves developed by Gordon (1991) are given in Table 2.5.

Table 2.5 Generic vibration criteria for vibration-sensitive facilities

Criterion Curve	RMS velocity (f =1 -100Hz) μm/s (μin/s)	Vibration Sensitivity
VC-A	50 (2000)	General laboratory sensitivity
VC-B	25 (1000)	General laboratory sensitivity
VC-C	12.5 (500)	General laboratory sensitivity
VC-D	6 (250)	The most sensitive
VC-E	3 (125)	Semiconductor & research facilities

2.2.3 Empirical Relations for Estimating Vibrations

As the ground waves travel away from the source of vibration, the amplitude of their particle motion attenuates. A portion of this attenuation is caused by the distribution of the generated vibration energy on the area of the continuous wave fronts. This type of attenuation is called radiation or geometric damping and is usually described by the following equation:

$$A_2 = A_1 \left(\frac{r_2}{r_1} \right)^{-\gamma} \tag{2.3}$$

Where A_2 is the amplitude of vibration at distance r_2 from the source, A_1 the amplitude of vibration at distance r_1 from the source and γ the attenuation rate due to radiation damping. The values of γ for different combinations of source location and size are presented by Kim, et al., (2000) as shown in Table 2.6.

Table 2.6 Values of attenuation coefficient due to radiation damping for various combinations of source location and type

Source location	Source type	Induced wave	γ
Surface	Point	Body wave	2.0
		Surface wave	0.5
	Infinite line	Body wave	1.0
		Surface wave	0.0
In-depth	Point	Body wave	1.0
	Infinite line	Surface wave	0.5

In addition to geometric damping, the ground waves attenuate due to the material damping of the soil in which they propagate. The material damping is described by the damping ratio, D. The effects of combined geometric and material damping are defined by the following wave equation after Bornitz (1931) as follows:

$$A_2 = A_1 \left(\frac{r_2}{r_1} \right)^{-\gamma} e^{\alpha(r_2 - r_1)} \tag{2.4}$$

where α is the attenuation coefficient due to material damping. The attenuation coefficient α for soil materials is reported by Woods and Jedele (1985) based on the results of measurements of man-made ground vibrations.

The attenuation coefficient due to material damping, α, depends on the type of soil and the frequency of vibration. This type of material damping is called frequency-dependent damping. Woods & Jedele (1985) recommended the values of the attenuation coefficients based on vibration data they collected on sites including blasting, dynamic compaction, pile driving and other sources of vibrations. The recommended values of the attenuation coefficients for different types of soils are given for vibration frequencies of 5 and 50 Hz in Table 2.7.

A simplified analysis of the mechanics of wave propagation in the ground was also studied by Massarsch, et al. (1995) which leads to the following equation for estimating the values of the attenuation coefficient, α:

$$\alpha = \frac{2\pi f \zeta}{C_R} \tag{2.5}$$

where C_R is the propagation velocity of R-waves, ζ is the damping ratio of the soil and f the frequency of vibration. It is clear in Eq. (2.6) that the value of attenuation coefficient, a, increases linearly with the frequency of vibration and with the damping ratio of the soil material whereas it decreases with the value of C_R (i.e. the stiffer soils have low attenuation rates). The attenuation coefficient α can also be computed for any other frequency, if the value of α is known for one frequency from the following equation:

$$\alpha_2 = \alpha_1 \left(\frac{f_2}{f_1} \right) \tag{2.6}$$

where α_1 is a known value at frequency f_1 and α_2 is an unknown value at frequency f_2.

Table 2.7 Classification of earth materials by attenuation coefficients

Soil Class	Attenuation Coefficient(α), 1/m (1/ft)		Description of Material
	5 Hz	50 Hz	
I	0.009 – 0.033 (0.003 – 0.010)	0.009 – 0.033 (0.003 – 0.010)	Weak or soft soils (shovel penetrates easily); loose soils, dry or partially saturated peat and muck, mud, loose beach or dune sand, recently plowed ground, soft spongy forest or jungle floor, organic soils, topsoil
II	0.003 – 0.009 (0.001 – 0.003)	0.033 – 0.098 (0.010 – 0.030)	Competent Soils (can dig with shovel): most sands, sandy clays, silty clays, gravel, silts, weathered rock
III	0.0003– 0.003 (0.0001 – 0.001)	0.003 – 0.033 (0.001 – 0.010)	Hard soils (cannot dig with shovel, must use pick to break up): dense compacted sand, dry consolidated clay, consolidated glacial till, some exposed rock
IV	<0.0003 (<0.0001)	<0.003 (<0.001)	Hard, competent rock (difficult to break with hammer); bedrock, freshly exposed hard rock

The attenuation coefficient, α, can also be defined as *frequency-independent* as noted by Yang (1995). This new attenuation coefficient, α_0, can be defined by writing Eq. (1.6) in the form of:

$$\alpha_0 = \frac{\alpha}{f} = \frac{2\pi\zeta}{C_R} \tag{2.7}$$

where α_0 is defined in seconds per meter (s/m). Yang (1995) has reported the values of the frequency-independent attenuation rates for soils ranging from loose sands and soft clays to rocks as shown in Table 2.8.

Table 2.8 Values of the frequency-independent attenuation coefficient, α_0, for various soil groups

Soil Group		$\alpha_0 \times 10^{-3}$ (s/m)
Rocks (covering layer within 1.5 to 2.0 m)	Shale, limestone	0.385–0.485
	Sandstone	0.580–0.775
Hard plastic clays		0.385–0.525
Broke stones of medium density Cobbles		0.850–1.100
Plastic clays, Coarse sands and gravels of medium density		0.965–1.200
Soft plastic clays, Silts, Slightly dense, Medium or coarse sands		1.255–1.450
Silty clays, Silts and saturated fine sands		1.200–1.300
Recently deposited clays and unsaturated loose sands		1.800–2.050

Another model for representing the attenuation of ground waves, known as *pseudo-attenuation* model, is presented by Wiss (1981). In his paper, Wiss (1981) obtained a best fit of field data in equation of the following form:

$$v = kd^{-n} \tag{2.8}$$

Where v is the peak particle velocity of wave, d is the distance from source to monitoring location (ft), k is the intercept at d=1 ft (in/s) and n is the slope (log units), or the pseudo-attenuation rate. To include the effect of the hammer's rated energy, Wiss (1981) also developed an equation so called *scaled-distance* equation as follows:

$$v = k\left[\frac{d}{\sqrt{E_n}}\right]^{-n} \tag{2.9}$$

where E_n is the energy of source in consistent units.

Woods and Jedele (1985) gathered field data from construction projects and developed energy-attenuation curves for each vibration energy source at each case. To

plot the peak particle velocity versus the scaled distance, they predicted the attenuation rates based on the ground class given in Table 2.4. Based on this empirical study, the *n*-term is defined as n=1.5 representing *Class II* soils and n=1.1 representing *Class III* soils. Class I and Class IV type of soils are not included in the study, because the soil types on site was neither in very poor condition nor in very good condition. The energy-attenuation relationship presented by Woods and Jedele (1985) is plotted in Figure 2.4.

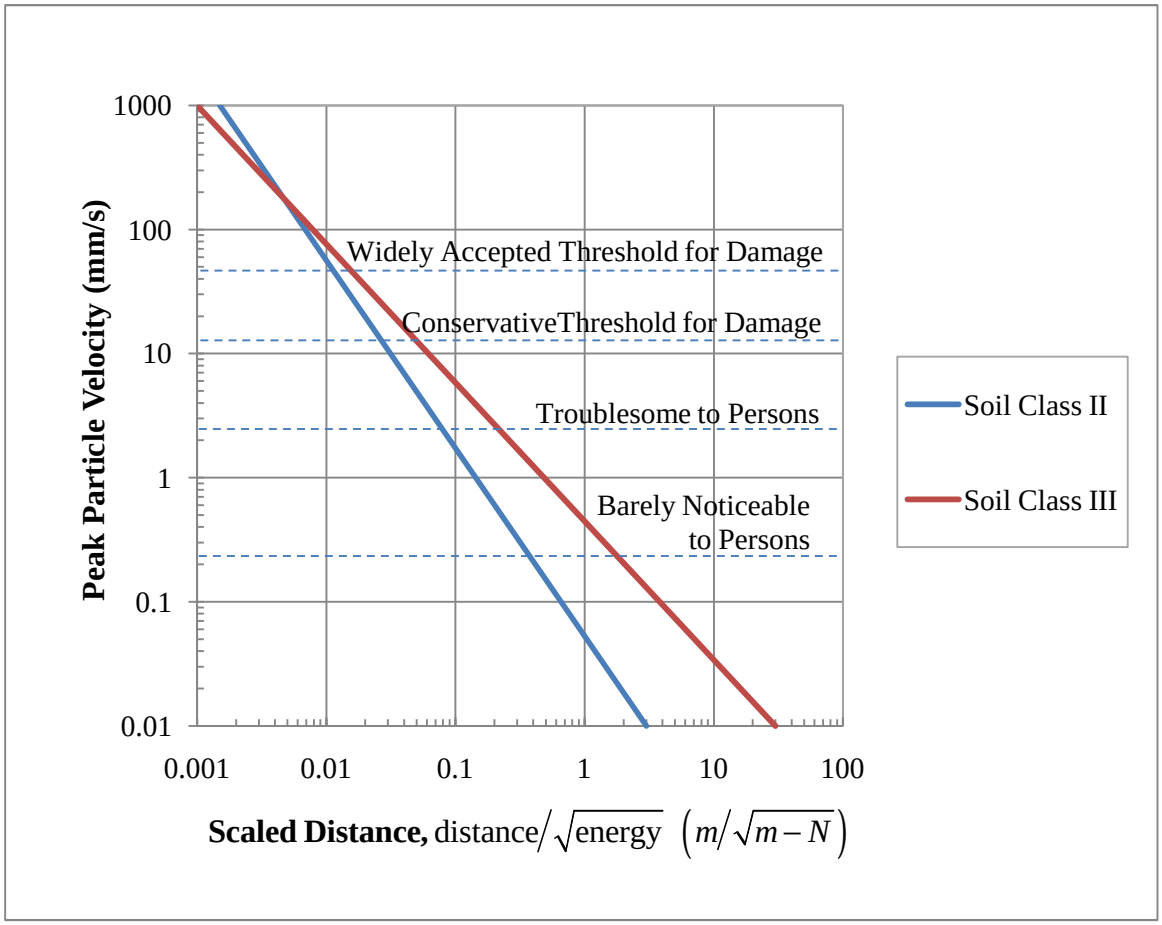

Figure 2.4 The peak velocity versus scaled distance.

2.3 Case Histories

In the last a few decades, many reports have included the results of ground vibration studies due to pile driving. Construction related vibration surveys and studies are being conducted frequently, however not all of them are available in the literature. This section is limited to the review of case histories that exhibit the vibration induced settlement due to impact pile driving.

Lacy and Gould (1985) reported the differential settlements of aeration tanks due to pile driving at a southern Brooklyn site in New York City, NY. The tanks were 5 m high and 80 m wide and were supported by timber piles. The surcharge load on the ground surface due to the weight of the tanks was 100 kPa. The closed-end pipe piles, which had diameters of 273.1 mm, were driven to depths of about 40 m in the close proximity to the existing tanks. A Vulcan 08 impact hammer was used to drive the piles. The soil profile on the site consists of organic fill from the ground surface to a depth of 10 m, followed by fine to coarse, medium dense sand reaching the end of the boring depth of 50 m. After about 100 piles were driven, settlement had already exceeded 25 mm (2 in). To prevent further settlement, the aeration tanks were emptied to reduce the surcharge load, however, the settlement during pile driving reached 70 mm. As a result, the installation of piles was halted. The remaining piles were replaced with augered cast-in-place piles. Vibrations were also monitored using a seismograph on the site. It was observed that the vibration amplitudes on the ground surface ranged from 2.5 to 23 mm/s at all times during pile driving. The attenuation coefficients were estimated from surface measurements as $0.02 – 0.05\ mm^{-1}$ for the upper organic soil layer.

Leathers et al. (1994) reported the densification of sand layers during pile driving at a project located in Boston, MA. The site was in the middle of a block of existing buildings. Two buildings were located immediately adjacent to the pile driving area. The primary soil profile at the site consists of 4 m of granular fill from the ground surface, followed by 8 m of silty clay layered on top of a 24 m of medium dense sand and

gravelly sand followed by a rock layer. A total number of 180 precast 360 × 360 mm concrete piles with lengths ranging from 29 to 39 m were driven on the site. A diesel hammer with a rated energy of 54 kJ was used for installing the piles. The measured peak particle velocities (PPV) on the ground surface ranged from 6.4 to 15 mm/s. The settlements observed after pile driving varied between 18 and 54 mm (0.7 and 2.1 in). It was observed that the settlements measured on the ground surface were almost identical to the ones measured on top of the sand layer. It was also noticed that the settlement occurred only during driving, and did not continue once the driving was complete. Consequently, the in situ measurements of settlements strongly indicated that the vibration induced settlements only occurred in the sand layer, and most likely, it happened due to the densification of the granular particles.

Hope and Hiller (2000) performed an extensive study of vibrations due to impact pile driving. They compared a number of existing prediction models. They then applied these results to a site where vibrations were carefully monitored during driving of an H-section driven by a Banut 700 piling rig, which has a hydraulic hammer with a ram weighing 11 kips. The rated energy of this hammer is nominally 29,000 ft-lbs. They recorded the peak particle velocities while also keeping careful track of the depth of penetration of the pile. They concluded that, while the predictions made by previous studies did give a reasonable upper bound prediction, that did not help to explain the wide range of vibration measurements observed as pile driving proceeded. They also noted that vibrations tended to increase as the stiffness of the soil increased.

Ashraf et al. (2002) drove 42 close-ended steel pipe piles that were 14 inches in diameter through fine to medium sands. Vibration mitigation measures included pre-augering the top 20 feet, as well as encasing the top 8 feet in a larger diameter steel shell filled with sand. The piles were driven with a Vulcan 01 hammer, which has a rated energy of 15,000 ft-lbs. The results showed that the measured PPVs are scattered out of the envelopes based on the Bornitz Equation.

In addition to the discussed cases above, many sites have been investigated for settlements caused by pile driving vibrations in the last few decades. Among those are sites are Leningrad (Dalmatov, et al., 1967), Embarcadero (Clough & Chameau, 1980), Lesaka (Picornell & del Monte, 1985), Cedar Creek (Lacy et al., 1986) and Tri-beca (Lacy et al., 1994). Settlements at the nearby foundation soils are recorded from as low as 6.0 mm to as high as 250 mm. Table 2.9 (modified after Kim et al., 1996) summarizes the measured settlements and pile driving vibration amplitudes recorded at different sites.

Table 2.9 Case histories of vibration-induced settlement

Investigated Sites	Measured Vibration Amplitudes (mm/s)	Measured Settlement (mm)
Leningrad (Dalmatov, et al., 1967)	2.8	6 – 11
Embarcadero (Clough & Chameau, 1980)	1 – 5	8 – 51
Brooklyn, West (Lacy et al., 1985)	2.5 – 15.2	61
Brooklyn, South (Lacy et al., 1994)	17.5	70
Back Bay (Leathers, 1994)	6.4 – 15	18 – 54
Lesaka (Picornell & del Monte, 1985)	17.5	250
Cedar Creek (Lacy et al., 1986)	5 – 10	13 – 19
Tri-beca (Lacy et al., 1994)	2.5 – 18	38 – 69

2.4 Numerical Studies

Mabsout et al. (1995) studied the analysis of impact pile driving using the finite element method. An axisymmetric finite element model is developed for this study, which takes into account the nonlinear behavior of the soil. The model consists of a cylindrical closed end concrete pile, which has a diameter of 0.25 m. It was driven into undrained, normally consolidated clayey soils with varying pre-bored depths of 6, 12 and 18 m. A linear elastic dynamic formulation was used for the pile. The soil was modeled using the bounding-surface plasticity model for cohesive soils after Kaliakin and Dafalias

(1989). A single blow, which was represented by a periodic forcing function with a peak force of 2000 kN, is applied on top of the pile.

First, the effect of pre-bored depths of the driven pile was investigated. Top displacements, velocities and accelerations were compared at pre-bored levels of 6, 12 and 18 m. The displacements varying from 0.05 m to 0.60 m were computed. Next, the change in the soil resistance with varying pre-bored depths was presented. While the tip resistance changed between 80 kN and 100 kN, the shaft resistance increased with the pre-bored depths varying from 50 kN to 400 kN. Then, the evolution of the state of deformation and stress in soil during the course of driving was investigated. Substantial increase in pore-water pressure, as much as six times of the vertical effective stress, was observed near the pile tip. The pore pressures remained almost same along the pile shaft. Finally, the permanent settlement of the pile tip and the shaft and tip resistances were compared with analytical methods. The study was only limited to the dynamic response of the pile and did not consider the wave propagation in the surrounding soil.

Ramshaw et al. (1998) conducted a finite and infinite element study using the finite element package ABAQUS. They modeled a 30-inch diameter, 70-foot long cast-in-place concrete pile that was dynamically load tested using a 4.8 kip drop hammer with a 1.2 m drop height. The pile was instrumented with a load cell to measure the force versus time. Vibrations were recorded at 18 and 54 ft from the pile. To predict the vibration records, Ramshaw et al. (1998) used a triangular impact force pulse of 5 seconds in duration. The finite element model was assumed to have two layers with purely elastic properties. The model generated compressive, shear and Rayleigh waves, and produced an expected ground movement in the radial direction of motion. The authors reported the match between measured and predicted values was satisfactory. However, the peak magnitude of the vibration at 54 feet from the pile was over predicted by a factor of 6 and the signal at 18 ft appeared to be overly damped.

Masoumi et al. (2006) presented a new numerical model for the prediction of free field vibrations due to vibratory and impact pile driving. The free field vibrations were calculated using a coupled finite element-boundary element (FE-BE) method based on a subdomain formulation. While the pile was modeled as the bounded domain using the FE method, the soil was modeled as unbounded domain using the BE method. The soil medium was assumed linear elastic with frequency independent material damping. The small deformation theory was employed for the model. The pile was embedded in a horizontally layered soil. Ground vibrations due to impact pile driving were studied using a concrete pile with a circular cross-section. The impact of the hammer was represented by a force function.

The peak particle velocities (PPV) versus the distance from the pile were computed for impact energy of 19.2 kJ at a penetration depth of 2 m, and impact energy of 3.4 kJ at a penetration depth of 10 m. The predicted vibrations are compared with the results of field measurements reported by Wiss (1981). The PPVs were overestimated compared with the results of the field measurements. It was concluded that during impact pile driving ground vibrations in the near field were controlled by the shear waves, whereas the ground vibrations on the far field were controlled by the Rayleigh (surface) waves. Although, this study focused on the dynamic response of a pile and free field vibrations, it has several shortcomings such as the lack of soil-pile friction and the lack of soil plasticity in the model. In a following study published by Masoumi et al. (2008), the results of in situ measurements dynamic pile testing from a construction site in Louvain-la-Neuve, Belgium were compared with the results from the coupled FE-BE model. Two piles with diameters of 0.46 m and embedment lengths of 8.55 m and 6.02 m were selected for dynamic testing on this site. The response of these piles and the resulting free field vibrations during dynamic loading were studied with two different material damping ratios. The vertical velocities at different distances from the pile head were computed and compared with the site results. Although the range of the velocities

had a good agreement, the dissipation of the stress waves was not represented accurately. It was concluded that at high frequencies and at long distances from the pile, results depend on the material damping ratio of the soil.

2.5 Summary and Discussion

In this chapter, the literature is reviewed for the studies conducted on pile driving and wave propagation in the ground. In the first section, the organization of this chapter is presented. In the second section, the generation of ground vibrations due to impact pile driving is explained, and the mechanics of wave propagation in soils is described. Then, vibration acceptance levels for human perception and threshold damage are discussed. Next, the empirical relations that are widely used to predict the peak particle velocities of ground vibrations are presented. In the third section, five case histories regarding the settlement of granular soils due to pile driving are presented. These case studies have shown that vibration amplitudes as low as 6.4 mm/s (0.25 in/s) can cause settlement of adjacent foundation soils due to the densification of the granular soils. In the fourth section, recent numerical studies that focus on simulating impact pile driving and wave propagation are presented. The first study (Mabsout, 1996) has only focused on dynamic response of a single pile under a single hammer blow. Wave propagation in soils was not covered by that study. The second study has covered the dynamic loading of a pile and wave propagation in soils. However, since the material damping coefficients were not introduced and explained clearly, the free field vibrations were computed five times the magnitude of the measured amplitudes in the far field. In the third study, the proposed model has simulated a single blow and predicted the ground vibrations in the far field. Although the model predicted the peak particle velocities within a reasonable accuracy in the close proximity of the pile, it did not predict the vibrations in the far field accurately.

CHAPTER 3

COUPLED ANALYSIS OF CONSOLIDATION PROBLEMS USING THE FINITE ELEMENT METHOD

3.1 Introduction

Soils are porous materials with a complex structure consisting of a solid skeleton of grains in contact with each other and voids filled with air and/or water or other fluid. Soil consolidation is the change in the volume of a porous medium with low permeability due to the drainage of water filling the pores as it responds to the increase in the total stress. Consolidation settlement occurs during dissipation of excess pore water pressure, and it is controlled by the gradual expulsion of water from voids in the soil leading to the associated compression of the soil skeleton. The aim of this chapter is to get a deeper understanding of the soil consolidation from an engineering point of view. It describes the theory of soil consolidation and the derivation of coupled solution numerical scheme using the finite element method in four sections. The first section overviews the literature and gives a comprehensive background on the numerical studies focusing on the theory of soil consolidation. Second section presents the derivation of governing equations for the consolidation of saturated porous medium for the analysis of saturated two-phase flow problems in deforming medium. For the full analysis, this section explains the averaging process, kinematic equations, balance equations and constitutive equations in details. Third section outlines the framework for the finite element formulation of the consolidation problem using the coupled displacement/pore pressure elements. The final section illustrates numerical examples for one-dimensional and two-dimensional consolidation problems.

3.2 Background

The theory of soil consolidation was first introduced by Terzaghi based on the assumption that the soil skeleton is elastic, the solid particles or grains constituting the

soil are bounded together by certain molecular forces and the voids are filled with water (Terzaghi, 1925). Terzaghi's consolidation theory is based on the principle of effective stress, which assumes that the portions of the material stress carried by the porous soil skeleton and by water filling the voids. The effective stress is the portion of the material stress that is transmitted through the solid phase of the porous skeleton. The pore fluid pressure or pore pressure is the portion of the material stress transmitted through the pore fluids. Although Terzaghi's consolidation theory is a powerful technique for the solution of a various number of different consolidation problems, it is restricted to only one-dimensional problems and ignore the dynamic behavior of soils.

Biot (1941) was first to extend Terzaghi's consolidation theory for the analysis of three-dimensional consolidation problem. He proposed a multi-phase continuum formulation for saturated porous media where the fluid flow through the solid phase obeys Darcy's law. He introduced a solution for consolidation problems, which is based on the principle of coupling the equations of pore water pressure with the equations of deformation of the porous solids. In his widely known theory, the following assumptions are made: (1) the material is isotropic and linear elastic; (2) the small strains theory is valid; (3) the pore water is incompressible; (4) the water may contain air bubbles and; (5) the water flows through the porous skeleton obeying Darcy's law (Biot 1941). Based on these assumptions, Biot proposed a solution for time-dependent displacements, pore fluid pressures, effective stresses and strains for problems of consolidation and the settlement of foundations. He then extended his consolidation theory to the analysis of porous anisotropic solids and porous viscoelastic anisotropic solids (Biot, 1955; 1956).

Although the consolidation theory of Biot did not take into account many important characteristics of soil such as material and geometrical nonlinearities, and path-dependency of stress-strain relationship, modern numerical analysis of soil consolidation is widely founded on Biot's Theory. Many researchers in geophysics, soil and rock

mechanics have made significant contributions toextend Biot's coupled equations for developing more realistic soil models.

Sandhu and Wilson (1969) used the finite element method to solve Biot's Theory as initial boundary value problems. In their work, they applied variational principles to the field equations of fluid flow treating the porous media as a fully saturated elastic continuum. Then, they used the finite element method to derive the weak form of the governing equations and solved the resulting coupled equations.

Ghaboussi and Wilson (1973) then presented a multi-dimensional finite element numerical scheme to solve Biot's dynamic field equations for saturated porous elastic solids. They also incorporated the pore fluid compressibility in Biot's formulation. Their solution was applicable for the analysis of dynamic soil-structure interaction and wave propagation problems in saturated porous media.

Zienkiewicz et *al.* have made significant contributions in extending Biot's theory of consolidation to include liquefaction of granular materials and wave propagation in saturated porous media (Zienkiewicz et *al.*, 1976;Zienkiewicz 1980; Zienkiewicz, Wood, et *al*. 1984; and Simon, et *al*. 1986). They have incorporated several different nonlinear constitutive models into their numerical models such as elastoplastic and hyperbolic models. They included fluid and solid compressibility, creep, and void ratio dependent permeability in their studies (Lewis, Roberts and Zienkiewicz 1976). Zienkiewicz et *al.* have also solved dynamic soil-structure interaction problems such as analysis of the Lower San Fernando dam under earthquake (Zienkiewicz and Simon, 1984).

Lewis and Schrefler (1987) carried out a comprehensive study to extend and modify Biot's coupled formulation using the volume fraction concept of the Modern Porous Media Theory. They developed field equations for solid, fluid and air phases for saturated and partially saturated flow in a deforming porous media. They discussed the application of the finite element method to the consolidation problems using linear and non-linear constitutive models.

3.3 Formulation of Coupled Consolidation Equations

The modern macroscopic porous media theory is a combination of the volume fraction concept and elements of the mixture theory, which was introduced by Green and Naghdi (1965), and Eringen and Ingram (1965 and 1967). Within the framework of the modern porous media theory, a saturated porous medium is viewed as an immiscible mixture of all constituents, so that it can be treated with the methods of continuum mechanics. The volume fraction concept contains the introduction of volume fractions, which relate the volume elements of the individual constituents such as solid, fluid or air to the bulk volume element. In accordance with the volume fraction concept, all geometric and physical quantities, such as motion, deformation, and stress are defined in a total control space, which is formed by the porous solid. Thus, the geometric and physical quantities can be interpreted as the statistical average values of the real quantities.

In this section, a simplified version of Biot's Theory is described combined with the modern macroscopic porous media theory based the modern volume fraction concept. The aim is to develop a numerical scheme for linear consolidation problems employing the finite element method. The consolidation problem is governed by macroscopic balance equations, which are:

(1) Mass balance equation, and

(2) Linear momentum balance equation.

The following assumptions are made for the model presented in this chapter:

- The porous medium is saturated. It is composed of only *two phases*, solid and water. Air and other gases are not present in the pores.
- The porous medium is composed of *incompressible* solid and water phases at the microscopic level. The averaged density of each phase is constant. The average density of the mixture can vary due to the volume fraction.

- *Small strains* and rotations are considered for the deformation of the porous medium. Geometric non-linearity is neglected.
- *Quasi-static conditions* are considered for the deformation of the porous medium and the flow of the pore fluid. The solid and fluid accelerations are neglected.
- Consolidation occurs under *isothermal conditions*. This means that energy balance equation is no longer necessary.

In the following subsections, the principle of averaging quantities is discussed first along with the kinematic equations of a multi-phase medium. The mass balance and linear momentum balance equations are derived next. Then, the governing equations for the analysis of a saturated two-phase (solid and fluid) porous medium are described. Next, the constitutive framework with an assumption of small strain elasticity theory under isothermal and isotropic conditions is discussed. Finally, the principle of effective stress in porous media is explained.

3.3.1 Averaging Principles

The non-homogeneous configuration of soil particles makes it difficult to model the soil heterogeneity rigorously at the microscopic level. Thus, in continuum mechanics, it is preferred to replace the micro-heterogeneous medium with a macro-homogeneous one, which macroscopically behaves in the same manner. This approach can be accomplished by averaging the geometric and physical quantities, such as motion, deformation and stress defined in a total control space. The averaging procedure exhibits how to link the equations describing the motion of all phases constituting the porous medium at the microscopic behavior (R.W. Lewis, 1998).

A multiphase medium can be defined by a total volume $\boldsymbol{\Omega}$ and bounded by a surface $\boldsymbol{\Gamma}$ with the constituent α and a partial volume V^{α}. A representative elementary volume (REV) which is an averaged volume element can be defined as dv. The REV is

considered small enough to be treated as a point of the heterogeneous medium (K.Z. Markov, 2000). The position of the center of the REV is defined by a position vector ***x***. The position of the microscopic volume element dv_m is considered as $\boldsymbol{r}$. The volume of the phase (constituent) α within a REV, which is called the average volume element, dv^α is defined as

$$\gamma^\alpha(\mathbf{r},t)=\begin{cases}1, & r\in dv^\alpha\\ 0, & r\in dv^\beta \alpha\neq\beta\end{cases} \tag{3.1}$$

where γ^α is the phase distribution function. The volume of a REV for phase-α is defined as

$$dv^\alpha(\mathbf{x},t)=\int_{dv}\gamma^\alpha(\mathbf{r},t)dv_m \tag{3.2}$$

in which dv_m is the microscopic volume element and the phase α and position vector **r** are defined as

$$\alpha=1,2,3,...,n$$
$$\mathbf{r}=x+\xi$$

The area of a REV for phase-α is

$$da^\alpha(\mathbf{x},t)=\int_{dv}\gamma^\alpha(\mathbf{r},t)da_m \tag{3.3}$$

where da_m is the microscopic area element.

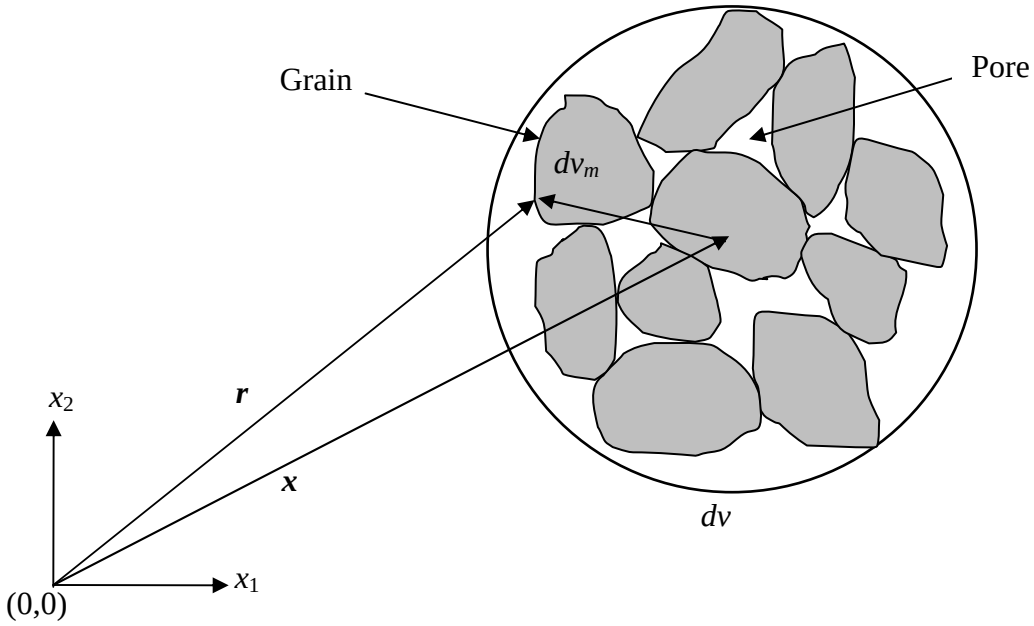

Figure 3.1 A representative elementary volume of a porous medium.

The volume fractions η^α relate the volume elements of the individual phases to the bulk volume element, where α denotes the individual phases (i.e. α=s: Solid, α=w: Water). The volume fraction is defined as follows:

$$\eta^\alpha = \frac{dv^\alpha}{dv} = \frac{1}{dv}\int_{dv} \gamma^\alpha(\mathbf{r},t)dv_m \tag{3.4}$$

with

$$\sum_{\alpha=1}^{n} \eta^\alpha = 1 \tag{3.5}$$

In this thesis, only two phases, solid and water, will be considered for the physical description of the soil skeleton. The solid mass and water are denoted by the superscripts *s* and *w*, respectively. The partial volumes of solid and water are denoted by dV^s and dV^w, respectively. The volume fractions are defined as

$$\eta^s = \frac{dV^s}{dV} = 1 - n$$
$$\eta^w = \frac{dV^w}{dV} = nS_w \tag{3.6}$$

in which n is the porosity of the soil skeleton and S_w is the degree of saturation. The porosity can also be defined in terms of void ratio, e as $n=e/(1+e)$. The averaged quantities are obtained by integrating (averaging) a microscopic quantity over the volume dv, mass density ρdv or the area da of a REV. The following averaging operators may be used to average a microscopic field variable $\zeta(\boldsymbol{x},t)$. The volume average operator at phase-α is defined as

$$\zeta_v^\alpha(\boldsymbol{x},t) = \frac{1}{dv}\int_{dv} \zeta(\boldsymbol{r},t)\gamma^\alpha(\boldsymbol{r},t)dv_m \tag{3.7}$$

The mass average operator at phase-α is

$$\zeta_m^\alpha(\boldsymbol{x},t) = \frac{\int_{dv} \rho(\mathbf{r},t)\zeta(\boldsymbol{r},t)\gamma^\alpha(\boldsymbol{r},t)dv_m}{\int_{dv} \rho(\mathbf{r},t)\gamma^\alpha(\boldsymbol{r},t)dv_m} \tag{3.8}$$

The area average operator at phase-α is

$$\zeta_a^\alpha(\boldsymbol{x},t) = \frac{1}{dv}\int_{dv} \zeta(\boldsymbol{r},t)\cdot\mathbf{n}\gamma^\alpha(\boldsymbol{r},t)dv_m \tag{3.9}$$

The volume averaged density of each phase-α, ρ_α can be defined using the volume average operator as:

$$\rho_\alpha = \eta^\alpha \rho^\alpha \tag{3.10}$$

where

$\rho_\alpha =$ macroscopic average density,
$\eta^\alpha =$ volume fraction of elemental volume dV at phase-α, and
$\rho^\alpha =$ microscopic mass density.

From this definition, the volume averaged density ρ of a two-phase mixture consisting of solid mass and water can be expressed as follows:

$$\rho = \sum_{\alpha=s,w} \rho_\alpha = \rho_s + \rho_w = (1-n)\rho^s + nS^w\rho^w \tag{3.11}$$

where ρ^s and ρ^w are intrinsic (microscopic) densities meaning densities at individual phases, and ρ_s and ρ_w are the partial densities (averaged over the volume) of the phases.

The area averaged Cauchy's stress tensor for an individual phase-α is defined as:

$$\boldsymbol{\sigma}_\alpha = \eta^\alpha \boldsymbol{\sigma}^\alpha \tag{3.12}$$

where

$\boldsymbol{\sigma}_\alpha =$ macroscopic average Cauchy stress tensor,
$\eta^\alpha =$ volume fraction of elemental volume dV at phase-α, and
$\boldsymbol{\sigma}^\alpha =$ microscopic Cauchy stress tensor.

For a two-phase material averaged Cauchy stress can be defined as:

$$\boldsymbol{\sigma} = \sum_{\alpha=s,w} \boldsymbol{\sigma}_\alpha = \boldsymbol{\sigma}_s + \boldsymbol{\sigma}_w = (1-n)\boldsymbol{\sigma}^s + nS^w\boldsymbol{\sigma}^w \tag{3.13}$$

where $\boldsymbol{\sigma}^s$ and $\boldsymbol{\sigma}^w$ denote Cauchy's stress tensors of the individual phases, and $\boldsymbol{\sigma}_s$ and $\boldsymbol{\sigma}_w$ are the stresses averaged over the surface of the REV.

3.3.2 Kinematic Equations

The kinematics of a multiphase medium i.e. solid-fluid phase, can be described either by a spatial or *Eulerian* coordinate system denoted by $\boldsymbol{x}$, or by a *Lagrangian* or material coordinate system denoted by $\boldsymbol{X}$. Assuming the soil skeleton as a material reference volume, the motion function is defined as

$$\mathbf{x}^\alpha = \mathbf{x}^\alpha(\mathbf{X}^\alpha, t) \tag{3.14}$$

In which x^α is the position of each spatial point at time t and a function of its replacement in a chosen reference configuration X^α at the current time, *t*. The deformation gradient tensor, $\mathbf{F}^\alpha$ can be defined as

$$\mathbf{F}^\alpha = grad\ \mathbf{x}^\alpha \tag{3.15}$$

where *grad* is the gradient operator and defined as

$$grad = \left[\frac{\partial}{\partial x}, \frac{\partial}{\partial y}, \frac{\partial}{\partial z} \right]^T \tag{3.16}$$

The velocity and acceleration fields in spatial coordinate system are as follows

$$\mathbf{v}^\alpha = \mathbf{v}^\alpha(\mathbf{x}^\alpha, t) \tag{3.17}$$

$$\mathbf{a}^\alpha = \frac{\partial \mathbf{v}^\alpha}{\partial y} + grad\ \mathbf{v}^\alpha \cdot \mathbf{v}^\alpha \tag{3.18}$$

The material time derivative of any differentiable function $f^\alpha(\mathbf{x}, t)$, can be written in terms of its spatial description where α denotes the phase of the moving particles as follows

$$\frac{D^\alpha f^\alpha}{Dt} = \frac{\partial f^\alpha}{\partial t} + grad\ f^\alpha \cdot \mathbf{v}^\alpha \tag{3.19}$$

Furthermore, if the material derivative operator is in another phase, presuming a prescribed phase β, then the above equation can be rewritten as

$$\frac{D^\beta f^\alpha}{Dt} = \frac{\partial f^\alpha}{\partial t} + grad\ f^\alpha \cdot \mathbf{v}^\beta \tag{3.20}$$

Subtracting Eq. (3.20) from Eq. (3.21) yields

$$\frac{D^\beta f^\alpha}{Dt} = \frac{\partial f^\alpha}{\partial t} + grad\ f^\alpha \cdot \mathbf{v}^{\beta\alpha} \tag{3.21}$$

where

$$\mathbf{v}^{\beta\alpha} = \mathbf{v}^\beta - \mathbf{v}^\alpha \tag{3.22}$$

is the velocity of the β phase with respect to α phase.

3.3.3 Balance Equations

The balance equation for a continuum at the microscopic level for a quantity ψ at any phase α can be written as

$$\frac{\partial(\rho\psi)}{\partial t} + div(\rho\psi\dot{\boldsymbol{r}}) - div\ \boldsymbol{i} - \rho\boldsymbol{b} = \rho G \tag{3.23}$$

in which div is the divergence operator, $\dot{\boldsymbol{r}}$ is the local value of the velocity field of the α-phase, $\boldsymbol{i}$is the flux vector, $\boldsymbol{b}$ is the external supply of ψ and,G is the net production of ψ.

A general average macroscopic balance equation is obtained from the microscopic balance equation by multiplying it with the distribution function $\psi^{\alpha}(\boldsymbol{r},t)$ and by integrating this product over the volume element dv and over the total volume V by using the previously defined volume averaging operator $\zeta(\boldsymbol{x},t)$ as follows:

$$\int_{V}\zeta(\boldsymbol{x},t)dV=\int_{V}\left[\frac{1}{dv}\int_{dv}\zeta(\boldsymbol{r},t)\gamma^{\alpha}(\boldsymbol{r},t)dv_{m}\right]dV \tag{3.24}$$

Continuing the averaging process and applying the divergence theorem by (Eringen, et al., 1964) allows us to write the macroscopic balance equation in more concise form as:

$$\frac{\partial}{\partial t}(\rho_{\alpha}\psi^{\alpha})+div(\rho_{\alpha}\psi^{\alpha}\mathbf{v}^{\alpha})-div\ \mathbf{i}^{\alpha}-\rho_{\alpha}\left[b^{\alpha}+e^{\alpha}(\rho\psi)+I^{\alpha}\right]=\rho_{\alpha}G^{\alpha} \tag{3.25}$$

where ρ_{α} is the volume averaged value of mass density of α-phase, ψ_{α} is any conserved generic quantity,i^{α} is the flux vector associated with ψ_{α}, b^{α} is the external supply of ψ_{α}, G^{α} is the net production of ψ_{α}, $\mathbf{v}^{\alpha}$ is the mass averaged velocity defined as

$$\mathbf{v}^{\alpha}=\dot{\mathbf{x}}^{\alpha}(\mathbf{x},t)=\dot{\mathbf{r}}^{\alpha}(\mathbf{x},t)=\frac{1}{dv\rho_{\alpha}}\int_{dv}\rho(\mathbf{r},t)\dot{\mathbf{r}}(\mathbf{r},t)\gamma^{\alpha}(\mathbf{r},t)dv_{m} \tag{3.26}$$

$e^{\alpha}(\rho\psi)$ is the mass exchange between different constituents defined as:

$$e^{\alpha}(\rho\psi)=\frac{1}{\rho_{\alpha}dv}\sum_{\alpha\neq\beta}\int_{da^{\alpha\beta}}\rho\psi(\mathbf{w}-\dot{\mathbf{r}})h^{\alpha\beta}da_{m} \tag{3.27}$$

and I^{α} is the exchange of ψ_{α} due to mechanical interactions between the constituents, which can be written as

$$I^{\alpha}=\frac{1}{\rho_{\alpha}dv}\sum_{\alpha\neq\beta}\int_{da^{\alpha\beta}}\mathbf{n}^{\alpha\beta}\cdot\mathbf{i}da_{m} \tag{3.28}$$

The averaged macroscopic mass balance equation of a constituent α is obtained from Eq. (3.25) by specifying the following variables

$$\psi^{\alpha}=1, \quad \boldsymbol{i}^{\alpha}=0, \quad b^{\alpha}=0, \quad I^{\alpha}=0, \quad G^{\alpha}=0 \tag{3.29}$$

$$\frac{\partial}{\partial t}\rho_{\alpha}+div(\rho_{\alpha}\mathbf{v}_{\alpha})=\rho_{\alpha}e^{\alpha}(\rho) \tag{3.30}$$

with

$$\sum_{\alpha=1}^{\kappa}\rho_{\alpha}e^{\alpha}(\rho)=0 \tag{3.31}$$

where ρ_{α} is the phase-averaged density, $\mathbf{v}_{\alpha}$ is the mass-averaged velocity and $\rho_{\alpha}e^{\alpha}(\rho)$ is the mass exchange term of the constituent α.

For solid phase, considering that the mass exchange term on the right hand side of Eq. (3.30) is zero, the mass balance equation becomes

$$\frac{\partial\rho_{s}}{\partial t}+div\ (\rho_{s}\mathbf{v}_{\alpha})=0 \tag{3.32}$$

The material derivative of phase-averaged solid mass density ρ_s can be written using Eq. (3.20) as follows

$$\frac{D^{s}\rho_{s}}{Dt}=\frac{\partial\rho_{s}}{\partial t}+grad(\rho_{s}\cdot\mathbf{v}^{s}) \tag{3.33}$$

Introducing Eq. (3.33) into Eq. (3.32) and considering that the relation between the gradient operator and divergence operator defined as

$$div\ (\rho_{s}\mathbf{v}^{s})=\rho_{s}div\ \mathbf{v}^{s}+grad(\rho_{s}\cdot\mathbf{v}^{s}) \tag{3.34}$$

The averaged macroscopic mass balance equation for solid phase becomes

$$\frac{1-n}{\rho_{s}}\frac{D^{s}\rho^{s}}{Dt}-\frac{D^{s}n}{Dt}+(1-n)div\ \mathbf{v}^{\mathbf{s}}=0 \tag{3.35}$$

For fluid phase, the macroscopic mass balance equation is written from Eq. (3.30) as follows

$$\frac{\partial \rho_w}{\partial t} + \nabla^T (\rho_w \mathbf{v}^w) = \rho_w e^w(\rho) \tag{3.36}$$

The material form of the mass balance equation for fluid is written in a similar way to the solid phase as

$$\frac{D^w \rho_w}{Dt} + \rho_w div\ \mathbf{v}^w = \rho_w e^w(\rho) \tag{3.37}$$

The material derivative of Eq. (3.37) in the solid phase can be written using Eq. (3.21) and Eq. (3.22) as,

$$\frac{D^s \rho_w}{Dt} + \mathbf{v}^{ws} \cdot div \rho_w + \rho_w\ grad(\mathbf{v}^s + \mathbf{v}^{ws}) = 0 \tag{3.38}$$

Eq. (3.38) can be expanded as follows

$$\frac{n}{\rho^w}\frac{D^s \rho^w}{Dt} + \frac{D^s n}{Dt} + \frac{n}{S^w}\frac{D^s S^w}{Dt} + \frac{1}{S^w \rho^w} div\ (nS^w \rho^w \mathbf{v}^{ws}) + ndiv\ \mathbf{v}^s = 0 \tag{3.39}$$

To eliminate the $D^s n/Dt$ term in the above equation, the mass balance equations for solids and fluids can be combined. The combination of Eq. (3.35) and Eq. (3.39) yields

$$\frac{1-n}{\rho_s}\frac{D^s \rho^s}{Dt} + \frac{n}{\rho^w}\frac{D^s \rho^w}{Dt} + \frac{n}{S^w}\frac{D^s S^w}{Dt} + \frac{1}{S^w \rho^w} div\ (nS^w \rho^w \mathbf{v}^{ws}) + div\ \mathbf{v}^s = 0 \tag{3.40}$$

The Darcy's law for fluids can be expressed in the following form

$$nS_w \mathbf{v}^{ws} = \frac{\mathbf{k}}{\mu^w}\left(-grad\ p^w + \rho^w \mathbf{g}\right) \tag{3.41}$$

where

$\mathbf{v}^{ws}$ is the relative velocity defined as

$$\mathbf{v}^{ws} = \mathbf{v}^w - \mathbf{v}^s \tag{3.42}$$

k is the permeability tensor defined as

$$\mathbf{k} = \begin{bmatrix} k_x & 0 & 0 \\ 0 & k_y & 0 \\ 0 & 0 & k_z \end{bmatrix} \tag{3.43}$$

p^w is the hydrostatic pressure and μ^w is the dynamic viscosity defined as

$$\mu^w = \rho^w \nu \tag{3.44}$$

g is the body force related to the gravity forces defined as

$$\mathbf{g} = \left\{ g_x, g_y, g_z \right\}^T \tag{3.45}$$

Introducing Darcy's law to Eq. (3.40) and assuming that S^w=1 (fully saturated case) yields

$$\frac{1-n}{\rho_s}\frac{D^s \rho^s}{Dt} + \frac{n}{\rho^w}\frac{D^s \rho^w}{Dt} + div\left(\frac{\mathbf{k}}{\mu^w}\left(-grad\ p^w + \rho^w \mathbf{g} \right) \right) + div\ \mathbf{v}^s = 0 \tag{3.46}$$

Furthermore, under isothermal conditions, the material derivatives can be defined in terms of hydrostatic pressure and Biot's constant α as

$$\frac{1-n}{\rho_s}\frac{D^s \rho^s}{Dt} = \frac{\alpha - n}{K_s}\frac{D^s (p^w S^w)}{Dt} - (1-\alpha)\ div\ \mathbf{v}^s \tag{3.47}$$

$$\frac{n}{\rho^w}\frac{D^s \rho^w}{Dt} = \frac{n}{K_w}\frac{D^s p^w}{Dt} \tag{3.48}$$

where K_s is the bulk modulus of the grain material and K_w is the bulk modulus of the fluid. Assuming that the porous media is fully saturated (S_w=1), substituting Eq. (3.47) and Eq. (3.48), into Eq. (3.46) yields

$$\left(\frac{\alpha - n}{K_s} + \frac{n}{K_w} \right)\frac{\partial p^w}{\partial t} + div\left(\frac{\mathbf{k}}{\mu^w}\left(-grad\ p^w + \rho^w \mathbf{g} \right) \right) + \alpha\ div\ \mathbf{v}^s = 0 \tag{3.49}$$

Eq. (3.43) is also known as the *continuity equation*. It should be noted that for incompressible grain material $1/K_s$=0 and α=1.

The continuity equation can be rewritten for "incompressible grain material" ($1/K_s$=0) and "compressible fluid" (α=1). Assuming that the porous medium is fully saturated (S_w=1), the continuity equation takes the final form of:

$$\frac{n}{K_w}\frac{\partial p}{\partial t} + div\left(\frac{\mathbf{k}}{\mu^w}\left(-grad\ p + \rho^w \mathbf{g} \right) \right) + div\ \mathbf{v}^s = 0 \tag{3.50}$$

The linear momentum balance equations at the macroscopic level are derived using the general macroscopic balance equation. The variables used in Eq. (3.23) are defined as follows:

$$\psi^{\alpha} = \boldsymbol{v}^{\alpha}, \quad \boldsymbol{i}^{\alpha} = \boldsymbol{\sigma}_{\alpha}, \quad b^{\alpha} = \mathbf{g}^{\alpha}, \quad I^{\alpha} = \hat{\mathbf{p}}^{\alpha}, \quad G^{\alpha} = 0 \tag{3.51}$$

where $\boldsymbol{v}^{\alpha}$ is the averaged velocity, $\boldsymbol{\sigma_{\alpha}}$ is the partial stress tensor, $\mathbf{g}^{\alpha}$ is external momentum supply related to gravitational effects and $\hat{\boldsymbol{p}}^{\alpha}$is the exchange of momentum due to mechanical interaction between different constituents. Substituting the variables into Eq. (3.51), the averaged linear momentum equation for constituent α can be written as follows:

$$div\ \boldsymbol{\sigma}_{\alpha} + \rho_{\alpha}(\boldsymbol{g}^{\alpha} - \mathbf{a}^{\alpha}) + \rho_{\alpha}\left[e^{\alpha}\left(\rho \boldsymbol{v}^{\alpha}\right) + \hat{\boldsymbol{p}}^{\alpha}\right] = \mathbf{0} \tag{3.52}$$

with

$$\sum_{\alpha=1}^{\kappa} \rho_{\alpha} \hat{\boldsymbol{p}}^{\alpha} = \mathbf{0} \tag{3.53}$$

For solid phase, Eq. (3.52) can be written as follows

$$div\ \boldsymbol{\sigma}_{s} + \rho_{s}(\boldsymbol{g}^{s} - \mathbf{a}^{s}) + \rho_{s} \hat{\boldsymbol{p}}^{s} = \mathbf{0} \tag{3.54}$$

For fluid phase, the linear momentum balance equation becomes

$$div\ \boldsymbol{\sigma}_{w} + \rho_{w}(\boldsymbol{g}^{w} - \mathbf{a}^{w}) + \rho_{w}\left[e^{w}\left(\rho \boldsymbol{v}^{w}\right) + \hat{\boldsymbol{p}}^{w}\right] = \mathbf{0} \tag{3.55}$$

The linear momentum balance equation for a two-phase medium is written as follows

$$div\ \boldsymbol{\sigma} + \rho \mathbf{g} + \rho_{w} e^{w}(\rho \boldsymbol{v}^{w}) = \rho(\mathbf{a}^{s} + \mathbf{a}^{w}) \tag{3.56}$$

in which $\boldsymbol{\sigma}$ and ρ are the averaged stress tensor and mass density defined by Eq. (3.11) and Eq. (3.13), respectively.

Under *quasi-static conditions*, the sum of momentum exchange terms of all constituents is defined as

$$\sum \rho_\alpha e^\alpha \left(\rho \mathbf{v}^\alpha\right) = \mathbf{0} \tag{3.57}$$

It is also given as a condition of linear momentum balance equations that, the sum of interaction forces between the constituent α and the other constituents with respect the volume of the REV is

$$\sum_{\alpha}^{\kappa} \rho_\alpha \hat{\mathbf{p}}^\alpha = \rho_s \hat{\mathbf{p}}^s + \rho_w \hat{\mathbf{p}}^w = \mathbf{0} \tag{3.58}$$

Thus, neglecting the acceleration terms, the final form of linear momentum balance equation at the macroscopic level is

$$div\ \boldsymbol{\sigma} + \rho\ \mathbf{g} = \mathbf{0} \tag{3.59}$$

3.3.4 Constitutive Framework

Hooke's law of linear isotropic elasticity is used as the stress-strain (constitutive) relationship for the elastic porous case between the stress, σ and strain, ε as follows

$$\boldsymbol{\sigma}' = \mathbf{D}_e \boldsymbol{\varepsilon} \tag{3.60}$$

where

$$\boldsymbol{\sigma} = \left\{\sigma_{xx}, \sigma_{yy}, \sigma_{zz}, \tau_{xy}, \tau_{yz}, \tau_{zx}\right\}^T \tag{3.61}$$

$$\boldsymbol{\varepsilon} = \left\{\varepsilon_{xx}, \varepsilon_{yy}, \varepsilon_{zz}, \gamma_{xy}, \gamma_{yz}, \gamma_{zx}\right\}^T \tag{3.62}$$

are the vector of stress components, and the vector of strain components, respectively. $\mathbf{D_e}$ is the elastic constitutive matrix defined as

$$\mathbf{D}_e = \frac{E}{(1+\nu)(1-2\nu)} \begin{bmatrix} 1-\nu & \nu & \nu & \dots & 0 & 0 & 0 \\ \nu & 1-\nu & \nu & \dots & 0 & 0 & 0 \\ \nu & \nu & 1-\nu & \dots & 0 & 0 & 0 \\ 0 & 0 & 0 & \dots & \frac{1-\nu}{2} & 0 & 0 \\ 0 & 0 & 0 & \dots & 0 & \frac{1-\nu}{2} & 0 \\ 0 & 0 & 0 & \dots & 0 & 0 & \frac{1-\nu}{2} \end{bmatrix} \tag{3.63}$$

where E is the Young's modulus and ν is the Poisson's ratio.

3.3.5 Principle of Effective Stress

The effective stress principle, which was proposed by Terzaghi, is based on the assumption that the effective stress is equal to the total stress minus the pore water pressure (Terzaghi, 1943). According to this theory, the effective stress controls the compressibility and the strength of the soil skeleton. The consolidation of soil associated with its void ratio depends on effective stress of the soil.

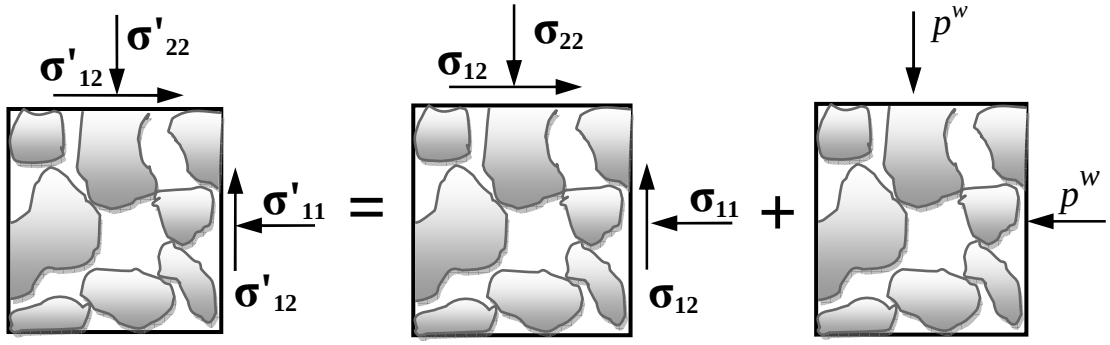

Figure 3.2 Total and effective stresses in saturated media.

The principle of effective stress was extensively studied by numerous researchers to extend Terzaghi's principle for unsaturated soils. The most noticeable modification was made by Bishop for saturated and unsaturated soils as follows:

$$\boldsymbol{\sigma}' = (\boldsymbol{\sigma} - \boldsymbol{\sigma}^a) + \chi(\boldsymbol{\sigma}^a - \boldsymbol{\sigma}^w) \tag{3.64}$$

in which $\boldsymbol{\sigma}'$ is the effective stress, $\boldsymbol{\sigma}$ is the total stress, $\boldsymbol{\sigma}^w$ is the hydrostatic stress, $\boldsymbol{\sigma}^a$ is the air pressure and χ is a parameter that depends on the degree of saturation, stress path, soil type, etc. (Bishop, 1959). In this thesis, fully saturated soils are studied and the air pressure is neglected in the pores. Therefore, the Bishop's expression for the principle stress tensor can be modified as

$$\boldsymbol{\sigma}' = \boldsymbol{\sigma} + \boldsymbol{m} S^w p^w \tag{3.65}$$

where $\boldsymbol{m}=\{1, 1, 1, 0, 0, 0\}^T$ and S_w is the degree of saturation.

In this study, the pore water pressure is treated as positive and compressive stresses are treated as negative. The effective stresses can also be expressed for fluid and solid phases separately. The stress tensor in the fluid phase is

$$\boldsymbol{\sigma}^w = \eta^w p^w \boldsymbol{m} = n S_w p^w \boldsymbol{m} \tag{3.66}$$

where $\eta^w = n S_w$ is the volume fraction. The stress tensor in the solid phase is

$$\boldsymbol{\sigma}^s = (1-n)(\boldsymbol{\sigma}'^s - \boldsymbol{m} p^s) \tag{3.67}$$

with the pressure in the solid phase and the effective stress tensor defined as

$$p^s = S^w p^w \quad \text{and} \quad \boldsymbol{\sigma}' = (1-n)\boldsymbol{\sigma}'^s \tag{3.68}$$

Substituting Eq. (3.68) into Eq. (3.67), the effective stress for the solid phase yields

$$\begin{aligned} \boldsymbol{\sigma}^s &= (1-n)(\boldsymbol{\sigma}'^s - \boldsymbol{m} S_w p^w) \\ &= \boldsymbol{\sigma}' + \boldsymbol{m}(1-n) S_w p^w \end{aligned} \tag{3.69}$$

The total stress $\boldsymbol{\sigma}$ acting on a unit area of a two-phase (solid and fluid) medium defined by Eq. (3.13) can be verified adding up the stress definitions for fluid and solid phases given by Equations (3.66) and (3.67) as follows

$$\begin{aligned} \boldsymbol{\sigma} &= \boldsymbol{\sigma}^s + \boldsymbol{\sigma}^w \\ &= \boldsymbol{\sigma}' + \boldsymbol{m}(1-n) S_w p^w + \boldsymbol{m} n S_w p^w \\ &= \boldsymbol{\sigma}' + \boldsymbol{m} S_w p^w \end{aligned} \tag{3.70}$$

3.4 Finite Element Framework

The linear momentum and mass flow balance equations are presented in this section under the assumptions of quasi-static conditions and small-strain theory. Then, the initial and boundary conditions for the governing equations are prescribed. Following that, the spatial discretization of the governing equations is carried out by defining the weak form of the governing equations using weighted residual-Galerkin approximations

procedure. Finally, the discretization in time domain is performed using θ-method and a solution for the linear elastic case is presented.

3.4.1 Governing Equations

The small strains theory, which assumes the small displacements and small strains in a prescribed domain, is adopted for developing the governing equations of the consolidation problem. The strains, $\boldsymbol{\varepsilon}$ of the soil skeleton are defined in terms of displacements as follows:

$$\boldsymbol{\varepsilon} = \frac{1}{2}\left[grad\ \boldsymbol{u} + (grad\ \boldsymbol{u})^T \right] \tag{3.71}$$

where

$$\boldsymbol{u} = \{u, v, w\}^T \tag{3.72}$$

$$grad = \left(\frac{\partial}{\partial x}, \frac{\partial}{\partial y}, \frac{\partial}{\partial z} \right) \tag{3.73}$$

are the displacement field and the gradient operator, respectively.

The balance equations of a two-phase (solid and fluid) deforming porous medium are derived in the previous section under quasi-static and isothermal conditions. The balance equations are defined as follows.

(1) Linear momentum balance equation:

$$\nabla^T\ \boldsymbol{\sigma} + \rho\, \mathbf{g} = \mathbf{0} \tag{3.74}$$

(2) Mass balance equation:

$$\frac{n}{K_w}\frac{\partial p}{\partial t} + div\left(\frac{\mathbf{k}}{\mu^w}\left(-grad\ p + \rho^w \mathbf{g} \right) \right) + div\ \boldsymbol{v}^s = 0 \tag{3.75}$$

in which

$$\boldsymbol{\sigma} = \{\sigma_x, \sigma_y, \sigma_z, \tau_{xy}, \tau_{xz}, \tau_{yz}\}^T \tag{3.76}$$

$$\rho = (1-n)\rho^s + nS_w\rho^w \tag{3.77}$$

$$\mathbf{g} = \left\{ g_x , g_y , g_z \right\}^{\mathrm{T}} \tag{3.78}$$

are the phase-averaged Cauchy's stress tensor; the phase-averaged mass density of the mixture and; a vector of applied body forces, respectively. ∇^T is the differential operator defined as

$$\nabla^T = \begin{Bmatrix} \dfrac{\partial}{\partial x} & 0 & 0 & \dfrac{\partial}{\partial y} & \dfrac{\partial}{\partial z} & 0 \\ 0 & \dfrac{\partial}{\partial y} & 0 & \dfrac{\partial}{\partial x} & 0 & \dfrac{\partial}{\partial z} \\ 0 & 0 & \dfrac{\partial}{\partial z} & 0 & \dfrac{\partial}{\partial x} & \dfrac{\partial}{\partial y} \end{Bmatrix} \tag{3.79}$$

Based on the small strains theory, the last term of the mass balance equation can be defined as

$$div\ \mathbf{v}^s = \boldsymbol{m}^T \frac{\partial \boldsymbol{\varepsilon}}{\partial t} = \boldsymbol{m}^T div \frac{\partial \boldsymbol{u}}{\partial t} = \boldsymbol{m}^{\mathrm{T}}\, \dot{\boldsymbol{\varepsilon}}_u \tag{3.80}$$

where $\dot{\boldsymbol{\varepsilon}}_u$ is the strain rate defined by

$$\dot{\boldsymbol{\varepsilon}}_u = \left\{ \dot{\varepsilon}_x , \dot{\varepsilon}_y , \dot{\varepsilon}_z , \dot{\gamma}_{xy} , \dot{\gamma}_{xz} , \dot{\gamma}_{yz} \right\}^{\mathrm{T}} \tag{3.81}$$

and $\boldsymbol{m}$ is a vector defined as

$$\boldsymbol{m} = \left\{ 1,\ 1,\ 1,\ 0,\ 0,\ 0 \right\}^{\mathrm{T}} \tag{3.82}$$

Thus, the continuity equation becomes

$$\frac{n}{K_w} \frac{\partial p}{\partial t} + div \left(\frac{\mathbf{k}}{\mu^w} \left(-grad\ p + \rho^w \mathbf{g} \right) \right) + m^T \dot{\boldsymbol{\varepsilon}} = 0 \tag{3.83}$$

3.4.2 Initial and Boundary Conditions

It is necessary to define the initial and boundary conditions for a boundary value problem. The initial conditions specify the full field of displacements and water pressures at time t=0 as follows

$$\boldsymbol{u} = \boldsymbol{u}_0,\ p = p_0 \ \text{ in } \Omega \text{ and on } \Gamma \tag{3.84}$$

where Ω is the domain of interest and Γ is its boundary. The imposed boundary conditions displacements and water pressures are as follows:

$$\begin{aligned} \boldsymbol{u} &= \hat{\boldsymbol{u}} \quad \text{on } \Gamma_u \\ p &= \hat{p} \quad \text{on } \Gamma_p \end{aligned} \tag{3.85}$$

The traction boundary condition for stresses is

$$\mathbf{I}^{\mathrm{T}}\boldsymbol{\sigma} = \mathbf{t} \quad \text{on } \Gamma_u \tag{3.86}$$

where the matrix **I** is related to the unit normal vector $\mathbf{n} = \{n_x, n_y, n_z\}^{\mathrm{T}}$ by

$$\mathbf{I} = \begin{bmatrix} n_x & 0 & 0 \\ 0 & n_y & 0 \\ 0 & 0 & n_z \\ n_x & n_y & 0 \\ 0 & n_z & n_y \\ n_z & 0 & n_x \end{bmatrix} \tag{3.87}$$

Finally, the flux boundary condition for water from Eq. (3.41) is

$$\left[\frac{\mathbf{k}}{\mu^w}\left(-grad\ p + \rho^w \mathbf{g}\right)\right]^T \cdot \mathbf{n} = q \quad \text{on } \Gamma_p \tag{3.88}$$

where q is the imposed mass flux normal to the boundary. Equations (3.85) and (3.86) are natural boundary conditions for the corresponding balance equations.

3.4.3 Weak Form and Galerkin Approximations

The weak form of the governing equations can be formed by multiplying the mass balance and linear momentum equations by weighting functions and integrate the combined equation over its defined domain. The linear momentum balance equations can be written in an explicit form as follows:

$$\begin{aligned}
&\frac{\partial \sigma_x}{\partial x}+\frac{\partial \tau_{xy}}{\partial y}+\frac{\partial \tau_{xz}}{\partial z}+\rho g_x=0\\
&\frac{\partial \sigma_y}{\partial y}+\frac{\partial \tau_{yx}}{\partial x}+\frac{\partial \tau_{yz}}{\partial z}+\rho g_y=0\\
&\frac{\partial \sigma_z}{\partial z}+\frac{\partial \tau_{zx}}{\partial x}+\frac{\partial \tau_{zy}}{\partial y}+\rho g_z=0
\end{aligned} \tag{3.89}$$

Similarly, the mass balance equation is expressed in the form of

$$\begin{aligned}
&\frac{n}{K_w}\frac{\partial p}{\partial t}+\frac{k_x}{\mu^w}\left(-\frac{\partial^2 p}{\partial x^2}+\rho^w\frac{\partial g_x}{\partial x}\right)+\frac{k_y}{\mu^w}\left(-\frac{\partial^2 p}{\partial y^2}+\rho^w\frac{\partial g_y}{\partial y}\right)\\
&\quad+\frac{k_z}{\mu^w}\left(-\frac{\partial^2 p}{\partial z^2}+\rho^w\frac{\partial g_z}{\partial z}\right)+\left(\dot{\varepsilon}_x+\dot{\varepsilon}_y+\dot{\varepsilon}_z\right)=0
\end{aligned} \tag{3.90}$$

Since there are four equations, four weighting functions are needed to construct the weak form of the governing equations. Denoting the weighting functions by $\bar{u},\bar{v},\bar{w}$ and $\bar{p}$, multiplying each equation by its weighting function, integrating over its domain, and adding all four terms gives us the weighted residual as follows:

$$\begin{aligned}
&\int_\Omega\left(\frac{\partial \sigma_x}{\partial x}+\frac{\partial \tau_{xy}}{\partial y}+\frac{\partial \tau_{xz}}{\partial z}+\rho g_x\right)\bar{u}\,d\Omega+\int_\Omega\left(\frac{\partial \sigma_y}{\partial y}+\frac{\partial \tau_{yx}}{\partial x}+\frac{\partial \tau_{yz}}{\partial z}+\rho g_y\right)\bar{v}\,d\Omega\\
&+\int_\Omega\left(\frac{\partial \sigma_z}{\partial z}+\frac{\partial \tau_{zx}}{\partial x}+\frac{\partial \tau_{zy}}{\partial y}+\rho g_z\right)\bar{w}\,d\Omega\\
&+\int_\Omega\left[\frac{n}{K_w}\frac{\partial p}{\partial t}-\frac{1}{\mu^w}\left(k_x\frac{\partial^2 p}{\partial x^2}+k_y\frac{\partial^2 p}{\partial y^2}+k_z\frac{\partial^2 p}{\partial z^2}\right)\right.\\
&\qquad\left.+\frac{\rho^w}{\mu^w}\left(k_x\frac{\partial g_x}{\partial x}+k_y\frac{\partial g_y}{\partial y}+k_z\frac{\partial g_z}{\partial z}\right)+\left(\dot{\varepsilon}_x+\dot{\varepsilon}_y+\dot{\varepsilon}_z\right)\right]\bar{p}\,d\Omega=0
\end{aligned} \tag{3.91}$$

Using the Green-Gauss theorem on each of the stress derivative, pressure derivative and body force derivative terms, the following expression is obtained.

$$
\begin{aligned}
&\int_{\Gamma_u}\left[\left(\sigma_x n_x+\tau_{xy}n_y+\tau_{xz}n_z\right)\bar{u}+\left(\tau_{yx}n_x+\sigma_y n_y+\tau_{yz}n_z\right)\bar{v}+\left(\tau_{zx}n_x+\tau_{zy}n_y+\sigma_z n_z\right)\bar{w}\right]d\Gamma\\
&-\int_{\Omega}\left[\left(\sigma_x\frac{\partial\bar{u}}{\partial x}+\tau_{xy}\frac{\partial\bar{u}}{\partial y}+\tau_{xz}\frac{\partial\bar{u}}{\partial z}\right)+\left(\sigma_y\frac{\partial\bar{v}}{\partial y}+\tau_{yx}\frac{\partial\bar{v}}{\partial x}+\tau_{yz}\frac{\partial\bar{v}}{\partial z}\right)\right.\\
&\left.+\left(\sigma_z\frac{\partial\bar{w}}{\partial z}+\tau_{zx}\frac{\partial\bar{w}}{\partial x}+\tau_{zy}\frac{\partial\bar{w}}{\partial y}\right)+\rho\left(g_x\bar{u}+g_y\bar{v}+g_z\bar{w}\right)\right]d\Omega\\
&+\int_{\Gamma_p}\left[-\frac{\bar{p}}{\mu^w}\left(k_x\frac{\partial p}{\partial x}n_x+k_y\frac{\partial p}{\partial y}n_y+k_z\frac{\partial p}{\partial z}n_z\right)+\frac{\rho^w}{\mu^w}\left(k_x g_x n_x+k_y g_y n_y+k_z g_z n_z\right)\bar{p}\right]d\Gamma\\
&-\int_{\Omega}\left[\bar{p}\frac{n}{K_w}\frac{\partial p}{\partial t}-\frac{1}{\mu^w}\left(k_x\frac{\partial p}{\partial x}\frac{\partial\bar{p}}{\partial x}+k_y\frac{\partial p}{\partial y}\frac{\partial\bar{p}}{\partial y}+k_z\frac{\partial p}{\partial z}\frac{\partial\bar{p}}{\partial z}\right)\right.\\
&\left.+\frac{\rho^w}{\mu^w}\left(k_x\frac{\partial\bar{p}}{\partial x}g_x+k_y\frac{\partial\bar{p}}{\partial y}g_y+k_z\frac{\partial\bar{p}}{\partial z}g_z\right)+\left(\dot{\varepsilon}_x+\dot{\varepsilon}_y+\dot{\varepsilon}_z\right)\bar{p}\right]d\Omega=0
\end{aligned}
\tag{3.92}
$$

Incorporating the boundary conditions defined by Eq. (3.86) and Eq. (3.88) into Eq. (3.92), the final weak form becomes

$$
\begin{aligned}
&\int_{\Omega}\left[\left(\sigma_x\frac{\partial\bar{u}}{\partial x}+\tau_{xy}\frac{\partial\bar{u}}{\partial y}+\tau_{xz}\frac{\partial\bar{u}}{\partial z}\right)+\left(\sigma_y\frac{\partial\bar{v}}{\partial y}+\tau_{yx}\frac{\partial\bar{v}}{\partial x}+\tau_{yz}\frac{\partial\bar{v}}{\partial z}\right)\right.\\
&\left.+\left(\sigma_z\frac{\partial\bar{w}}{\partial z}+\tau_{zx}\frac{\partial\bar{w}}{\partial x}+\tau_{zy}\frac{\partial\bar{w}}{\partial y}\right)+\rho\left(g_x\bar{u}+g_y\bar{v}+g_z\bar{w}\right)\right]d\Omega\\
&+\int_{\Omega}\left[\bar{p}\frac{n}{K_w}\frac{\partial p}{\partial t}-\frac{1}{\mu^w}\left(k_x\frac{\partial p}{\partial x}\frac{\partial\bar{p}}{\partial x}+k_y\frac{\partial p}{\partial y}\frac{\partial\bar{p}}{\partial y}+k_z\frac{\partial p}{\partial z}\frac{\partial\bar{p}}{\partial z}\right)\right.\\
&\left.+\frac{\rho^w}{\mu^w}\left(k_x\frac{\partial\bar{p}}{\partial x}g_x+k_y\frac{\partial\bar{p}}{\partial y}g_y+k_z\frac{\partial\bar{p}}{\partial z}g_z\right)+\left(\dot{\varepsilon}_x+\dot{\varepsilon}_y+\dot{\varepsilon}_z\right)\bar{p}\right]d\Omega\\
&=\int_{\Gamma_u}\left(t_x\bar{u}+t_y\bar{v}+t_z\bar{w}\right)d\Gamma+\int_{\Gamma_p}\bar{p}\ \frac{q}{\rho^w}\,d\Gamma
\end{aligned}
\tag{3.93}
$$

where the applied surface tractions are

$$
\begin{aligned}
t_x&=\sigma_x n_x+\tau_{xy}n_y+\tau_{xz}n_z\\
t_x&=\tau_{yx}n_x+\sigma_y n_y+\tau_{yz}n_z\\
t_x&=\tau_{zx}n_x+\tau_{zy}n_y+\sigma_z n_z
\end{aligned}
\tag{3.94}
$$

and the outward flow per unit area is

$$q = -\frac{\rho^w}{\mu^w}\left[k_x\left(\frac{\partial p}{\partial x} - \rho^w g_x\right)n_x + k_y\left(\frac{\partial p}{\partial y} - \rho^w g_y\right)n_y + k_z\left(\frac{\partial p}{\partial z} - \rho^w g_z\right)n_z \right] \tag{3.95}$$

If the weighting functions are interpreted as virtual displacements and their derivatives as virtual strain:

$$\begin{gathered} \frac{\partial \bar{u}}{\partial x} = \bar{\varepsilon}_x; \quad \frac{\partial \bar{v}}{\partial y} = \bar{\varepsilon}_y; \quad \frac{\partial \bar{w}}{\partial z} = \bar{\varepsilon}_z; \\ \frac{\partial \bar{u}}{\partial y} + \frac{\partial \bar{v}}{\partial x} = \bar{\gamma}_{xy}; \quad \frac{\partial \bar{v}}{\partial z} + \frac{\partial \bar{w}}{\partial y} = \bar{\gamma}_{yz}; \quad \frac{\partial \bar{u}}{\partial z} + \frac{\partial \bar{w}}{\partial x} = \bar{\gamma}_{zx} \end{gathered} \tag{3.96}$$

Substituting these in the weak form and rearranging the terms yields

$$\begin{aligned} &\int_\Omega \left(\sigma_x\bar{\varepsilon}_x + \sigma_x\bar{\varepsilon}_y + \sigma_x\bar{\varepsilon}_z + \tau_{xy}\bar{\gamma}_{xy} + \tau_{yz}\bar{\gamma}_{yz} + \tau_{zx}\bar{\gamma}_{zx}\right)d\Omega - \int_\Omega \rho\left(g_x\bar{u} + g_y\bar{v} + g_z\bar{w}\right)d\Omega \\ &+\int_\Omega \left[\bar{p}\frac{n}{K_w}\frac{\partial p}{\partial t} - \frac{1}{\mu^w}\left(k_x\frac{\partial p}{\partial x}\frac{\partial \bar{p}}{\partial x} + k_y\frac{\partial p}{\partial y}\frac{\partial \bar{p}}{\partial y} + k_z\frac{\partial p}{\partial z}\frac{\partial \bar{p}}{\partial z}\right)\right. \\ &\qquad \left. + \frac{\rho^w}{\mu^w}\left(k_x\frac{\partial \bar{p}}{\partial x}g_x + k_y\frac{\partial \bar{p}}{\partial y}g_y + k_z\frac{\partial \bar{p}}{\partial z}g_z\right) + \left(\dot{\varepsilon}_x + \dot{\varepsilon}_y + \dot{\varepsilon}_z\right)\bar{p}\right] d\Omega \\ &= \int_{\Gamma_u}\left(t_x\bar{u} + t_y\bar{v} + t_z\bar{w}\right)d\Gamma + \int_{\Gamma_p}\bar{p}\ \frac{q}{\rho^w}\,d\Gamma \end{aligned} \tag{3.97}$$

The matrix form of the virtual terms used in the above equations are written as

$$\begin{aligned} \bar{\boldsymbol{u}} &= \left\{\bar{u}, \bar{v}, \bar{w}\right\}^T \\ \bar{\boldsymbol{\varepsilon}}_u &= \left\{\frac{\partial \bar{u}}{\partial x}, \frac{\partial \bar{v}}{\partial y}, \frac{\partial \bar{w}}{\partial z}, \frac{\partial \bar{u}}{\partial y} + \frac{\partial \bar{v}}{\partial x}, \frac{\partial \bar{v}}{\partial z} + \frac{\partial \bar{w}}{\partial y}, \frac{\partial \bar{u}}{\partial z} + \frac{\partial \bar{w}}{\partial x}\right\}^T \\ \bar{\boldsymbol{\varepsilon}}_p &= \left\{\frac{\partial \bar{p}}{\partial x}, \frac{\partial \bar{p}}{\partial y}, \frac{\partial \bar{p}}{\partial z}\right\}^T \end{aligned} \tag{3.98}$$

Thus, the final weak form becomes:

$$\begin{aligned} &\int_\Omega \left[\left\{\bar{\boldsymbol{\varepsilon}}_u^{\,T}\boldsymbol{\sigma} - \bar{\boldsymbol{u}}^{\mathrm{T}}\,\rho\boldsymbol{g}\right\} + \left\{ \bar{p}\frac{n}{K_w}\,\dot{p} + \bar{\boldsymbol{\varepsilon}}_p^{\,T}\frac{\mathbf{k}}{\mu_w}\left(-grad\ p + \rho^w\mathbf{g}\right) + \bar{p}\boldsymbol{m}^{\mathrm{T}}\,\dot{\boldsymbol{\varepsilon}}\right\}\right] d\Omega \\ &= \int_{\Gamma_u}\bar{\boldsymbol{u}}^T\mathbf{t}\,d\Gamma + \int_{\Gamma_p}\bar{p}\ \frac{q}{\rho^w}\,d\Gamma \end{aligned} \tag{3.99}$$

where

$$\mathbf{t} = \{t_x, t_y, t_z\}^T \tag{3.100}$$

is the surface traction vector, and

$$q = \left[\rho^w \frac{\mathbf{k}}{\mu_w} \left(grad\ p - \rho \mathbf{g} \right) \right]^{\mathrm{T}} \cdot \mathbf{n} = \mathbf{v}^{\mathrm{T}} \cdot \mathbf{n} \tag{3.101}$$

is the prescribed outward flow per unit area and $\mathbf{n} = \left\{ n_x, n_y, n_z \right\}^{\mathrm{T}}$ is a vector of direction cosines for the unit normal to Γ.

3.4.4 Finite Element Equations

A finite element solution to Eq. 3.99 can be obtained using shape functions to describe the variation of the displacements and pore water pressures for each element. For an element with *n* nodes, the displacement field at any internal point is assumed to be of the form

$$\tilde{\mathbf{u}} \approx \hat{\mathbf{u}} = \sum_i^n \mathbf{N}_{ui} \mathbf{u}_i = \mathbf{N}_u \boldsymbol{u} \tag{3.102}$$

with an explicit form

$$\tilde{\boldsymbol{u}} = \begin{bmatrix} u \\ v \\ w \end{bmatrix} = \begin{bmatrix} \mathbf{N}_{u1} & 0 & 0 & \mathbf{N}_{u2} & 0 & 0 & \ldots & \mathbf{N}_{un} & 0 & 0 \\ 0 & \mathbf{N}_{u1} & 0 & 0 & \mathbf{N}_{u2} & 0 & \ldots & 0 & \mathbf{N}_{un} & 0 \\ 0 & 0 & \mathbf{N}_{u1} & 0 & 0 & \mathbf{N}_{u2} & \ldots & 0 & 0 & \mathbf{N}_{un} \end{bmatrix} \begin{bmatrix} u_1 \\ v_1 \\ w_1 \\ . \\ . \\ u_n \\ v_n \\ w_n \end{bmatrix} \equiv \mathbf{N}_u \boldsymbol{u} \tag{3.103}$$

where $\mathbf{N}_u$ is a matrix of shape functions and $u_1, v_1, w_1, u_2, v_2, w_3, \ldots$ are the nodal degrees of freedom. Similarly, the field of pore pressures for an element with pore pressure freedoms at *m* nodes is assumed to be of the form

$$\tilde{p} \approx \hat{p} = \sum_i^m \mathbf{N}_{pi} p_i = \mathbf{N}_p \boldsymbol{p} \tag{3.104}$$

with an explicit form

$$\tilde{p} = \begin{bmatrix} \mathrm{N}_{p1} \; \mathrm{N}_{p2} \; ... \; \mathrm{N}_{pm} \end{bmatrix} \begin{bmatrix} p_1 \\ p_2 \\ . \\ . \\ . \\ p_m \end{bmatrix} \equiv \mathbf{N}_p \boldsymbol{p} \tag{3.105}$$

where $\mathbf{N}_p^T$ is a matrix of shape functions and $\boldsymbol{p}$ is a vector of nodal pore pressures. Thus, the complete set of assumed solution is written as

$$\begin{bmatrix} \tilde{\boldsymbol{u}} \\ \tilde{p} \end{bmatrix} = \begin{bmatrix} \boldsymbol{N}_u & \mathbf{0} \\ \mathbf{0} & \boldsymbol{N}_p \end{bmatrix} \begin{bmatrix} \boldsymbol{u} \\ \boldsymbol{p} \end{bmatrix} \tag{3.106}$$

The strains from the assumed displacements defined as $\boldsymbol{\varepsilon}_u = \mathbf{B}_u \boldsymbol{u} = \bar{\nabla} \mathbf{N}_u \boldsymbol{u}$ are written as

$$\boldsymbol{\varepsilon}_u = \begin{bmatrix} \frac{\partial N_{u1}}{\partial x} & 0 & 0 & ... & \frac{\partial N_{un}}{\partial x} & 0 & 0 \\ 0 & \frac{\partial N_{u1}}{\partial y} & 0 & ... & 0 & \frac{\partial N_{un}}{\partial y} & 0 \\ 0 & 0 & \frac{\partial N_{u1}}{\partial z} & ... & 0 & 0 & \frac{\partial N_{un}}{\partial z} \\ \frac{\partial N_{u1}}{\partial y} & \frac{\partial N_{u1}}{\partial x} & 0 & ... & \frac{\partial N_{un}}{\partial y} & \frac{\partial N_{un}}{\partial x} & 0 \\ \frac{\partial N_{u1}}{\partial z} & 0 & \frac{\partial N_{u1}}{\partial x} & ... & \frac{\partial N_{un}}{\partial z} & 0 & \frac{\partial N_{un}}{\partial x} \\ 0 & \frac{\partial N_{u1}}{\partial z} & \frac{\partial N_{u1}}{\partial y} & ... & 0 & \frac{\partial N_{un}}{\partial z} & \frac{\partial N_{u1}}{\partial y} \end{bmatrix} \begin{bmatrix} u_1 \\ v_1 \\ w_1 \\ . \\ . \\ . \\ u_n \\ v_n \\ w_n \end{bmatrix} \equiv \mathbf{B}_u \boldsymbol{u} \tag{3.107}$$

Similarly, the strains from the assumed pore pressures defined as $\boldsymbol{\varepsilon}_p = \mathbf{B}_p \boldsymbol{p} = \bar{\nabla} \mathbf{N}_p \boldsymbol{p}$ are written as

$$\boldsymbol{\varepsilon}_p = \begin{bmatrix} \dfrac{\partial N_{p1}}{\partial x} & \dfrac{\partial N_{p2}}{\partial x} & \cdots & \dfrac{\partial N_{pm}}{\partial x} \\ \dfrac{\partial N_{p1}}{\partial y} & \dfrac{\partial N_{p2}}{\partial y} & \cdots & \dfrac{\partial N_{pm}}{\partial y} \\ \dfrac{\partial N_{p1}}{\partial z} & \dfrac{\partial N_{p2}}{\partial z} & \cdots & \dfrac{\partial N_{pm}}{\partial z} \end{bmatrix} \begin{bmatrix} p_1 \\ p_2 \\ . \\ . \\ . \\ p_m \end{bmatrix} \equiv \mathbf{B}_p \boldsymbol{p} \tag{3.108}$$

The total stress tensor is split into effective stress and pore pressure parts using the principle of effective stresses as $\boldsymbol{\sigma}' = \boldsymbol{\sigma} + \boldsymbol{m}p$, and defined in integral form as

$$\int_\Omega \bar{\boldsymbol{\varepsilon}}_u^{\,T} \boldsymbol{\sigma}' \, \mathrm{d}\Omega = \int_\Omega \bar{\boldsymbol{\varepsilon}}_u^{\,T} \boldsymbol{\sigma} \, \mathrm{d}\Omega + \int_\Omega \bar{\boldsymbol{\varepsilon}}_u^{\,T} \boldsymbol{m} p \, \mathrm{d}\Omega \tag{3.109}$$

The effective stress can be expressed using the constitutive relationship as

$$\boldsymbol{\sigma}' = \mathbf{D}_e \boldsymbol{\varepsilon}_u = \mathbf{D}_e \mathbf{B}_u \boldsymbol{u} \tag{3.110}$$

Similarly, the strain rate can be defined as

$$\dot{\boldsymbol{\varepsilon}}_u = \mathbf{B}_u \dot{\mathbf{u}} \tag{3.111}$$

Substituting the assumed solutions above into the weak form yields

$$\begin{aligned} &\int_\Omega \Bigg[\left\{ \bar{\boldsymbol{\varepsilon}}_u^{\,T} \left(\mathbf{D}_e \mathbf{B}_u \boldsymbol{u} - \boldsymbol{m} \boldsymbol{N}_p^T \boldsymbol{p} \right) - \bar{\boldsymbol{u}}^{\mathrm{T}} \rho \boldsymbol{g} \right\} \\ &+ \left\{ \bar{p}^T \frac{n}{K_w} \mathbf{N}_p \dot{\boldsymbol{p}} + \bar{\boldsymbol{\varepsilon}}_p^{\,T} \frac{\mathbf{k}}{\mu_w} \left(\mathbf{B}_p \boldsymbol{p} - \rho^w \mathbf{g} \right) + \bar{p}^T \boldsymbol{m}^{\mathrm{T}} \mathbf{B}_u \dot{\boldsymbol{u}} \right\} \Bigg] \mathrm{d}\Omega \\ &= \int_{\Gamma_u^q} \bar{\boldsymbol{u}}^T \mathbf{t} \, d\Gamma + \int_{\Gamma_u^q} \bar{p} \, \frac{q}{\rho^w} \, \mathrm{d}\Gamma \end{aligned} \tag{3.112}$$

The sets of weighting functions are the columns of the matrix of the assumed solution functions defined as follows:

$$\begin{pmatrix} \bar{\boldsymbol{u}} \\ \bar{p} \end{pmatrix} \rightarrow \begin{pmatrix} \mathbf{N}_u & \mathbf{0} \\ \mathbf{0} & \mathbf{N}_p \end{pmatrix} \quad \text{and} \quad \begin{pmatrix} \bar{\boldsymbol{\varepsilon}}_u \\ \bar{\boldsymbol{\varepsilon}}_p \\ \bar{p} \end{pmatrix} \rightarrow \begin{pmatrix} \mathbf{B}_u & \mathbf{0} \\ \mathbf{B}_p & \mathbf{0} \\ \mathbf{0} & \mathbf{N}_p \end{pmatrix} \tag{3.113}$$

Substituting the weighting functions into the assumed solution as expressed by Eq. (3.113) yields

$$\int_\Omega \mathbf{B}_u^T \mathbf{D}_e \mathbf{B}_u \boldsymbol{u} \, \mathrm{d}\Omega - \int_\Omega \mathbf{B}_u^{\,T} \boldsymbol{m} \mathbf{N}_p \boldsymbol{p} \, \mathrm{d}\Omega = \int_\Omega \mathbf{N}_u^T \rho \mathbf{g} \, \mathrm{d}\Omega + \int_\Gamma \mathbf{N}_u^T \mathbf{t} \, \mathrm{d}\Gamma \tag{3.114}$$

$$\int_{\Omega} \mathbf{N}_p^{\mathrm{T}} \frac{n}{K_w} \mathbf{N}_p \dot{\boldsymbol{p}} + \int_{\Omega} \mathbf{N}_p^{\mathrm{T}} \boldsymbol{m}^{\mathrm{T}} \mathbf{B}_u \dot{\boldsymbol{u}} \, \mathrm{d}\Omega + \int_{\Omega} \mathbf{B}_p^{\mathrm{T}} \frac{\mathbf{k}}{\mu_w} \mathbf{B}_p \boldsymbol{p} \, \mathrm{d}\Omega = \int_{\Gamma_w^q} \mathbf{N}_p^{\mathrm{T}} \frac{q^w}{\rho^w} \, \mathrm{d}\Gamma + \int_{\Omega} \mathbf{B}_p^{\mathrm{T}} \frac{\mathbf{k}}{\mu_w} \rho^w \mathbf{g} \, \mathrm{d}\Omega \tag{3.115}$$

These equations express the linear momentum balance and continuity equations for each element. They can be written in the compact forms as follows:

$$\mathbf{K}_m \boldsymbol{u} - \mathbf{Q} \boldsymbol{p} = \boldsymbol{f}^u \tag{3.116}$$

$$\mathbf{Q}^{\mathrm{T}} \dot{\boldsymbol{u}} + \mathbf{S} \dot{\boldsymbol{p}} + \mathbf{K}_c \boldsymbol{p} = \boldsymbol{f}^p \tag{3.117}$$

in which

$$\mathbf{K}_m = \int_{\Omega} \mathbf{B}_u^{\mathrm{T}} \mathbf{D}_{\mathrm{e}} \mathbf{B}_u \mathrm{d}\Omega \tag{3.118}$$

$$\mathbf{Q} = \int_{\Omega} \mathbf{B}_u^{\mathrm{T}} \boldsymbol{m} \mathbf{N}_p \mathrm{d}\Omega \tag{3.119}$$

$$\mathbf{S} = \int_{\Omega} \mathbf{N}_p^{\mathrm{T}} \frac{n}{K_w} \mathbf{N}_p \, \mathrm{d}\Omega \tag{3.120}$$

$$\mathbf{K}_c = \int_{\Omega} \mathbf{B}_p^{\mathrm{T}} \frac{\mathbf{k}}{\mu_w} \mathbf{B}_p \, \mathrm{d}\Omega \tag{3.121}$$

$$\boldsymbol{f}^u = \int_{\Omega} \mathbf{N}_u^{\mathrm{T}} \rho \mathbf{g} \, \mathrm{d}\Omega + \int_{\Gamma} \mathbf{N}_u^{\mathrm{T}} \mathbf{t} \, \mathrm{d}\Gamma \tag{3.122}$$

$$\boldsymbol{f}^p = \int_{\Omega} \mathbf{B}_p^{\mathrm{T}} \frac{\mathbf{k}}{\mu_w} \rho^w \mathbf{g} \, \mathrm{d}\Omega + \int_{\Gamma_w^q} \mathbf{N}_p^{\mathrm{T}} \frac{q^w}{\rho^w} \, \mathrm{d}\Gamma \tag{3.123}$$

The final form of coupled set of equations can be defined in matrix form as

$$\begin{bmatrix} \mathbf{K}_m & -\mathbf{Q} \\ \mathbf{0} & \mathbf{K}_c \end{bmatrix} \begin{Bmatrix} \mathbf{u} \\ \mathbf{p} \end{Bmatrix} + \begin{bmatrix} \mathbf{0} & \mathbf{0} \\ \mathbf{Q}^{\mathrm{T}} & \mathbf{S} \end{bmatrix} \begin{Bmatrix} \dot{\mathbf{u}} \\ \dot{\mathbf{p}} \end{Bmatrix} = \begin{Bmatrix} \mathbf{f}^u \\ \mathbf{f}^p \end{Bmatrix} \tag{3.124}$$

where $\mathbf{K}_m$ is the elemental elastic stiffness matrix, $\mathbf{Q}$ is the coupling matrix, $\mathbf{S}$ is the compressibility matrix, $\mathbf{K}_c$ is the permeability (flow) matrix, $\boldsymbol{f}_u$ is the elemental vector of external forces, and $\boldsymbol{f}^p$ is the fluid supply vector.

It is apparent that the final form of coupled equations is not symmetric. To make Eq. (3.124) symmetric, the first set of equations is differentiated with respect to time and multiplied by -1 in the following form:

$$\begin{bmatrix} -\mathbf{K}_m & \mathbf{Q} \\ \mathbf{Q}^{\mathrm{T}} & \mathbf{S} \end{bmatrix} \begin{Bmatrix} \dot{\mathbf{u}} \\ \dot{\mathbf{p}} \end{Bmatrix} + \begin{bmatrix} \mathbf{0} & \mathbf{0} \\ \mathbf{0} & \mathbf{K}_c \end{bmatrix} \begin{Bmatrix} \mathbf{u} \\ \mathbf{p} \end{Bmatrix} = \begin{Bmatrix} -\dot{\mathbf{f}}^{u} \\ \mathbf{f}^{p} \end{Bmatrix} \tag{3.125}$$

3.4.5 Discretization in Time Domain

To solve the initial value problem defined by Eq. (3.125) for elastic solids with constant permeability, the finite differences method is used to constitute a system of linear first order differential equations of the form

$$\mathbf{B}\,\dot{\boldsymbol{x}} + \mathbf{C}\,\boldsymbol{x} = \mathbf{F}(t) \tag{3.126}$$

where

$$\mathbf{B} = \begin{bmatrix} -\mathbf{K}_m & \mathbf{Q} \\ \mathbf{Q}^{\mathrm{T}} & \mathbf{S} \end{bmatrix} \qquad \text{and} \qquad \mathbf{C} = \begin{bmatrix} \mathbf{0} & \mathbf{0} \\ \mathbf{0} & \mathbf{K}_{\mathrm{c}} \end{bmatrix} \tag{3.127}$$

are matrices of constants, $\mathbf{F}(t)$ is a time dependent forcing function defined by

$$\mathbf{F}(t) = \begin{Bmatrix} -\dot{\mathbf{f}}^{\mathrm{u}} \\ \mathbf{f}^{\mathrm{p}} \end{Bmatrix} \tag{3.128}$$

and $x = \{u, p\}$ with $\dot{\boldsymbol{x}} = d\boldsymbol{x}/dt$. The discretization in time domain for solving Eq. (3.126) is carried out by the θ-scheme which approximates the mean value of $\boldsymbol{x}$ at two consecutive time steps t_n and t_{n+1} by the weighted average of $\dot{\boldsymbol{x}}$. The scheme is defined by

$$\frac{\boldsymbol{x}_{n+1} - \boldsymbol{x}_n}{\Delta t} = \theta \dot{\boldsymbol{x}}_{n+1} + (1-\theta)\dot{\boldsymbol{x}}_n, \qquad 0 \le \theta \le 1 \tag{3.129}$$

where $\Delta t = t_{n+1} - t_n$, and the suffix n represents the value of the quantity at time t_n. The weight θ refers to some well-known schemes, which are

$$\theta = \begin{cases} 0, & \text{Forward difference "explicit" scheme,} \\ 1, & \text{Backward difference "implicit" scheme,} \\ 1/2, & \text{Crank-Nicholson scheme.} \end{cases} \tag{3.130}$$

The θ-method is at least first order accurate and, provided $\theta \geq 0.5$, is unconditionally stable. The unconditional stability is an essential characteristic for an efficient consolidation scheme since it is often necessary to integrate over long periods using large time steps. When θ is set zero, it is called the forward difference or "explicit" scheme. Although the "explicit" scheme is simple, it requires excessive number of steps because it is only stable when Δt is small. Choosing a value of $\theta = 1$ gives the well-known backward Euler "fully implicit" scheme. This scheme is first order accurate; unconditionally stable and oscillation free (Wood, 1990). For the special case of $\theta = 0.5$, the θ-method is second order accurate and corresponds to the ubiquitous Crank-Nicolson scheme. This scheme can lead to oscillatory results, however the oscillations can be smoothed out by using the fully implicit version with $\theta = 1$. In this thesis, the Crank-Nicolson scheme will be used in the solution of the coupled transient problems. For the nth time step, Eq. (3.126) may be expressed in two consecutive time steps as follows

$$\mathbf{B}\,\dot{\boldsymbol{x}}_n + \mathbf{C}\,\boldsymbol{x}_n = \mathbf{F}_n \tag{3.131}$$

$$\mathbf{B}\,\dot{\boldsymbol{x}}_{n+1} + \mathbf{C}\,\boldsymbol{x}_{n+1} = \mathbf{F}_{n+1} \tag{3.132}$$

Using the θ-scheme, the sum of Equations (3.131) and (3.132) can be expressed as

$$[\mathbf{B} + \theta\,\Delta t\,\mathbf{C}]\,x_{n+1} + \left[-\mathbf{B} + (1 - \theta)\Delta t\,\mathbf{C}\right]\,x_n = \Delta t\theta\,\mathbf{F}_{n+1} + \Delta t(1 - \theta)\,\mathbf{F}_n \tag{3.133}$$

The process assumes that $\boldsymbol{x_0}$at time $t_0$is known. For the case of an elastic soil with constant permeability, the matrices **B** and **C**are independent of $\boldsymbol{x}$ and Eq. (3.133) defines a system of linear equations which can be solved for $\boldsymbol{x}_n$. Assuming the application of θ-method to the set of coupled consolidation equations defined by Eq. (3.125) yields the final form of the complete set of equations as follows:

$$\begin{bmatrix} -\mathbf{K}_m & \mathbf{Q} \\ \mathbf{Q}^{\mathbf{T}} & \Delta t\theta\mathbf{K}_c + \mathbf{S} \end{bmatrix}_{n+1} \begin{Bmatrix} \mathbf{u} \\ \mathbf{p} \end{Bmatrix}_{n+1} - \begin{bmatrix} -\mathbf{K}_m & \mathbf{Q} \\ \mathbf{Q}^{\mathbf{T}} & (1-\theta)\Delta t\mathbf{K}_c + \mathbf{S} \end{bmatrix}_n \begin{Bmatrix} \mathbf{u} \\ \mathbf{p} \end{Bmatrix}_n = \theta\Delta t \begin{Bmatrix} -\dot{\mathbf{f}}^u \\ \mathbf{f}^p \end{Bmatrix}_{n+1} + (1-\theta)\Delta t \begin{Bmatrix} -\dot{\mathbf{f}}^u \\ \mathbf{f}^p \end{Bmatrix}_n \tag{3.134}$$

3.4.6 Solution of Elastic Consolidation Problems

It is convenient to apply the external loads incrementally to a given system to allow plastic stress redistribution to equilibrate at each step. This method is especially desirable for the solution of non-linear systems that will be dealt in the next chapters. For the linear-elastic case, the same approach may be adopted. The total force $\{\boldsymbol{f}^u\}$ applied on the system in the incremental form using the θ-method can be defined as

$$\Delta\mathbf{f}^u = \mathbf{f}_{n+1} - \mathbf{f}_n = \Delta t\ [\theta\dot{\mathbf{f}}_{n+1} + (1-\theta)\dot{\mathbf{f}}_n], \qquad 0 \le \theta \le 1 \tag{3.135}$$

Substituting Eq. (3.135) into Eq. (3.134) and neglecting the compressibility matrix and the fluid supply vector, so that $\mathbf{S}=\mathbf{0}$ and $\mathbf{f}^{\boldsymbol{p}} = \mathbf{0}$ results in

$$\begin{bmatrix} -\mathbf{K}_m & \mathbf{Q} \\ \mathbf{Q}^{\mathbf{T}} & \Delta t\theta\ \mathbf{K}_{\mathbf{c}} \end{bmatrix} \begin{Bmatrix} \mathbf{u}_{n+1} - \mathbf{u}_n \\ \mathbf{p}_{n+1} - \mathbf{p}_n \end{Bmatrix} = -\begin{Bmatrix} \mathbf{f}^u_{n+1} - \mathbf{f}^u_n \\ \Delta t\theta\ \mathbf{K}_{\mathbf{c}}\mathbf{p}_n \end{Bmatrix} \tag{3.136}$$

Eq. (3.136) can be expressed using the incremental form of the applied external forces defined by Eq. (3.135) as follows

$$\begin{bmatrix} -\mathbf{K}_m & \mathbf{Q} \\ \mathbf{Q}^{\mathbf{T}} & \Delta t\theta\ \mathbf{K}_c \end{bmatrix} \begin{Bmatrix} \Delta\mathbf{u} \\ \Delta\mathbf{p} \end{Bmatrix} = -\begin{Bmatrix} \Delta\mathbf{f}^{\mathrm{u}} \\ \Delta t\ \mathbf{K}_c\mathbf{p}_n \end{Bmatrix} \tag{3.137}$$

with the resulting changes in displacement, Δu and excess pore pressures, Δp in the incremental form defined as

$$\Delta\boldsymbol{u} = \boldsymbol{u}_{n+1} - \boldsymbol{u}_n = \Delta t\ [\theta\dot{\boldsymbol{u}}_{n+1} + (1-\theta)\dot{\boldsymbol{u}}_n], \qquad 0 \le \theta \le 1 \tag{3.138}$$

$$\Delta\boldsymbol{p} = \boldsymbol{p}_{n+1} - \boldsymbol{p}_n = \Delta t\ [\theta\dot{\boldsymbol{p}}_{n+1} + (1-\theta)\dot{\boldsymbol{p}}_n], \qquad 0 \le \theta \le 1 \tag{3.139}$$

The Eq. (3.137) is the incremental recurrence form of the coupled set of consolidation equations as derived by (Sandhu, et al., 1969) and (Griffiths, 1994). The left hand side element matrix of Eq. (3.137) is formed by its constituent matrices and is symmetric.

The right hand side vector consists of load increments $\{\Delta \boldsymbol{f}\}$ and fluid loads are given by $\Delta t \boldsymbol{k}_c \boldsymbol{p}_n$. The fluid term is computed without any need for assembly using an element by element product approach. At each time step, dependent variables are updated using Eqs. (3.138) and (3.139) as follows

$$\begin{aligned} \boldsymbol{u}_{n+1} &= \boldsymbol{u}_n + \Delta \boldsymbol{u} \\ \boldsymbol{p}_{n+1} &= \boldsymbol{p}_n + \Delta \boldsymbol{p} \end{aligned} \tag{3.140}$$

The assembly approach is chosen for the solution of the coupled equations. This approach involves the setting up the coupled global stiffness matrix on the left hand side of these equations, followed by an update of the variables from Eq. (3.140). Considering the constant element properties and the time step Δt, the left hand side needs to be factorized only once. The remainder of the solution, which involves the vector multiplication on the right hand side, is followed by forward and backward substitution. A numerical example using the linear-elastic form of coupled equations is illustrated in the next section.

3.5 Numerical Applications

3.5.1 One-Dimensional Consolidation Problem

This example illustrates the one-dimensional plane strain consolidation analysis of a soil column using 8/4-**u**/*p* quadrilateral elements as shown in Figure 3.3. The elements are comprised of rectangular quadrilaterals for displacements coupled to 4-node rectangular quadrilaterals for pressures. Degrees of freedom are numbered in the order *u* and *p*, denoting displacements and excess pore pressure, respectively. The material chosen for the example is a plain strain odometer specimen. The finite element model consists of four 8-node poro-elastic solid elements as shown in Figure 3.3. The material is elastic and homogeneous. The material properties that include the isotropic permeability coefficient k, modulus of elasticity E, and the Poisson's ratio ν are given in Table 3.1.

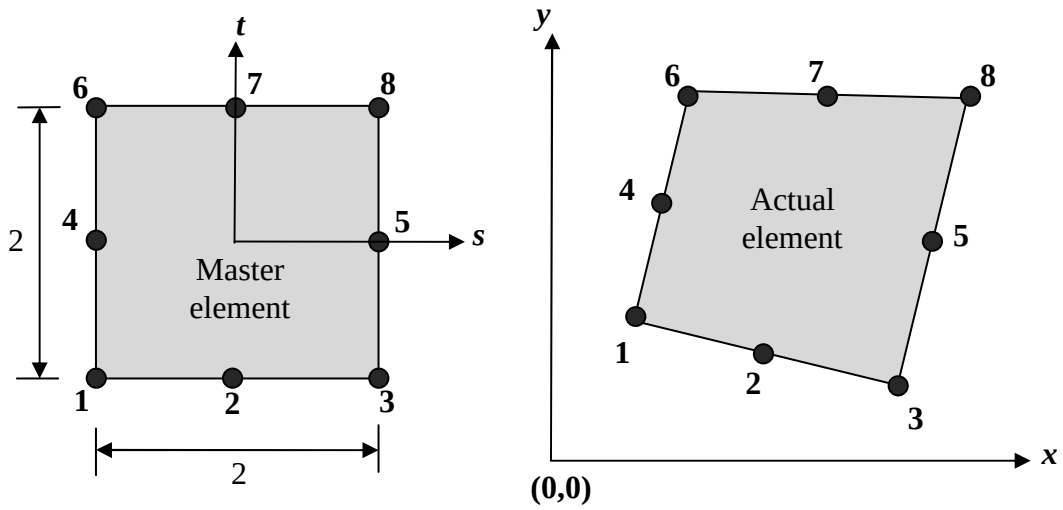

Figure 3.3 Eight-node quadrilateral master and actual elements.

The boundary conditions for the model are as follows: the bottom is fixed and the sides are bounded by smooth rollers. No drainage is allowed through the base and the sides. The top of the specimen is drained and subjected to a ramp loading of the form as shown in Figure 3.4. The initial time value is t_0=0.5 seconds where the ramp load reaches its maximum at $q = 1\,kN/m^2$. The finite element computations including complete the spatial and time discretization are carried out by the commercial computer program named *Mathematica*®. The element equations are developed using the interpolation functions with the plane strain formulation as follows

$$\varepsilon_z = \gamma_{yz} = \gamma_{zx} = 0 \Rightarrow \sigma_z = \frac{E\nu(\varepsilon_x + \varepsilon_y)}{(1+\nu)(1-2\nu)}; \quad \tau_{yz} = 0; \quad \tau_{zx} = 0 \tag{3.141}$$

The finite element formulation for the eight-node displacement/pore pressure element is derived using the interpolation functions. The interpolation functions for displacements are as follows:

$$\mathbf{N}_u^T = \begin{bmatrix} -\frac{1}{4}(-1+s)(-1+t)(1+s+t) \\ \frac{1}{2}(-1+s^2)(-1+t) \\ \frac{1}{4}(-1+t)(1-s^2+t+st) \\ -\frac{1}{2}(1+s)(-1+t^2) \\ \frac{1}{4}(1+s)(1+t)(-1+s+t) \\ -\frac{1}{2}(-1+s^2)(1+t) \\ \frac{1}{4}(-1+s)(1+s-t)(1+t) \\ \frac{1}{2}(-1+s)(-1+t^2) \end{bmatrix} \tag{3.142}$$

The interpolation functions for pressure are as follows:

$$\mathbf{N}_p^T = \begin{bmatrix} \frac{1}{4}(1-s)(1-t) \\ \frac{1}{4}(s+1)(1-t) \\ \frac{1}{4}(s+1)(t+1) \\ \frac{1}{4}(1-s)(t+1) \end{bmatrix} \tag{3.143}$$

The element strain vector is defined as follows:

$$\boldsymbol{\varepsilon} = \begin{Bmatrix} \varepsilon_x \\ \varepsilon_y \\ \gamma_{xy} \end{Bmatrix} = \begin{Bmatrix} \frac{\partial u}{\partial x} \\ \frac{\partial v}{\partial y} \\ \frac{\partial u}{\partial y} + \frac{\partial v}{\partial x} \end{Bmatrix}$$

$$= \begin{bmatrix} \frac{\partial N_{u1}}{\partial x} & 0 & \frac{\partial N_{u2}}{\partial x} & 0 & \ldots & \frac{\partial N_{u7}}{\partial x} & 0 & \frac{\partial N_{u8}}{\partial x} & 0 \\ 0 & \frac{\partial N_{u1}}{\partial y} & 0 & \frac{\partial N_{u2}}{\partial y} & \ldots & 0 & \frac{\partial N_{u7}}{\partial y} & 0 & \frac{\partial N_{u8}}{\partial y} \\ \frac{\partial N_{u1}}{\partial y} & \frac{\partial N_{u1}}{\partial x} & \frac{\partial N_{u2}}{\partial y} & \frac{\partial N_{u2}}{\partial x} & \ldots & \frac{\partial N_{u7}}{\partial y} & \frac{\partial N_{u7}}{\partial x} & \frac{\partial N_{u8}}{\partial y} & \frac{\partial N_{u8}}{\partial x} \end{bmatrix} \begin{Bmatrix} u_1 \\ v_1 \\ u_2 \\ v_2 \\ . \\ . \\ u_8 \\ v_8 \end{Bmatrix} = \mathbf{B^T u} \qquad (3.144)$$

The assumed solution is as follows:

$$\begin{pmatrix} u \\ v \\ p \end{pmatrix} = \begin{pmatrix} N_{u1} & 0 & N_{u2} & 0 & \ldots & N_{u8} & 0 & 0 & 0 & 0 \\ 0 & N_{u1} & 0 & N_{u2} & \ldots & 0 & N_{u8} & 0 & 0 & 0 \\ 0 & 0 & 0 & 0 & \ldots & 0 & N_{p1} & N_{p2} & N_{p3} & N_{p4} \end{pmatrix} \begin{pmatrix} u_1 \\ v_1 \\ u_2 \\ v_2 \\ . \\ . \\ p_1 \\ p_2 \\ p_3 \\ p_4 \end{pmatrix} \qquad (3.145)$$

The derivatives of the interpolation functions with respect to x and y are computed using the mapping as follows

$$x = \begin{pmatrix} N_{u1} & N_{u2} & \ldots \end{pmatrix} \begin{pmatrix} x_1 \\ x_2 \\ . \\ . \end{pmatrix} \quad \text{and} \quad y = \begin{pmatrix} N_{u1} & N_{u2} & \ldots \end{pmatrix} \begin{pmatrix} y_1 \\ y_2 \\ . \\ . \end{pmatrix} \qquad (3.146)$$

where x_i and y_i are the nodal coordinates. The Jacobian matrix of the mapping and its determinant are as follows:

$$\boldsymbol{J}=\begin{pmatrix}\dfrac{\partial x}{\partial s} & \dfrac{\partial x}{\partial t}\\ \dfrac{\partial y}{\partial s} & \dfrac{\partial y}{\partial t}\end{pmatrix}=\begin{pmatrix}J_{11} & J_{12}\\ J_{21} & J_{22}\end{pmatrix};\qquad \det\ \boldsymbol{J}=\left|\frac{\partial x}{\partial s}\frac{\partial y}{\partial t}-\frac{\partial x}{\partial t}\frac{\partial y}{\partial s}\right| \tag{3.147}$$

The derivatives of the interpolation functions with respect to *x* and *y* are computed as follows:

$$\begin{aligned}\frac{\partial N_i}{\partial x}&=\frac{1}{\det\ \boldsymbol{J}}\left(J_{22}\frac{\partial N_i}{\partial s}-J_{21}\frac{\partial N_i}{\partial t}\right)\\ \frac{\partial N_i}{\partial y}&=\frac{1}{\det\ \boldsymbol{J}}\left(-J_{12}\frac{\partial N_i}{\partial s}+J_{11}\frac{\partial N_i}{\partial t}\right)\end{aligned} \tag{3.148}$$

The constitutive relationship, in the state of plane strain, for the elastic case is written as (Timoshenko, et al., 1982)

$$\begin{Bmatrix}\sigma_x\\ \sigma_y\\ \tau_{xy}\end{Bmatrix}=\frac{E(1-\nu)}{(1+\nu)(1-2\nu)}\begin{bmatrix}1 & \dfrac{\nu}{1-\nu} & 0\\ \dfrac{\nu}{1-\nu} & 1 & 0\\ 0 & 0 & \dfrac{1-2\nu}{2(1-\nu)}\end{bmatrix}\begin{Bmatrix}\varepsilon_x\\ \varepsilon_x\\ \gamma_{xy}\end{Bmatrix} \tag{3.149}$$

where σ_x, σ_y and τ_{xy} are the stress components, *E* is the modulus of elasticity, ν is Poisson's ratio, and ε_x, ε_y and γ_{xy} are the small strain components.

The incremental solution method is adopted for the solution of this example. Hence, Eq. (3.137) that was derived at Section 3.3.6 can be rewritten as follows

$$\begin{bmatrix}-\mathbf{K}_m & \mathbf{Q}\\ \mathbf{Q}^{\mathrm{T}} & \Delta t\theta\ \mathbf{K}_c\end{bmatrix}\begin{Bmatrix}\Delta\mathbf{u}\\ \Delta\mathbf{p}\end{Bmatrix}=-\begin{Bmatrix}\Delta\mathbf{f}^{\mathrm{u}}\\ \Delta t\ \mathbf{K}_c\mathbf{p}_n\end{Bmatrix} \tag{3.150}$$

The left hand side of Eq. (3.150) that is interpreted as the equivalent stiffness matrix, $\mathbf{K}_e$, is computed using a three point Gauss quadrature formula as described below. The element equations are obtained by using the numerical integration method. The thickness of the element, *h* is chosen constant; therefore, the volume integral is reduced to

area integration and the surface integration to line integrals. The 16 × 16 element stiffness matrix, $\mathbf{K}_{me}$ is:

$$\begin{aligned}\mathbf{K}_{me} &= h\iint_A \mathbf{B}_u^T\ \boldsymbol{D}\ \mathbf{B}_u dA = h\int_{-1}^{1}\int_{-1}^{1} \mathbf{B}_u^T\ \boldsymbol{D}\ \mathbf{B}_u \det \boldsymbol{J}\ ds\ dt \\ &= h\sum_{i=1}^{m}\sum_{j=1}^{n} w_i w_j \mathbf{B}_u^T(s_i,t_j)\ \boldsymbol{D}(s_i,t_j)\ \mathbf{B}_u(s_i,t_j) \det \boldsymbol{J}(s_i,t_j)\end{aligned} \tag{3.151}$$

where $\boldsymbol{D}$ is the constitutive matrix for the elastic case defined as

$$\boldsymbol{D} = \frac{E(1-\nu)}{(1+\nu)(1-2\nu)}\begin{bmatrix} 1 & \dfrac{\nu}{1-\nu} & 0 \\ \dfrac{\nu}{1-\nu} & 1 & 0 \\ 0 & 0 & \dfrac{1-2\nu}{2(1-\nu)} \end{bmatrix} \tag{3.152}$$

The 16 × 4 element coupling matrix, $\mathbf{Q}_e$ is:

$$\begin{aligned}\mathbf{Q}_e &= h\iint_A \mathbf{B}_u^T\ \boldsymbol{m}\ \mathbf{N}_p dA = h\int_{-1}^{1}\int_{-1}^{1} \mathbf{B}_u^T\ \boldsymbol{m}\ \mathbf{N}_p \det \boldsymbol{J}\ ds\ dt \\ &= h\sum_{i=1}^{m}\sum_{j=1}^{n} w_i w_j \mathbf{B}_u^T(s_i,t_j)\ \boldsymbol{m}\ \mathbf{N}_p(s_i,t_j) \det \boldsymbol{J}(s_i,t_j)\end{aligned} \tag{3.153}$$

The 4 × 4 element permeability matrix, $\mathbf{K}_{ce}$ is:

$$\begin{aligned}\mathbf{K}_{ce} &= h\iint_A \mathbf{B}_p^T\ \frac{\mathbf{k}}{\mu^w}\ \mathbf{B}_p\ dA = h\int_{-1}^{1}\int_{-1}^{1} \mathbf{B}_p^T\ \frac{\mathbf{k}}{\mu^w}\ \mathbf{B}_p\ \det \boldsymbol{J}\ ds\ dt \\ &= h\sum_{i=1}^{m}\sum_{j=1}^{n} w_i w_j\ \mathbf{B}_p^T(s_i,t_j)\ \frac{\mathbf{k}}{\mu^w}\ \mathbf{B}_p(s_i,t_j)\ \det \boldsymbol{J}(s_i,t_j)\end{aligned} \tag{3.154}$$

The 4 × 4 element compressibility matrix, $\mathbf{S}_e$ is:

$$\begin{aligned}\mathbf{S}_e &= h\iint_A \mathbf{N}_p^T \frac{n}{K_w} \mathbf{N}_p\ dA = h\frac{n}{K_w}\int_{-1}^{1}\int_{-1}^{1} \mathbf{N}_p^T\ \mathbf{N}_p \det \boldsymbol{J}\ ds\ dt \\ &= h\frac{n}{K_w}\sum_{i=1}^{m}\sum_{j=1}^{n} w_i w_j \mathbf{N}_p^T(s_i,t_j)\ \mathbf{N}_p(s_i,t_j)\ \det \boldsymbol{J}(s_i,t_j)\end{aligned} \tag{3.155}$$

The element load vector due to body forces is:

$$\mathbf{R}_b = h\iint_A \mathbf{N}_u^T \begin{pmatrix} b_x \\ b_y \end{pmatrix} dA = h\int_{-1}^{1}\int_{-1}^{1} \mathbf{N}_u^T \begin{pmatrix} b_x \\ b_y \end{pmatrix} \det \boldsymbol{J}\ ds\ dt$$
$$= h\sum_{i=1}^{m}\sum_{j=1}^{n} w_i w_j \mathbf{N}_u^T(s_i,t_j) \begin{pmatrix} b_x \\ b_y \end{pmatrix} \det \boldsymbol{J}(s_i,t_j) \tag{3.156}$$

The equivalent load vector due to distributed loads is:

$$\mathbf{R}_q = h\iint_A \mathbf{N}_{cu}^T \begin{pmatrix} q_x \\ q_y \end{pmatrix} dA = h\int_{-1}^{1}\int_{-1}^{1} \mathbf{N}_{cu}^T \begin{pmatrix} q_x \\ q_y \end{pmatrix} \det \boldsymbol{J}_c\ ds\ dt$$
$$= h\sum_{i=1}^{m}\sum_{j=1}^{n} w_i w_j \mathbf{N}_{cu}^T(s_i,t_j) \begin{pmatrix} q_x \\ q_y \end{pmatrix} \det \boldsymbol{J}_c(s_i,t_j) \tag{3.157}$$

where *cu* subscript denotes that the interpolation functions must be written in terms of a coordinate along a prescribed side.

Using the procedure described above, the finite element equations for each element are developed. The element equations are then assembled in the global matrix. After incorporating the essential boundary conditions and applying the prescribed loads on the specified surface, the global matrices are solved for the unknowns -displacements and pressures- using the incremental load method.

The unknowns of the one-dimensional consolidation problem are displacements (settlements) and excess pore pressures at the nodes. Time histories of the pore pressures and degrees of consolidation in the middle of the soil column are plotted in Figures 3.6 to 3.9. In Figure 3.6, the excess pore pressure is plotted versus time factor for two different ramp rise times, $t_0 = 0.1$ and $t_0 = 0.5$ seconds. The time factor, *T* (Terzaghi, 1943) is the dimensionless number.

$$T = \frac{c_v t}{D^2} \tag{3.158}$$

where *D*=1 m is the maximum drainage path within the specimen, c_v is the coefficient of consolidation defined as

$$c_v = \frac{k}{m_v \gamma_w} \tag{3.159}$$

in which

$$m_v = \frac{(1+\nu)(1-2\nu)}{E(1-\nu)} \tag{3.160}$$

k is the soil permeability and γ_w is the unit weight of water. Substituting $\nu = 0$ and $E = 0$ into Eq. (3.160) yields $m_v = 1$ Similarly, $k/\gamma_w = 1.0$ in the example, so that the time factor is equal to step time as $T = t$. For t_0*=0.1 s*, the pore pressure at the middle of the model (0.5 m. from the top) is approximately 0.9 kN/m^2. For t_0*=0.5 s*, the pore pressure in the middle is computed as about 0.5 kN/m$^{2.}$ When the loading takes place in a shorter period, dissipation of pore water pressure takes longer period of time, because under rapid loading greater excess pore water pressure builds up in the pores. Same results were computed by Smith in his related work (Smith, et al., 1976).

In Figure 3.7, the change of degree of consolidation with the time factor is shown. The degree of consolidation is the fraction of the excess pore water pressure that has dissipated. It is expressed in percentage and defined as follows:

$$U(t) = \frac{\Delta u_0 - \Delta u(t)}{\Delta u_0} \times 100\% \tag{3.161}$$

where Δu_0 is the initial settlement and $\Delta u(t)$ is the increment of the settlement at every time step, *t.* A load placed on the soil specimen is first carried by water trapped in pores which causes excess pore water pressure. Then, water gradually escapes from the pores during loading and load is carried by soil particles which creates effective stress in the specimen. While the effective stress increases during loading, excess pore water dissipates until the equilibrium is reached. When the equilibrium is reached, the average degree of consolidation, U_{avg}, is 1.0 which indicates that the soil specimen used for the consolidation test is 100% consolidated.

In Figure 3.7, for t_0=0.1 s, the soil specimen is 10% consolidated at the end of the ramp loading, the total consolidation is then completed in 3 s. For t_0=0.5 s, the initial consolidation is around 45%, the total consolidation is completed in 3 s. During rapid loading (t_0=0.1 s), the soil specimen consolidates approximately 5 times less than the soil specimen under slow loading (t_0=0.5 s). In both Figures 3.6 and 3.7, the results are in good agreement with the work of Smith et al. (Smith, et al., 1976).

Figures 3.8 and 3.9 illustrate the variation of pore pressures and degrees of consolidation with time in the middle of the soil specimen. The results computed by the finite element method are compared with the results obtained from Terzaghi's effective stress and consolidation theories. In Figure 3.8, the pore pressures that are calculated by Terzaghi's method are closer to the results of rapid loading (t_0=0.1 s) of the soil specimen. This is because Terzaghi's principle of effective stress describes the pore pressures as independent of loading rate (*viz.* Section 3.2.7). Thus, it does not capture the pore pressure change of a slowly loaded soil specimen. In Figure 3.9, degrees of consolidation that are calculated using Terzaghi's consolidation theory are closer to the rapid loading of the soil specimen that is calculated using the finite element method, because Terzaghi's method is independent of loading rate.

Figures 3.10 and 3.11 show the contour plots for pore pressures and effective stresses in the soil column at t_0=0.1 s and t_0=0.1 s, respectively. Approximately 99% of the applied load is carried by pore water during rapid loading (Figure 3.10). On the other hand, during slow loading (Figure 3.11), approximately 99% of the load is carried by the soil particles.

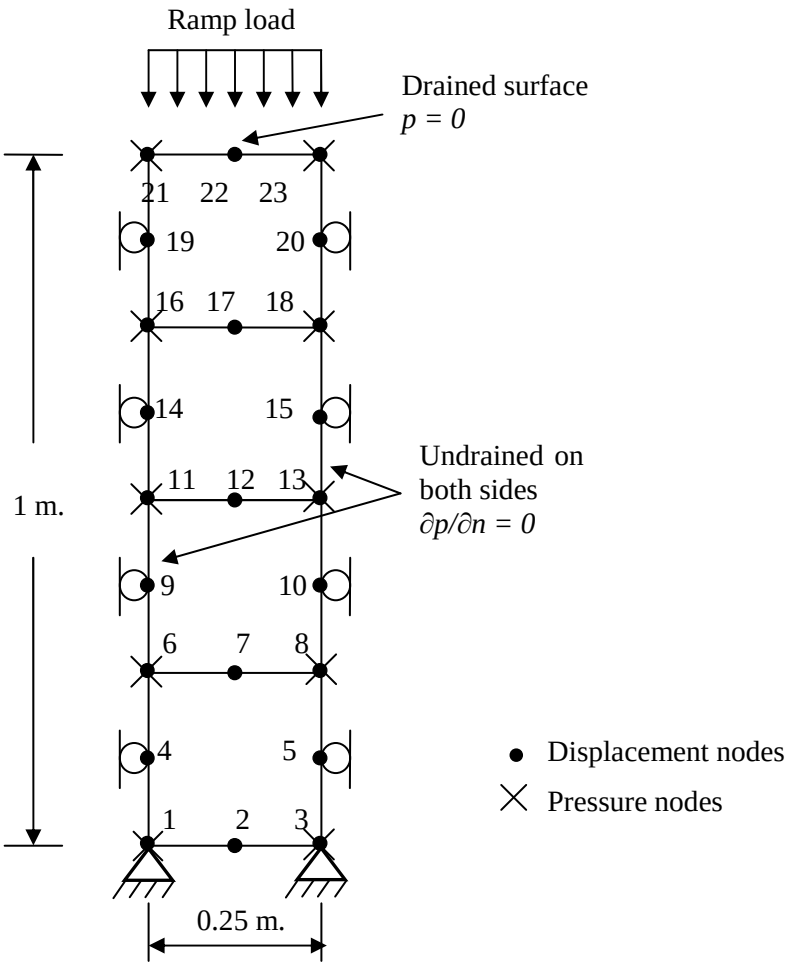

Figure 3.4 The finite element mesh consisting of four 8-noded elements.

Table 3.1 Material parameters of the odometer specimen in Example 3.1

Material Parameter	Notation	Value	Units
	General		
Unit weight of water	γ_w	9.81	kN/m^3
Permeability	k_x	9.81	m/sec
	k_y	9.81	m/sec
	Elastic		
Modulus of elasticity	E	1.0	MPa
Poisson's ratio	ν	0.0	-

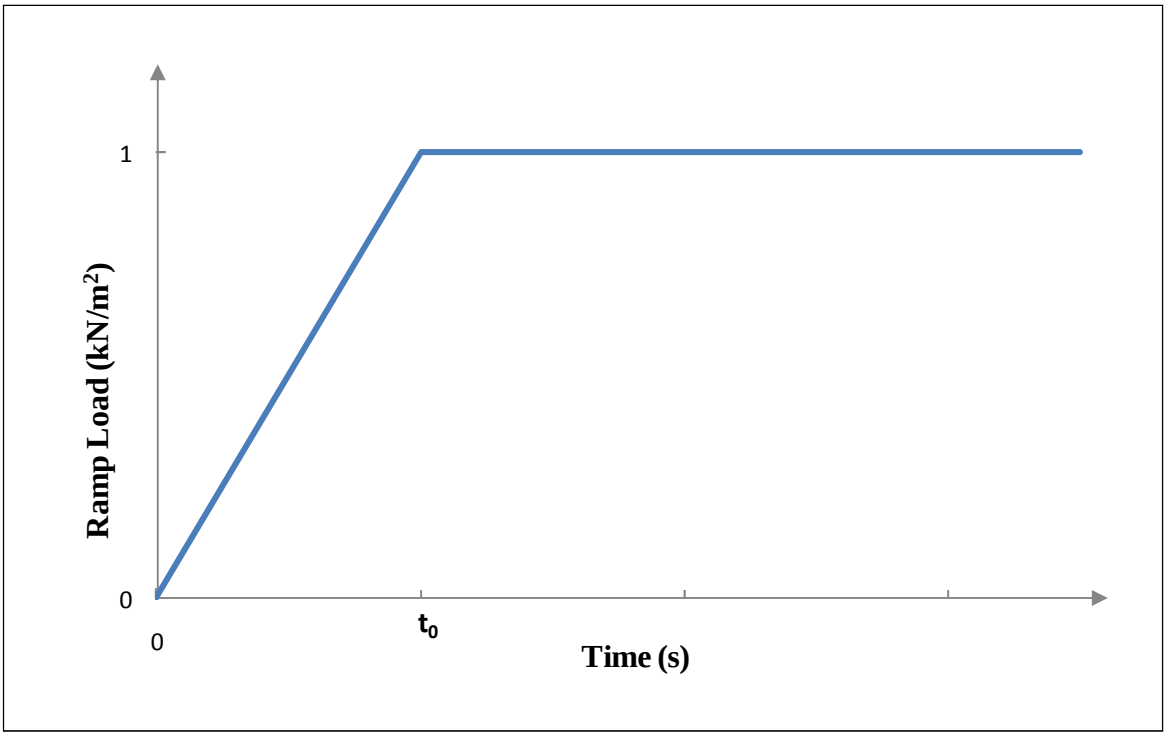

Figure 3.5 Ramp load versus time.

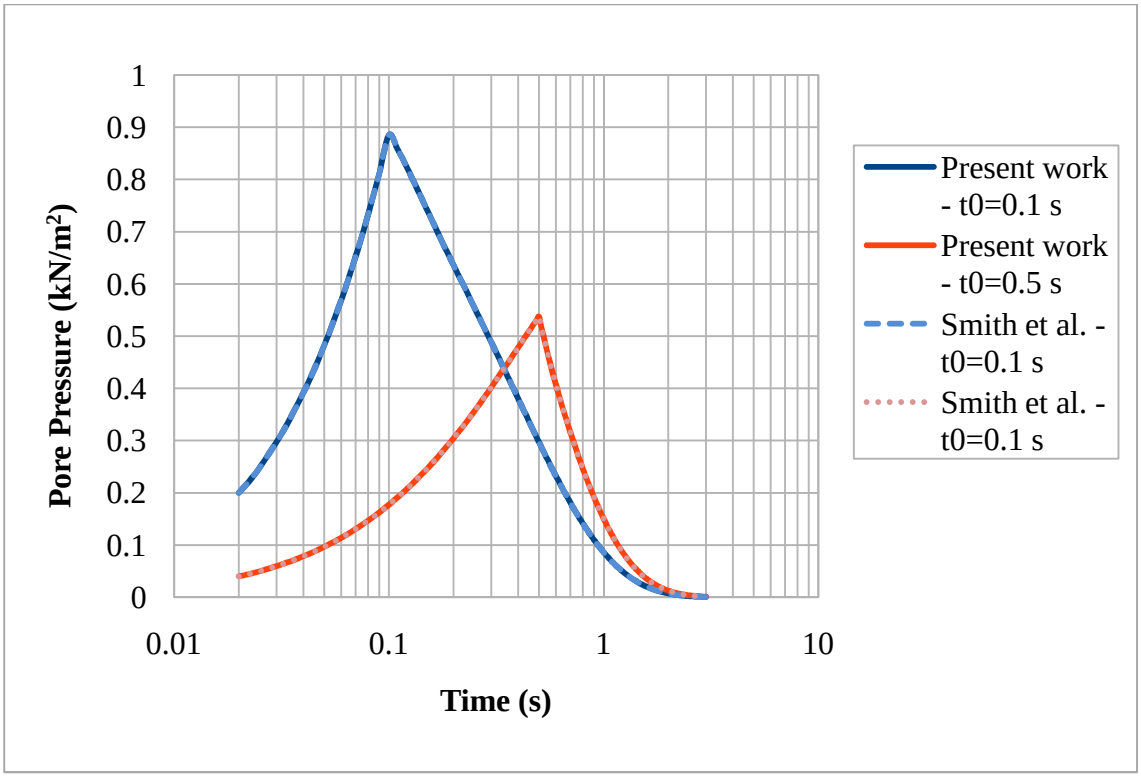

Figure 3.6 Pore pressure vs. time for t_0=0.1 s and t_0=0.5 s computed using FEM (present work) compared with the published data.

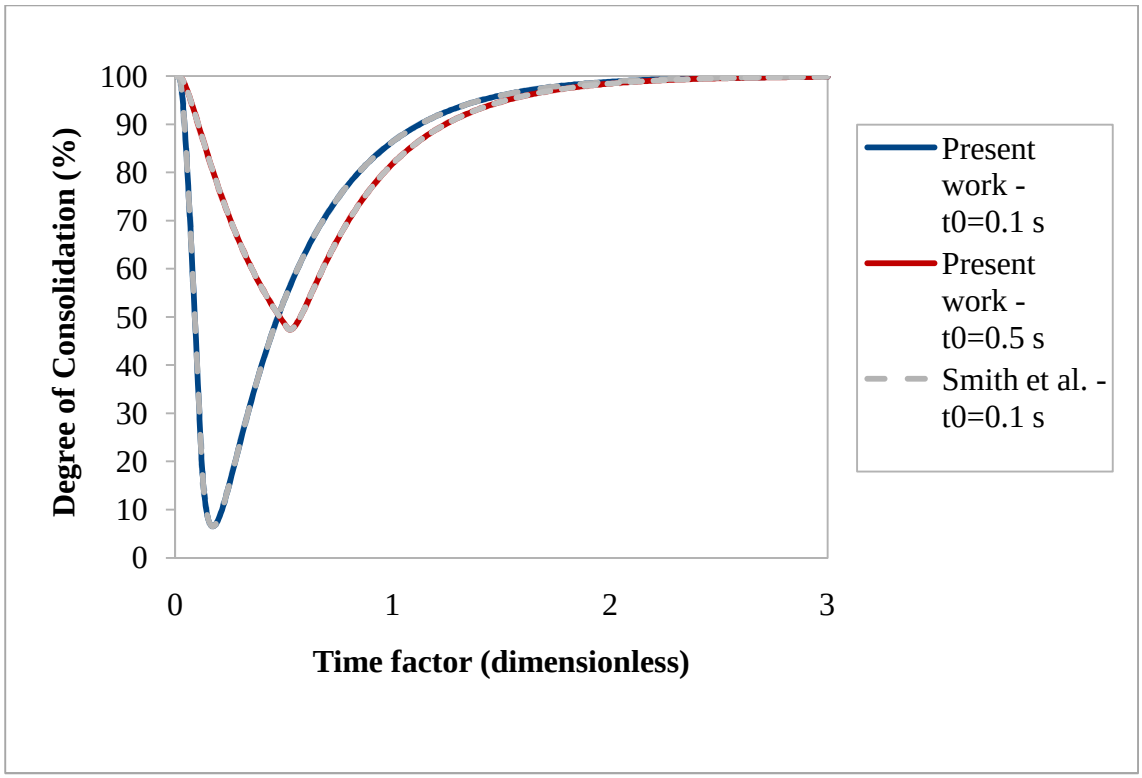

Figure 3.7 Degree of consolidation vs. time factor for t_0=0.1 s and t_0=0.5 s computed using the FEM (present work) and the published data.

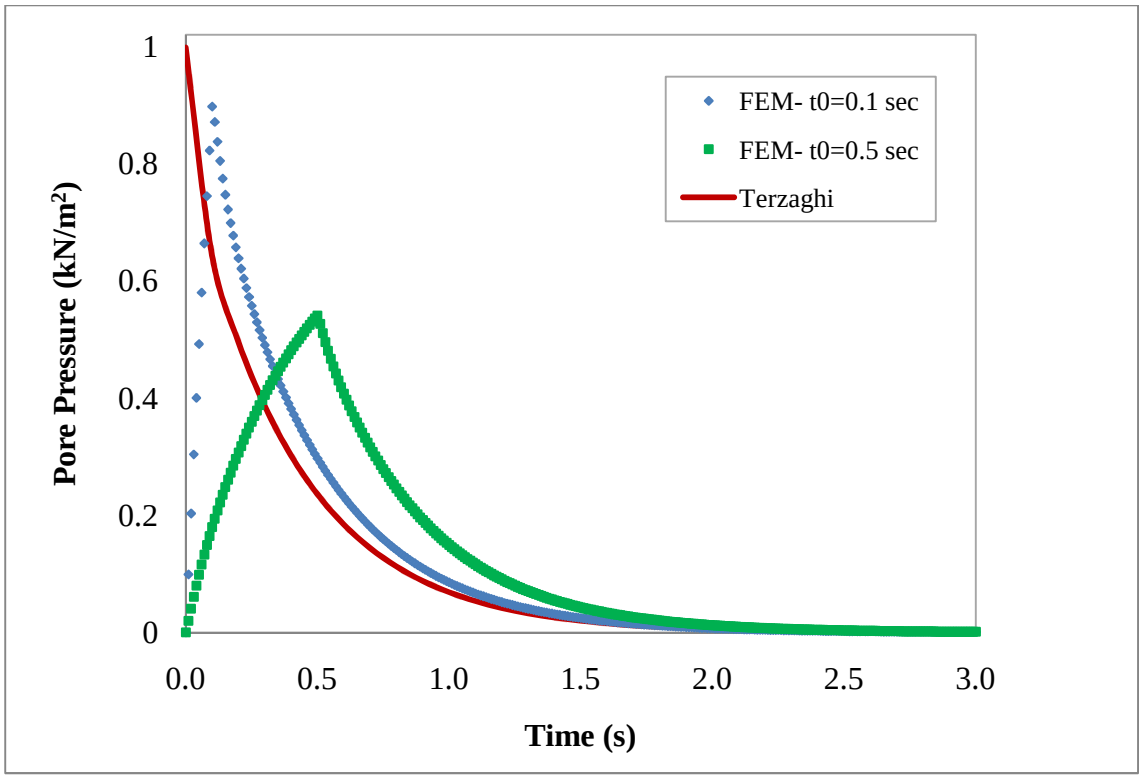

Figure 3.8 Pore pressure vs. time for t_0=0.1 s and t_0=0.5 s computed using FEM (present work) compared with the Terzaghi's method.

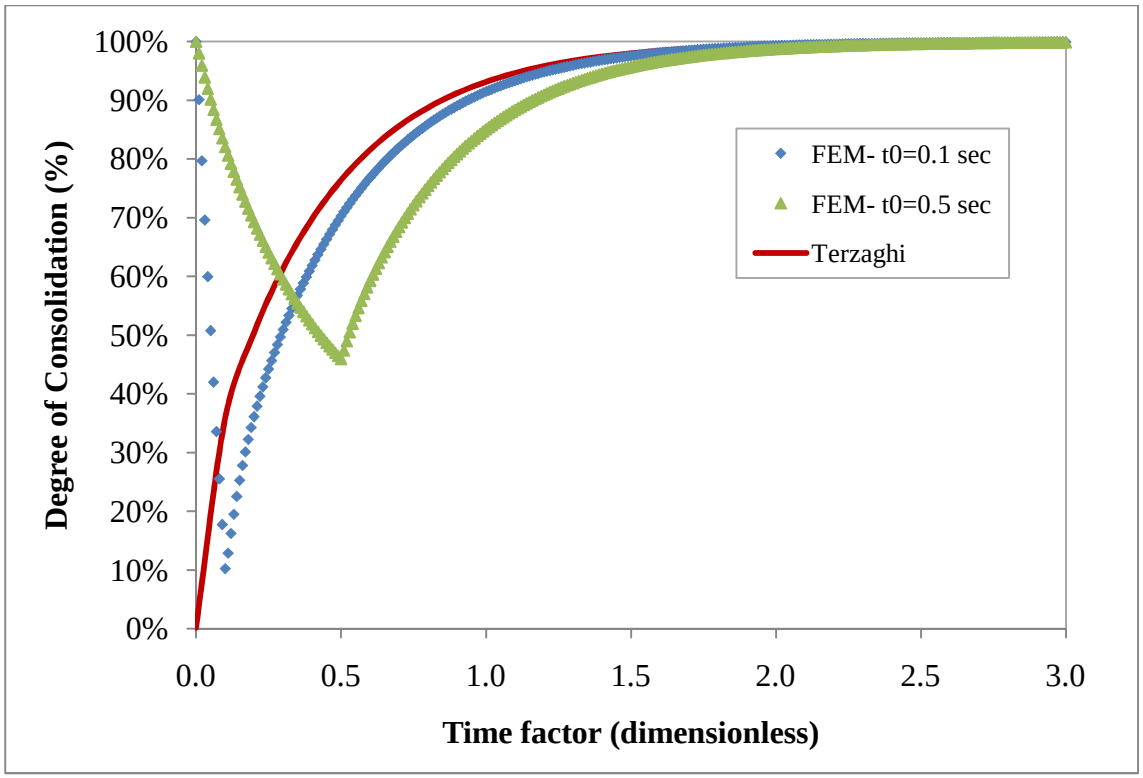

Figure 3.9 Degree of consolidation vs. time factor for t_0=0.1 s and t_0=0.5 s computed using FEM (present work) compared with the Terzaghi's method.

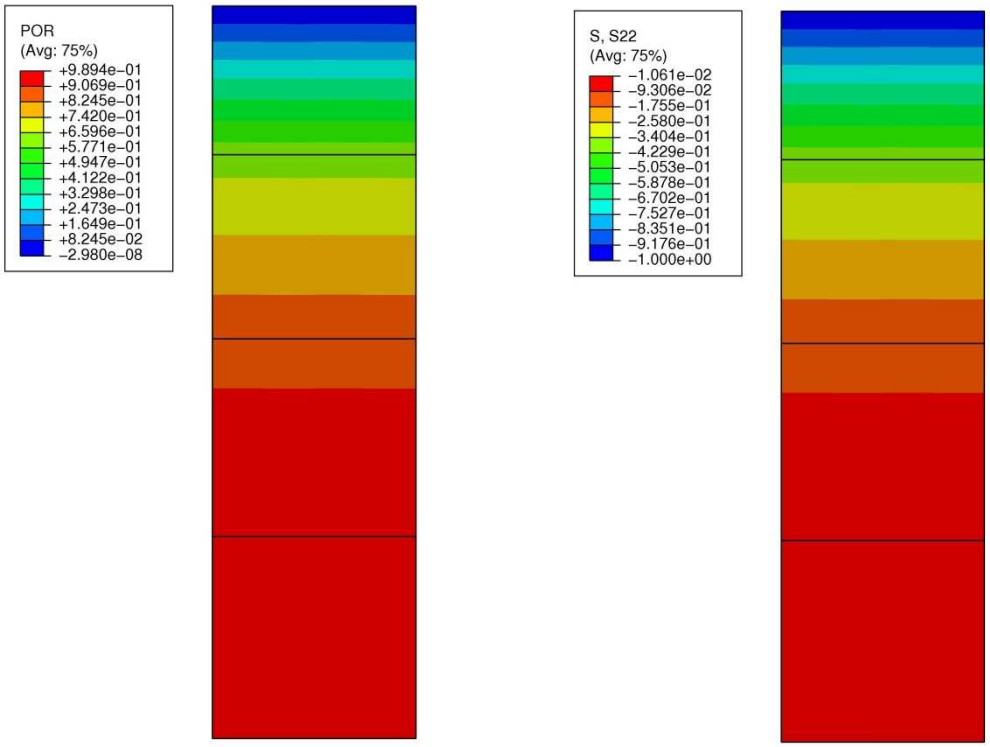

Figure 3.10 Contour plots of pore pressure and effective stresses at t=0.1 sec for the t_0=0.1 initial loading.

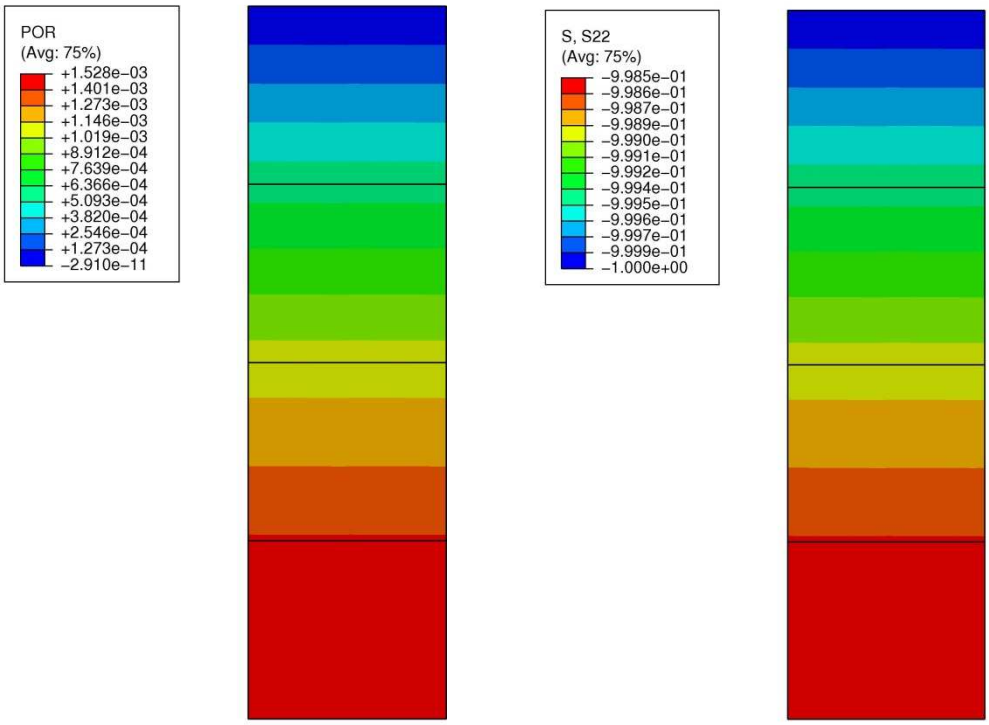

Figure 3.11 Contour plots of pore pressure and effective stresses at t=0.5 sec for the t_0=0.5 initial loading.

3.5.2 Two Dimensional Consolidation Problem

Two-dimensional plane strain consolidation analysis of a Biot poro-elastic solid is considered in this example. A finite strip of soil is loaded over its central portion. For the sake of simplicity, only half portion of the soil strip is modeled. The ratio of the loaded part to the half portion of the geometry is chosen as 1:5 with a half-width of 60 m. The example is modeled and solved using the finite element software *ABAQUS*®. 8-node biquadratic displacement, bilinear pore pressure, reduced integration elements (CPE8R) are used in the model. The geometry of the mesh is given in Figure 3.12. The material is chosen as elastic with a Young's modulus of 6.895 MPa and a Poisson's ratio of 0.0. The initial void ratio is chosen as 1.5. Coefficients of permeability vary with the void ratios and are chosen as 5.08×10^{-7} m/s at the void ratio of 1.5 and 5.08×10^{-8} m/s at void ratio of 1.0. The material properties are given in Table 3.2. The strip of soil is assumed to lie on rigid, impermeable and smooth base. The applied pressure on the soil strip is 500 kPa. Neither horizontal displacement nor pore fluid flow is permitted along the vertical sides of the model. Free drainage is only allowed on the top surface of the model.

The analysis is performed using two steps. In the first step, the full load is applied over two equal fixed time increments. The load remains constant in the subsequent step during which the soil undergoes consolidation. The analysis considers finite-strain effects, and the soil permeability varies with the void ratio. The reason for employing the finite-strain method is to simulate the soil consolidation assuming that the permeability of the soil decreases as it is compressed which is physically realistic in soil mechanics.

The deformed shape of the soil model is shown in Figure 3.13. The contour plot of the model for von Mises stresses is shown in Figure 3.14. As seen in Figure 3.14, the maximum stress is 484 kPa, and it occurs where the distributed load is applied. The stresses underneath the foundation gradually decrease with depth. The pattern of the stress distribution is circular (spherical for a three dimensional model). The pore water pressure distribution in the model is shown in Figure 3.15. The pore pressures are

approximately zero at the end of the analysis, because the drainage is allowed on the top surface.

Table 3.2 Material properties of the specimen in Example 3.2

Material Parameter	Notation	Value	Units
	General		
Initial void ratio	e_0	1.5	-
Permeability			
at void ratio, e=1.5	$k_{1.5}$	5.08×10^{-7}	m/sec
at void ratio, e=1.0	$k_{1.0}$	5.08×10^{-8}	m/sec
	Elastic		
Modulus of elasticity	E	6.895	MPa
Poisson's ratio	N	0.0	-

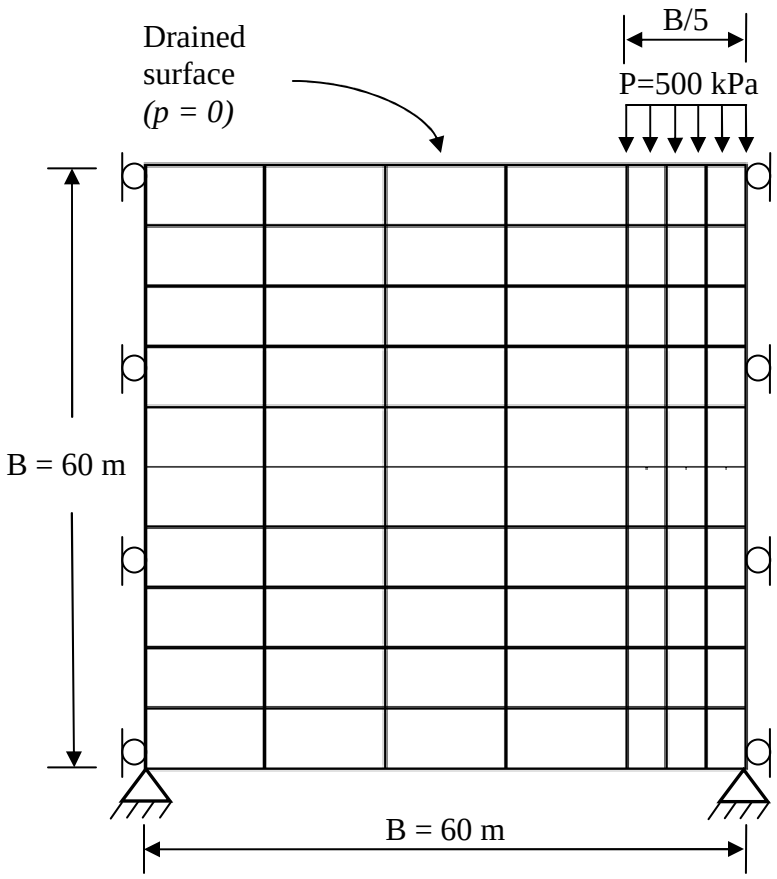

Figure 3.12 The undeformed meshed geometry of the 2-D consolidation problem.

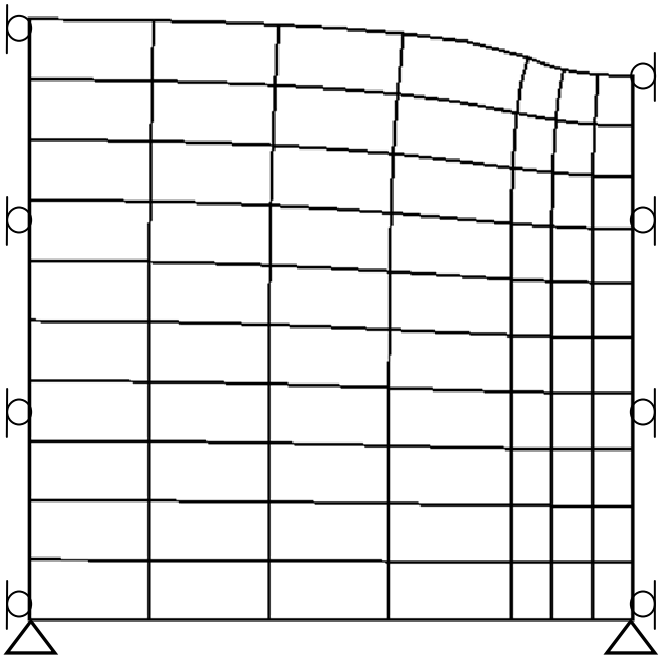

Figure 3.13 The deformed shape after loading.

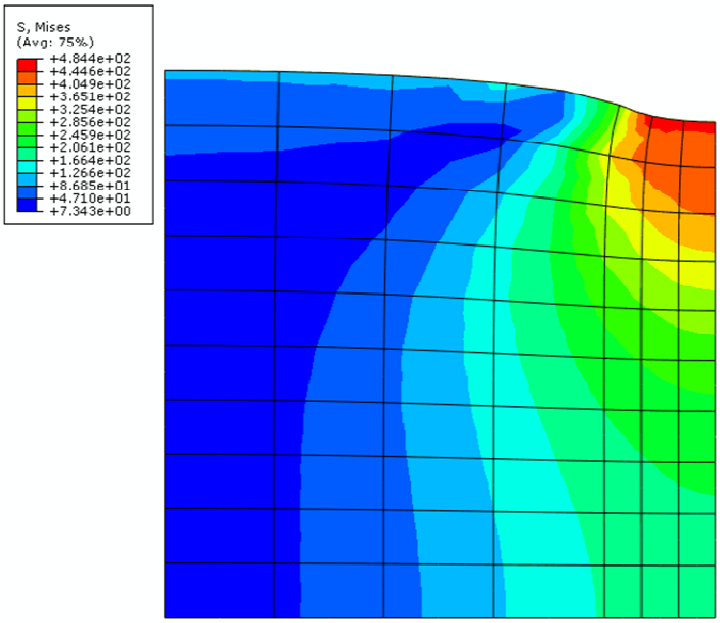

Figure 3.14 Contour plot of von Mises stresses on the deformed body

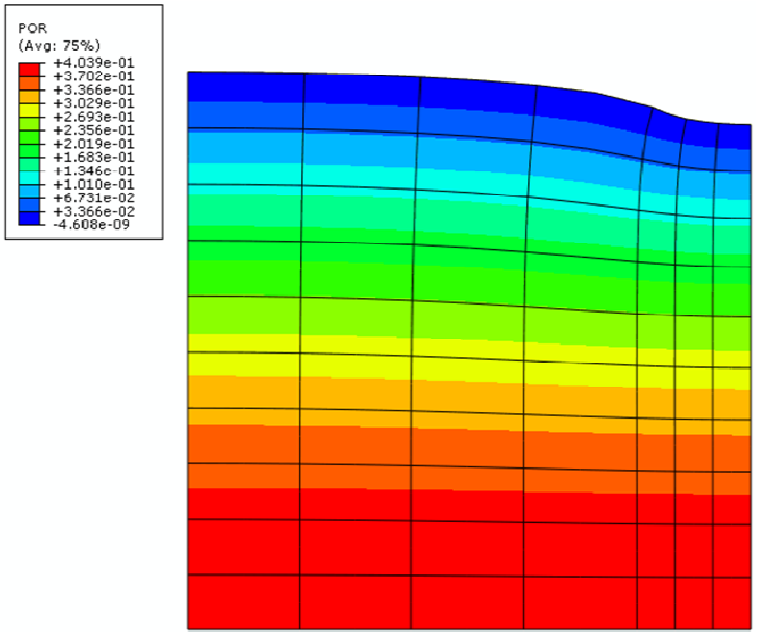

Figure 3.15 The contour plot of pore pressures on the deformed body.

3.6 Summary and Discussion

In this chapter, the finite element formulation of a coupled pore pressure and displacement problem is described. First, a consolidation problem is considered. Using the principal of averages, the balance equations are derived followed by the principle of effective stress. Next, the finite element framework for the coupled problem is explained and the finite element equations are derived for the solution of consolidation problems. Then, the finite element equations are verified solving two steady-state consolidation problems using the commercial software Mathematica®. The elastic behavior of porous media was analyzed. The change in the state of the stress, deviatoric stress and pore pressure, was observed with a great accuracy. The results were in good agreement with the related references.

CHAPTER 4
COUPLED DYNAMIC ANALYSIS OF POROUS MEDIA USING THE FINITE ELEMENT METHOD

4.1 Introduction

The coupled dynamic analysis of soil-pore fluid interaction problems is of tremendous interest in geotechnical engineering and geotechnical earthquake engineering due to its application from pile driving to earthquake response of soil structures. The dynamic behavior of fully saturated porous media was first investigated by Biot (Biot, 1956). In his study, Biot expanded his original work on coupled systems (Biot, 1941) to dynamic problems using the displacement of the solid skeleton **u** and relative fluid displacement **w** as variables. Ghaboussi and Wilson (1972) proposed the first multi-dimensional finite-element formulation to solve the linear coupled governing equations.

Zienkiewicz *et al.* then introduced a simple formulation coupling the displacement of the soil skeleton **u** and pore fluid pressure *p* (Zienkiewicz, et al., 1980). The non-linear behavior of soils including large deformations and non-linear material behavior was also taken into account by Zienkiewicz *et al.* The incremental form of dynamic equations was derived in their studies (Zienkiewicz, 1982; and Zienkiewicz and Shiomi, 1984).

The objective of this chapter is to develop the finite element framework for the solution of the couple dynamic pore pressure/displacement equations to have a better understanding of dynamic soil-pore pressure problems. The organization of this chapter is as follows: First, the finite element framework is developed using the Mathematica software to solve the fully coupled Biot (1941) dynamic equations using the u-p formulation. Then, numerical examples are carried out for the transient analyses of soils. Next, the results are compared with commercial finite element package ABAQUS. Finally, the chapter is summarized and conclusions are presented.

4.2 Governing Equations

The governing equations for the dynamic behavior of soils are similar to those derived for the quasi-static case explained in the previous section. The mass balance equation for the dynamic case is equivalent to the equation used for the static case with the assumption of the grains are incompressible, pore fluid is compressible and the soil is saturated. The dynamic formulation for the linear momentum balance equation for a two-phase medium can be expressed assuming that the interaction forces and the acceleration of the fluid term in Eq. (3.75) are neglected. The final form of mass balance and linear momentum balance equations are defined as follows:

$$\frac{n}{K_w}\frac{\partial p}{\partial t} + div\left[\frac{\mathbf{k}}{\mu^w}\left(-grad\ p + \rho^w \mathbf{g}\right)\right] + div\ \dot{\boldsymbol{u}}^s = 0 \tag{4.1}$$

$$\nabla^T \boldsymbol{\sigma} + \rho \mathbf{g} = \rho \ddot{\boldsymbol{u}}^s \tag{4.2}$$

4.3 Initial and Boundary Conditions

It is necessary to define the initial and boundary conditions for a boundary value problem. The initial conditions specify the full field of displacements and water pressures at time t=0 as follows

$$\boldsymbol{u} = \boldsymbol{u}_0,\ p = p_0 \ \text{ in } \Omega \text{ and on } \Gamma \tag{4.3}$$

where Ω is the domain of interest and Γ is its boundary. The imposed boundary conditions displacements and water pressures are as follows:

$$\begin{aligned} \boldsymbol{u} &= \hat{\boldsymbol{u}} \quad \text{on } \Gamma_u \\ p &= \hat{p} \quad \text{on } \Gamma_p \end{aligned} \tag{4.4}$$

The traction boundary condition for stresses is

$$\boldsymbol{I}^T \boldsymbol{\sigma} = \boldsymbol{t} \ \text{ on } \Gamma_u \tag{4.5}$$

Finally, the flux boundary condition for water from Eq. (3.28) is

$$\rho^w \frac{\mathbf{k}}{\mu^w}\left(-grad\ p + \rho^w \mathbf{g}\right)^T \cdot \mathbf{n} = q \ \text{ on } \Gamma_p \tag{4.6}$$

where q is the imposed mass flux normal to the boundary. Equations (4.4) and (4.5) are natural boundary conditions for the corresponding balance equations.

4.4 Finite Element Implementation

4.4.1 Weak Form

$$\begin{aligned}&\int_\Omega \left[\left\{ \bar{\boldsymbol{\varepsilon}}_u^{\,T} \boldsymbol{\sigma} - \bar{\mathbf{u}}^{\mathrm{T}} \rho\left(\mathbf{g} - \ddot{\mathbf{u}}^s\right)\right\} + \left\{ \bar{p}\frac{n}{K_w}\dot{p} + \bar{\boldsymbol{\varepsilon}}_p^{\,T} \frac{\mathbf{k}}{\mu_w}\left(-grad\ p + \rho^w \mathbf{g}\right) + \bar{p}\mathbf{m}^{\mathrm{T}}\dot{\boldsymbol{\varepsilon}} \right\} \right] \mathrm{d}\Omega \\ &= \int_{\Gamma_u} \bar{\mathbf{u}}^T \mathbf{t}\, d\Gamma + \int_{\Gamma_p} \bar{p}\ \frac{q}{\rho^w}\, \mathrm{d}\Gamma\end{aligned} \tag{4.7}$$

where the virtual displacements, virtual strains and virtual pore pressure derivatives are

$$\begin{aligned}\bar{\mathbf{u}} &= \left\{\bar{u}, \bar{v}, \bar{w}\right\}^T \\ \bar{\boldsymbol{\varepsilon}}_u &= \left\{\frac{\partial \bar{u}}{\partial x}, \frac{\partial \bar{v}}{\partial y}, \frac{\partial \bar{w}}{\partial z}, \frac{\partial \bar{u}}{\partial y} + \frac{\partial \bar{v}}{\partial x}, \frac{\partial \bar{v}}{\partial z} + \frac{\partial \bar{w}}{\partial y}, \frac{\partial \bar{u}}{\partial z} + \frac{\partial \bar{w}}{\partial x}\right\}^T \\ \bar{\boldsymbol{\varepsilon}}_p &= \left\{\frac{\partial \bar{p}}{\partial x}, \frac{\partial \bar{p}}{\partial y}, \frac{\partial \bar{p}}{\partial z}\right\}^T\end{aligned} \tag{4.8}$$

4.4.2 Finite Element Equations

The displacements $\tilde{\mathbf{u}}$ and the pore pressures $\tilde{p}$ are approximated using the weighted residuals method (Galerkin approximations) described in Section 3.3 in the following form:

$$\tilde{\mathbf{u}} \approx \hat{\mathbf{u}} = \sum_i^n \mathbf{N}_{ui}\mathbf{u}_i = \mathbf{N}_u \mathbf{u} \tag{4.9}$$

$$\tilde{p} \approx \hat{p} = \sum_{i}^{m} \mathbf{N}_{pi} p_i = \mathbf{N}_p \mathbf{p} \tag{4.10}$$

where $\boldsymbol{u}$ and $\boldsymbol{p}$are nodal parameters of each field and $\mathbf{N}_u$ and $\mathbf{N}_p$ are the appropriate shape functions. Substituting the assumed solutions into the weak form yields

$$\begin{aligned} &\int_{\Omega} \Bigg[\left\{ \bar{\boldsymbol{\varepsilon}}_u^{\,T} \left(\mathbf{D}_e \mathbf{B}_u \boldsymbol{u} - \boldsymbol{m} \mathbf{N}_p^T \boldsymbol{p} \right) - \bar{\boldsymbol{u}}^{\mathrm{T}} \rho \boldsymbol{g} - \bar{\boldsymbol{u}}^{\mathrm{T}} \rho \mathbf{N}_u \ddot{\boldsymbol{u}}^s \right\} \\ &+ \left\{ \bar{p}^T \frac{n}{K_w} \mathbf{N}_p \dot{\boldsymbol{p}} + \bar{\boldsymbol{\varepsilon}}_p^{\,T} \frac{\mathbf{k}}{\mu_w} \left(\mathbf{B}_p \boldsymbol{p} - \rho^w \mathbf{g} \right) + \bar{p}^T \boldsymbol{m}^{\mathrm{T}} \mathbf{B}_u \dot{\boldsymbol{u}} \right\} \Bigg] \, \mathrm{d}\Omega \\ &= \int_{\Gamma_u^q} \bar{\boldsymbol{u}}^T \mathbf{t} \, d\Gamma + \int_{\Gamma_u^q} \bar{p} \, \frac{q}{\rho^w} \, \mathrm{d}\Gamma \end{aligned} \tag{4.11}$$

The sets of weighting functions are the columns of the matrix of the assumed solution functions defined as follows:

$$\begin{pmatrix} \bar{\boldsymbol{u}} \\ \bar{p} \end{pmatrix} \rightarrow \begin{pmatrix} \mathbf{N}_u & \mathbf{0} \\ \mathbf{0} & \mathbf{N}_p \end{pmatrix} \quad \text{and} \quad \begin{pmatrix} \bar{\boldsymbol{\varepsilon}}_u \\ \bar{\boldsymbol{\varepsilon}}_p \\ \bar{p} \end{pmatrix} \rightarrow \begin{pmatrix} \mathbf{B}_u & \mathbf{0} \\ \mathbf{B}_p & \mathbf{0} \\ \mathbf{0} & \mathbf{N}_p \end{pmatrix} \tag{4.12}$$

Incorporating the shape functions and their derivatives into the weak form, the following sets of equations are obtained.

$$\begin{aligned} &\int_{\Omega} \rho (\mathbf{N}_u^T \mathbf{N}_u) \ddot{\boldsymbol{u}} \, \mathrm{d}\Omega + \int_{\Omega} (\mathbf{B}_u^T \mathbf{D}_e \mathbf{B}_u) \boldsymbol{u} \, \mathrm{d}\Omega - \int_{\Omega} (\mathbf{B}_u^{\,T} \boldsymbol{m} \mathbf{N}_p) \boldsymbol{p} \, \mathrm{d}\Omega \\ &= \int_{\Omega} \mathbf{N}_u^T \rho \mathbf{g} \, \mathrm{d}\Omega + \int_{\Gamma} \mathbf{N}_u^T \mathbf{t} \, \mathrm{d}\Gamma \end{aligned} \tag{4.13}$$

$$\begin{aligned} &\int_{\Omega} \mathbf{N}_p^{\mathrm{T}} \mathbf{m}^{\mathrm{T}} \mathbf{B}_u \dot{\boldsymbol{u}} \, \mathrm{d}\Omega + \int_{\Omega} \mathbf{N}_p^{\mathrm{T}} \frac{n}{K_w} \mathbf{N}_p \dot{\boldsymbol{p}} + \int_{\Omega} \mathbf{B}_p^{\mathrm{T}} \frac{\mathbf{k}}{\mu_w} \mathbf{B}_p \boldsymbol{p} \, \mathrm{d}\Omega = \\ &\int_{\Gamma_w^q} \mathbf{N}_p^{\mathrm{T}} \frac{q^w}{\rho^w} \, \mathrm{d}\Gamma + \int_{\Omega} \mathbf{B}_p^{\mathrm{T}} \frac{\mathbf{k}}{\mu_w} \rho^w \mathbf{g} \, \mathrm{d}\Omega \end{aligned} \tag{4.14}$$

The final form of the spatially discretized linear momentum and mass balance equations are then written in the compact forms as follows:

$$\mathbf{M}_s\ddot{\boldsymbol{u}}+\mathbf{K}_m\,\boldsymbol{u}-\mathbf{Q}\,\boldsymbol{p}=\mathbf{f}^u \tag{4.15}$$

$$\mathbf{Q}^{\mathrm{T}}\dot{\boldsymbol{u}}+\mathbf{S}\,\dot{\boldsymbol{p}}+\mathbf{K}_c\,\boldsymbol{p}\;=\mathbf{f}^p \tag{4.16}$$

in which

$$\mathbf{M}_s\;=\;\int_\Omega \rho\mathbf{N}_u^{\mathrm{T}}\mathbf{N}_u\mathrm{d}\Omega \tag{4.17}$$

$$\mathbf{K}_m\;=\;\int_\Omega \mathbf{B}_u^{\mathrm{T}}\mathbf{D}_{\mathrm{e}}\mathbf{B}_u\mathrm{d}\Omega \tag{4.18}$$

$$\mathbf{Q}=\;\int_\Omega \mathbf{B}_u^{\mathrm{T}}\mathbf{m}\mathbf{N}_p\mathrm{d}\Omega \tag{4.19}$$

$$\mathbf{S}=\int_\Omega \mathbf{N}_p^{\mathrm{T}}\frac{n}{K_w}\mathbf{N}_p\;\mathrm{d}\Omega \tag{4.20}$$

$$\mathbf{K_c}=\int_\Omega \mathbf{B}_p^{\mathrm{T}}\frac{\mathbf{k}}{\mu_w}\mathbf{B}_p\;\mathrm{d}\Omega \tag{4.21}$$

$$\mathbf{f}^u=\int_\Omega \mathbf{N}_u^{\mathrm{T}}\rho\mathbf{g}\;\mathrm{d}\Omega+\int_\Gamma \mathbf{N}_u^{\mathrm{T}}\mathbf{t}\;\mathrm{d}\Gamma \tag{4.22}$$

$$\mathbf{f}^p=\int_\Omega \mathbf{B}_p^{\mathrm{T}}\frac{\mathbf{k}}{\mu_w}\rho^w\mathbf{g}\;\mathrm{d}\Omega+\int_{\Gamma_w^q}\mathbf{N}_p^{\mathrm{T}}\frac{q^w}{\rho^w}\;\mathrm{d}\Gamma \tag{4.23}$$

where $\mathbf{M_s}$ is the mass matrix for the solid phase, $\mathbf{K}_m$ is the elemental elastic stiffness matrix, $\mathbf{Q}$ is the coupling matrix, $\mathbf{S}$ is the compressibility matrix, $\mathbf{K_c}$ is the permeability (flow) matrix, $\mathbf{f}^u$ is the elemental vector of external forces, and $\mathbf{f}^p$ is the fluid supply vector. The final matrix form of the coupled dynamic equations for consolidation is expressed as

$$\begin{bmatrix}\mathbf{M}_s & \mathbf{0}\\ \mathbf{0} & \mathbf{0}\end{bmatrix}\begin{Bmatrix}\ddot{\mathbf{u}}\\ \ddot{\mathbf{p}}\end{Bmatrix}+\begin{bmatrix}\mathbf{K}_m & -\mathbf{Q}\\ \mathbf{0} & \mathbf{K}_c\end{bmatrix}\begin{Bmatrix}\mathbf{u}\\ \mathbf{p}\end{Bmatrix}+\begin{bmatrix}\mathbf{0} & \mathbf{0}\\ \mathbf{Q}^{\mathrm{T}} & \mathbf{S}\end{bmatrix}\begin{Bmatrix}\dot{\mathbf{u}}\\ \dot{\mathbf{p}}\end{Bmatrix}=\begin{Bmatrix}\mathbf{f}^{\mathrm{u}}\\ \mathbf{f}^{\mathrm{p}}\end{Bmatrix} \tag{4.24}$$

4.5 Discretization in Time using the Newmark Algorithm

The total discrete equilibrium equations for the soil-fluid mixture were developed using the finite element method in the previous section. In this section, the discretization

process will be carried out in the time domain to present a solution for the transient problems including linear and non-linear cases. To perform the step-by-step time discretization, the *Newmark algorithm* (Newmark, 1959) which is a widely applicable finite difference approximation will be used for the solution of the dynamic coupled equations in the time domain (Zienkiewicz, et al., 1985). Assuming that the nodal displacement vector $\boldsymbol{u}_n$ and the nodal velocity vector $\dot{\boldsymbol{u}}_n$ at time $\boldsymbol{t}_n$ are known, the approximations for $\boldsymbol{u}_{n+1}$ and $\dot{\boldsymbol{u}}_{n+1}$ at time $\boldsymbol{t}_{n+1}$ can be written as follows:

$$\begin{aligned}
\mathbf{u}_{n+1} &= \mathbf{u}_n + \Delta t\dot{\mathbf{u}}_n + \left(\frac{1}{2}-\beta\right)\Delta t^2\ddot{\mathbf{u}}_n + \beta\Delta t^2\ddot{\mathbf{u}}_{n+1} \\
&= \mathbf{u}_n + \Delta t\dot{\mathbf{u}}_n + \frac{1}{2}\Delta t^2\ddot{\mathbf{u}}_n - \beta\Delta t^2\ddot{\mathbf{u}}_n + \beta\Delta t^2\ddot{\mathbf{u}}_{n+1} \equiv \mathbf{u}^p_{n+1} + \beta\Delta t^2\Delta\ddot{\mathbf{u}}_{n+1} \\
\dot{\mathbf{u}}_{n+1} &= \dot{\mathbf{u}}_n + (1-\gamma)\Delta t\ddot{\mathbf{u}}_n + \gamma\Delta t\ddot{\mathbf{u}}_{n+1} \\
&= \dot{\mathbf{u}}_n + \Delta t\ddot{\mathbf{u}}_n - \gamma\Delta t\ddot{\mathbf{u}}_n + \gamma\Delta t\ddot{\mathbf{u}}_{n+1} \equiv \dot{\mathbf{u}}^p_{n+1} + \gamma\Delta t\Delta\ddot{\mathbf{u}}_{n+1}
\end{aligned} \tag{4.25}$$

where

$$\begin{aligned}
\mathbf{u}^p_{n+1} &= \mathbf{u}_n + \Delta t\dot{\mathbf{u}}_n + \frac{1}{2}\Delta t^2\ddot{\mathbf{u}}_n \\
\dot{\mathbf{u}}^p_{n+1} &= \dot{\mathbf{u}}_n + \Delta t\ddot{\mathbf{u}}_n
\end{aligned} \tag{4.26}$$

For the approximation of the pore pressure variable $\mathbf{p}_{n+1}$ at t_{n+1}, the approximation of $\mathbf{p}_{n+1}$ is written as follows:

$$\begin{aligned}
\mathbf{p}_{n+1} &= \mathbf{p}_n + (1-\theta)\Delta t\dot{\mathbf{p}}_n + \theta\Delta t\dot{\mathbf{p}}_{n+1} \\
&= \mathbf{p}_n + \Delta t\dot{\mathbf{p}}_n - \theta\Delta t\dot{\mathbf{p}}_n + \theta\Delta t\dot{\mathbf{p}}_{n+1} \equiv \mathbf{p}^p_{n+1} + \theta\Delta t\Delta\dot{\mathbf{p}}_{n+1}
\end{aligned} \tag{4.27}$$

where

$$\mathbf{p}^p_{n+1} = \mathbf{p}_n + \Delta t\dot{\mathbf{p}}_n \tag{4.28}$$

with the unknown terms defined as

$$\Delta\ddot{\mathbf{u}}_{n+1} = \ddot{\mathbf{u}}_{n+1} - \ddot{\mathbf{u}}_n \quad \text{and} \quad \Delta\dot{\mathbf{p}}_{n+1} = \dot{\mathbf{p}}_{n+1} - \dot{\mathbf{p}}_n \tag{4.29}$$

The variables with superscript '*p*' in the above equations such as $\mathbf{u}_{n+1}^{p}$, etc. denote the values that can be 'predicted' from the known parameters at time t_n.

The finite element discrete approximations for the dynamic coupled governing equations (Equations 4.15 and 4.16) were already derived in the previous section. To perform the discretization in time domain, the approximations for the nodal displacement, pore pressure and their derivatives with respect to time are substituted in the governing equations as follows:

$$\begin{aligned} \mathbf{M}_s\ddot{\mathbf{u}}_{n+1} + \mathbf{K}_m\mathbf{u}_{n+1} - \mathbf{Q}\mathbf{p}_{n+1} - \mathbf{f}_{n+1}^{u} &= \mathbf{0} \\ \mathbf{Q}^{\mathrm{T}}\dot{\mathbf{u}}_{n+1} + \mathbf{S}\dot{\mathbf{p}}_{n+1} + \mathbf{K}_c\mathbf{p}_{n+1} - \mathbf{f}_{n+1}^{p} &= \mathbf{0} \end{aligned} \tag{4.30}$$

Substituting the approximated description of $\mathbf{u}_{n+1}$ and $\mathbf{p}_{n+1}$ in the first governing equation above yields

$$\begin{aligned} &\mathbf{M}_s\ddot{\mathbf{u}}_{n+1} + \mathbf{K}_m\left[\mathbf{u}_n + \Delta t\dot{\mathbf{u}}_n + \left(\frac{1}{2}-\beta\right)\Delta t^2\ddot{\mathbf{u}}_n + \beta\Delta t^2\ddot{\mathbf{u}}_{n+1}\right] \\ &\quad - \mathbf{Q}\left[\mathbf{p}_n + (1-\theta)\Delta t\dot{\mathbf{p}}_n + \theta\Delta t\dot{\mathbf{p}}_{n+1}\right] - \mathbf{f}_{n+1}^{u} = \mathbf{0} \end{aligned} \tag{4.31}$$

Substituting the predictable values into Eq. (4.32) yields

$$\mathbf{M}_s\left(\ddot{\mathbf{u}}_n + \Delta\ddot{\mathbf{u}}_{n+1}\right) + \mathbf{K}_m\left(\mathbf{u}^{p}{}_{n+1} + \beta\Delta t^2\Delta\ddot{\mathbf{u}}_{n+1}\right) - \mathbf{Q}\left(\mathbf{p}_{n+1}^{p} + \theta\Delta t\Delta\dot{\mathbf{p}}_{n+1}\right) - \mathbf{f}_{n+1}^{u} = \mathbf{0} \tag{4.32}$$

Rearranging the terms by writing the unknown terms on the left hand side and known terms (the terms to be predicted) on the right side leads

$$\left(\mathbf{M}_s + \beta\Delta t^2\mathbf{K}_m\right)\Delta\ddot{\mathbf{u}}_{n+1} - \left(\theta\Delta t\mathbf{Q}\right)\Delta\dot{\mathbf{p}}_{n+1} = -\mathbf{M}_s\ddot{\mathbf{u}}_n - \mathbf{K}_m\mathbf{u}_{n+1}^{p} + \mathbf{Q}\mathbf{p}_{n+1}^{p} + \mathbf{f}_{n+1}^{u} \tag{4.33}$$

Similarly the second governing equation can be expressed as follows:

$$\begin{aligned} &\mathbf{Q}^{\mathrm{T}}\left[\dot{\mathbf{u}}_n + (1-\gamma)\Delta t\ddot{\mathbf{u}}_n + \gamma\Delta t\ddot{\mathbf{u}}_{n+1}\right] + \mathbf{S}\dot{\mathbf{p}}_{n+1} \\ &+\mathbf{K}_c\left[\mathbf{p}_{n+1} + (1-\theta)\Delta t\dot{\mathbf{p}} + \theta\Delta t\dot{\mathbf{p}}_{n+1}\right] - \mathbf{f}_{n+1}^{p} = \mathbf{0} \end{aligned} \tag{4.34}$$

Rearranging the predictable terms yields

$$\mathbf{Q}^{\mathrm{T}}\left(\dot{\mathbf{u}}_{n+1}^{p}+\gamma\Delta t\Delta\ddot{\mathbf{u}}_{n+1}\right)+\mathbf{S}\left(\dot{\mathbf{p}}_{n}+\Delta\dot{\mathbf{p}}_{n+1}\right)+\mathbf{K}_{c}\left(\mathbf{p}_{n+1}^{p}+\theta\Delta t\Delta\dot{\mathbf{p}}_{n+1}\right)-\mathbf{f}_{n+1}^{p}=\mathbf{0} \tag{4.35}$$

The terms can then be rearranged as follows:

$$\left(\gamma\Delta t\mathbf{Q}^{\mathrm{T}}\right)\Delta\ddot{\mathbf{u}}_{n+1}+\left(\theta\Delta t\mathbf{K}_{c}+\mathbf{S}\right)\Delta\dot{\mathbf{p}}_{n+1}=-\mathbf{Q}^{\mathrm{T}}\dot{\mathbf{u}}_{n+1}^{p}-\mathbf{S}\dot{\mathbf{p}}_{n}-\mathbf{K}_{c}\mathbf{p}_{n+1}^{p}+\mathbf{f}_{n+1}^{p} \tag{4.36}$$

The governing equations in terms of approximated variables can be coupled and presented in a matrix form as follows:

$$\begin{bmatrix}\mathbf{M}_{s}+\beta\Delta t^{2}\mathbf{K}_{m} & -\theta\Delta t\mathbf{Q}\\ \gamma\Delta t\mathbf{Q}^{\mathrm{T}} & \theta\Delta\mathrm{t}\mathbf{K}_{c}+\mathbf{S}\end{bmatrix}_{n+1}\begin{Bmatrix}\Delta\ddot{\mathbf{u}}\\ \Delta\dot{\mathbf{p}}\end{Bmatrix}_{n+1}=\begin{Bmatrix}-\mathbf{M}_{s}\ddot{\mathbf{u}}_{n}-\mathbf{K}_{m}\mathbf{u}_{n+1}^{p}+\mathbf{Q}\mathbf{p}_{n+1}^{p}+\mathbf{f}_{n+1}^{u}\\ -\mathbf{Q}^{\mathrm{T}}\dot{\mathbf{u}}_{n+1}^{p}-\mathbf{S}\dot{\mathbf{p}}_{n}-\mathbf{K}_{c}\mathbf{p}_{n+1}^{p}+\mathbf{f}_{n+1}^{p}\end{Bmatrix} \tag{4.37}$$

where

$$\begin{aligned}\mathbf{f}^{u}&=\int_{\Omega}\mathbf{N}_{u}^{\mathrm{T}}\tilde{\rho}\mathbf{g}\ \mathrm{d}\Omega+\int_{\Gamma}\mathbf{N}_{u}^{\mathrm{T}}\mathbf{t}\ \mathrm{d}\Gamma\\ \mathbf{f}^{p}&=\int_{\Omega}\mathbf{B}_{p}^{\mathrm{T}}\frac{\mathbf{k}}{\mu_{w}}\rho^{w}\mathbf{g}\ \mathrm{d}\Omega+\int_{\Gamma_{w}^{q}}\mathbf{N}_{p}^{\mathrm{T}}\frac{q^{w}}{\rho^{w}}\ \mathrm{d}\Gamma\end{aligned} \tag{4.38}$$

In a more compact form, the above equation may be written as

$$\begin{bmatrix}\mathbf{M}_{s}+\beta\Delta t^{2}\mathbf{K}_{m} & -\theta\Delta t\mathbf{Q}\\ \gamma\Delta t\mathbf{Q}^{\mathrm{T}} & \theta\Delta\mathrm{t}\mathbf{K}_{c}+\mathbf{S}\end{bmatrix}_{n+1}\begin{Bmatrix}\Delta\ddot{\mathbf{u}}\\ \Delta\dot{\mathbf{p}}\end{Bmatrix}_{n+1}=\begin{Bmatrix}\mathbf{R}_{u}\\ \mathbf{R}_{p}\end{Bmatrix}_{n} \tag{4.39}$$

in which

$$\begin{aligned}\mathbf{R}_{u}&=-\mathbf{M}_{s}\ddot{\mathbf{u}}_{n}-\mathbf{K}_{m}\mathbf{u}_{n+1}^{p}+\mathbf{Q}\mathbf{p}_{n+1}^{p}+\mathbf{f}_{n+1}^{u}\\ &=-\mathbf{M}_{s}\ddot{\mathbf{u}}_{n}-\mathbf{K}_{m}\left(\mathbf{u}_{n}+\Delta t\dot{\mathbf{u}}_{n}+\frac{1}{2}\Delta t^{2}\ddot{\mathbf{u}}_{n}\right)+\mathbf{Q}\left(\mathbf{p}_{n}+\Delta t\dot{\mathbf{p}}_{n}\right)+\mathbf{f}_{n+1}^{u}\\ \mathbf{R}_{p}&=-\mathbf{Q}^{\mathrm{T}}\dot{\mathbf{u}}_{n+1}^{p}-\mathbf{S}\dot{\mathbf{p}}_{n}-\mathbf{K}_{c}\mathbf{p}_{n+1}^{p}+\mathbf{f}_{n+1}^{p}\\ &=-\mathbf{Q}^{\mathrm{T}}\left(\dot{\mathbf{u}}_{n}+\Delta t\ddot{\mathbf{u}}_{n}\right)-\mathbf{S}\dot{\mathbf{p}}_{n}+\mathbf{K}_{c}\left(\mathbf{p}_{n}+\Delta t\dot{\mathbf{p}}_{n}\right)+\mathbf{f}_{n+1}^{p}\end{aligned} \tag{4.40}$$

The solution procedure for the final form of the equation system is as follows:

1. Select the Newmark parameters γ, β and θ. The selection of the Newmark parameters γ, β and θ is very important, because the solution can be unstable if these parameters are not selected correctly. The Newmark algorithm is unconditionally stable and thus fully implicit when the following conditions are satisfied (Zienkiewicz, et al., 1985):

$$\gamma \geq \frac{1}{2}, \qquad \beta \geq \frac{1}{4}, \qquad \theta \geq \frac{1}{2} \tag{4.41}$$

2. Enter the prescribed initial conditions at t_n in the final form of the dynamic governing equation system.
3. Solve the equation system, Eq. (4.40), at time t_{n+1} for the incremental nodal acceleration and nodal rate form of pore pressures $\Delta\ddot{\mathbf{u}}_{n+1}$ and $\Delta\dot{\mathbf{p}}_{n+1}$.
4. Update the solution to find the nodal accelerations at the rate form of pore pressures at time t_{n+1}.
5. Repeat steps 1 through 4 at each time step with an increment of Δt until the solution is complete.

4.6 Numerical Applications

4.6.1 Transient Analysis of a Soil Column

An elastic soil column, which is shown in Figure 4.1, is subjected to a surface step loading of 1.0 kN/m^2. The step loading is applied with an initial time of 0.1 second as shown in Figure 4.2. The soil column has a width of 3 m and a height of 30 m. It is modeled using ten 8/4-**u**/*p* elements where 8-node displacements coupled to 4-node pore pressures. The porous medium is considered as fully saturated with water. The material is considered as isotropic and elastic. The material properties are given in Table 4.1. The boundary conditions are shown in Figure 4.1. Drainage is not allowed in the first 0.1 s.

The drainage is allowed only on the top surface after the initial loading is complete remaining constant until the end of the analysis. The other sides are kept undrained during the analysis. A direct implicit algorithm is adopted for the solution of the problem. Time-stepping parameters are chosen as $\beta=0.3025$, $\theta=0.6$ and $\gamma=0.6$.

The solution for the analysis of consolidation in the soil column is obtained for two time intervals with different time steps. The first analysis is run within a total time of t_f=20 s with a time step of Δt=0.05 s. The second analysis is run within a total time of t_f =200 s with a time step of Δt=0.2 s. The reason for choosing two different time steps is to show the effect of loading rate on the change of pore pressures. Three nodes namely Node 1, Node 26 and Node 46 are selected to show the pore pressure change in the soil column. Node 1 is located at the bottom, Node 26 is located in the middle and Node 46 is located at the top of the soil column. Time history of pore pressures for t_f=20 s and t_f=200 s are plotted for Nodes 1, 26 and 46 as shown in Figures 4.3 and 4.4, respectively.

In Figure 4.3, the pore pressures vs. time are plotted at Nodes 1, 26 and 46 for a total loading time of t_f=20 s with a time step of $\Delta t = 0.05\,\text{s}$. The pore water pressures at Nodes 1 and 26 are constant throughout the analysis and have a value of 1 kN/m^2. The pore water pressure at Node 46 has a value of 1.2 kN/m^2 at time t=0.1 s and gradually decreases to a value of approximately 0.6 kN/m^2 at the end of the analysis as shown in Figure 4.3. The initial excessive pore pressure of 0.2 kN/m^2 occurs at Node 46, because the load is applied rapidly on the top surface. Since the load is applied within a very short period of time, the trapped water in the pores creates excessive pressure before it leaves the pores.

Figure 4.4 shows the pore pressures at Nodes 1, 26 and 46 for an analysis period of t_f=200 s with a time step of $\Delta t = 0.2\,\text{s}$. The pore pressure at the bottom of the soil column remains constant throughout the analysis and has a value of 1.0 kN/m^2. The pore pressure in the middle decreases gradually from 1.0 kN/m^{2}to 0.8 kN/m^2. The pore pressure on the top surface decreases from 1.2 kN/m^2 to 0.2 kN/m^2 during the analysis.

The top surface is drained, thus the pore pressures close to the top surface dissipate with a faster rate compared to the pore pressures in the bottom of the soil column. That is the reason the pore pressures at the bottom remain constant throughout the analysis. All of the results are in good agreement with the published data (Huang, et al., 1998).

In Figure 4.5, the pore pressures for the same example obtained from the finite element package ABAQUS are plotted. The results shown in Figure 4.5 match perfectly with the present work which is conducted using the finite element code implemented in Mathematica software. The contour plots of the pore pressure distribution in the soil column for tf=20 s and tf=200s are shown in Figure 4.6. The first plot shows pore water pressure decreases from 0.0 kN/m^2on the top surface to 0.9 kN/m^2 to a depth of approximately 6 m from top. The second plot shows that pore water pressure changes from 1.0 kN/m^2 to0.9 kN/m^2within a depth of approximately 21 m from the top surface. This comparison shows the effect of time that is required for dissipation of pore water pressure. The longer the analysis time, the greater the dissipation occurs in the soil column.

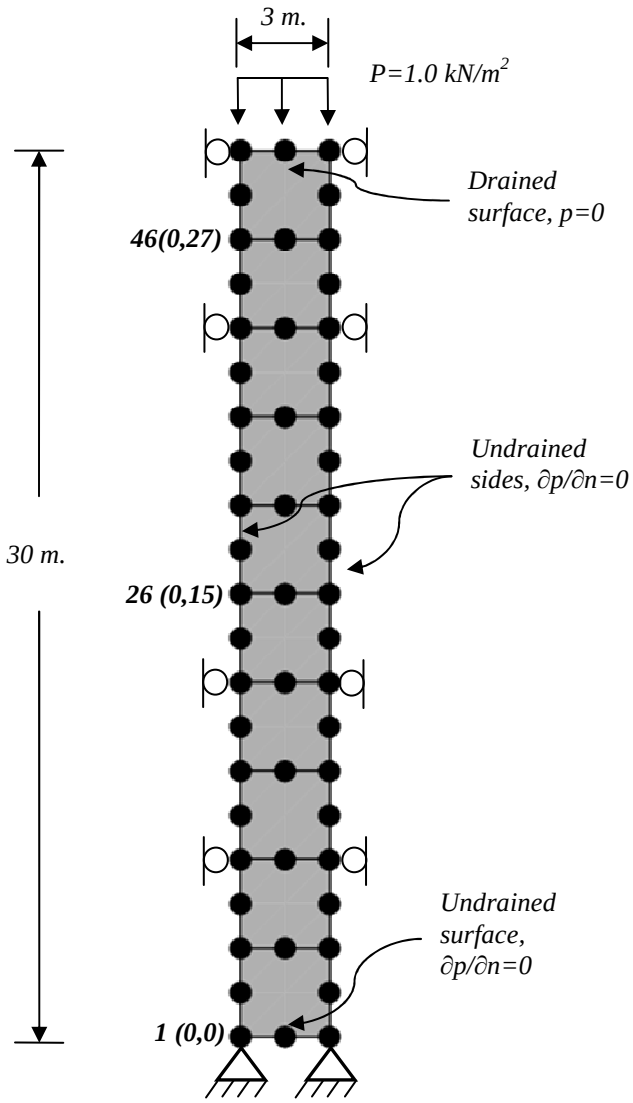

Figure 4.1 Finite element mesh of the one-dimensional elastic soil column.

Table 4.1 Material properties of the soil column

Material Parameter	Notation	Value	Units
	General		
Density of solid	ρ_s	2.0×10^{3}	kg/m^3
Density of water	ρ_w	1.0×10^{4}	kg/m^3
Permeability	k	1.0×10^{-4}	*m/sec*
Porosity	n	0.3	-
	Elastic		
Modulus of elasticity	E	3.0×10^{4}	kN/m^2
Poisson's ratio	v	0.2	-

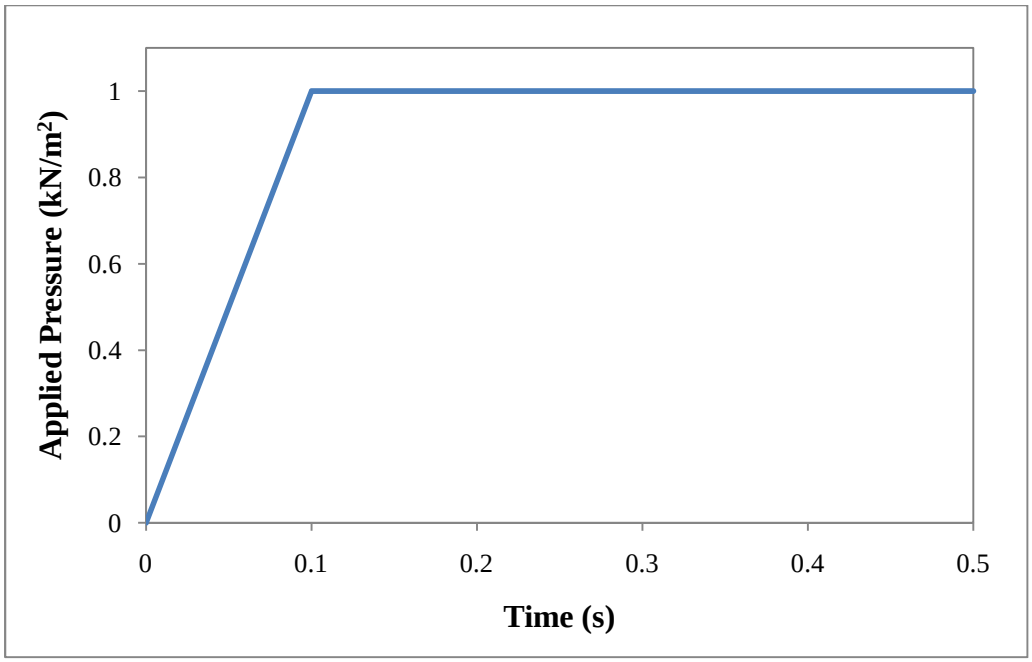

Figure 4.2 Ramp load versus time.

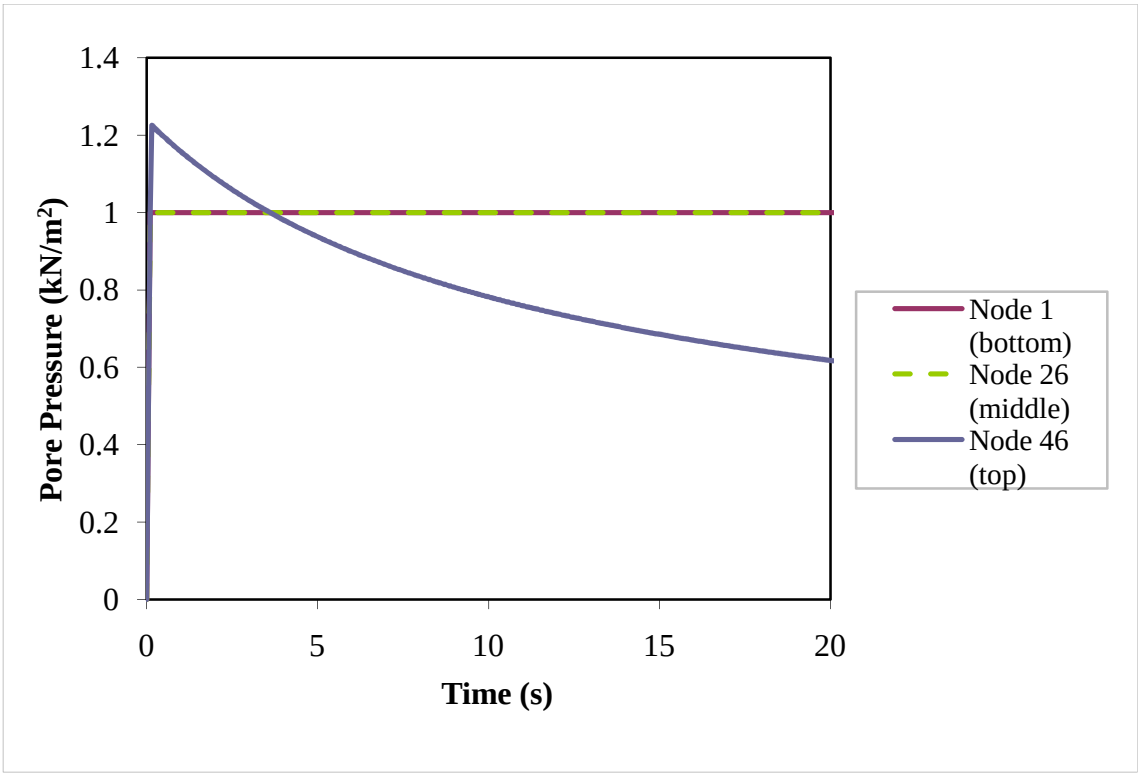

Figure 4.3 Pore pressure vs. time at nodes *1*, *26* and *46* at t_f=20 sec with Δt=0.05 s.

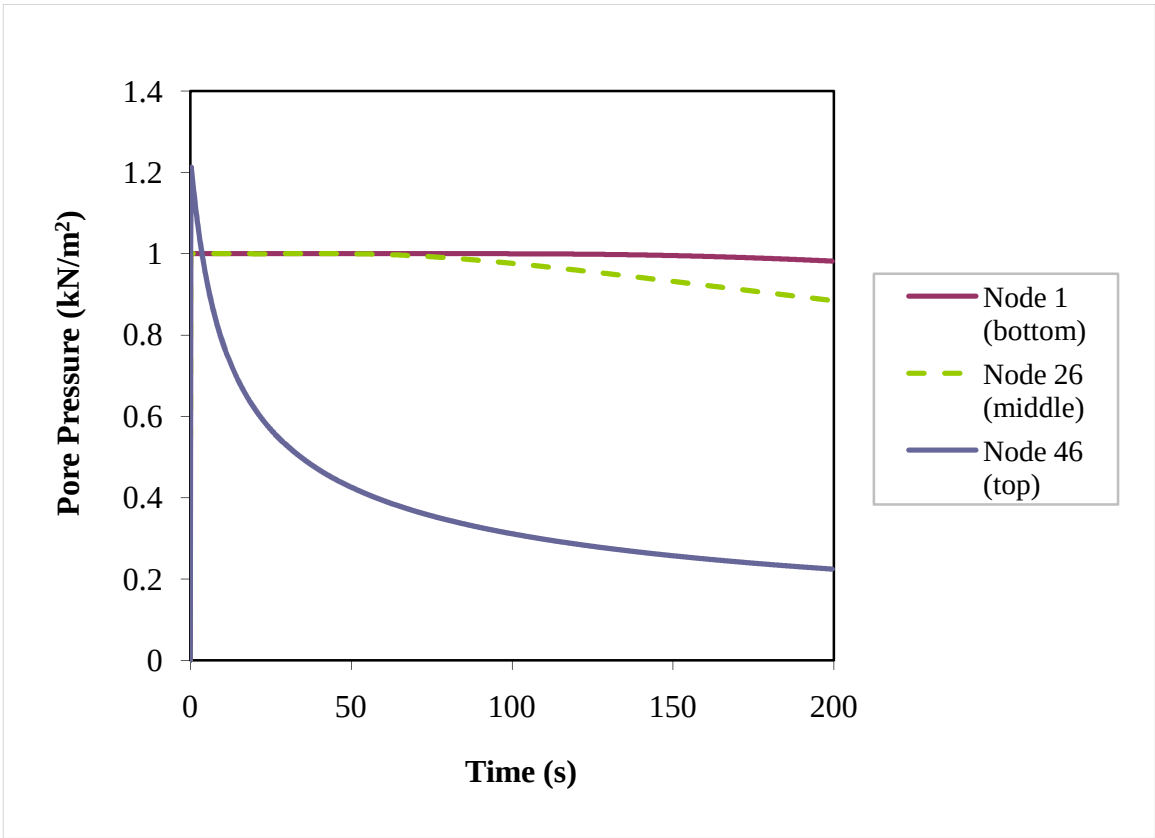

Figure 4.4 Pore pressure vs. time at nodes *1, 26* and *46* at t_f=200 sec with Δt=0.2 s

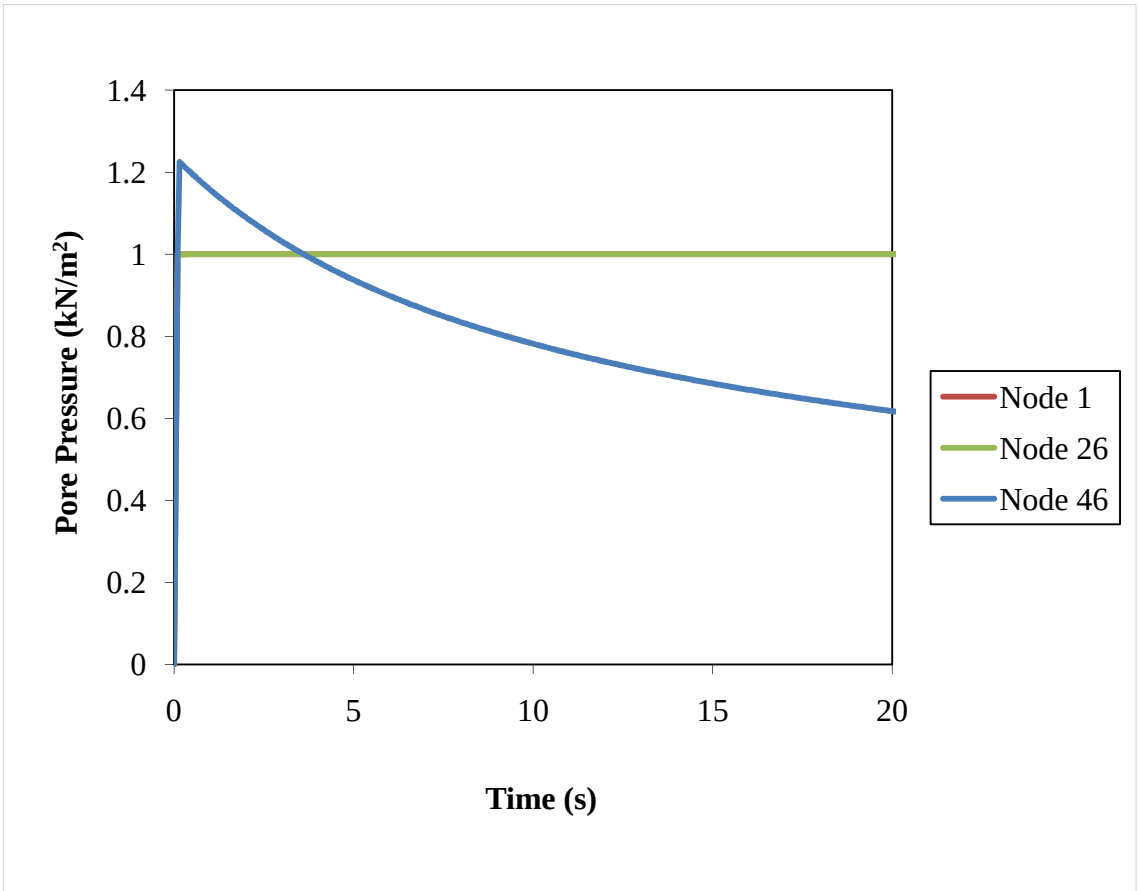

Figure 4.5 Pore pressure vs. time at t_f=20 sec using the ABAQUS software.

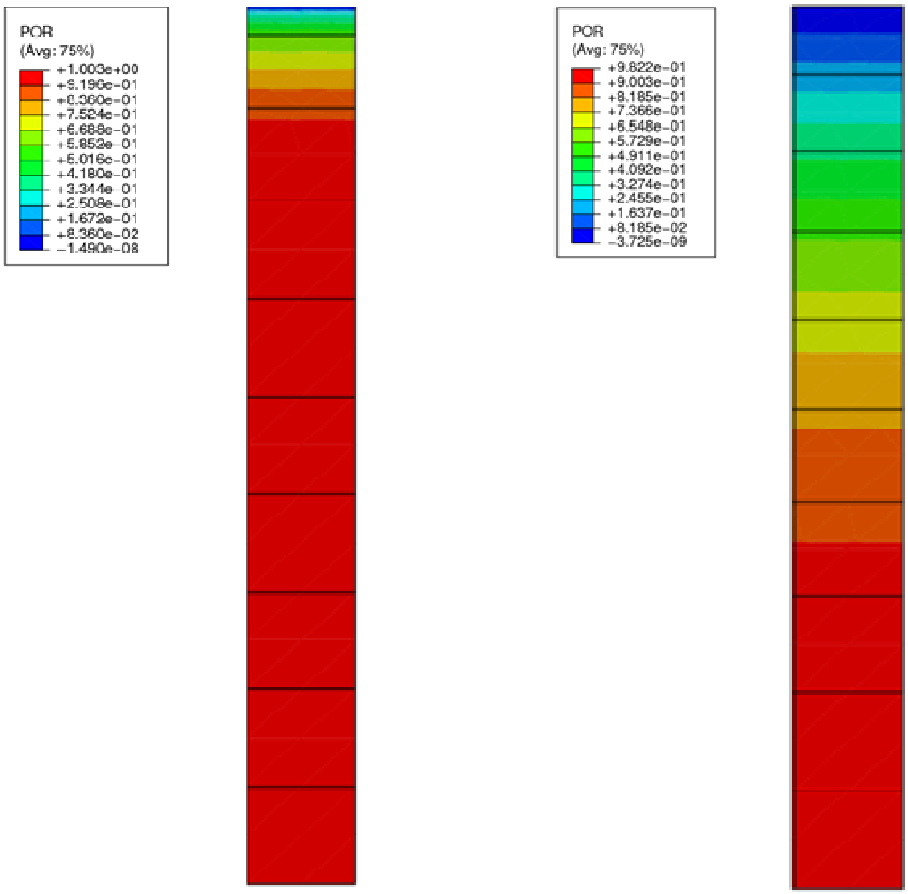

(a) (b)

Figure 4.6 Contour plot of pore pressure distribution in the soil column at (a) t_f=20 s and (b) t_f=200 s.

4.6.2 Transient Analysis of a Soil Foundation

An elastic soil foundation is subjected to a surface step loading is analyzed in this numerical application. The finite element mesh of the model and the boundary condition are shown in Figure 4.7. The commercial finite element package ABAQUS is used for this analysis. Eight-noded, continuum, biquadratic, coupled displacement/pore pressure element elements are used in this analysis. The element type CPE8P which is available in the ABAQUS element library is shown in Figure 4.8.

The material properties are identical to those used in Example 4.6.1 as shown in Table 4.1. The elastic soil foundation is considered fully saturated. A surface step loading of 350 kN/m^2 is applied at an initial time of 0.1 s. The drainage is not allowed during initial loading. After t=0.1 s, drainage is allowed only on the top surface until the end of the analysis. The soil consolidation is analyzed until t_f= 50 s with fixed time steps of $\Delta t = 0.05$ s.

Three nodes are selected to analyze the pore water pressure change in the finite element model. Nodes A, B and C are located at 6 m, 12 m and 15 m below the foundation level respectively (Figure 4.7). The pore water pressures versus time are plotted at Nodes A, B and C as shown in Figure 4.9. The pore pressure at Node A starts from approximately $110kN/m^2$and increases to $120kN/m^2$, and decrease gradually to a level of $60kN/m^2$. The initial increase occurs within the first six seconds. This can be explained by the rapid loading of the foundation. The pore pressure at Node B starts from approximately 65 $kN/m^2$and increases to 67 kN/m^2within the first 25 seconds and then decreases to $65kN/m^2$. At Node C, the pore pressure remains almost constant at the level of 58 kN/m^2 during the analysis. As the depth increases, the effect of the applied load on the pore pressures becomes less significant. This can also be explained by evaluating the contour plot of pore pressures as shown in Figure 4.10. In this Figure, the pore pressure distribution at t_f= 50 s is plotted. The pore pressure is$0kN/m^2$ on the top surface and gradually increases to 68 kN/m^2 at a depth of approximately 15 m below the

ground surface, then decreases to 50kN/m^2 at the level of 30 m below the ground surface. The pore pressures dissipate further away from the foundation as shown in Figure 4.10. The Von Mises stresses in the finite element model are shown in Figure 4.11. The stresses start from 245kN/m^2at the ground level and decrease to 0kN/m^2 at 30 m below the ground surface. As shown in Figure 4.11, the stress distribution follows a circular pattern underneath the foundation. The results are consistent with those of Huang, et al. (1998).

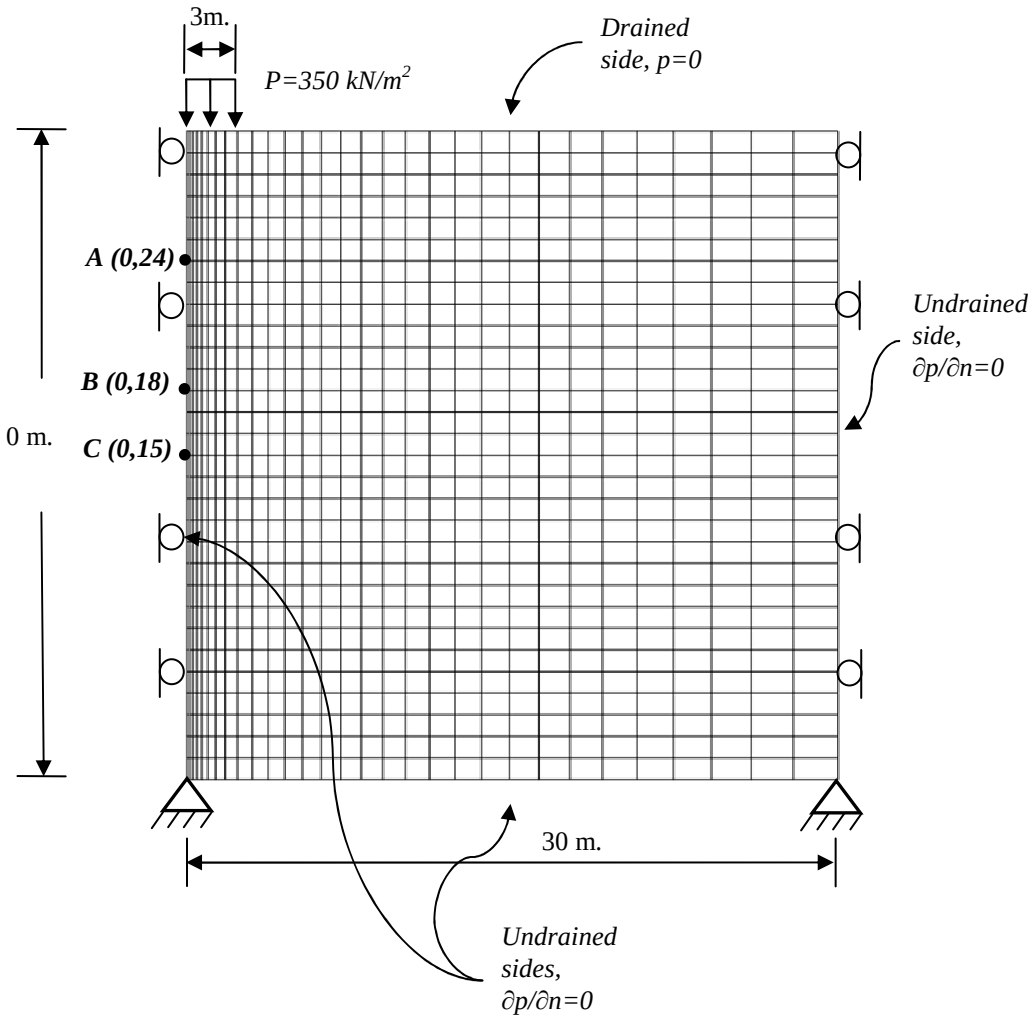

Figure 4.7 Finite element mesh of an elastic soil foundation.

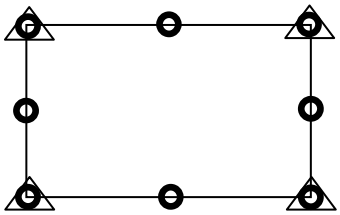

d_x, d_y displacement degrees of freedom

d_x, d_y and p displacement and pore pressure

Figure 4.8 Representation of eight-noded, continuum, biquadratic, coupled displacement/pore pressure element in ABAQUS/Standard.

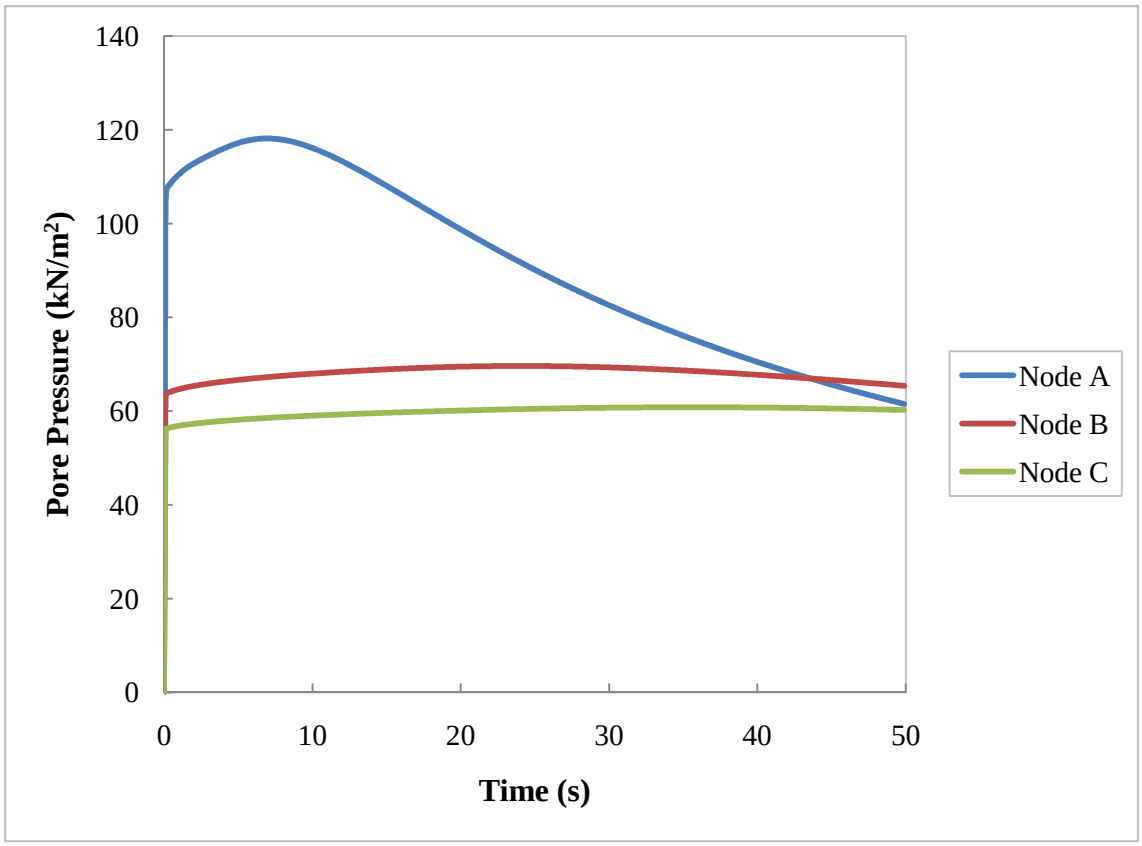

Figure 4.9 Pore pressure vs. time at nodes *A*, *B* and *C*.

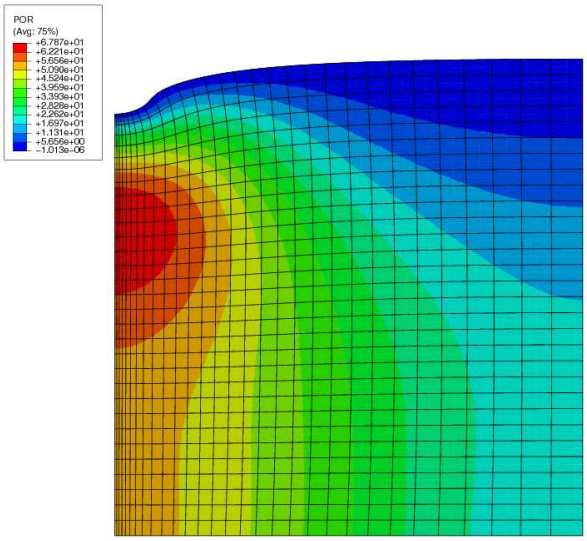

Figure 4.10 Pore pressure distribution at t_f = 50 s in the soil foundation.

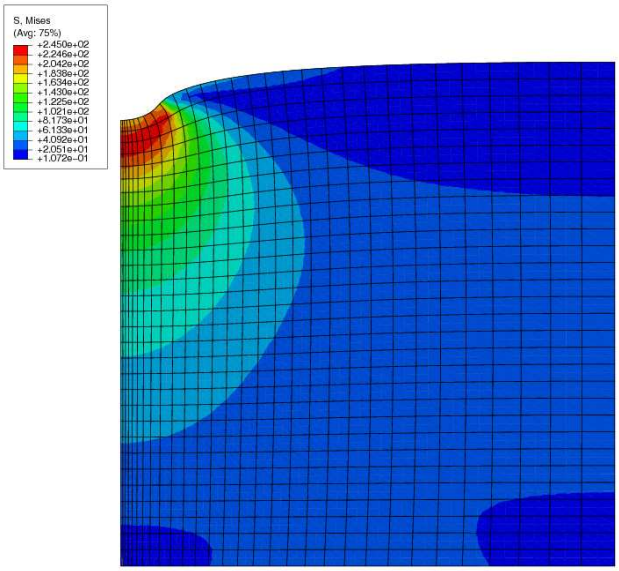

Figure 4.11 Von Mises stress distribution at t_f = 50 s in the soil foundation.

4.7 Summary and Discussion

Transient analysis of porous medium is formulated using the finite element method based on the works of Zienkiewicz and his colleagues (1980, 1982, and 1984). The governing equations for the dynamic behavior of soils are derived using the mass balance and linear momentum balance equations. The soil is considered as comprised of soil skeleton and pore water. It is assumed that the soil grains are incompressible and the pore water is compressible. The soil is assumed to be fully saturated. The interaction forces and the acceleration terms are neglected in the governing equations.

Finite element equations are developed by discretization the governing equations in spatial and time domains. The discretization in spatial domain is carried out and the final forms of governing equations are described. The discretization in time domain is performed using the Newmark algorithm (Newmark, 1959).Based on the final form the coupled dynamic equations, a finite element code is developed using Mathematica software.

Numerical applications are exhibited for validating the finite element code. In the first application, a soil column is analyzed under dynamic loading. The change of pore water pressure over time is illustrated under drained conditions. In the second application, a strip foundation is analyzed under dynamic loading. The effects of pore pressure changes caused by rapid loading are investigated. It is found that the rate of loading has a significant impact on the magnitude of excessive pore water pressures. These applications are also carried out by ABAQUS software. The finite element code has been beneficial for interpreting the results obtained from ABAQUS. The results are found to be consistent with the published data.

CHAPTER 5

ELASTO-PLASTIC CONSTITUTIVE MODELS

Constitutive modeling of soil behavior under general loading and variable site conditions plays a key role in obtaining accurate numerical results. A linear elastic constitutive relationship has been widely used to represent soils in early numerical studies; however soil behavior is highly nonlinear in most cases. The choice of an appropriate stress-strain relationship and idealization of the soil material behavior with the assumptions of continuum mechanics become essential. In this chapter, first the stress-strain relations in continuum mechanics are reviewed followed by the equations of stress equilibrium. Next, the generalized theory of plasticity is explained. Then, the extended version of the Mohr-Coulomb plasticity model is described in detail. Subsequently, the Drucker-Prager plasticity model is explained. Finally, the summary of these constitutive models is presented.

5.1 State of Stress

5.1.1 Stress Tensor

The state of stress for three-dimensional point is defined by a matrix containing nine stress components as shown in Figure 5.1. The nine components of the stress at any point form a second order tensor, known as the stress tensor which can be defined as:

$$\boldsymbol{\sigma} = \begin{bmatrix} \sigma_{xx} & \sigma_{xy} & \sigma_{xz} \\ \sigma_{yx} & \sigma_{yy} & \sigma_{yz} \\ \sigma_{zx} & \sigma_{zy} & \sigma_{zz} \end{bmatrix} \tag{5.1}$$

The shear stresses in the stress tensor have the following relationships due to the moment equilibrium as follows:

$$\sigma_{xy} = \sigma_{yx};\ \ \sigma_{xz} = \sigma_{zx};\ \ \sigma_{yz} = \sigma_{zy} \tag{5.2}$$

As a result the stress tensor is composed of six independent components. These components are called normal stresses $(\sigma_{xx}, \sigma_{yy}, \sigma_{zz})$ and shear stresses $(\sigma_{xy}, \sigma_{yz}, \sigma_{xz})$.

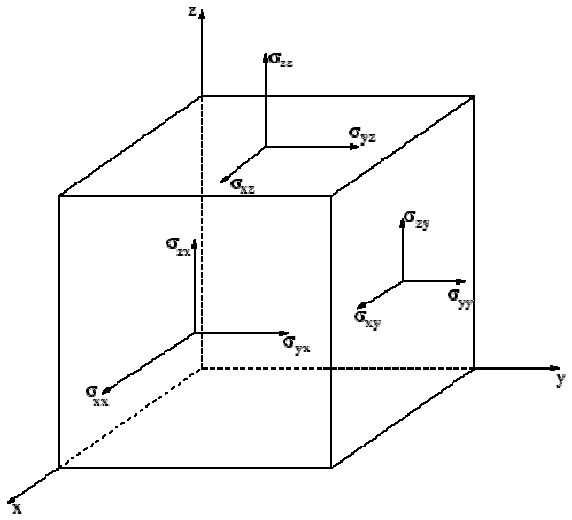

Figure 5.1 Stress state for three-dimensional elements

5.1.2 Principle Stresses

The state of stress at a point can also be defined in terms of principle stresses σ_1, σ_2 and σ_3. The principle stresses are related to the components of the stress tensor by the following equation:

$$\sigma^3 - I_1\sigma + I_2\sigma + I_3 = 0 \tag{5.3}$$

whereI_1, I_2 and I_3 are known as the first, second and third stress invariant, respectively. These stress invariants are defined as follows:

$$\begin{aligned} I_1 &= \sigma_{xx} + \sigma_{yy} + \sigma_{zz} \\ I_2 &= \sigma_{xx}\sigma_{yy} + \sigma_{yy}\sigma_{yy} + \sigma_{zz}\sigma_{xx} - {\sigma_{xy}}^2 - {\sigma_{yz}}^2 - {\sigma_{xz}}^2 \\ I_3 &= \sigma_{xx}\sigma_{yy}\sigma_{zz} - \sigma_{xx}{\sigma_{yz}}^2 - \sigma_{yy}{\sigma_{xz}}^2 - \sigma_{zz}{\sigma_{xy}}^2 - 2\sigma_{xy}\sigma_{yz}\sigma_{xz} \end{aligned} \tag{5.4}$$

The stress invariants can also be expressed in terms of principal stresses in the form of:

$$\begin{aligned} I_1 &= \sigma_1 + \sigma_2 + \sigma_3 \\ I_2 &= \sigma_1\sigma_2 + \sigma_2\sigma_3 + \sigma_3\sigma_1 \\ I_3 &= \sigma_1\sigma_2\sigma_3 \end{aligned} \tag{5.5}$$

5.1.3 Mean Stress and Deviatoric Stresses

The state of stress at a point tensor can be expressed as the sum of two other stresses: the mean stress (volumetric stress), p, which tends to change the volume of the stressed body; and the deviatoric stress s_{ij} which tends to distort it. The mean stress of a stressed point is defined as the average of normal stresses in three directions as:

$$p = \frac{1}{3}\left(\sigma_{xx} + \sigma_{yy} + \sigma_{zz}\right) = \frac{1}{3} I_1 \tag{5.6}$$

The deviatoric components of the stress are defined by

$$s_{ij} = \sigma_{ij} - p\delta_{ij} \tag{5.7}$$

where δ_{ij} is the *Kronecker delta* function defined as:

$$\delta_{ij} = \begin{cases} 1; & \text{for } i = j \\ 0; & \text{for } i \neq j \end{cases} \tag{5.8}$$

The three invariants of deviatoric stress are

$$\begin{aligned} J_1 &= s_{kk} = 0 \\ J_2 &= \frac{1}{2} s_{ij} s_{ij} = \frac{1}{3}\left(I_1^{\,2} + 2I_3\right) \\ J_3 &= \frac{1}{3} s_{ij} s_{jk} s_{ki} = \frac{1}{27}\left(2I_1^{\,3} + 9I_1 I_2 + 27I_3\right) \end{aligned} \tag{5.9}$$

It is noted that in the theory of soil plasticity, the most useful stress invariants are I_1, J_2 and J_3. Physically, I_1 indicates the effect of mean stress, J_2 represents the magnitude of shear stress, and J_3 determines the direction of shear stress. All these three quantities have a key role in the theory of elastic-plastic stress-strain relations. In soil

mechanics (Roscoe and Burland, 1968; Muir Wood, 1990), the mean stress p is often used in pair with a generalized shear stress q defined as:

$$\begin{aligned} q &= \frac{1}{\sqrt{2}}\left[\left(\sigma_1-\sigma_2\right)^2+\left(\sigma_2-\sigma_3\right)^2+\left(\sigma_3-\sigma_1\right)^2\right]^{1/2} \\ &= \sqrt{3J_2} \end{aligned} \tag{5.10}$$

The stress invariants can also be interpreted geometrically in the principal stress space. The state of stress at material point A in the principal stress coordinate system is shown in Figure 5.2. The angle θ is called the Lode angle which is defined as:

$$\theta = -\frac{1}{3}\sin^{-1}\left[\frac{3\sqrt{3}}{2}\frac{J_3}{J_2^{3/2}}\right] \tag{5.11}$$

In terms of the mean stress p and the shear stress q, the principal stresses can be expressed as follows:

$$\begin{aligned} \sigma_1 &= p+\frac{2}{3}q\sin\left(\theta+120^\circ\right) \\ \sigma_2 &= p+\frac{2}{3}q\sin\left(\theta\right) \\ \sigma_3 &= p+\frac{2}{3}q\sin\left(\theta-120^\circ\right) \end{aligned} \tag{5.12}$$

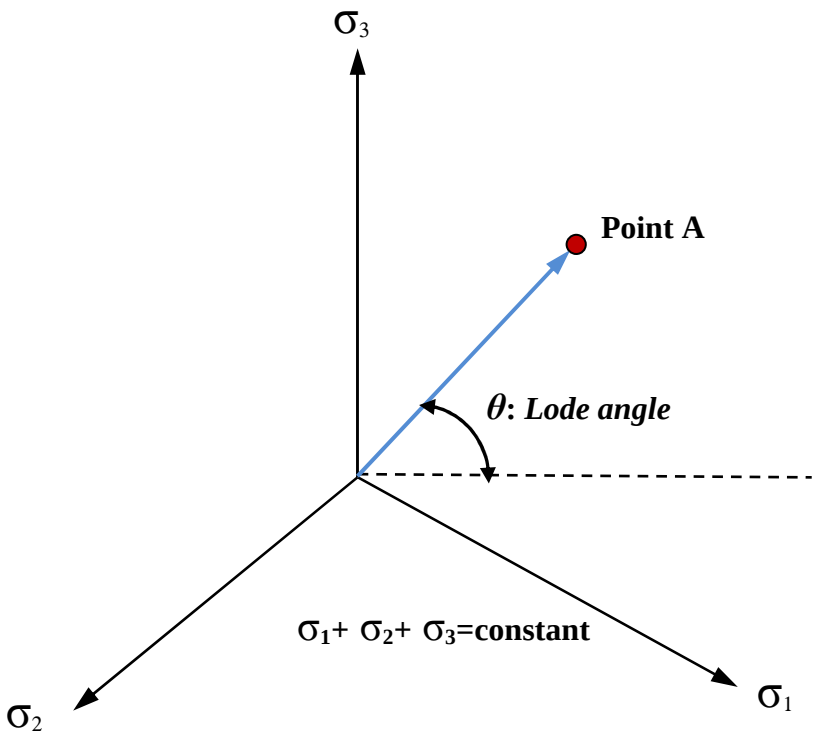

Figure 5.2 Lode angle on a deviatoric plane.

5.2 Generalized Theory of Plasticity

Soil deformation contains elastic (recoverable) and plastic (irrecoverable) strains upon loading and unloading paths. Elastic strains account for small fractions of the total soil deformation (Koolen and Kuiper, 1983 and Shen and Kushwaha, 1998). The reversible behavior of elastic strains upon removal of loading could be of linear or non-linear forms (Chen and Mizuno, 1990). Incremental theory of plasticity has been used successfully in describing the deformation of a wide range of materials including soils. In this theory, there are three components of the constitutive model that need to be defined:

- the yield criterion, which defines the transition of elastic to plastic deformation;
- the plastic flow potential, which dictates the relative amounts of each component of the plastic flow; and
- the evolution of the microstructure, which in turn defines the resistance to further deformation.

For an elastoplastic material with isotropic hardening, the *yield surface* is described by a yield function of the form $f(\boldsymbol{\sigma}, \kappa)$, where $\boldsymbol{\sigma}$ is a vector of the current stresses and κ is some hardening parameter. If $f(\boldsymbol{\sigma}, \kappa) < 0$, the stress point lies within the yield surface and the material behaves elastically according to

$$\boldsymbol{\sigma} = \mathbf{D}_e \, \boldsymbol{\varepsilon} \tag{5.13}$$

where $\mathbf{D}_e$ is the elastic stress-strain matrix, $\boldsymbol{\sigma} = \left\{\sigma_x, \sigma_y, \sigma_z, \tau_{xy}, \tau_{xz}, \tau_{yz}\right\}^T$ is a vector of stress components, and $\boldsymbol{\varepsilon} = \left\{\varepsilon_x, \varepsilon_y, \varepsilon_z, \gamma_{xy}, \gamma_{xz}, \gamma_{yz}\right\}^T$ is a vector of strain components.

Once yielding takes place, $f(\boldsymbol{\sigma}, \kappa) = 0$ and the stresses remain on the yield surface as plastic deformation occurs. When yielding begins, the rate form of the yield function which is also known as the *consistency condition* can be expressed as follows:

$$df = \left(\frac{\partial f}{\partial \boldsymbol{\sigma}}\right)^T d\boldsymbol{\sigma} + \frac{\partial f}{\partial \kappa} d\kappa = \mathbf{a}^T d\boldsymbol{\sigma} + \frac{\partial f}{\partial \kappa} d\kappa = 0 \tag{5.14}$$

where $d\boldsymbol{\sigma}$ is a vector of stress rates, $d\kappa \dfrac{\partial f}{\partial \kappa}$ is a hardening rate, and

$$\mathbf{a} = \frac{\partial f}{\partial \boldsymbol{\sigma}} = \left\{ \frac{\partial f}{\partial \sigma_x}, \frac{\partial f}{\partial \sigma_y}, \frac{\partial f}{\partial \sigma_z}, \frac{\partial f}{\partial \tau_{xy}}, \frac{\partial f}{\partial \tau_{xz}}, \frac{\partial f}{\partial \tau_{yz}} \right\}^{\mathrm{T}} \tag{5.15}$$

is the gradient to the yield surface. At this stage, plasticity theory makes two key assumptions. The first is that the total strain rate, $d\boldsymbol{\varepsilon}$, can be expressed as the sum of an elastic strain rate, $d\boldsymbol{\varepsilon}_{\mathrm{e}}$, and a plastic strain rate, $d\boldsymbol{\varepsilon}_{\mathrm{p}}$, according to

$$d\boldsymbol{\varepsilon} = d\boldsymbol{\varepsilon}_{\mathrm{e}} + d\boldsymbol{\varepsilon}_{\mathrm{p}} \tag{5.16}$$

The second is that the direction of the plastic strain rates is normal to a surface called the plastic potential. This assumption is called *the flow rule*, and it can be expressed as

$$d\boldsymbol{\varepsilon}_{\mathrm{p}} = \mathrm{d}\lambda \frac{\partial \mathrm{g}}{\partial \boldsymbol{\sigma}} = \mathrm{d}\lambda\, \mathbf{h} \tag{5.17}$$

where g is *the plastic potential*, $d\lambda$ is a positive constant known as the plastic strain rate multiplier, and

$$\mathbf{h} = \frac{\partial \mathrm{g}}{\partial \boldsymbol{\sigma}} = \left\{ \frac{\partial \mathrm{g}}{\partial \sigma_{\mathrm{x}}}, \frac{\partial \mathrm{g}}{\partial \sigma_{\mathrm{y}}}, \frac{\partial \mathrm{g}}{\partial \sigma_{\mathrm{z}}}, \frac{\partial \mathrm{g}}{\partial \tau_{\mathrm{xy}}}, \frac{\partial \mathrm{g}}{\partial \tau_{\mathrm{xz}}}, \frac{\partial \mathrm{g}}{\partial \tau_{\mathrm{yz}}} \right\}^{\mathrm{T}} \tag{5.18}$$

is the gradient to the plastic potential. For convenience, the plastic potential is usually assumed to have a form similar to that of the yield criterion. When the gradients to the plastic potential and the yield criterion are coincident, plastic flow takes place in a direction which is normal to the yield surface and the flow rule is said to be associated. Any other type of flow rule is said to be nonassociated. Associated flow rules are often used in metal plasticity studies and a number of important uniqueness theorems can be derived for them (Hill, 1950).

Differentiating Eq. (5.12) with respect to time and substituting Equations 5.15 and 5.16 yields

$$d\boldsymbol{\sigma} = \mathbf{D}_{\mathrm{e}} \left(\mathrm{d}\boldsymbol{\varepsilon} - d\lambda \mathbf{h} \right) \tag{5.19}$$

Inserting Eq. (5.18) in Eq. (5.13), the consistency condition, the plastic multiplier may be written as

$$d\lambda = \frac{\mathbf{a}^T \mathbf{D}_e d\boldsymbol{\varepsilon}}{H + \mathbf{a}^T \mathbf{D}_e \mathbf{h}} \tag{5.20}$$

where the parameter $H$is given by

$$H = - \frac{\partial f}{\partial \kappa} \frac{d\kappa}{d\lambda} \tag{5.21}$$

Substituting the expression for $d\lambda$ from Eq. (5.19) into Eq. (5.18) yields

$$d\boldsymbol{\sigma} = \mathbf{D}_e \left(d\boldsymbol{\varepsilon} - \frac{\mathbf{a}^T \mathbf{D}_e d\boldsymbol{\varepsilon}}{H + \mathbf{a}^T \mathbf{D}_e \mathbf{h}} \right) \tag{5.22}$$

which can also be expressed as

$$d\boldsymbol{\sigma} = \left(\mathbf{D}_e - \frac{\mathbf{D}_e \mathbf{h} \mathbf{a}^T \mathbf{D}_e}{H + \mathbf{a}^T \mathbf{D}_e \mathbf{h}} \right) d\boldsymbol{\varepsilon} \tag{5.23}$$

The final form of the standard elastoplastic stress-strain relations is defined as

$$d\boldsymbol{\sigma} = \mathbf{D}_{ep} d\boldsymbol{\varepsilon} \tag{5.24}$$

where

$$\mathbf{D}_{ep} = \mathbf{D}_e - \frac{\mathbf{D}_e \mathbf{h} \mathbf{a}^T \mathbf{D}_e}{H + \mathbf{a}^T \mathbf{D}_e \mathbf{h}} \tag{5.25}$$

is known as the elastoplastic stress-strain matrix. Given that the strain rate $d\boldsymbol{\varepsilon}$ is known, Eq. 5.23 describes a small system of ordinary differential equations which can be integrated over a specified time interval to obtain the unknown stresses and hardening parameter. The initial conditions for this system are the known stresses and hardening parameter at the start of the time interval.

5.3 Mohr-Coulomb Plasticity Model

The Mohr-Coulomb plasticity model is a perfect plasticity model which was proposed by Coulomb (1773) for cohesive frictional materials. The yield criterion is

expressed in terms of shear stress τ and normal stress σ_n acting on a plane. The model suggests that the yielding begins as long as the shear stress and the normal stress satisfy the following equation:

$$|\tau| = c + \sigma_n \tan\phi \tag{5.26}$$

where c is the cohesion and ϕ is the friction angle. The Mohr-Coulomb model is based on plotting Mohr's circle for states of stress at failure in the plane of the maximum and minimum principal stresses. The failure line is the best straight line that touches these Mohr's circles as shown in Figure 5.3.

5.3.1 Yield Criterion

The Mohr-Coulomb model can also be expressed in terms of principal stresses. The yield criterion is defined as:

$$f = (\sigma_1 - \sigma_3) - (\sigma_1 + \sigma_3)\sin\phi - 2c\cos\phi = 0 \tag{5.27}$$

for $\sigma_1 \geq \sigma_2 \geq \sigma_3$ where σ_1 and σ_3 are the maximum and minimum principal stresses (positive in tension). The Mohr-Coulomb yield surface on deviatoric plane is shown in Figure 5.4.In terms of stress invariants and Lode's angle, the Mohr-coulomb yield criterion takes the following form:

$$f = \sqrt{J_2} - \frac{m(\theta,\phi)\sin\phi}{3} I_1 - m(\theta,\phi)\, c\cos\phi = 0 \tag{5.28}$$

where

$$m(\theta,\phi) = \frac{\sqrt{3}}{\left(\sqrt{3}\cos\theta + \sin\theta\sin\phi\right)} \tag{5.29}$$

5.3.2 Plastic Potential

In the Mohr-Coulomb model, the plastic potential takes a very similar form of the yield function. In the plastic potential, instead of the friction angle, the dilation angle (smaller angle) is used as follows:

$$g = \sqrt{J_2} - \frac{m(\theta,\psi)\sin\psi}{3} I_1 - m(\theta,\psi)\, c\cos\psi = 0 \tag{5.30}$$

where

$$m(\theta,\psi) = \frac{\sqrt{3}}{\left(\sqrt{3}\cos\theta + \sin\theta\sin\psi\right)} \tag{5.31}$$

If the flow rule is associated, then the yield criterion and the plastic potential coincides which yields: $\phi = \psi$. In the non-associated flow case, the plastic potential and the yield criterion must be linked by a stress-dilatancy equation. The most widely used relationship between the angles of friction and dilation is developed by Rowe (1962) and further simplified by Bolton (1986) is as follows:

$$\psi = 1.25\left(\phi - \phi_{cv}\right) \tag{5.32}$$

where ϕ_{cv} is the angle of friction at the critical state.

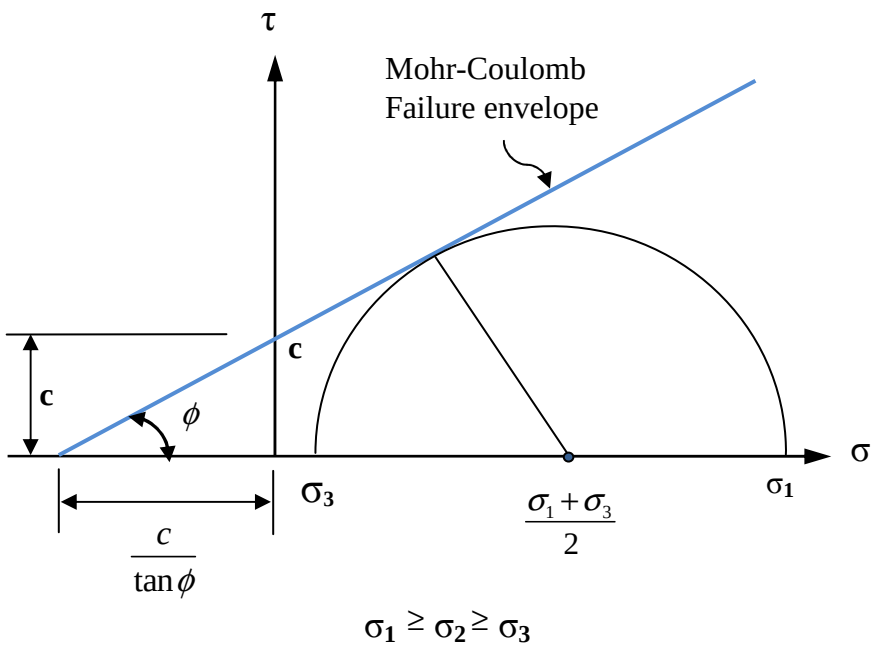

Figure 5.3 The Mohr-Coulomb failure envelope on σ-τ plane.

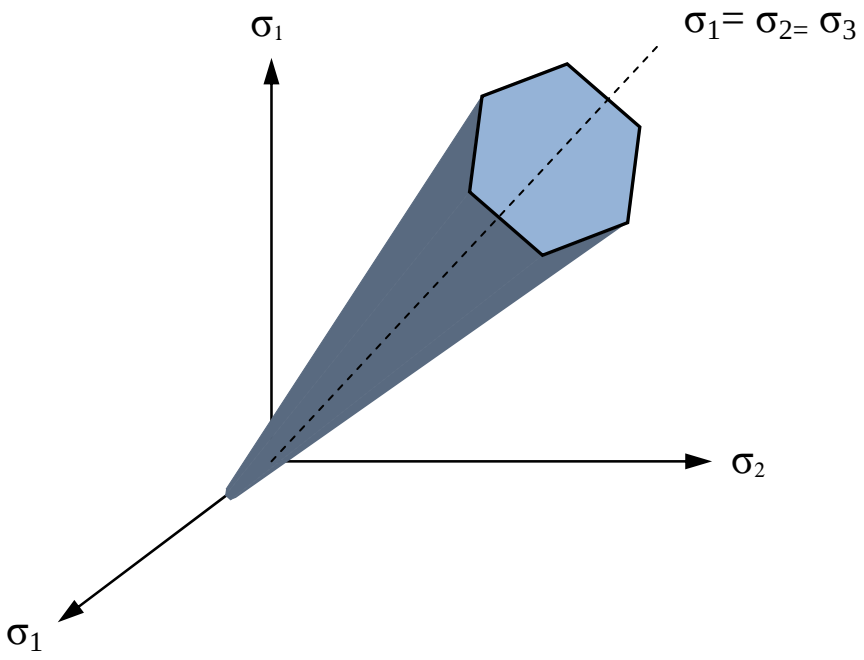

Figure 5.4 The Mohr-Coulomb yield criterion on a deviatoric plane.

5.3.3 Mohr-Coulomb Model in ABAQUS

The Mohr-Coulomb model in ABAQUS is an extension of the classical Mohr-Coulomb failure criterion. ABAQUS offers a Mohr-Coulomb model which uses the classical Mohr-Coulomb yield criterion: a straight line in the meridional plane and a six-sided polygon in the deviatoric plane. However, the ABAQUS Mohr-Coulomb model has a completely smooth flow potential instead of the classical hexagonal pyramid: the flow potential is a hyperbola in the meridional plane, and it uses the smooth deviatoric section proposed by Menétrey and William(1995).The yield function, *f*, is defined based on the classical Mohr-Coulomb constitutive model with isotropic hardening or softening.. The flow potential, *g*, however, which is defined after the work of Menétrey and William (1995), is a hyperbolic function in the meridional stress plane $(p-R_{mc}q)$ and has no corners in the deviatoric stress. The yield function, *f*, for the Mohr-Coulomb model in ABAQUS is defined as:

$$f = R_{mc}q - p\tan\phi - c = 0 \tag{5.33}$$

in which

$$R_{mc} = \frac{1}{\sqrt{3}\cos\phi}\sin\left(\theta+\frac{\pi}{3}\right)+\frac{1}{3}\cos\left(\theta+\frac{\pi}{3}\right)\tan\phi \tag{5.34}$$

$$p = -\frac{1}{3}trace(\boldsymbol{\sigma}) \tag{5.35}$$

$$q = \sqrt{\frac{3}{2}(\mathbf{S}:\mathbf{S})} \tag{5.36}$$

$$r = \left(\frac{9}{2}\mathbf{S}\cdot\mathbf{S}:\mathbf{S}\right)^{1/3} \tag{5.37}$$

$$\left(\frac{r}{q}\right)^3 = \cos\theta \tag{5.38}$$

$$\mathbf{S} = \boldsymbol{\sigma} + p\mathbf{I} \tag{5.39}$$

where R_{mc} is a measure of the shape of the yield surface in the π-plane; p is the pressure stress; q is the von Mises equivalent stress; r is the third invariant; **S** is the deviatoric stress tensor; $\boldsymbol{\sigma}$ is the total stress (negative in compression); **I** is the unit tensor; ϕ is the angle of internal friction of the material and; θ is the deviatoric polar angle defined after Chen and Han (1988).

The flow potential, g, which was proposed by Menétrey and William (1995) is in hyperbolic shape in the p-$R_{mc}q$ plane (meridional plane) and in smooth elliptic shape in the π-plane (deviatoric stress plane). It is defined as follows:

$$g = \sqrt{(\varepsilon c \tan\psi)^2 + (R_{mv} q)^2} - p \tan\psi \tag{5.40}$$

in which

$$R_{mv} = \frac{4\left(1-e^2\right)\left(\cos\theta\right)^2 + \left(2e-1\right)^2}{2\left(1-e^2\right)\cos\theta + \left(2e-1\right)\sqrt{4\left(1-e^2\right)\left(\cos\theta\right)^2 + 5e^2 - 4e}} R_{mc}\left(\frac{\pi}{3}, \phi\right) \tag{5.41}$$

where ε is the meridional eccentricity; c is the cohesion of the material; ψ is the angle of dilation and; e is the deviatoric eccentricity. The family of Menétrey-William hyperbolic flow potentials in the meridional plane is shown in Figure 5.5. The comparison of Menétrey-William flow potentials in the deviatoric plane with the Rankine and von Mises theories are shown in Figure 5.6.

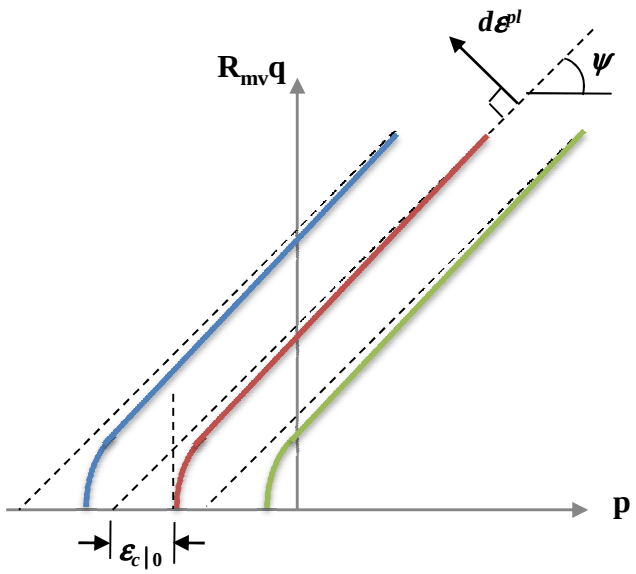

Figure 5.5 The family of Menétrey-William hyperbolic flow potentials in the meridional plane.

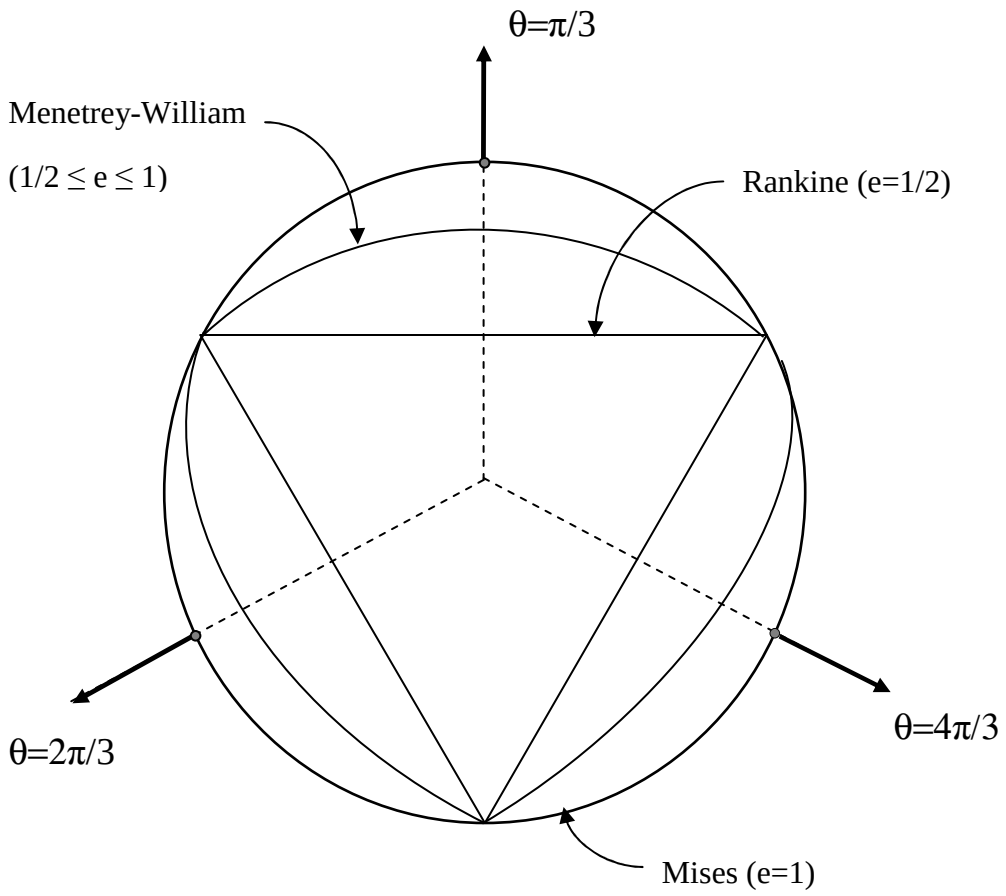

Figure 5.6 Menétrey-William flow potential in the deviatoric plane.

5.4 Drucker-Prager Plasticity Model

The Drucker-Prager plasticity model was proposed by Drucker and Prager (1952) for frictional soils including the effect of mean stress as observed in soil experiments. The yield criterion and the plastic potential of the plasticity model are explained in the following subsections.

5.4.1 Yield Criterion

The yield criterion for the Drucker-Prager plasticity model is defined as follows:

$$f = q - p\tan\beta - d = 0 \tag{5.42}$$

where $q = \sqrt{3J_2}$ is the generalized shear stress, $p = 1/3(I_1)$ is the mean stress, β is the friction angle of the material and, d is the cohesion of the material. The parameters β and d can be matched with the Mohr-Coulomb material parameters c (cohesion) and ϕ (angle of internal friction) for two different flow cases using a certain criterion as summarized in Table 5.1. The Drucker-Prager yield surface is compared with the Mohr-Coulomb yield surface in Figure 5.6. While the Mohr-Coulomb yield surface is a hexagonal on the deviatoric plane, the Drucker-Prager yield surface is a circular shape. The three-dimensional yield surface which is a cone is illustrated in Figure 5.7.

Table 5.1 The relationship between Drucker-Prager material constants and the Mohr-Coulomb material parameters

Flow rule	Drucker-Prager Material Constants	
Associated flow, $\psi = \phi$	$\tan\beta = \dfrac{\sqrt{3}\sin\phi}{\sqrt{1+\frac{1}{3}\sin^2\phi}}$	$d = \dfrac{\sqrt{3}c\cos\phi}{\sqrt{1+\frac{1}{3}\sin^2\phi}}$
Non-associative flow, $\psi = 0$	$\tan\beta = \sqrt{3}\sin\phi$	$d = \sqrt{3}c\cos\phi$

5.4.2 Plastic Potential

To complete the formulation of the Drucker-Prager plasticity model, a plastic potential should be defined. Similar to the Mohr-Coulomb plasticity, a plastic potential can be adopted which coincides with the yield surface as follows:

$$g = q - \frac{6\sin\psi}{3-\sin\psi} p = \text{constant} \tag{5.43}$$

where the angle of friction is replaced by the angle of dilation ψ.

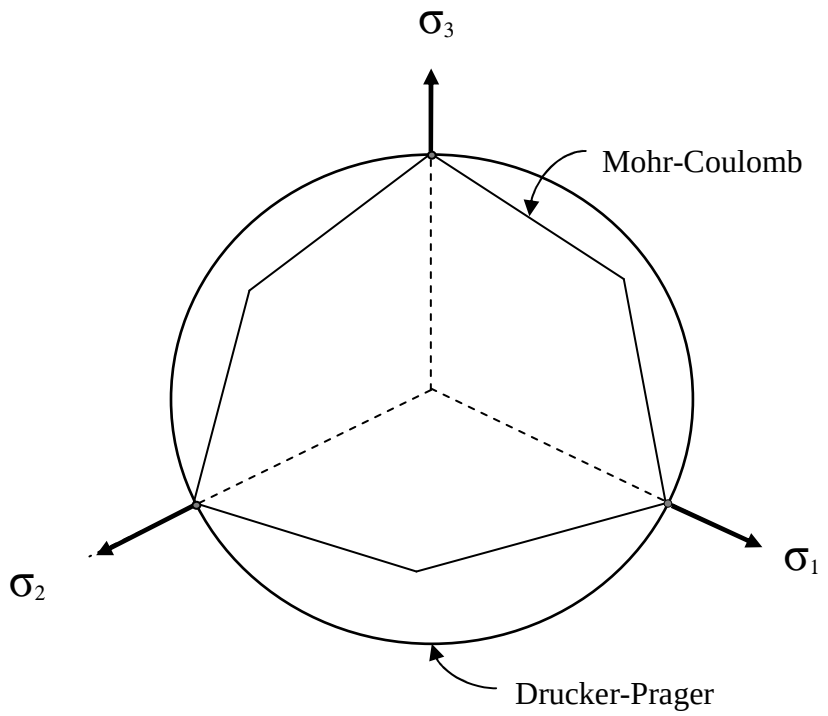

Figure 5.7 Mohr-Coulomb and Drucker-Prager yield surfaces on a deviatoric plane.

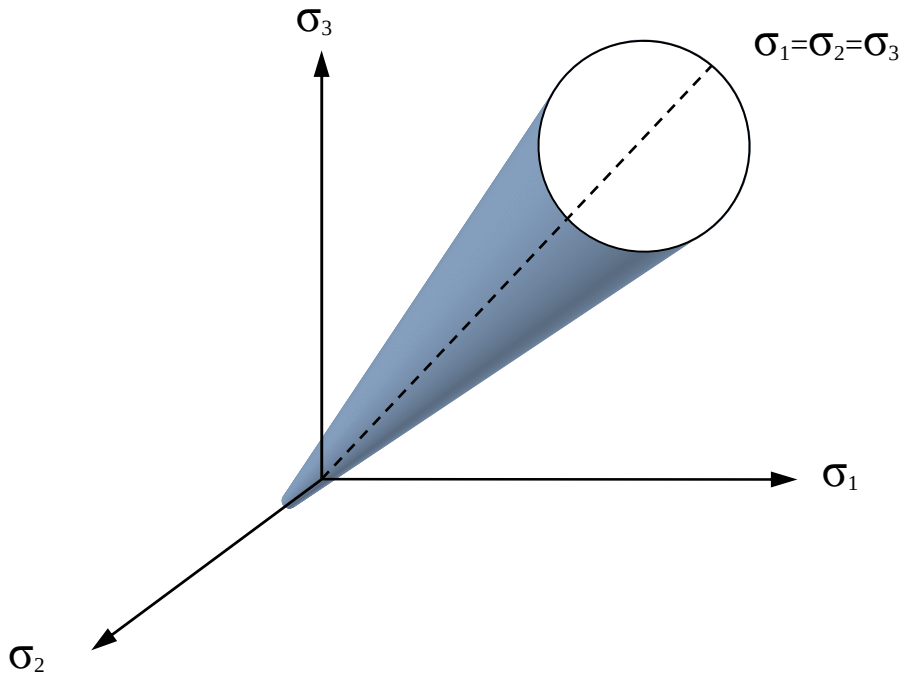

Figure 5.8 The Drucker-Prager failure surface on a deviatoric plane.

5.5 Summary and Discussion

The general plasticity and two soil constitutive models available in ABAQUS have been reviewed in this chapter. The theory of the Mohr-Coulomb plasticity model and the Drucker-Prager model are presented. The advantages and limitations of these two constitutive models are given in Table 5.2.

Table 5.2 The advantages and limitations of soil models

Constitutive Model	Advantages	Limitations
Mohr-Coulomb		
	Simple	Yield surface has corners
	Valid for many soil types	Neglect the effects of intermediate principal stress
	Model parameters can be obtained easily from soil experiments	-
Drucker-Prager	Simple to use	Excessive plastic dilatancy at yielding
	Can be matched with Mohr-Coulomb model	Cannot reproduce the hysteretic behavior within the failure surface
	Analysis techniques can be implemented	Cannot predict the pre pressure build-up during an undrained cyclic shear loading
	Satisfy the associated flow rule	-

CHAPTER 6

LOAD CAPACITY ANALYSIS OF SINGLE PILES

6.1 Introduction

A number of numerical and analytical methods have been developed for analyzing axially loaded piles. These methods are (1) the simplified analytical approach (Randolph, et al., 1978; Randolph, et al., 1979); (2) the load transfer methods (Seed, et al., 1957; Coyle, et al., 1966); (3) the subgrade reaction method (Chow, 1986); (4) the integral equation or the boundary element method (Poulos, 1968; Poulos, et al., 1968; Butterfield, et al., 1971; Banerjee, et al., 1978; Poulos, 1979; Poulos, et al., 1980) and; (5) the finite element method(Ellison, et al., 1971; Desai, et al., 1974; Ottaviani, 1975; Poulos, et al., 1986; Cheung, et al., 1991; De Nicola, et al., 1993; Wakai, et al., 1999 and Zhang, et al., 2002).

The finite element method is a general and direct approach for investigating the fundamental behavior and response of single piles. In this method, soil medium is treated as continuum based on the elastic continuum theory. The major advantages of modeling the pile-soil interaction using the finite element method are: (1) The displacement and the pore water pressure can be coupled in the analysis so that the pile, surrounding soil and the pile-soil interface can be represented by finite elements using only one model; (2) the deformation patterns in the pile-soil model can be analyzed at the element level which gives us a tremendous opportunity to analyze the local stresses and strains at the locations where the intensity of the stress is high and; (3) the soil-pile interface can be modeled with interface elements so that the friction between the pile and the surrounding soil can be represented with a high level of accuracy.

This chapter focuses on the load capacity analysis of single piles using the finite element (FE) method along with the theoretical methods that are used to estimate the ultimate pile load capacity. Dynamic analysis of a single pile will be discussed in the

next chapter. The organization of this chapter is as follows. The first section briefly discusses the numerical and analytical methods that have been developed for analyzing load capacity of single piles. The second section includes the major analytical methods for determining the pile load capacity. The estimation of end bearing capacity and skin friction resistance of piles are explained in details. The next section explains the finite element formulation that is used in this chapter to determine the stresses and strains in the pile and soil. Numerical applications that illustrate estimation of pile load capacity using the finite element method and the analytical methods are presented next. A single pile which is embedded in normally consolidated clay is modeled with and without interface element to investigate the effect of soil-pile interaction. The factors affecting the pile capacity such as the frictional properties of the soil-pile interface are also investigated in this section. Finally, the analytical methods that are used to estimate the pile capacities are compared with the results of the finite element analyses. In the last section, the results obtained from the analytical methods and the finite element analyses are compared. The limitations of the analytical methods and the effects of the interface elements are discussed.

6.2 Ultimate Bearing Capacity of Single Piles

A single pile subjected to axial loading is shown in Figure 5.1. When an axial load is applied on the pile head, the load is supported by two mechanisms: the end bearing at the tip of the pile, and the skin friction along the shaft. The ultimate axial capacity, Q_{ult}, of a single pile is, therefore, equal to the sum of the end bearing, Q_e, and the skin fiction, Q_s as follows:

$$\begin{aligned} Q_{ult} &= Q_e + Q_s \\ &= q_e A_e + f_s A_s \end{aligned} \tag{6.1}$$

where q_e is the unit end bearing, A_e is the area of the tip, f_s is the unit skin friction, and A_s is the area of the pile shaft.

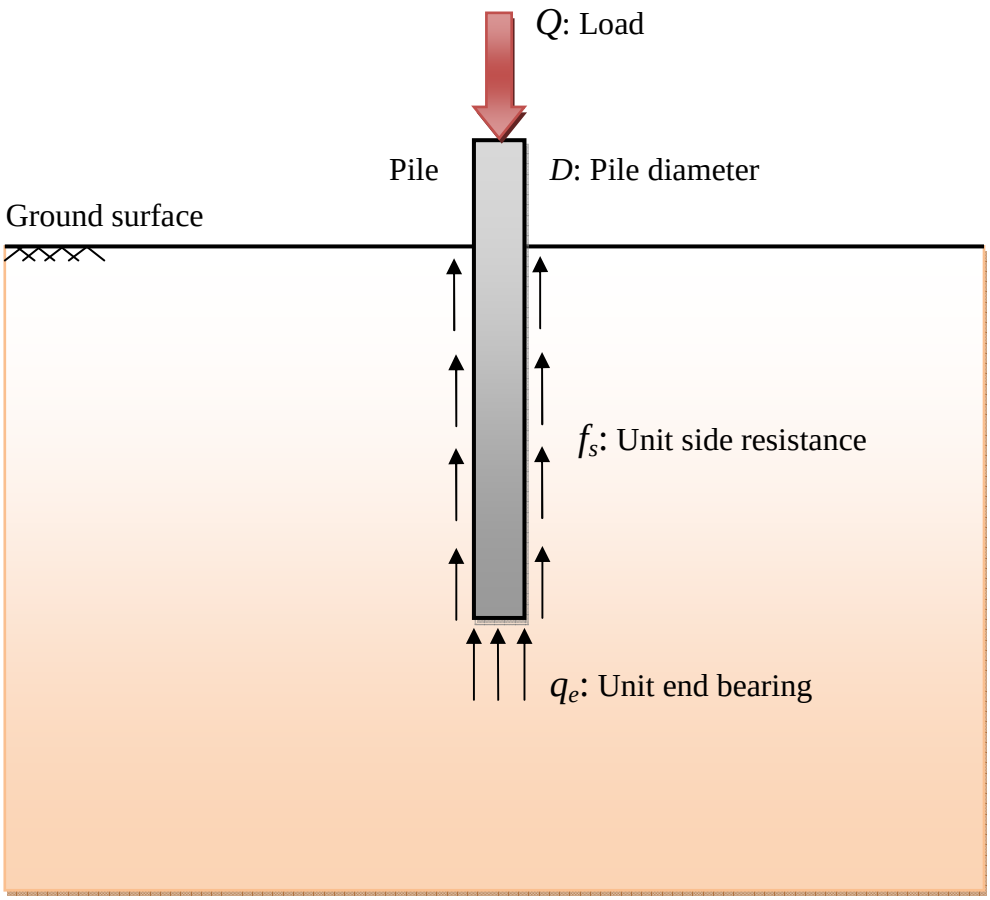

Figure 6.1 Axial loading of a single pile

6.3 End Bearing Capacity

6.3.1 General End Bearing Capacity Formula

The general end bearing capacity formula is presented by Meyerhof (1951) which can be applied to both rough shallow and deep foundations. The formula is expressed as follows:

$$Q_e = \left[cN_c^* + q'N_q^* + \frac{1}{2}\gamma' BN_\gamma^* \right] A_e \tag{6.2}$$

where Q_e is the ultimate end bearing capacity, N_c^*, N_q^*, N_γ^* are bearing capacity factors, c is the cohesion intercept, q' is the effective overburden pressure at the base level of the pile, γ' is the effective unit weight of the bearing soil at the base level, and B is the width or diameter of the shaft at the base level. The bearing capacity factors are dependent on the internal friction angle of the soil. These parameters have been interpreted from pile load tests and published by several researchers including Terzaghi (1943), Meyerhof (1963), Berezantsev (1961) and Vesic (1963 and 1972). Table 6.3 illustrates the bearing capacity factors vs. internal friction angles proposed by different researchers.

For cohesive soils, the cohesive intercept may be interpreted as the undrained shear strength of the soil (c=S_u). Also, the term $1/2\gamma' BN_\gamma^*$ can be neglected because the width of the pile is relatively smaller than conventional foundations. Therefore, the general end bearing capacity formulation takes the final form of:

$$Q_e = \left(9S_u\right) A_e \tag{6.3}$$

6.3.2 Vesic's Method

Vesic (1970) proposed the end bearing capacity formula based on the expansion of cavities theory which is related to the earth pressure and effective stresses in soil. The end bearing capacity of Vesic is as follows:

$$Q_e = \left[cN_c^* + \sigma_0' N_\sigma^* \right] A_e \tag{6.4}$$

where Q_e is the ultimate end bearing capacity, σ_0' is the average normal effective stress at the base level of the pile, N_c^*, N_σ^* are the bearing capacity factors given in Table 6.3.The parameters σ_0' and K_0 are defined as:

$$\sigma_0' = \left(\frac{1+2K_0}{3}\right) q_0' \tag{6.5}$$

$$K_0 = 1 - \sin\phi \tag{6.6}$$

where q_0' is the effective vertical stress at the base level, K_0 is the coefficient of earth pressure, and ϕ is the internal angle of friction. The bearing capacity factors are defined as follows:

$$N_c^* = \left(N_q^* - 1\right)\cot\phi \tag{6.7}$$

$$N_\sigma^* = \frac{3N_q^*}{1+2K} \tag{6.8}$$

in which N_q^* is the bearing capacity factor presented by Vesic. The values of N_q^* based on the internal angle of friction are given in Table 6.3.

6.3.3 Janbu's Method

Janbu (1976) proposed an end bearing capacity formula based on the internal friction angle ϕ and the parameter ψ which is expressed in the form of:

$$Q_e = \left(cN_c^* + q_0' N_q^*\right) A_e \tag{6.9}$$

where Q_e is the ultimate end bearing capacity, q_0' is the effective vertical stress at the base level, and N_c^*, N_q^* are the bearing capacity factors given in Table 6.3.The bearing capacity factors are estimated by Janbu as:

$$N_c^* = \left(N_q^* - 1\right)\cot\phi \tag{6.10}$$

$$N_q^* = \left[\tan\phi + \left(1+\tan^2\phi\right)^{1/2}\right]^2 \exp\left(2\psi\tan\phi\right) \tag{6.11}$$

in which ψ is an angle defining the shear surface around the pile tip. The angle ψ ranges from 60º for soft clays to 105ºdegrees for dense sands.

6.3.4 Meyerhof's Method

Meyerhof's method to estimate the end bearing capacity includes two formulae which are used to calculate the bearing capacities for *cohesionless* and *cohesive* soils. These equations are shown below.

For cohesionless soils

$$Q_e = \left(q_0' N_q^*\right) A_e \le \left(50 N_q^* \tan\phi\right) A_e \tag{6.12}$$

For cohesive soils

$$Q_e = \left(c_u N_c^*\right) A_e \tag{6.13}$$

with

$$N_c^* = \left(N_q^* - 1\right)\cot\phi \tag{6.14}$$

where c_u is the undrained cohesion. The values of the bearing capacity factor N_q^* are plotted in Figure 6.1.

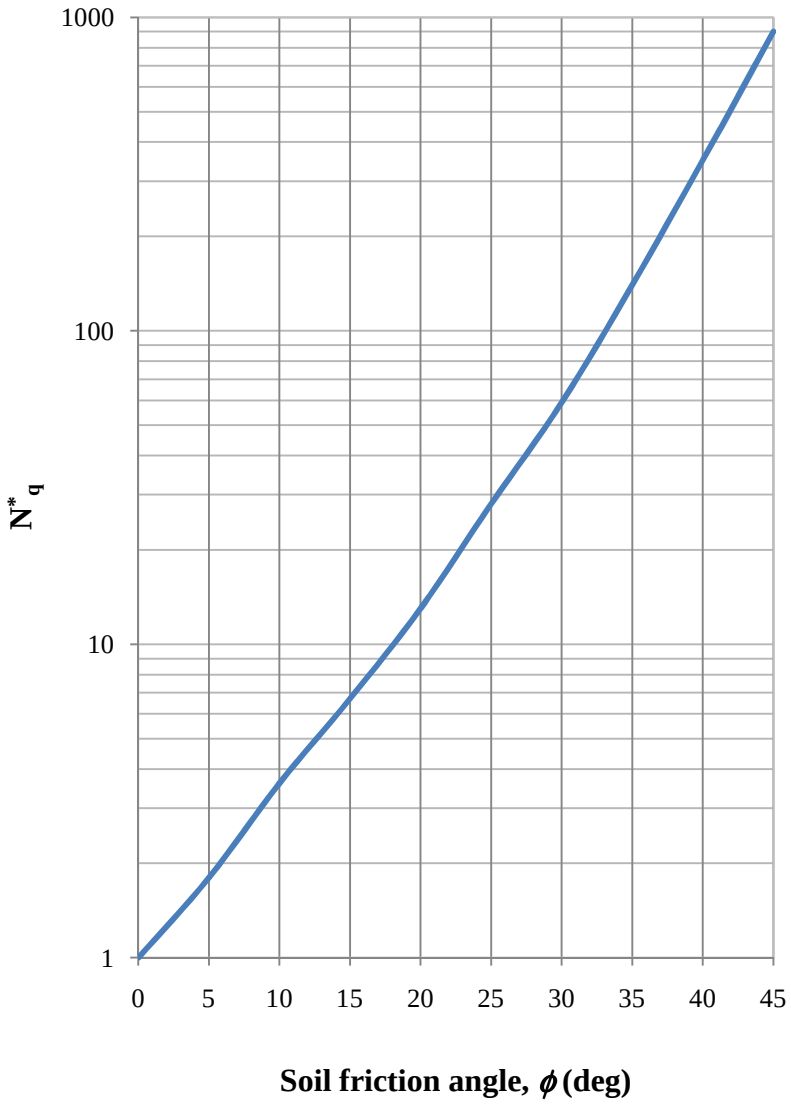

Figure 6.2 Variation of N_q^* with internal friction angle, ϕ .

6.3.5 Coyle & Castello's Method

The end bearing capacity formulation proposed by Coyle and Castello (1981) which is only used for *cohesionless soils* is defined as follows:

$$Q_e = \left(q_0' N_q^*\right) A_e \tag{6.15}$$

where Q_e is the ultimate bearing capacity, q_0' is the effective vertical stress at the base level, and N_q^* is the bearing capacity factor given in Table 6.1.

Table 6.1 The bearing capacity factors for piles in cohesionless soils

Theories	Approximate values of N_q for Various Friction Angles, ϕ (degrees)				
	25	*30*	*35*	*40*	*45*
Terzaghi (1943)					
General shear	12.7	22.5	41.4	81.3	173.3
Localized shear	5.6	8.3	12.6	20.5	35.1
Meyerhof (1953) Driven Piles	38	89	255	880	4000
Vesic (1972),I_r= 60	20	27	40	59	85
Coyle & Castello (1981) (Driven piles)	12	25	53	120	230

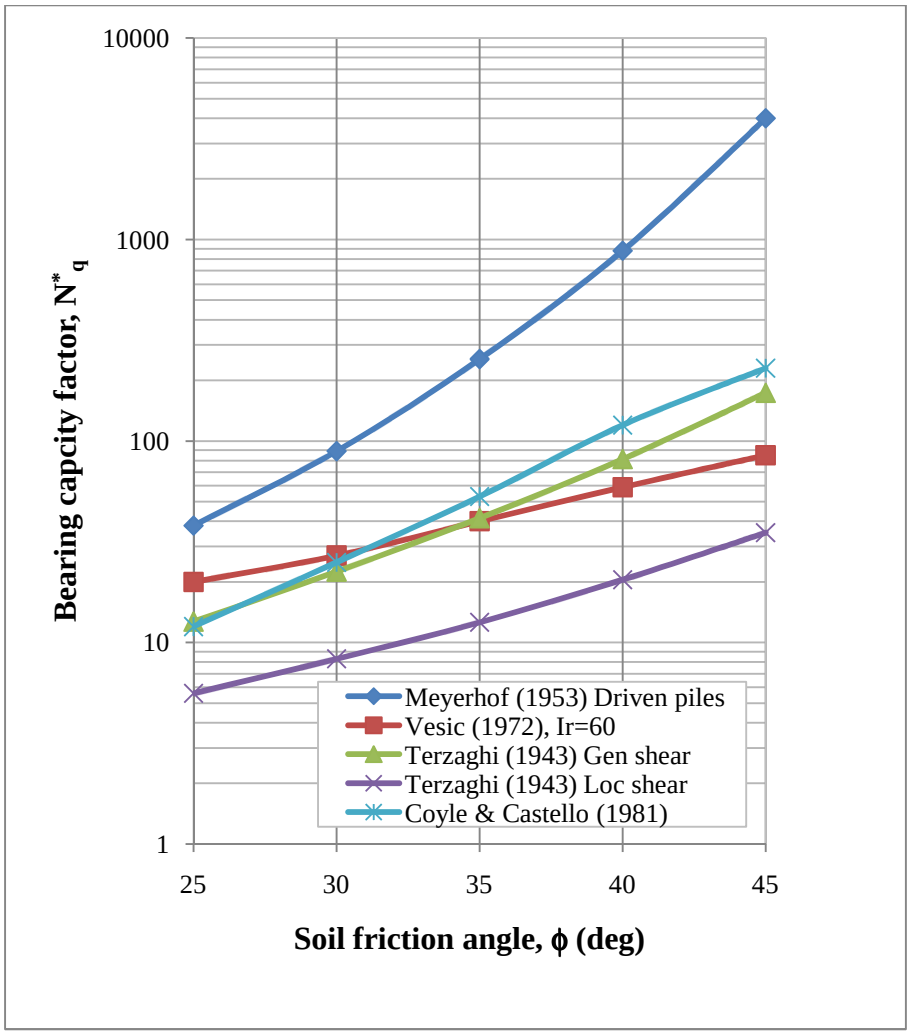

Figure 6.3 Variation of N_q^* with internal friction angle, ϕ.

6.4 Skin Friction Resistance

6.4.1 Alpha Method

The alpha method (α-method) of Randolph and Murphy (Randolph and Murphy, 1963) relates the maximum skin friction to the degree of over-consolidation of the soil, reducing the influence of the measurement of the shear resistance on the calculation of the bearing capacity. This method is based on the total-stress concept and, is only valid for *cohesive soils*. It is also known as the American Petroleum Institute (API) 1991 method, because the API method directly derived the calculation of the skin friction in cohesive soils from the α-method. The ultimate skin resistance based on the α-method is defined as:

$$Q_s = (\alpha S_u) A_s \tag{6.16}$$

where α is the adhesion factor, S_u is the undrained shear strength of soil along the shaft, and A_s is the skin area of the shaft. Randolph and Murphy (Randolph, et al., 1985) defined the α-function that varies with the normalized shear strength S_u / σ'_v as shown in Figure 6.4.

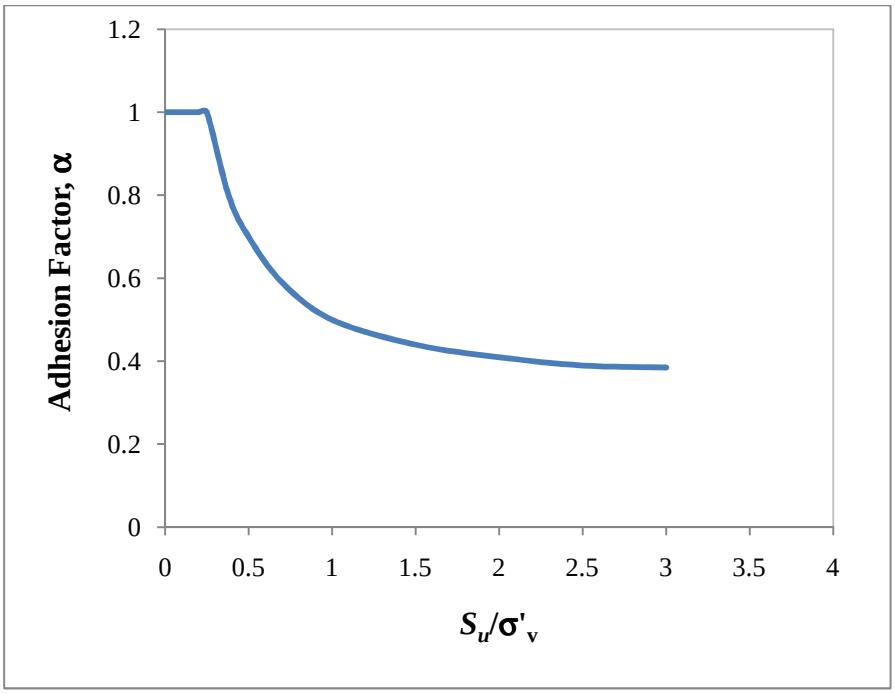

Figure 6.4 Variations of α with the normalized shear strength, S_u / σ'_v.

6.4.2 Beta Method

In the Beta method (β-method), Burland (1973) proposed a calculation method for the skin friction resistance along a shaft for both *cohesive* and *cohesionless* soils. This method is based on the total-stress concept and uses the coefficient β as a primary parameter which is calculated from lateral earth pressure and the friction angle of soil.

The skin friction capacity of a shaft based on the β-method is calculated as follows:

$$Q_u = \left(\beta \sigma_v'\right) A_s \tag{6.17}$$

where Q_u is the ultimate skin friction capacity, σ_v' is the vertical effective stress at measured point, and A_s is the total skin area of the shaft. The β coefficient can be estimated for cohesive and cohesionless soils using different methods. For cohesive soils, the formulation for estimating the β-coefficient is as follows:

$$\beta = K_0 \tan\delta \tag{6.18}$$

in which

$$K_0 = 1 - \sin\phi \text{ (for normally consolidated clays)}$$

and

$$K_0 = \left(1 - \sin\phi\right)\sqrt{OCR} \text{ (for over consolidated clays)}$$

where K_0 is the coefficient of lateral earth pressure, δ is the friction angle between soil and pile, ϕ is the internal friction angle of soil, and OCR is the over consolidation ratio of the clay. The friction angle between pile and soil, δ, is dependent on the type of pile and the internal friction angle of soil, ϕ. For different pile types, it is suggested to use the values of δ given in Table 6.2 (U.S. Navy 1986).

For Cohesionless soils, different values of β were suggested by different researchers based on the pile load test data. McClellend (1974) suggested values of β

ranging from 0.15 to 0.35. Meyerhof (1976) suggested β values ranging from 0.44 to 1.2 as shown in Table 6.3.

Table 6.2 The friction angle between a pile and soil based on the pile type

Pile Type	Friction angle, δ (degrees)
Steel	*20 degrees*
Concrete	*¾ ϕ*
Timber	*¾ ϕ*

Table 6.3 The β-coefficient for cohesionless soils based on the internal friction angle

β-coefficient	Internal friction angle, ϕ (degrees)
0.44	*28*
0.75	*35*
1.2	*37*

6.4.3 Lambda Method

The lambda method (λ-method) which is used for the calculation of skin friction resistance in *cohesive soil*s was first presented by Vijayvergiya and Focht (1972). This method is founded on the effective stress concept. Based on the available pile load test data in cohesive soils, the lambda concept expresses the average skin friction as a percentage of the average undrained shear strength and the effective overburden stress. The skin friction capacity based on the λ-method is as follows:

$$Q_s = \lambda\left(\bar{\sigma}_v' + 2\bar{S}_u\right)A_s \tag{6.19}$$

where Q_u is the ultimate skin friction capacity, λ is the friction capacity coefficient, $\bar{\sigma}_v$ is the average effective vertical stress for depth of pile embedment, $\bar{S}_u$ is the average undrained shear strength for depth of pile embedment. The empirical factor λ can be obtained from Figure 6.5.

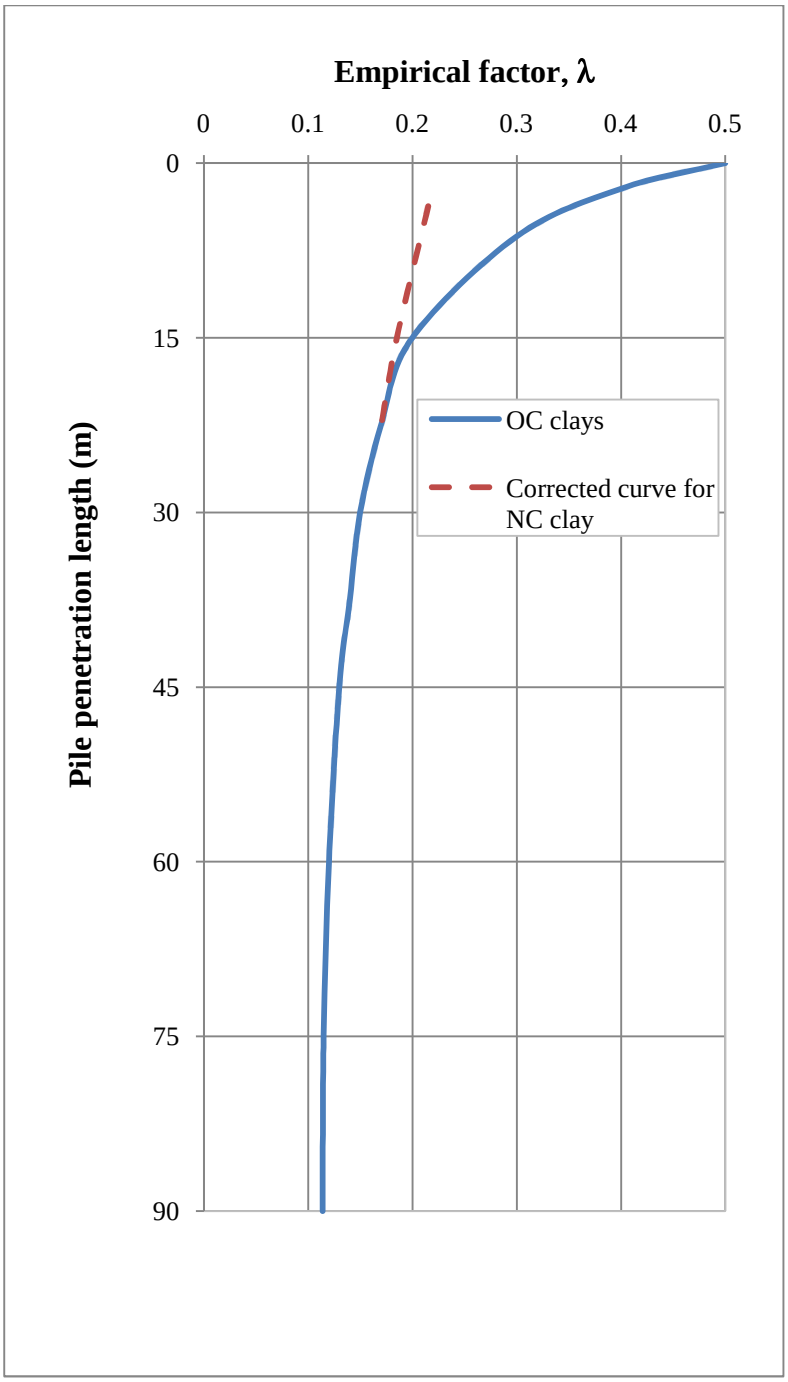

Figure 6.5 Variations of λ with the pile penetration length, L.

6.5 Limitations of Analytical Methods

The formulas for estimating the end bearing capacity and skin resistance of single piles may not be used for all types of soils. The limitations for the calculation methods for the end bearing capacity of piles are shown in Table 6.4. The limitations for the calculation of skin resistance of single piles are shown in Table 6.5.

Table 6.4 The end bearing capacity calculation methods

Calculation Method for End Bearing Capacity	Cohesionless Soil	Cohesive Soil
General formula	Yes	Yes
Vesic's method	Yes	Yes
Janbu's method	Yes	Yes
Coyle & Castello's method	No	Yes
Meyerhof's method	Yes	Yes

Table 6.5 The skin friction resistance calculation methods

Calculation Method for Skin Friction Resistance	Cohesionless Soil	Cohesive Soil
α-Method	No	Yes
β-Method	Yes	Yes
λ-Method	No	Yes

6.6 Finite Element Analysis of Single Piles

This section outlines the procedure for analyzing the load capacity of single piles using the finite element package ABAQUS. Two examples are chosen for the static analysis of piles embedded in clay. In the first example, the pile is installed in a single layer of stiff clay whereas in the second example, it is embedded in three layers of clay that is ranging from soft to stiff. The analyses are performed with and without elements. The objectives of these examples are (1) to find the axial load capacity of single piles in clays under undrained conditions and; (2) to investigate the effect of the soil-pile interface on the load capacity of the pile.

The pile elements are modeled using solid continuum elements. The soil elements are modeled using the coupled displacement and pore water pressure elements as explained in Chapter 4. The constitutive behavior of the pile is assumed elastic. The soil is modeled using an appropriate elasto-plastic constitutive model which is discussed in Chapter 5. The interface between the soil and pile elements is modeled based on the master-slave contact algorithm that is described in the following section.

The solution procedure is as follows: (1) The geometry of the model is created; (2) the material properties are entered; (3) the finite element mesh is generated; (4) the interaction surfaces are selected; (5) the boundary conditions are applied; (6) the initial conditions are entered; (7) the loading and time stepping are entered and; (8) the model is solved. The results obtained from the analyses are discussed at the end of each numerical application.

6.7 Soil-Pile Interface Model

The use of continuum elements in a finite element analysis prohibits the relative movement of a pile element with respect to the adjacent soil element at the soil-pile interface. Due to the compatibility of displacements at the nodes, the soil and adjacent pile element are forced to move together. On the other hand, the restriction of the relative movement at the interface creates very large shear strains. Hence, the appropriate finite element modeling of the soil-pile interface becomes extremely important.

To fully represent the pile behavior at the interface, the interface elements are often used in finite element analysis to model the soil-pile boundary. The major advantages of using interface elements are (1) the frictional behavior at the soil-pile interface is fully represented in the model and; (2) the differential movement of the soil and the pile (i.e., slippage) is allowed.

In the soil-pile interaction problem, the pile elements are assumed to be rigid and the surrounding soil is deformable. The surface of the pile elements which are in contact with the soil elements at the interface are selected as the “master surface”. The surfaces of the soil elements at the interface are selected as “slave surface”. These surfaces are called the contact pair in ABAQUS. The contact pair representing the soil-pile interface is shown in Figure 6.6.

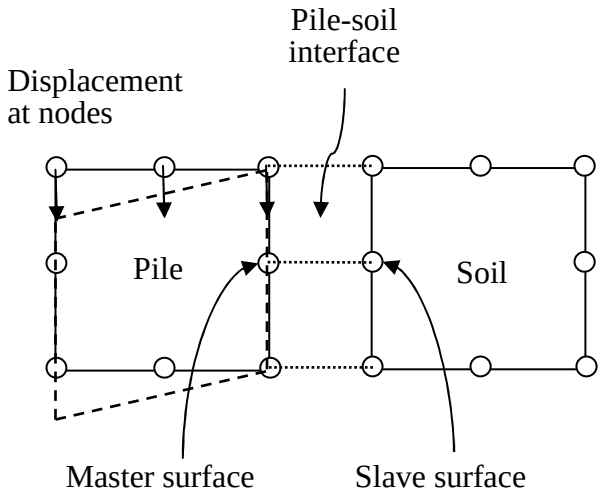

(a) No sliding

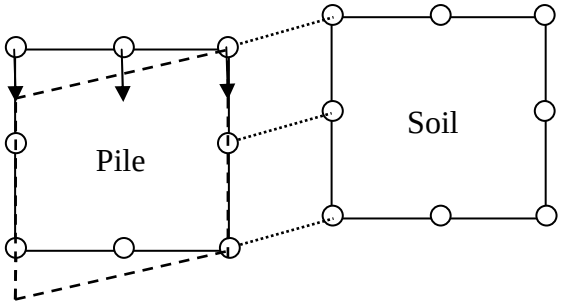

(b) Sliding

Figure 6.6 The representation of pile-soil interface in ABAQUS.

The shear behavior between two surfaces is defined by the Coulomb frictional law. The Coulomb friction model relates the maximum allowable frictional (shear) stress across an interface to the contact pressure between the contacting bodies. The model specifies the shear behavior in terms of normal and tangential components as follows:

$$\tau_{crit} = \mu p \tag{6.20}$$

where τ_{crit} is the critical shear stress at contact surface, μ is the coefficient of friction and, p is the contact pressure between two surfaces.

The Coulomb friction model states that two contacting surfaces can carry shear stresses up to a certain magnitude across their interface before they start sliding relative to one another. This state is known as sticking. The Coulomb friction model defines this critical shear stress, τ_{crit}, at which sliding of the surfaces starts as a fraction of the contact pressure, p, between the surfaces. In other words, the contacting surfaces will not slip until the shear stress across their interface equals the critical frictional shear stress, τ_{crit}. The solid line in Figure 6.7 summarizes the behavior of the Coulomb friction model. There is zero relative motion (slip) of the surfaces when they are sticking.

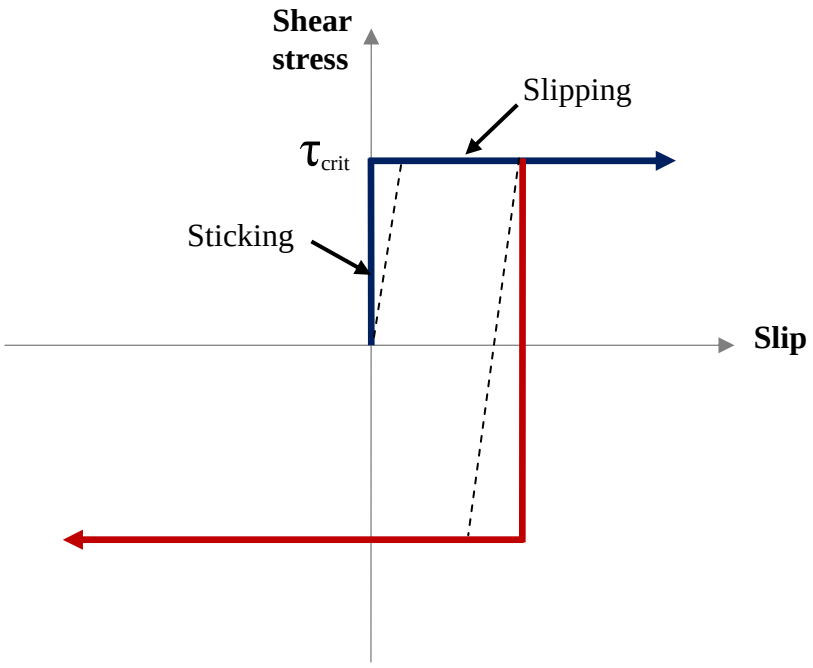

Figure 6.7 Contact frictional behavior for slipping and sticking.

The contact algorithm employed in ABAQUS is described in a flow chart as shown in Figure 6.8. The algorithm can be summarized as follows:

1. Determine the state of all contact interactions by checking whether each slave node is open (clearance is greater than zero) or closed(clearance is equal to zero) at the beginning of each increment.
2. Apply a constraint for each closed slave node if it is still closed or remove the constraint if the contact status of that node is changed from closed to open. Determine whether the closed node is sticking or sliding.
3. Perform an iteration to calculate the contact conditions at each slave node after constraint checks. After updating the contact state, check the equilibrium of forces and/or moments for that increment.
4. Check the state of contact pressure, *p*, and the clearance, *h*, at each slave node. If the contact pressure becomes negative after the iteration, then the

status of contact at that slave node is changed from “closed to open”. On the other hand, if the clearance becomes negative or zero after the iteration, then the status of contact at each node is changed from “open to closed”. In either case, the status is defined as “severe discontinuity iteration” and the equilibrium is not checked.

5. Update the contact constraints after the first iteration followed by the second iteration. Repeat the iteration procedure until there are no changes in the contact status.
6. The last iteration is called the “first equilibrium iteration”. After this iteration is completed, check the normal equilibrium for convergence.
7. Repeat the entire process until the convergence is achieved.

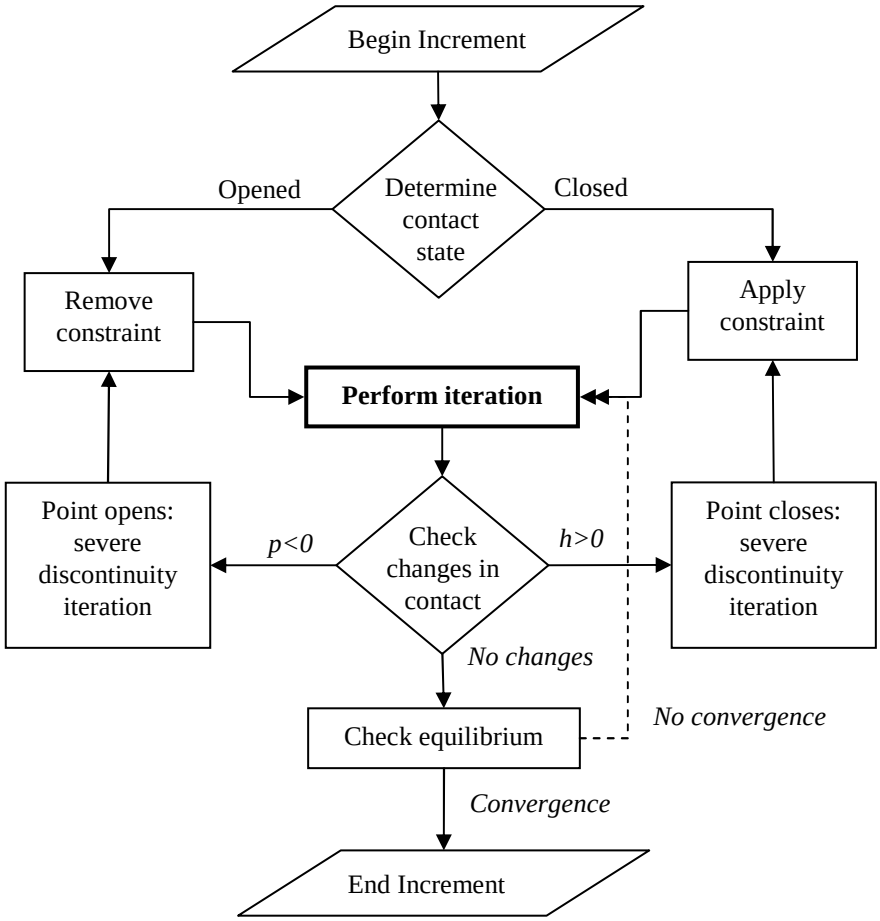

Figure 6.8 The master-slave contact algorithm.

6.8 Numerical Applications

6.8.1 Load Capacity Analysis in Stiff Clays

A cylindrical pipe pile with a diameter of 1 m and a length of 20 m is installed in a clayey deposit as shown in Figure 6.9. The pile is vertically loaded under undrained conditions. The pile is assumed to be very stiff with an elastic material behavior. The clay is considered to have an elasto-plastic material behavior represented by the Mohr-Coulomb model. The pile is modeled using a Young's Modulus E=20 × 10^6 kN/m^2 and a Poisson's ratio v = 0.15. The soil is modeled using an elastic-ideal-plastic constitutive model with the Mohr-Coulomb yield criterion. The elastic properties of the normally consolidated (NC) clay is represented by a Young's modulus E=1.0 × 10^5 kN/m^2 and a Poisson's ratio v = 0.49. The Mohr-Coulomb parameters of the clay are: c = 100 kN/m^2 and $\phi = 26°$, where c is the cohesion and ϕ is the internal angle of friction. The unconfined compressive strength of the stiff clay is S_u=100 kN/m^2. The saturated unit weight of the clay is γ_{sat}= 18 kN/m^3. The coefficient of earth pressure at rest is K_o= 1. The initial void ratio is defined as e_o = 1.0. The coefficient of friction between the concrete pile and the soil is calculated as f_c = 0.35 using the β-method. The material properties of the NC clay and the pile are summarized in Tables 6.6 and 6.7, respectively.

The finite element mesh shown in Figure 6.9 is generated by the commercial finite element package *ABAQUS/Standard*. A two-dimensional axisymmetric finite element model consisting of 1131 eight-noded elements is used for the analysis of the problem. The pile has a diameter of 1 m and a length of 20 m. The whole model has a width of 100 m and a height of 55 m. One half of the model is analyzed due to axisymmetry. The pile is modeled with eight-node axisymmetric, quadratic displacement elements (CAX8) whereas the soil is modeled with axisymmetric, eight-node biquadratic displacement and bilinear pore pressure elements(CAX8P) elements. These elements are available in the *ABAQUS/Standard* element library. The CAX8P element is similar to the

CPE8P element which is defined in Chapter 4. The contact pairs for the soil-pile interface are represented by a master-slave algorithm.

The boundary conditions consist of restricting both vertical and horizontal movements on the base of the mesh and horizontal movements on the right hand side of the mesh and along the axis of symmetry. The loading of the pile is modeled by applying increments of vertical displacements on its top. A total vertical displacement of 0.04 m on the pile top is applied with an increment of 0.001 m/s.

The initial stresses are calculated using the saturated unit weight of clay $\gamma_{sat} = 18$ kN/m^3 and the initial void ratio $e_0 = 1.0$. The initial effective stress in terms of the depth of the clay layer, z, can be defined as

$$\sigma'_z = [\gamma_{sat} - \gamma_w](z - z_0) \tag{6.21}$$

in which γ_w is the unit weight of water and the reference depth z_0.Knowing that the depth of the model is z = 55 m, the initial effective stress in the clay layer is calculated as:

$$\begin{aligned}\sigma'_z &= [\gamma_{sat} - \gamma_w](z - z_0) \\ &= \left[18\ (\text{kN/m}^3) - 10\ (\text{kN/m}^3)\right](55\ \text{m} - 0) \\ &= 440\ \text{kN/m}^2\end{aligned}$$

The initial pore water pressure can be expressed as:

$$p = \gamma_w (z - z_o) \tag{6.22}$$

where γ_w is the unit weight of water, z is the given depth and z_0 is the reference depth. Substituting the depth and the unit weight of water in the formulation yields

$$\begin{aligned}p &= \gamma_w (z - z_o) \\ &= 10\ (\text{kN/m}^3) \cdot (55\ \text{m} - 0) \\ &= 550\ \text{kN/m}^2\end{aligned}$$

The initial effective stress and the pore water pressure in the finite element model are plotted in Figure 6.5.

The problem is run in two steps: (1) the geostatic step, and (2) the static analysis step. In the first step, the geostatic state of the problem is defined. A geostatic state is a steady-state equilibrium configuration of the undisturbed soil or rock body under geostatic loading. In this step, the *in situ* loads are defined (i.e., the surcharge, earth's gravity). The only *in situ* load in this example is the earth's gravity acting on the soil layer. Under the GEOSTATIC option in ABAQUS, the gravitational acceleration is defined as 9.81 N/kg in the downward direction. In the second step, the transient coupled pore pressure/effective stress analysis is carried out using the SOILS, CONSOLIDATION option with an automatic time stepping. The UTOL parameter which controls the accuracy of the time integration is chosen as 5.0×10^{12} kN/m^2. This parameter specifies the allowable pore pressure change per time step. If the pore pressure change per time step is greater than the defined UTOL parameter, the program will quit the analysis, otherwise it will complete the analysis at the end of the final time step. In this example, a relatively large UTOL parameter is selected to avoid any interruptions due to sudden pore pressure changes during the analysis. The initial time step is selected as $t_i = 1.0 \times 10^{-2}$ s. The total time is defined as $t_f = 25$ s. The minimum and maximum values of time steps are chosen as 1.0×10^{-7} sec and 2.0 s, respectively.

In the first analysis, it is assumed that there is no contact between the pile and soil elements along the shaft of the pile. In other words, the pile elements are perfectly bonded to soil elements along the pile-soil interface. In this analysis, the displacement is applied gradually on the pile top and the reaction forces at the nodes on the pile head are calculated. Figure 6.11 shows the load-displacement curves for the total, shaft and end bearing capacities at the pile top. These curves are obtained from the finite element analysis and from the work of Potts (2001). It is clear that the present work is consistent with the published data (Potts, et al., 2001). The total capacity of the pile is calculated as 7,100 kN. The ultimate shaft capacity is predicted as 6,391 which is close to the capacity

obtained from the simple calculation in which the shaft area (62.83 m^2) times the undrained shear strength of clay (100 kPa) resulting in 6,283 kN.

In the second analysis, the soil-pile interface is defined by master-slave contact algorithm with the Coulomb frictional law. The details of this contact algorithm are explained in Section 6.5. The coefficients of friction (f_c) between the pile and soil are selected as 0.35 and 0.50 for two different cases. Figure 6.12 illustrates the load displacement curves for the cases in which there is no friction at the interface, fc=0.5 at the interface, and f_c=0.35 at the interface. The total load capacities for these cases are calculated as 7,100 kN, 5,560 kN and 3,780 kN, respectively. The differences between these capacities occur because if the decrease in the skin friction resistance. As seen in Figure 6.12, the total capacity decreases 22% for the case with f_c=0.50, and 47% for the case with f_c=0.35. Figure 6.13 shows the total, end bearing and skin friction capacities for the case with f_c=0.35. While the ratio of shaft capacity to the total capacity is 0.90 in the case with no friction at the interface, this ratio is 0.53 for the case with f_c=0.35. In other terms, the skin friction resistance is 53% of the total capacity as shown in Figure 6.13. The inclusion of friction between the pile and soil yields more conservative shaft capacity estimation which is consistent with the theoretical methods that are explained in Section 6.3.The comparison of the theoretical methods and the finite element method for shaft capacity estimation is given in the following section.

The end bearing capacities of the pile in this problem are re-calculated using the theoretical methods that are introduced in Section 6.3. These methods are: General Method, Vesic's Method, Janbu's Method, Meyerhof's Method and Coyle & Castello's method. The theoretical methods are compared with the finite element results. The objective of this comparison is to investigate the reliability of these methods and to determine where the finite element method stands among those methods. The parameters that are used to calculate the end bearing capacities with the theoretical methods are given in Table 6.10. The calculations based on these methods are shown in Table 6.11.

The end bearing capacities calculated from each method are compared with the finite element method results as shown in Figure 6.15. The end bearing capacity calculated by the finite element method is 2,003 kN. The closest value to that is estimated by Coyle & Castello's and Janbu's methods which results in 1,760 kN and 2,472 kN, respectively. The Vesic's and Meyerhof's methods predict the end bearing capacities as 5,860 kN and 3,864 kN, respectively, which can be interpreted as overestimation. On the other hand, the general formula which predicts a capacity of 707 kN underestimates the end bearing capacity.

The skin friction resistance is recalculated by three theoretical methods namely Alpha, Beta and Lambda methods which are described in Section 6.3. The parameters and calculation methods are shown in Tables 6.12 and 6.13. The results from these methods are compared with the finite element results in Figure 6.16. The calculations show that Beta method predicts the skin friction resistance as 1,709 kN which is close to the result obtained from the finite element method, 1,777 kN. However, the Lambda and the Alpha methods overestimate the skin friction resistance as 2,777 kN and 4,084 kN, respectively.

Table 6.6 Material properties of the normally consolidated clay

Material Parameter	Notation	Value	Units
	General		
Saturated unit weight	γ_{sat}	17.0	kN/m^3
Initial void ratio	e_o	1.5	-
Permeability	k	1.0×10^{-8}	*m/sec*
Coefficient of earth pressure at rest	K_o	1.0	-
	Elastic-Plastic		
Modul	E	1.0×10^{5}	kN/m^2
Poisson's ratio	v	0.49	-
Undrained shear strength	S_u	100.0	kN/m^2
Cohesion	c	100.0	kN/m^2
Angle of internal friction	ϕ	26	*Degree (°)*

Table 6.7 Material properties of the concrete pile

Material Parameter	Notation	Value	Units
	General		
Bulk unit weight	γ_{bulk}	24.0	kN/m^3
	Elastic		
Modulus of elasticity	E	2.0×10^{7}	kN/m^2
Poisson's ratio	N	0.15	-

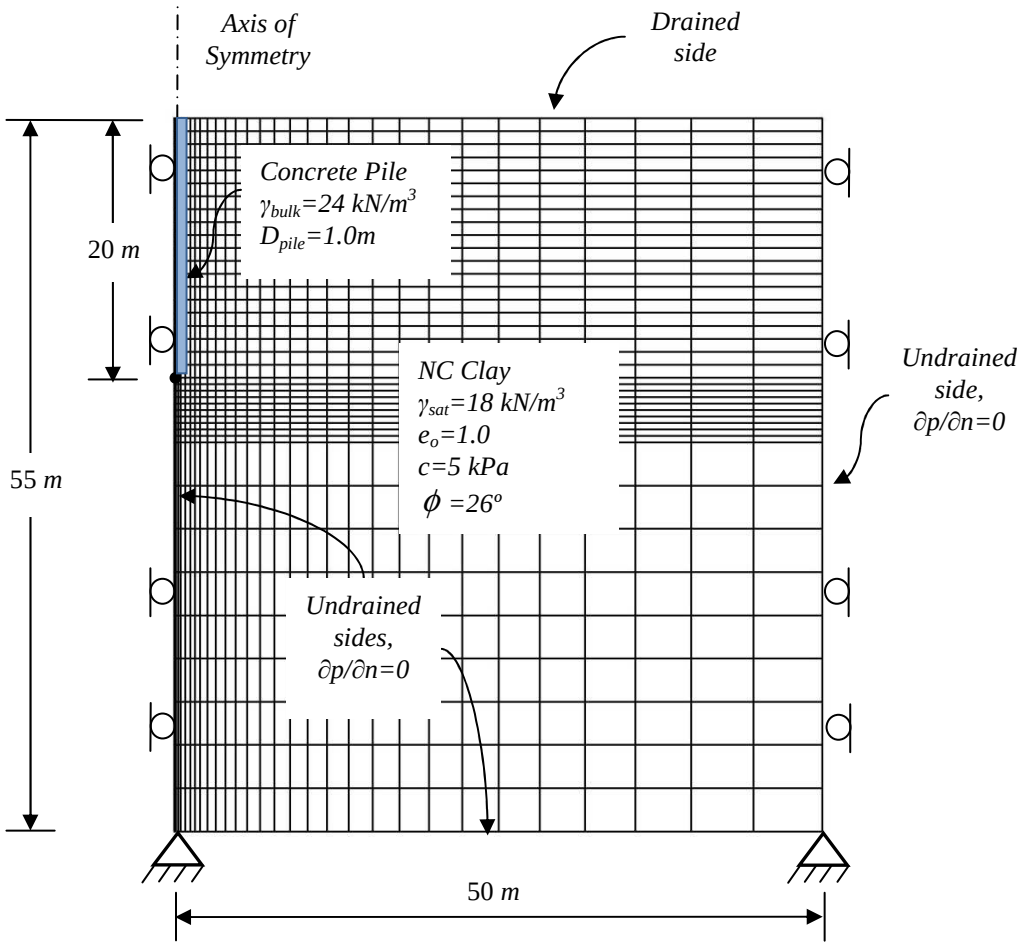

Figure 6.9 Axisymmetric finite element mesh of a single pile in clay deposit.

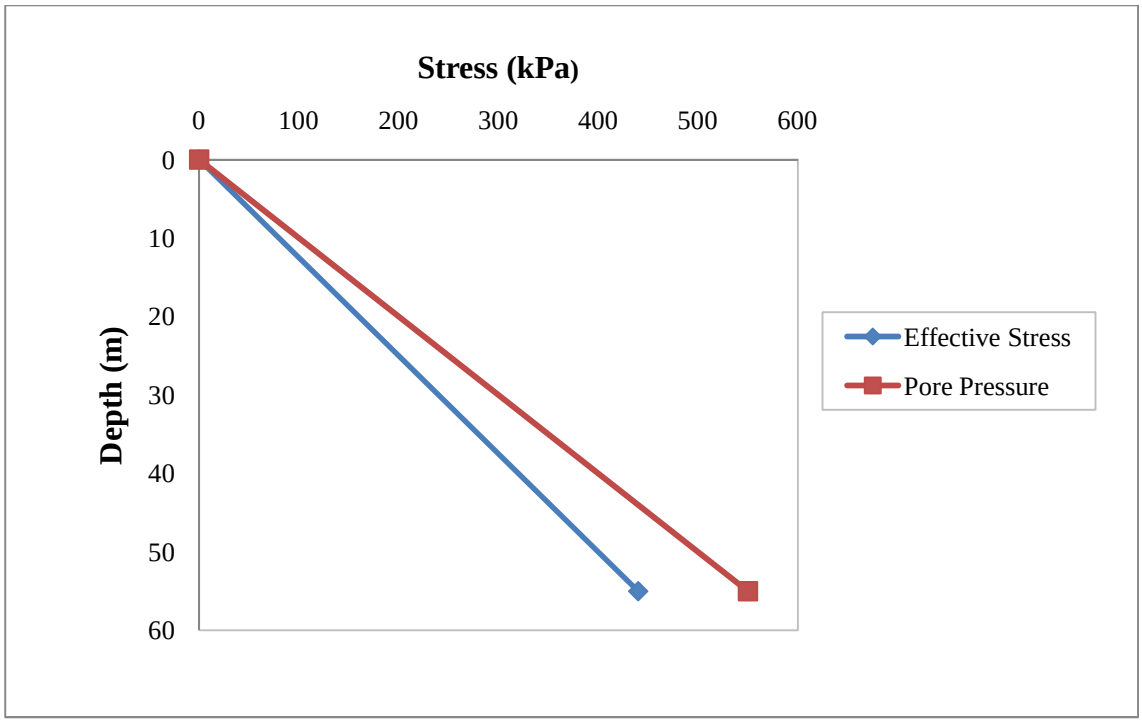

Figure 6.10 The initial stresses in the soil model.

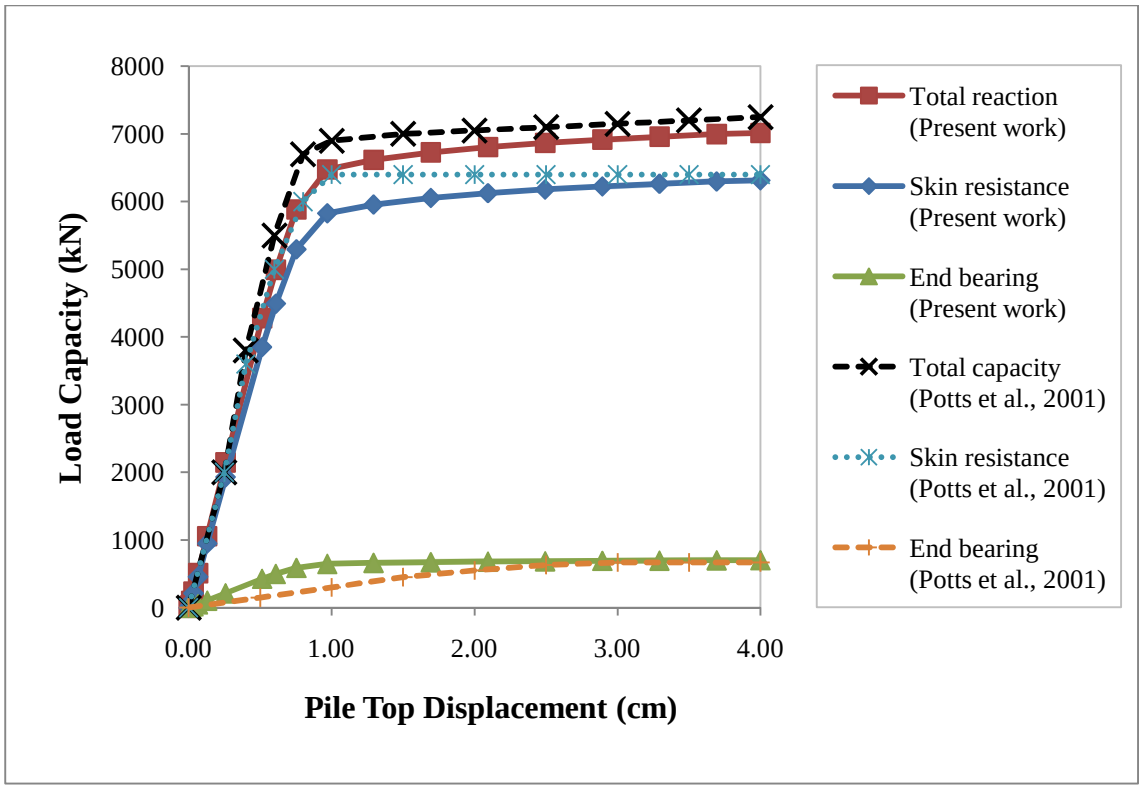

Figure 6.11 The load-displacement curve for the model with no slippage.

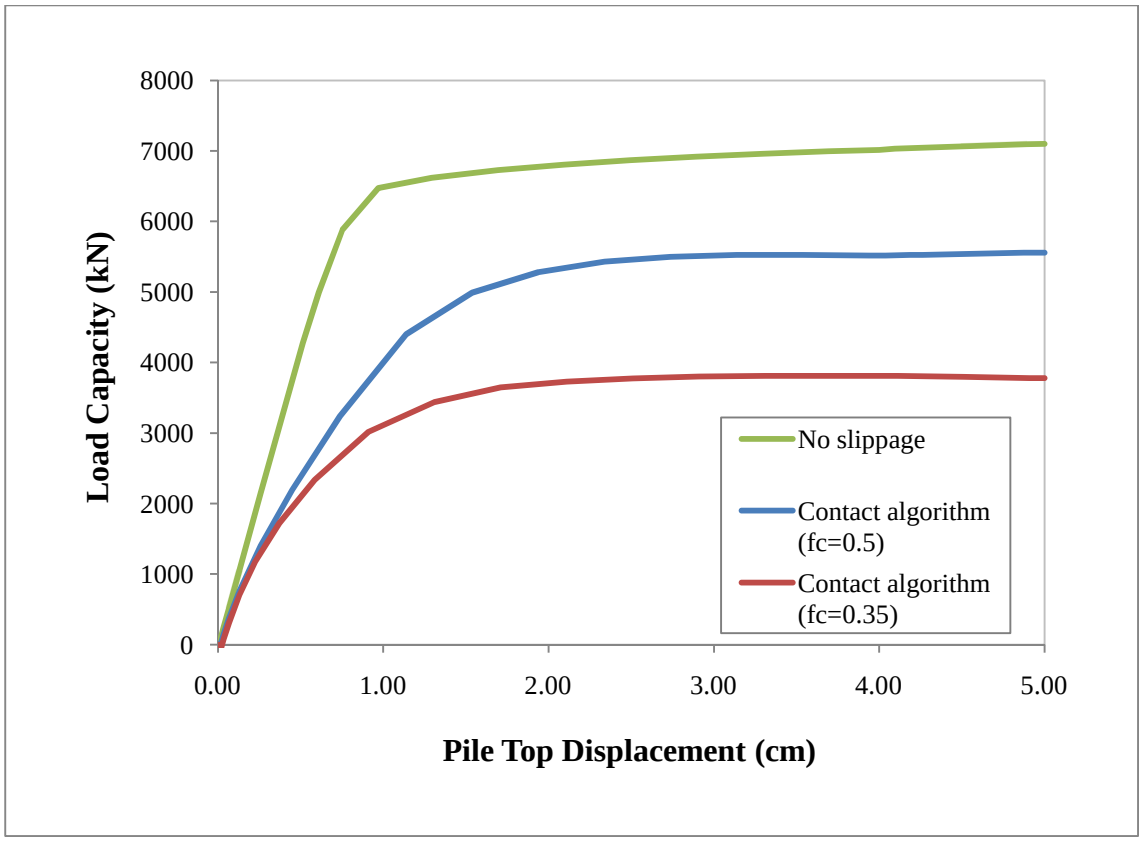

Figure 6.12 The comparison of load-displacement curves with no slippage and with coefficients of frictions 0.35 and 0.5 at the interface.

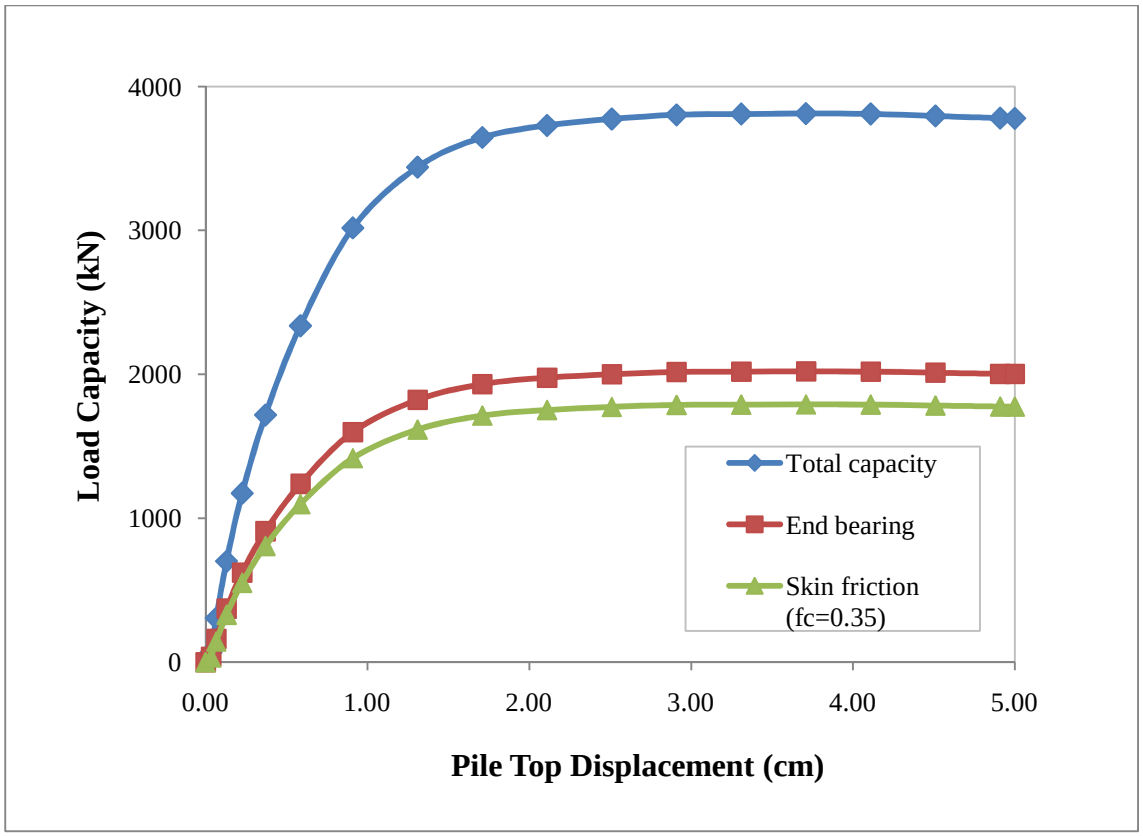

Figure 6.13 The end bearing, skin resistance and total capacities of a pile with coefficient of friction 0.35 at the soil-pile interface.

Table 6.8 The parameters used for the end bearing capacities of piles

Theoretical Methods	Parameters				
	N_q*	N_c*	N_σ*	K_0	ψ
General Formula	9.0	-	-	-	-
Vesic's Method	21.0	41.0	29.7	0.56	-
Janbu's Method	9.18	16.78	-	-	75.0
Meyerhof's Method	24.0	49.20	-	-	-
Coyle & Castello's Method	14.0	-	-	-	-

Table 6.9 The calculation of end bearing capacities

Calculation Method	Depth(m)	Effective stress, q_0' (kPa)	Average effective stress, σ_o' (kPa)	Unit end bearing (kPa)	Tip area (m^2)	Ultimate end bearing capacity (kN)
General	0.0	-	-	0.00	0.00	0.00
	20.0	-	-	900.00	0.79	706.86
Vesic's	0.0	0.00	0.00	0.00	0.00	0.00
	20.0	160.00	113.24	7460.61	0.79	5859.55
Janbu's	0.0	0.00	-	0.00	0.00	0.00
	20.0	160.00	-	3146.88	0.79	2471.56
Meyerhof's	0.0	-	-	0.00	0.00	0.00
	20.0	-	-	4920.00	0.79	3864.16
Coyle and Castello's	0.0	0.00	-	0.00	0.00	0.00
	20.0	160.00	-	2240.00	0.79	1759.29

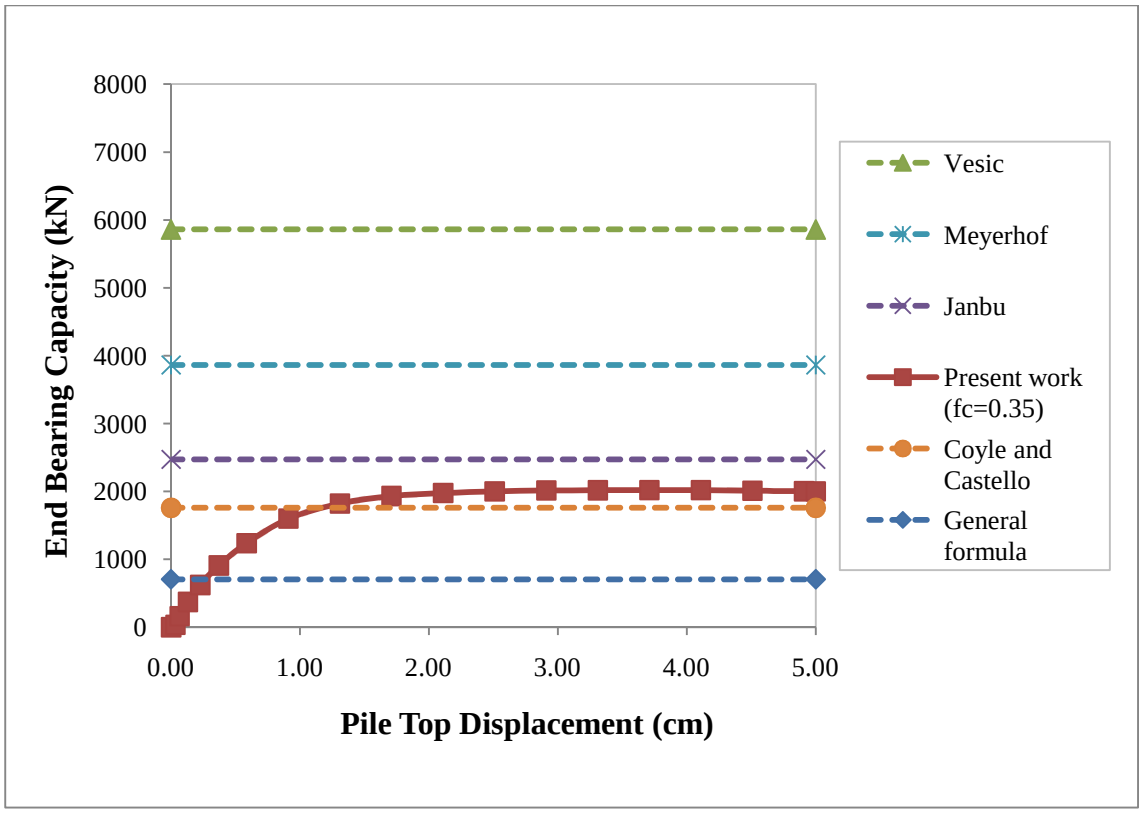

Figure 6.14 The comparison of end bearing capacities.

Table 6.10 The parameters used for the theoretical methods

Theoretical Methods	Parameters				
	α	β	λ	K_0	$tan\delta$
Alpha Method	0.65	-	-	-	-
Beta Method	-	0.20	-	0.56	0.35
Lambda Method	-	-	0.17	-	-

Table 6.11 The calculation of skin friction resistance

Calculation Method	Depth (m)	Effective Vertical Stress, σ_v' (kPa)	Unit Skin Resistance, q_s (kPa)	Skin Area, A_s (m^2)	Ultimate Skin Resistance, Q_s (kN)
Alpha	0.0	-	0.00	0.00	0.00
	20.0	-	65.00	62.83	4084.1
Beta	0.0	0.00	0.00	0.00	0.00
	20.0	160.00	31.82	62.83	1999.4
Lambda	0.0	0.00	0.00	0.00	0.00
	20.0	160.00	61.20	62.83	2777.1

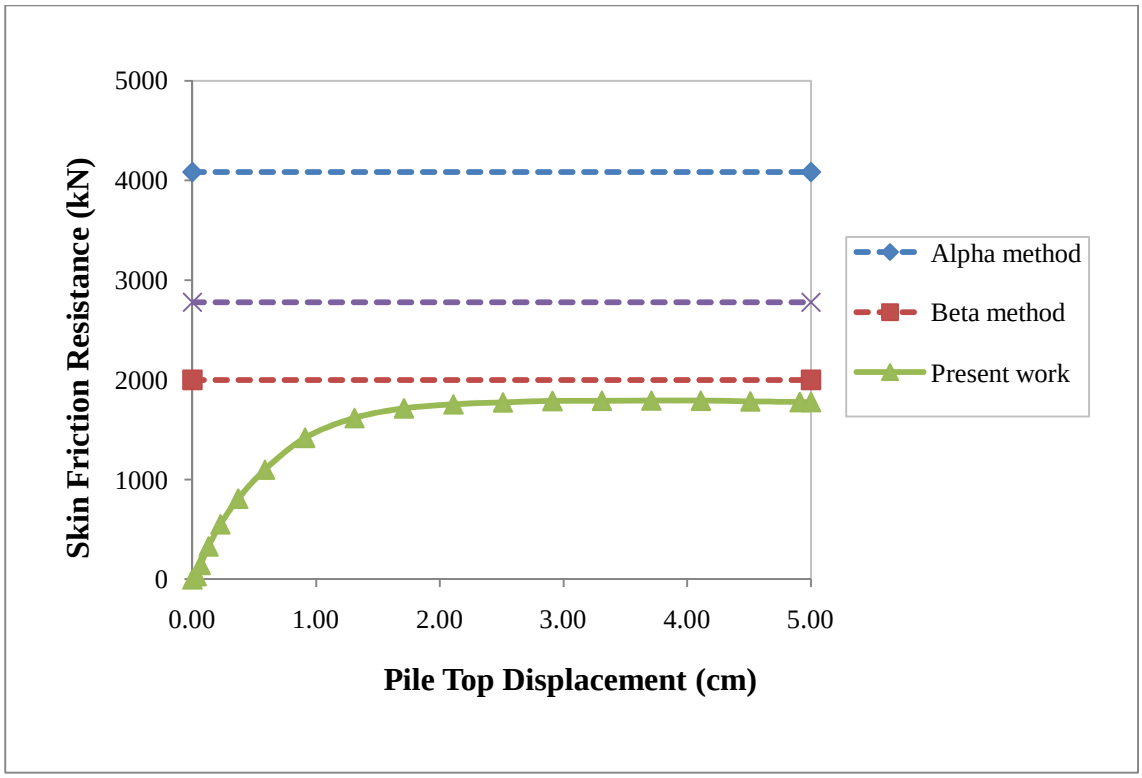

Figure 6.15 The comparison of skin friction resistance.

6.8.2 Load Capacity Analysis in Layered Clays

This example considers the finite element analysis of a single vertical pile under axial loading in layered clay. A 1-m in diameter cylindrical pile with an embedded length of 20.0 m is considered. The surrounding clay is considered as 50.0 m in width and 55.0 m in height with three different layers. The symmetry permits to model half of the cylindrical pile and the surrounding soil. A two-dimensional axisymmetric model is chosen for the finite element analysis. The finite element mesh is shown in Figure 6.17.

The normally consolidated clay is modeled using the Drucker-Prager (DP) constitutive model. The clay deposit is considered consisting of three layers. The undrained shear strength of the clay is S_u = 20 kPa on the top surface and increases at a rate of 4 kN/m^2 per meter from the top layer. The modulus of elasticity of the clay is E = 30 × 10^{3}kPa on the top surface and increases 1.0 × 10^{3}kPa per meter with depth. The angle of internal friction is constant, ϕ =12º. The DP constitutive model parameters are: $\tan\beta = 0.36$ and $d = 1.69c$ where c is the cohesion of the clay for each layer. The Poisson's ratio is v=0.4. The material behavior of the single pile is assumed to be linear elastic with a modulus of elasticity E = 30 × 10^6 kN/m^{2}and a Poisson's ratio v=0.20. The coefficient of friction between pile and soil is f_c=0.15. The material properties of the clay layers and the concrete pile are summarized in Tables 6.8 and 6.9.

The soil strip is assumed to have a rigid, impermeable and smooth base. Neither horizontal displacements nor pore water flow is allowed on the vertical sides. Free drainage is only allowed along the top surface. The pile loading is represented by applying displacements on the pile head. The nodes of the pile head are connected so that a uniform displacement can be applied on the pile head. A total of 0.005 m of displacement is applied on the pile head nodes using an automatic time stepping. The initial stresses are applied on the model is shown in Figure 6.18.

The analysis is performed using a GEOSTATIC step followed by the SOILS, CONSOLIDATION step. In the geostatic step, a gravitational acceleration of g = 9.81

kN/m^2 is applied on all elements in the model. In the following step, a total displacement of 0.030 m is applied on the pile head in the downwards direction using an automatic time stepping scheme under small-strain conditions. The displacements are applied using an initial time step of t_i=1.0 × 10^{-2} sec for a total duration of t=30 seconds. The automatic time stepping is used during the analysis where the time steps are allowed to be between Δt_{min}=1.0 × 10^{-7} sec and Δt_{max}=2.0 s. The tolerance on the pore pressure change in any increment is set using the UTOL option. The UTOL option is set to 5.0 × 10^{12} kN/m^2. If the maximum change in pore pressure at any node is greater than UTOL, the increment is repeated with proportionally reduced time step, otherwise the time step is increased.

Two analyses are run for the load capacity analysis of the pile. The first analysis takes into account the coefficient of friction between pile and soil as f_c=0.15. The ultimate pile capacity obtained from the load-displacement curve is2,090 kN as shown in Figure 6.18. The shaft capacity is 941 kN, and the end bearing capacity is 1,149 kN. The second analysis which is shown in Figure 6.19 is run based on the coefficient of friction f_c=0.50. The total, shaft and end bearing capacities are calculated as 4,047 kN, 2,847 kN and 1,173 kN, respectively. It is clear that while the end bearing capacities in both cases are close to each other, in the second analysis the skin friction resistance is almost three times higher than the one in the first analysis. This is due to the increase in the coefficient of friction. Increasing the coefficient of friction three times yields three times higher shaft capacity. Thus, modeling the interface and choosing the right frictional parameters is the key in the load capacity analysis of piles. Figure 6.20 compares the total capacities for both cases reveals that the total capacity in the second case is two times of higher than the capacity in the first case.

For the comparison of finite element results, the load capacity calculations are performed using the theoretical methods. The parameters used for the calculations are given in Table 6.14. The results for each theoretical method are given in Table 6.15. The end bearing capacities calculated from each method are plotted in Figure 6.22. The

calculations show that Janbu's method and Coyle & Castello's method predict the end bearing capacity close to the finite element method results. Meyerhof's and Vesic's methods overestimate the end bearing capacity by a factor of 2.5 and 4.5, respectively. The general formula underestimates the end bearing almost 30% less than the finite element results.

The skin friction resistance is calculated using three theoretical methods. The results from these methods are compared with the finite element results. The parameters used in these five methods are given in Table 6.16. The results are given in Table 6.23 for each theoretical method. The skin friction resistances calculated from each method are plotted in Figure 6.23. The calculations show that the Beta method predicts the skin friction resistance close to the finite element method. However, the Alpha and Lambda methods overestimate the skin friction resistance by a factor of 2.0 and 3.0, respectively.

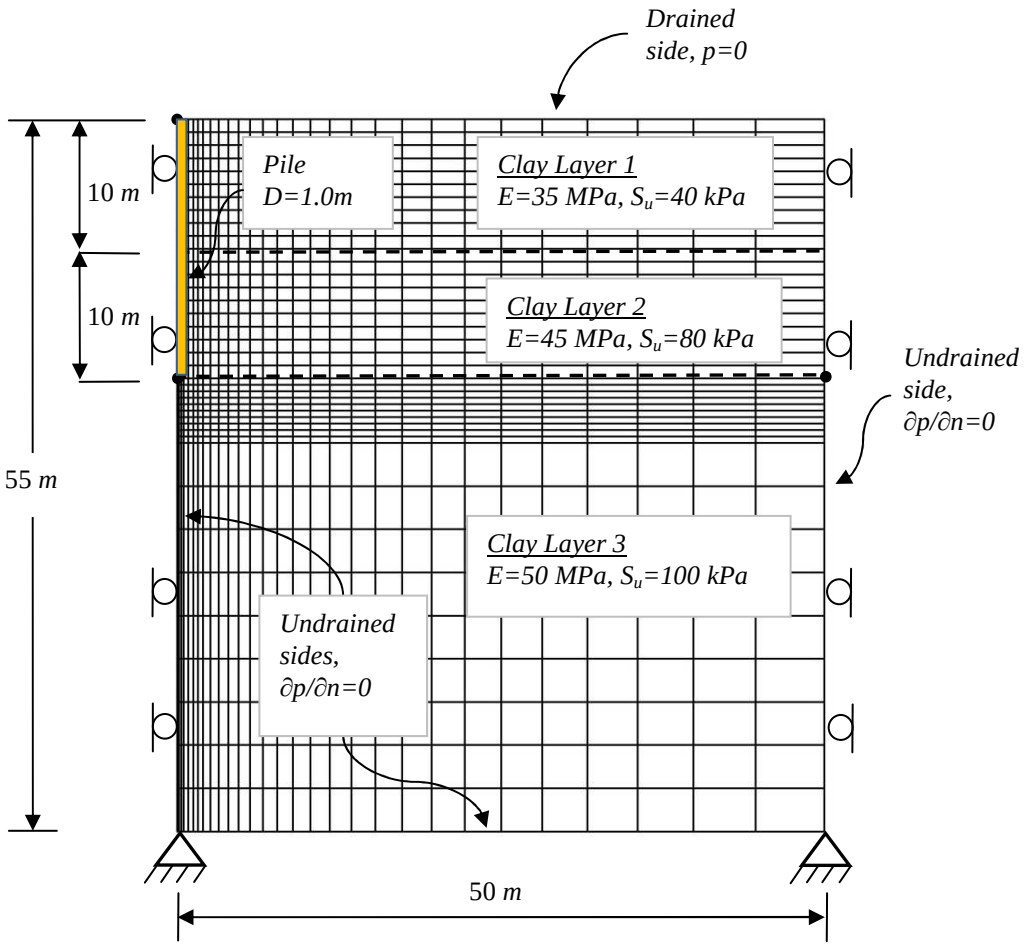

Figure 6.16 The finite element mesh of the soil-pile model.

Table 6.12 Material properties of the normally consolidated clay

Material Parameter	Notation	Value	Units
	General		
Saturated unit weight	γ_{sat}	17.0	kN/m^3
Initial void ratio	e_o	1.5	-
Permeability	k	1.0×10^{-8}	*m/sec*
Coefficient of earth pressure at rest	K_o	1.0	-
	Elastic-Plastic		
Layer 1			
Modulus of elasticity	E	35.0×10^3	kN/m^2
Poisson's ratio	v	0.20	-
Undrained shear strength	S_u	40.0	kN/m^2
Friction angle	ϕ	12	*Degree (°)*
Layer 2			
Modulus of elasticity	E	40.0×10^3	kN/m^2
Poisson's ratio	v	0.20	-
Undrained shear strength	S_u	80.0	kN/m^2
Friction angle	ϕ	12	*Degree (°)*
Layer3			
Modulus of elasticity	E	45.0×10^3	kN/m^2
Poisson's ratio	v	0.20	-
Undrained shear strength	S_u	100.0	kN/m^2
Friction angle	ϕ	12	*Degree (°)*

Table 6.13 Material properties of the concrete pile

Material Parameter	Notation	Value	Units
	General		
Bulk unit weight	γ_{bulk}	24.0	kN/m^3
	Elastic		
Modulus of elasticity	E	3.0×10^7	kN/m^2
Poisson's ratio	N	0.40	-

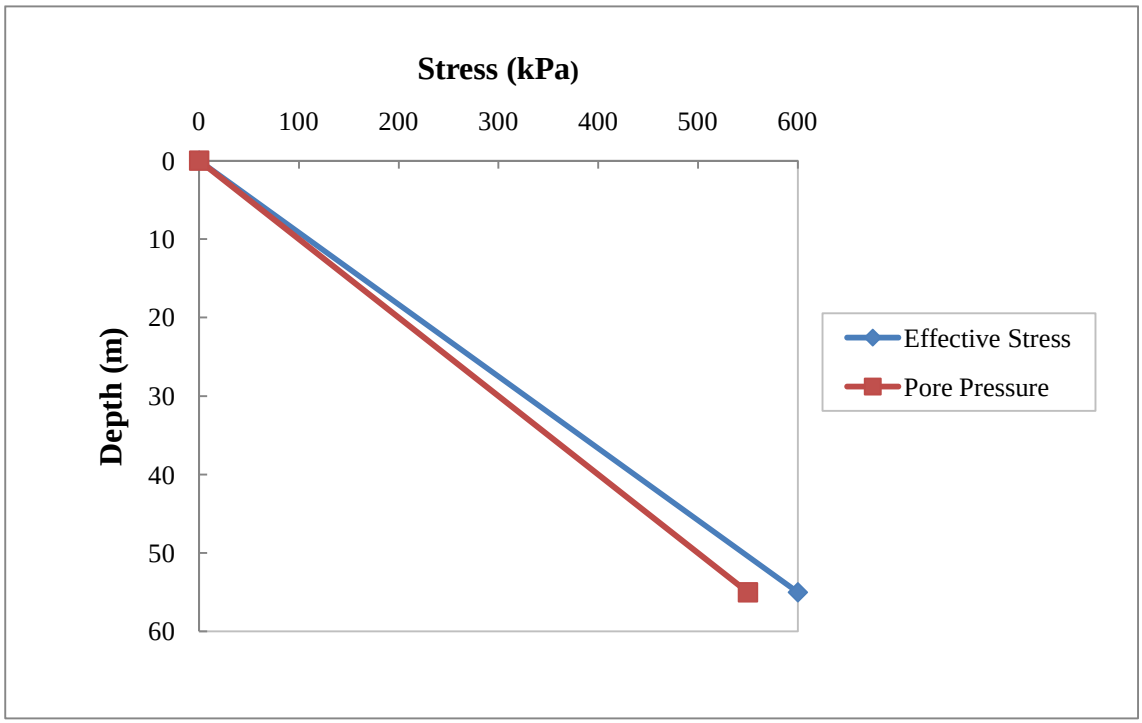

Figure 6.17 The initial stresses defined in ABAQUS.

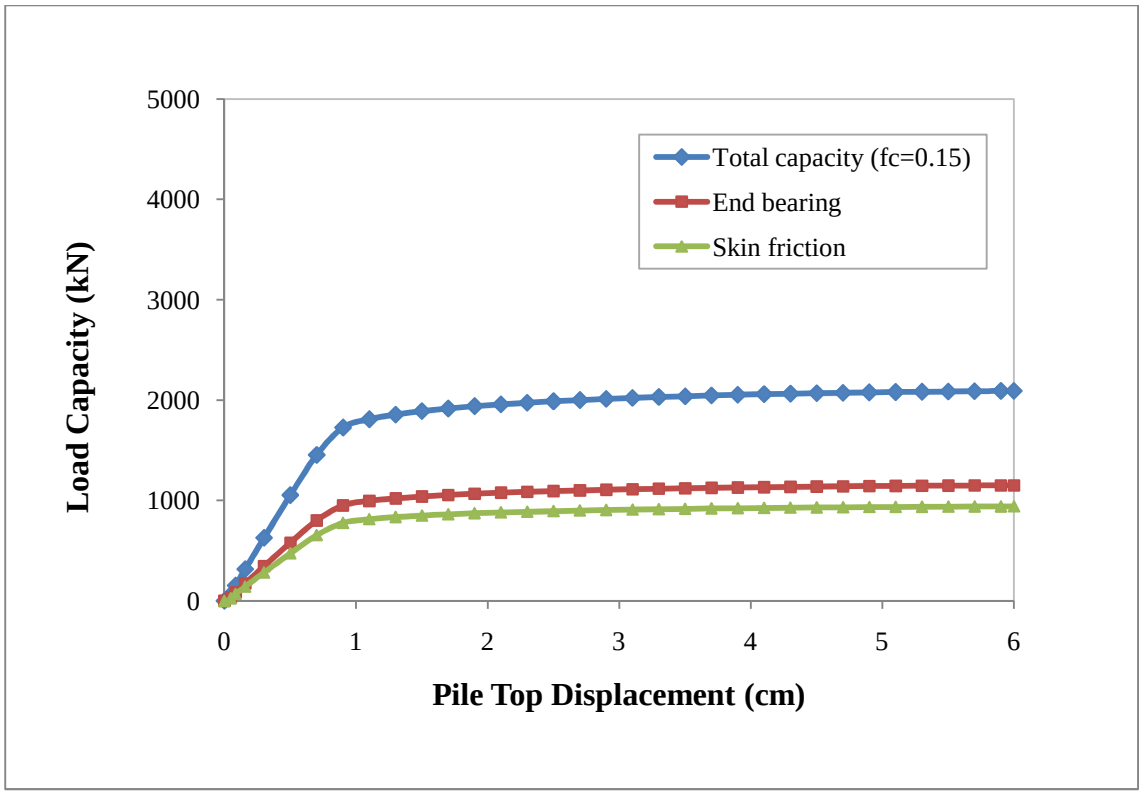

Figure 6.18 The load-displacement curve for f_c=0.15 at the interface.

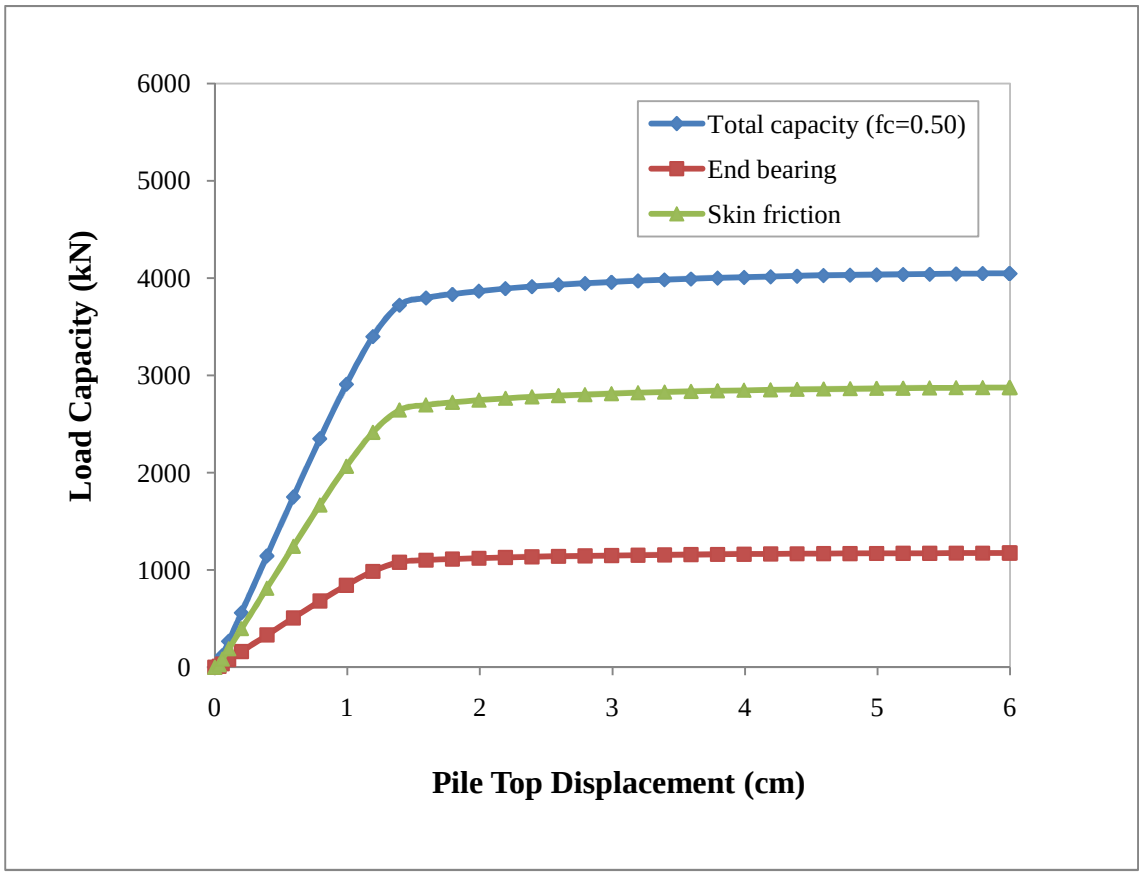

Figure 6.19 The load-displacement curve for f_c= 0.50 at the interface.

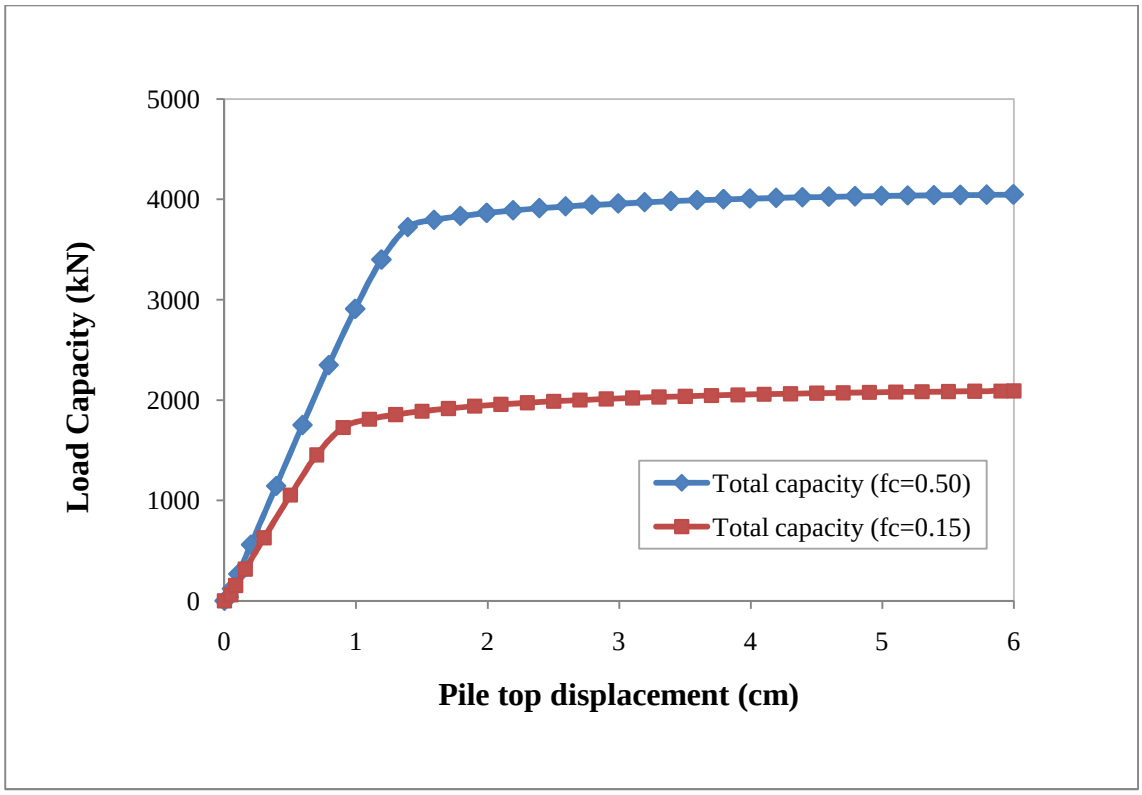

Figure 6.20 The load-displacement curve using interface elements with coefficients of frictions 0.15 and 0.5 at the interface.

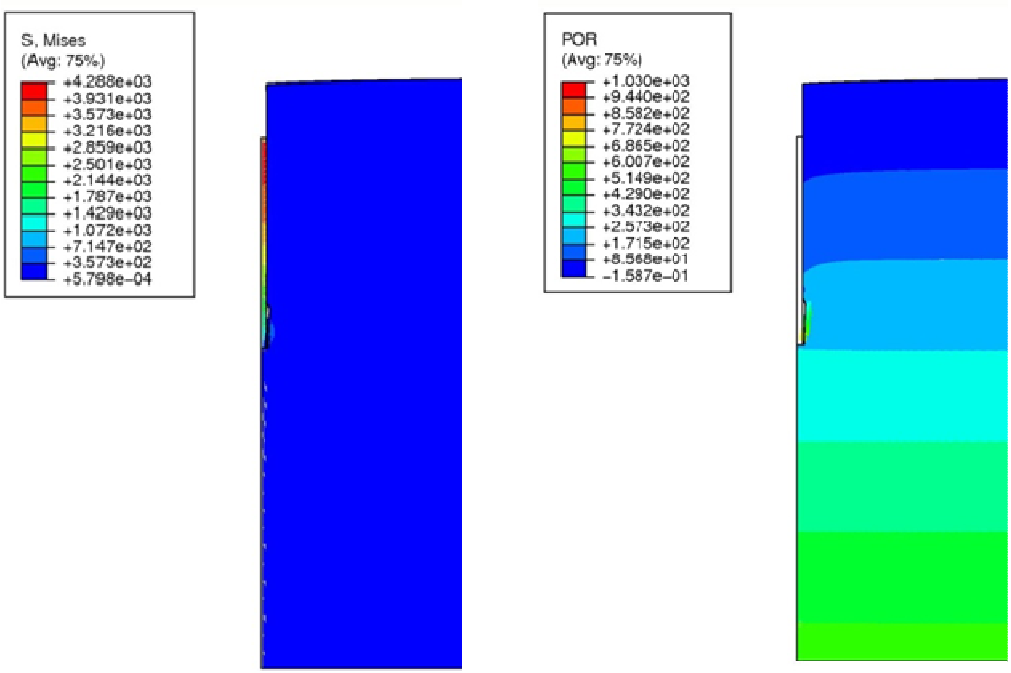

(a) (b)

Figure 6.21 The contour plot of (a) von Mises stresses, (b) pore water pressure.

Table 6.14 The parameters used for the theoretical methods

Theoretical Methods	Parameters				
	N_q*	N_c*	N_σ*	K_0	ψ
General Formula	9.0	-	-	-	-
Vesic's Method	10.0	42.3	11.6	0.79	-
Janbu's Method	2.66	7.81	-	-	75.0
Meyerhof's Method	8.0	32.93	-	-	-
Coyle & Castello's Method	8.0	-	-	-	-

Table 6.15 The calculation of end bearing capacities

Calculation Method	Depth(m)	Effective stress, q_0' (kPa)	Average effective stress, σ_o' (kPa)	Unit end bearing (kPa)	Tip area (m^2)	Ultimate end bearing capacity (kN)
General	0.0	-	-	0.00	0.00	0.00
	20.0	-	-	900.00	0.79	706.86
Vesic's	0.0	0.00	0.00	0.00	0.00	0.00
	20.0	140.00	120.59	5634.17	0.79	4425.06
Janbu's	0.0	0.00	-	0.00	0.00	0.00
	20.0	140.00	-	1153.57	0.79	906.01
Meyerhof's	0.0	-	-	0.00	0.00	0.00
	20.0	-	-	3293.24	0.79	2586.51
Coyle and Castello's	0.0	0.00	-	0.00	0.00	0.00
	20.0	140.00	-	1120.00	0.79	879.65

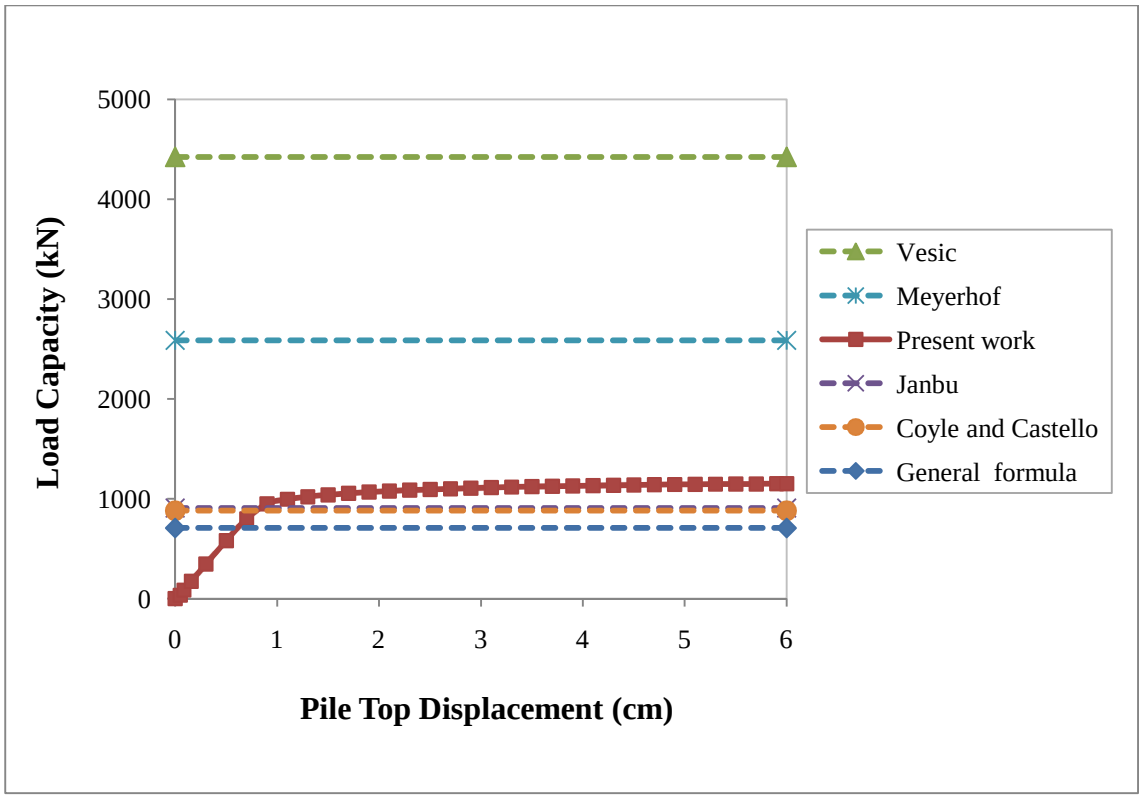

Figure 6.22 The comparison of end bearing capacities.

Table 6.16 The parameters used for the theoretical methods

Theoretical Methods	Parameters				
	α	β	λ	K_0	$tan\delta$
Alpha Method	0.65	-	-	-	-
Beta Method	-	0.13	-	0.79	0.16
Lambda Method	-	-	0.17	-	-

Table 6.17 The calculation of the skin friction resistance

Calculation Method	Depth (m)	Effective Vertical Stress, σ_v' (kPa)	Unit Skin Resistance, q_s (kPa)	Skin Area, A_s (m^2)	Ultimate Skin Resistance, Q_s (kN)
Alpha	0.0	-	0.00	0.00	0.00
	10.0	-	26.00	31.42	816.8
	20.0	-	80.00	31.42	2513.3
					3330.09
Beta	0.0	0.00	0.00	0.00	0.00
	10.0	70.00	8.78	31.42	275.92
	20.0	140.00	18.20	31.42	571.84
					847.77
Lambda	0.0	0.00	0.00	0.00	0.00
	10.0	35.00	19.55	31.42	614.26
	20.0	105.00	45.05	31.42	1415.47
					2029.73

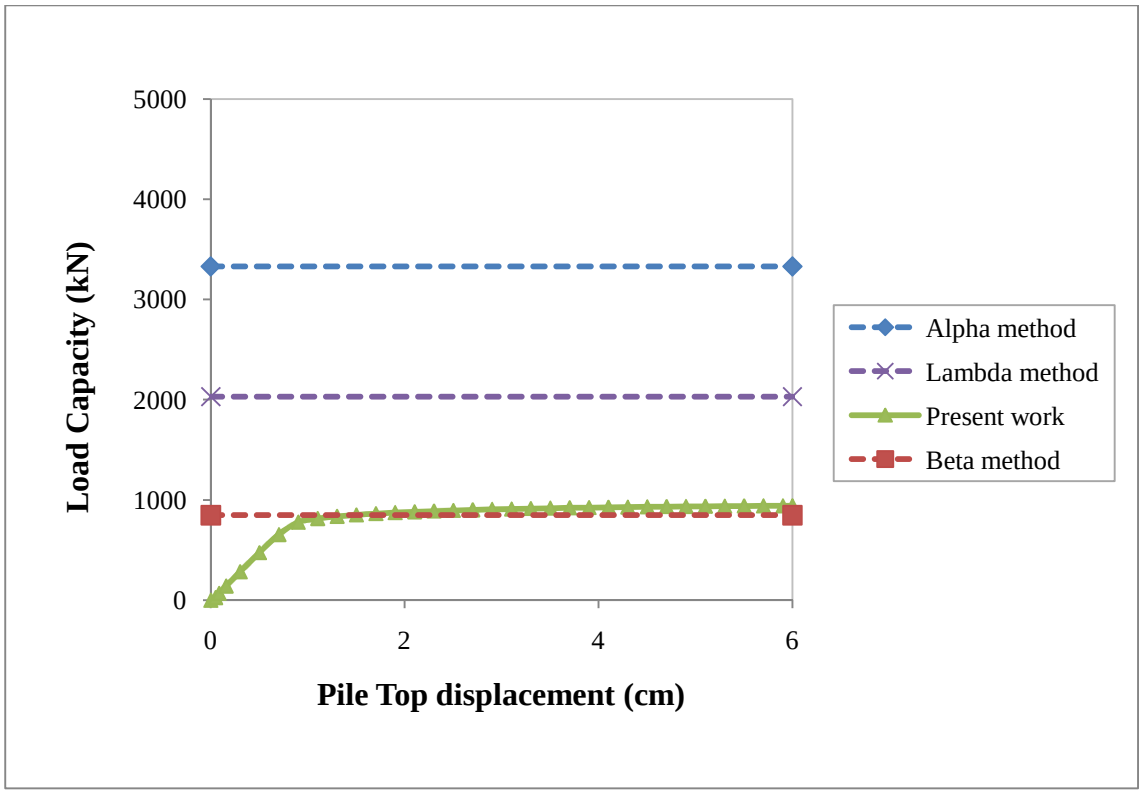

Figure 6.23 The comparison of skin friction resistance.

6.9 Summary and Discussion

Load capacity analysis of a single pile is investigated in this chapter using the finite element method. The efficiency of the finite element method is supported by widely recognized theoretical methods. These methods are employed to estimate load capacities of single piles. The theoretical methods that are used to estimate the end bearing capacities are: (1) General Formula, (2) Vesic's Method, (3) Janbu's Method, (4) Meyerhof's Method, and (5) Coyle& Castello's Method. The estimation of skin friction resistance (shaft capacity) of single piles is performed using the (1) Alpha method, (2) Beta method, and (3) Lambda method.

A non-linear static axisymmetric model which assumes small deformations is developed for the finite element analysis. This model simulates an axially loaded pile which is embedded in a normally consolidated clay deposit. The Mohr-Coulomb plasticity model is used to represent the inelastic behavior of clay. The soil pile interface is modeled using contact pairs which complies with the master-slave contact algorithm defined in ABAQUS/Standard. The frictional interaction between soil and pile is defined by the Coulomb frictional law. A transient coupled pore pressure/effective stress analysis is performed using an automatic time stepping scheme. Small increments of displacements are applied on the pile top under undrained conditions until the pile is fully mobilized.

Two numerical applications are carried out to estimate the load capacity of single piles in normally consolidated clays. The first numerical application consists of a solid cylindrical concrete pile with a diameter D = 1.0 m and length L= 20 m embedded in a thick homogenous stiff clay layer. The load capacity analysis is performed with and without interface elements. The analysis that considers no interface elements predicts an ultimate end bearing capacity of 710 kN, shaft capacity of 6,391 kN, and a total capacity of 7,101 kN which is consistent with the published data. The analysis shows that the shaft capacity mobilizes first followed by the end bearing capacity. This is due to the load

bearing mechanism of piles which proves that the applied load is carried first by the shaft then the tip of the pile. The analysis with interface elements is modeled using two different coefficients (f_c = 0.35 and f_c = 0.50) of friction at the soil pile interface. The total capacities are calculated as 5,559 kN for f_c = 0.50 and 3,779 kN for f_c = 0.35. The decrease in the load capacities can be explained by the decrease in friction at the soil pile interface. It is examined that the model with no interface predicts almost twice as much load capacity as the model with interface. The finite element results are also compared with theoretical methods that are used to estimate the pile load capacities. In regards with the end bearing capacities, Coyle & Castello's method is found to be most conservative followed by the finite element method, then Janbu's method, then Meyerhof's method, and finally Vesic's method. In respect to skin friction resistance, the finite element is found to be the most conservative method, followed by Beta, then Lambda, and then Alpha. These comparisons confirm that modeling of soil pile interface is essential to obtaining reliable results for the load capacities of piles. The second numerical application is carried out using a three layer clay deposit for the load capacity analysis of a single pile. The layers are modeled from soft to stiff starting at the ground surface. The end bearing capacity, skin friction resistance, and the total capacity are calculated as 1,150 kN, 941kN, and 2,091 kN, respectively. Although the strength of the soil at the pile tip remains the same, the end bearing capacity decreases almost 50 percent compared to the first application. This outcome is obtained because the stiffness of the clay at the pile tip is almost 50 percent less than in the first numerical application. The skin friction resistance is also found to be almost 50 percent less. This result is attained because the coefficient of friction is lower due to the lower internal angle of the clay.

In conclusion, modeling of the soil pile interface is critical to accurately compute the shaft capacity of a pile. The results show that use of frictional contact between soil and pile makes a significant difference in estimating the load capacity of piles. The theoretical methods support the results obtained in the numerical applications.

CHAPTER 7
DYNAMIC ANALYSIS OF PILE DRIVING AND WAVE PROPAGATION IN UNDRAINED SOILS

7.1 Introduction

The finite element method is a powerful tool to investigate the generation of ground vibrations due to pile driving. It is because the stress waves generated by pile driving are usually complex, and recorded signals exhibit a combination of body and surface waves (Attewell and Farmer, 1973) as shown in Figure 7.1. When a hammer strikes the head of a pile during pile driving, the impact energy is transmitted from the hammer to the pile. This energy travels along the pile in the form of compressive waves, called the primary body waves or P-waves (Goble et al., 1976). A large portion of this energy is used for advancing the pile, while the rest of the energy is transmitted to the soil by means of two ways: (1) through the pile shaft in the form of shear waves or S-wave propagating on a cylindrical wave front; and (2) at the pile toe in the form of P-waves propagating on a spherical wave front. Another type of wave is generated on the ground surface which is called the surface or the Rayleigh wave that propagates outwards from the pile shaft around a circumferentially expanding wave front.

Generation of ground motion depends on many factors including (a) source parameters (method of pile driving, energy, and pile depth), (b) the interaction between the pile and the soil, and (c) the propagation of the waves through the geological structure at the site (Masoumi et al., 2008). Although simple numerical models may contain valuable data on general tendencies of wave propagation at a site, they cannot take into account spatial variations of soil properties. Thus, these models may not produce accurate and complete ground vibration records at a point of interest. Hence, when modeling pile driving and wave propagation in soils, all of these factors should be taken into account carefully to increase the precision of the outcome.

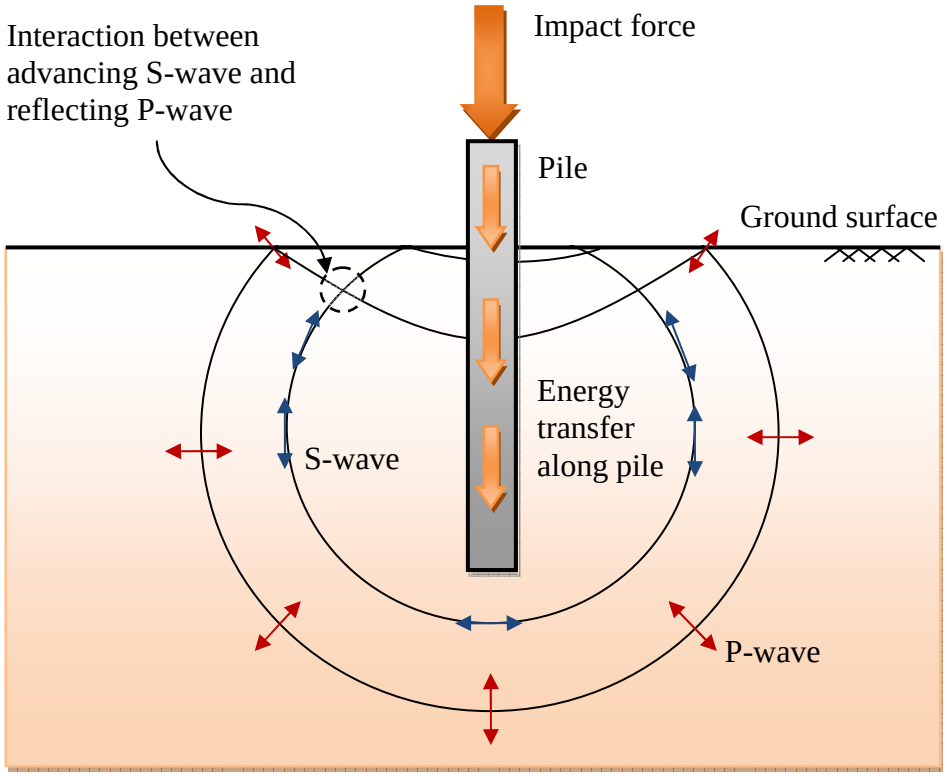

Figure 7.1 The mechanics of wave propagation due to impact pile driving.

In this chapter, a complete finite element model is proposed to simulate the dynamic loading of a single pile and generated wave propagation in soils. The proposed model includes (a) geostatic stresses prior to the dynamic analysis; (b) elasto-plastic behavior of soil and; (c) shear slip at the pile-soil interface. The aim of this study is to investigate the effect of major factors such as soil plasticity, pile penetration length and hammer energy on the transmission of pile driving induced ground vibrations. The organization of this chapter is as follows: first, the governing equations and the finite element equations used for the quasi-static analysis of porous media are summarized. Then, the finite element modeling procedure including the special boundary conditions, the constitutive law and the solution procedure of the finite element equations are explained. Next, the finite element model developed to simulate pile driving induced ground vibrations is implemented in two numerical applications. Then, the effect of soil properties, pile penetration length and the variation of hammer energy are investigated. Finally, the ground vibrations at different depths are studied followed by the summary and conclusions.

7.2 Governing Equations

7.2.1 Balance Equations

The balance equations consisting of mass balance and linear momentum balance equations are explained in Chapter 3. In this chapter, these equations are revisited, and they are combined with an elasto-plastic constitutive law. The balance laws for a fully saturated two-phase mixture can be written in general form as

(1) Mass balance equation:

$$\frac{D^{\alpha}\rho_{\alpha}}{Dt} + \rho_{\alpha} div\ \mathbf{v}^{\alpha} = \rho_{\alpha} e^{\alpha}(\rho) \qquad (\alpha = s,\ w) \tag{7.1}$$

(2) Linear momentum balance equation:

$$div\ \boldsymbol{\sigma}_{\alpha} + \rho_{\alpha}(\mathbf{g}^{\alpha} - \mathbf{a}^{\alpha}) + \rho_{\alpha}\left[e^{\alpha}\left(\rho \mathbf{v}^{\alpha}\right) + \hat{\mathbf{p}}^{\alpha} \right] = \mathbf{0} \qquad (\alpha = s,\ w) \tag{7.2}$$

where α is the indicator of the phase (α=s, w) where s and w refer to solid and fluid respectively; D^{α}/Dt is the material derivative following the motion of α-phase; $\rho_{\alpha} = \eta^{\alpha}\rho^{\alpha}$ is the macroscopic mass density where $\eta^{\alpha} = dV^{\alpha}/dV$ is the fraction of the representative element volume dV occupied by the α-phase subjected to $\sum_{\alpha=s,w} \eta^{\alpha} = \eta^{s} + \eta^{w} = (1-n) + n = 1$ where n is the porosity; $\mathbf{v}^{\alpha}$ and $\mathbf{a}^{\alpha}$ are the spatial velocity and acceleration vectors, respectively; $\mathbf{g}^{\alpha}$ is the gravitational force per body mass; $\boldsymbol{\sigma}_{\alpha} = \eta^{\alpha}\boldsymbol{\sigma}^{\alpha}$ is the partial (Cauchy) stress tensor; $\hat{\mathbf{p}}^{\alpha}$ is the exchange of momentum between two phases and; $e^{\alpha}(\rho)$ is the exchange of mass between two phases.

7.2.2 Field Equations

For the computation of mass balance equations, it is assumed that the sum of mass exchange is zero as follows:

$$\sum_{\alpha=s,w} \rho_{\alpha} e^{\alpha}(\rho v^{\alpha}) = 0 \tag{7.3}$$

Based on this assumption, the mass balance equation for each phase can be defined after the general form (Eq. 7.1) in terms of macroscopic quantities. For the solid phase, the mass balance equation is:

$$\frac{D^s \rho_s}{Dt} + \rho_s div\ \mathbf{v}^s = 0 \tag{7.4}$$

For the fluid phase, the mass balance equation is:

$$\frac{D^w \rho_w}{Dt} + \rho_w div\ \mathbf{v}^w = 0 \tag{7.5}$$

In Chapter 3, under the "Kinematics Equations" section, the derivation of quantities in the material and spatial coordinate system are described in detail. Recalling the material derivative of one phase with respect to other phase, the following relation can be defined as follows:

$$\frac{D^\beta f^\alpha}{Dt} = \frac{\partial f^\alpha}{\partial t} + grad\ f^\alpha \cdot \mathbf{v}^\beta \tag{7.6}$$

where $f^\alpha(\mathbf{x},t)$ is any differentiable function in the α-phase and D^β / Dt is the material time derivative operator for a prescribed phase β. The solid and fluid phases can then be combined and simplified using the above relationship as follows:

$$\frac{1-n}{\rho_s}\frac{D^s \rho^s}{Dt} + \frac{n}{\rho^w}\frac{D^s \rho^w}{Dt} + \frac{1}{\rho^w} div\ (n\rho^w \boldsymbol{v}^{ws}) + div\ \boldsymbol{v}^s = 0 \tag{7.7}$$

where $\boldsymbol{v}^{ws} = \boldsymbol{v}^w - \boldsymbol{v}^s$ is the relative velocity.

The fluid flow in the porous media can be explained by Darcy's Law which relates the seepage velocity to the porosity of the mixture, permeability of the material, viscosity of the fluid, pore-fluid pressure and mass of the flowing fluid. For a two-phase mixture, Darcy's law can be defined as follows:

$$n(\boldsymbol{v}^w - \boldsymbol{v}^s) = \frac{\boldsymbol{k}}{\mu^w}(-grad\ p + \rho^w \mathbf{g}) \tag{7.8}$$

where $\boldsymbol{k}$ is the permeability tensor, μ_w is the dynamic viscosity, and p is the pore-water pressure.

For the derivation of the linear momentum balance equations it is assumed that (a) the mass exchange between each phase is not allowed and; (b) the sum of interaction forces between each phase is zero as defined in the following:

$$\sum_{\alpha=s,w} \rho_\alpha e^\alpha (\rho v^\alpha) = 0 \tag{7.9}$$

$$\sum_{\alpha=s,w} \rho_\alpha \hat{\mathbf{p}}^\alpha = \rho_s \hat{\mathbf{p}}^s + \rho_w \hat{\mathbf{p}}^w = \mathbf{0} \tag{7.10}$$

Based on the general form of the linear momentum balance equation, Eq. (7.2), the balance equations in terms of macroscopic quantities can be defined for each phase. For the solid phase, the linear momentum balance equation is:

$$div\ \boldsymbol{\sigma}_s + \rho_s (\boldsymbol{g}^s - \mathbf{a}^s) = \mathbf{0} \tag{7.11}$$

For the fluid phase, the linear momentum balance equation is:

$$div\ \boldsymbol{\sigma}_w + \rho_w (\boldsymbol{g}^w - \mathbf{a}^w) = \mathbf{0} \tag{7.12}$$

The principle of effective stress of Terzaghi states that the total stress in a porous medium consists of effective stresses which are associated with the solid skeleton and the pore-water pressure which is associated with the pore fluid. In this study, a modified version of this principle is used after Bishop (1959). Under fully saturated conditions, the principle of effective stress can then be defined as:

$$\boldsymbol{\sigma}' = \boldsymbol{\sigma} + \boldsymbol{m}p \tag{7.13}$$

where $\boldsymbol{\sigma}'$ is the effective stress (positive in tension); $\boldsymbol{\sigma}$ is the total stress; p is the pore-fluid pressure and; $\boldsymbol{m}$ is a vector defined as $\boldsymbol{m}=\{1, 1, 1, 0, 0, 0\}^T$.

For the derivation of the mass balance equation, it is assumed that (a) the motion occurs under isothermal conditions; (b) the porous medium is fully saturated and; (c) the grain material is incompressible and the fluid is compressible. To get the final form of

mass balance equation, the mass balance equations in the solid and fluid phases are combined with Darcy's Law and the quantities are simplified as follows:

$$\frac{n}{K_w}\frac{\partial p}{\partial t} + div\left[\frac{\boldsymbol{k}}{\mu^w}\left(-grad\ p + \rho^w \mathbf{g}\right)\right] + div\ \boldsymbol{v}^s = 0 \tag{7.14}$$

where K_w is the bulk modulus of pore fluid.

To obtain the final form of the linear momentum balance law, the equations for solid and fluid phases, Eqs (7.8) and (7.9), are combined as follows:

$$div\ \boldsymbol{\sigma} + \rho\ \mathbf{g} = \mathbf{0} \tag{7.15}$$

where **g** is the body force and; $\boldsymbol{\sigma}$ and ρ are the averaged total stress and mass density, respectively, which can be defined as

$$\boldsymbol{\sigma} = (1-n)\boldsymbol{\sigma}^s + n\boldsymbol{\sigma}^w \tag{7.16}$$

$$\rho = (1-n)\rho^s + n\rho^w \tag{7.17}$$

Furthermore, introducing the principle of effective stress, the above equation can be reduced to the following form:

$$div\ \left(\boldsymbol{\sigma}' + \boldsymbol{m}p\right) + \rho\ \mathbf{g} = \mathbf{0} \tag{7.18}$$

7.2.3 Weak Form and Finite Element Equations

The non-linear behavior of a material can be defined by an incremental constitutive form with a tangential modulus $\mathbf{D}_\mathrm{T}$ dependent on the effective stress, $\boldsymbol{\sigma}'$, and strain, $\boldsymbol{\varepsilon}$, as follows:

$$d\boldsymbol{\sigma}' = \mathbf{D}_\mathrm{T} d\boldsymbol{\varepsilon} \tag{7.19}$$

in which

$$\boldsymbol{\varepsilon} = \nabla^T \mathbf{u} \tag{7.20}$$

where ∇^T is the differential operator defined as:

$$\nabla^T = \begin{Bmatrix} \frac{\partial}{\partial x} & 0 & 0 & \frac{\partial}{\partial y} & \frac{\partial}{\partial z} & 0 \\ 0 & \frac{\partial}{\partial y} & 0 & \frac{\partial}{\partial x} & 0 & \frac{\partial}{\partial z} \\ 0 & 0 & \frac{\partial}{\partial z} & 0 & \frac{\partial}{\partial x} & \frac{\partial}{\partial y} \end{Bmatrix} \tag{7.21}$$

The initial conditions specify the full field of displacements and water pressures at time t=0 as follows:

$$\boldsymbol{u} = \boldsymbol{u}_0,\ p = p_0 \ \text{ in } \Omega \text{ and on } \Gamma \tag{7.22}$$

where Ω is the domain of interest and Γ is its boundary. The imposed boundary displacements and water pressures are as follows:

$$\begin{aligned} \boldsymbol{u} &= \hat{\boldsymbol{u}} \quad \text{on } \Gamma_u \\ p &= \hat{p} \quad \text{on } \Gamma_p \end{aligned} \tag{7.23}$$

$$\mathbf{I}^{\mathrm{T}}\boldsymbol{\sigma} = \mathbf{t} \ \text{ on } \Gamma_u \tag{7.24}$$

$$\left[\frac{\mathbf{k}}{\mu^w}\left(-grad\ p + \rho^w \mathbf{g}\right)\right]^T \cdot \mathbf{n} = q \ \text{ on } \Gamma_p \tag{7.25}$$

where the matrix $\mathbf{I}$ is related to the unit normal vector $\mathbf{n} = \{n_x, n_y, n_z\}^{\mathrm{T}}$ by

$$\mathbf{I} = \begin{bmatrix} n_x & 0 & 0 \\ 0 & n_y & 0 \\ 0 & 0 & n_z \\ n_x & n_y & 0 \\ 0 & n_z & n_y \\ n_z & 0 & n_x \end{bmatrix} \tag{7.26}$$

The weak form is recalled from Chapter 3 and written as:

$$\int_{\Omega}\left[\left\{\bar{\boldsymbol{\varepsilon}}_u^{\,T}\boldsymbol{\sigma}-\bar{\boldsymbol{u}}^{\mathrm{T}}\,\rho\boldsymbol{g}\right\}+\left\{\bar{p}\,\frac{n}{K_w}\,\dot{p}+\bar{\boldsymbol{\varepsilon}}_p^{\,T}\,\frac{\mathbf{k}}{\mu_w}\left(-grad\ p+\rho^w\mathbf{g}\right)+\bar{p}\boldsymbol{m}^{\mathrm{T}}\,\dot{\boldsymbol{\varepsilon}}\right\}\right]d\Omega$$
$$=\int_{\Gamma_u}\bar{\boldsymbol{u}}^T\mathbf{t}\;d\Gamma+\int_{\Gamma_p}\bar{p}\;\frac{q}{\rho^w}\,d\Gamma \tag{7.27}$$

where

$$\mathbf{t}=\{t_x,t_y,t_z\}^T \tag{7.28}$$

is the surface traction vector,

$$q=\left[\rho^w\frac{\mathbf{k}}{\mu_w}\left(grad\ p-\rho\mathbf{g}\right)\right]^{\mathrm{T}}\cdot\mathbf{n}=\mathbf{v}^{\mathrm{T}}\cdot\mathbf{n} \tag{7.29}$$

is the prescribed outward flow per unit area and $\mathbf{n}=\left\{n_x\ ,n_y\ ,n_z\right\}^{\mathrm{T}}$ is a vector of direction cosines for the unit normal to Γ.

For an element with *n* displacement degrees of freedom and *m* pore pressure degrees of freedom, the spatial approximation can be defined in the form of:

$$\hat{\mathbf{u}}=\sum_i^n\mathbf{N}_{ui}\mathbf{u}_i=\mathbf{N}_u\boldsymbol{u} \tag{7.30}$$

$$\hat{p}=\sum_i^m\mathbf{N}_{pi}p_i=\mathbf{N}_p\boldsymbol{p} \tag{7.31}$$

Applying the Galerkin method to the final form of balance equations, the following finite element discrete form is obtained:

$$\mathbf{M}_s\ddot{\mathbf{u}}+\int_{\Omega}\mathbf{B}^T\boldsymbol{\sigma}'d\Omega-\mathbf{Q}\boldsymbol{p}=\boldsymbol{f}_s \tag{7.32}$$

$$\mathbf{Q}^T\dot{\mathbf{u}}+\mathbf{K}_c\mathbf{p}+\mathbf{S}\dot{\mathbf{p}}=\boldsymbol{f}_p \tag{7.33}$$

in which

$$\mathbf{M}_s\ =\ \int_{\Omega}\mathbf{N}_u^{\mathrm{T}}\rho\mathbf{N}_u\mathrm{d}\Omega \tag{7.34}$$

$$\mathbf{Q} = \int_{\Omega} \mathbf{B}_u^{\mathrm{T}} \mathbf{m} \mathbf{N}_p \mathrm{d}\Omega \tag{7.35}$$

$$\mathbf{S} = \int_{\Omega} \mathbf{N}_p^{\mathrm{T}} \frac{n}{K_w} \mathbf{N}_p \ \mathrm{d}\Omega \tag{7.36}$$

$$\mathbf{K_c} = \int_{\Omega} \mathbf{B}_p^{\mathrm{T}} \frac{\mathbf{k}}{\mu_w} \mathbf{B}_p \ \mathrm{d}\Omega \tag{7.37}$$

$$\mathbf{f}^u = \int_{\Omega} \mathbf{N}_u^{\mathrm{T}} \rho \mathbf{g} \ \mathrm{d}\Omega + \int_{\Gamma} \mathbf{N}_u^{\mathrm{T}} \mathbf{t} \ \mathrm{d}\Gamma \tag{7.38}$$

$$\mathbf{f}^p = \int_{\Omega} \mathbf{B}_p^{\mathrm{T}} \frac{\mathbf{k}}{\mu_w} \rho^w \mathbf{g} \ \mathrm{d}\Omega + \int_{\Gamma} \mathbf{N}_p^{\mathrm{T}} \frac{q^w}{\rho^w} \ \mathrm{d}\Gamma \tag{7.39}$$

where $\mathbf{M_s}$ is the mass matrix for the solid phase; $\mathbf{Q}$ is the coupling matrix; $\mathbf{S}$ is the compressibility matrix; $\mathbf{K_c}$ is the permeability (flow) matrix; $\mathbf{f}^u$ is the elemental vector of external forces, and $\mathbf{f}^p$ is the fluid supply vector.

7.3 Finite Element Modeling Procedure

7.3.1 Finite Element Mesh and Element Size

The dynamic loading of a single pile is simulated for the analysis of pile driving and wave propagation in soils using the finite element method. A precast concrete pile with a circular cross-section is chosen for this simulation. The pile is considered to be fully embedded in soil. Four-node axisymmetric quadratic displacement elements are used to represent the pile; whereas four-node, axisymmetric, biquadratic displacement and bilinear pore pressure elements are selected to represent the soil elements.

The element sizes are chosen very carefully, because in vibration analysis, choosing the right element size for the finite elements is essential to capture the motion of waves accurately. The common practice is to choose an element with a minimum length of $\lambda_s / 6$, where λ_s is the shear wavelength. The shear wavelength can be defined in terms of shear wave speed and time as follows:

$$\lambda_s = c_s \Delta t \tag{7.40}$$

with

$$c_S = \sqrt{\frac{G}{\rho - n\rho_w}} \tag{7.41}$$

where c_s is the shear wave velocity, Δt is the time step, G is the Lamé's constant, n is the porosity, ρ and ρ_w are the densities of saturated soil and water, respectively. The element sizes are selected based on the material properties in the numerical applications. The finite element model used for this study is shown in Figure 7.3. The detail views of the axis of symmetry and the pile tip are shown in Figure 7.4.

7.3.2 Analytical Rigid Surface

In an axisymmetric finite element model, to allow the penetration of the pile into the soil, the defined nodes on the axis of symmetry should be set free of constraints. To remove those constraints and allow the soil nodes at the contact to slide on the surface of the pile elements, it is suggested to define an analytical rigid surface 1 mm away from the axis of symmetry as shown in Figure 7.7. This modeling technique allows is introduced as a rigid tube in an earlier study (Hügel, et al., 2008). The rigid analytical surface that is available in ABAQUS, is in frictionless contact with the pile and soil elements. This technique allows the pile to slide over the rigid surface, and the soil elements to separate from this surface during the penetration of the pile.

7.3.3 Artificial Non-Reflecting Boundary

In the analysis of stress wave propagation in soils due to pile driving, the reflection of waves from the far boundary causes significant problems. When these waves bounce back from the boundary, they mix with the progressing waves. Thus, the magnitudes of the waves calculated by the FE package become inaccurate. To minimize the effect of reflecting waves on the results, one of the options is to define a sufficiently

long finite element mesh. A longer mesh will be time consuming and it is difficult to determine whether the mesh is sufficiently long.

Another option would be the use of infinite elements as boundary elements to minimize or prevent the reflection of stress waves in the finite elements. A finite element mesh of finite end infinite elements representing soil, pile and the far field is shown in Figure 7.1. However, the use of infinite elements brings significant difficulties by itself when defining the geostatic step in the dynamic soil analysis. It is because static forces such as the self-weight of soil cannot be applied on infinite elements, because the formulation of the damper is based on the resistance to velocity, not displacement. When static forces are applied to establish an equilibrium state, the relative displacement of finite elements with respect to infinite elements becomes excessive resulting in inaccurate results as shown in Figure 7.2.

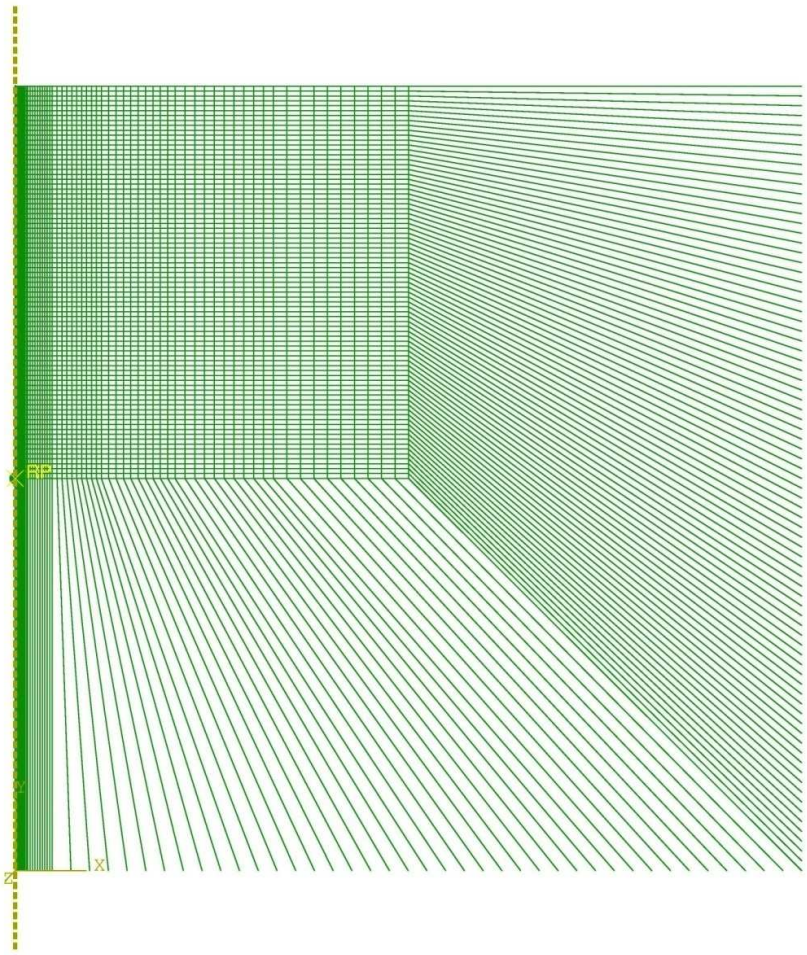

Figure 7.2 The finite element mesh of soil and pile combined with infinite element.

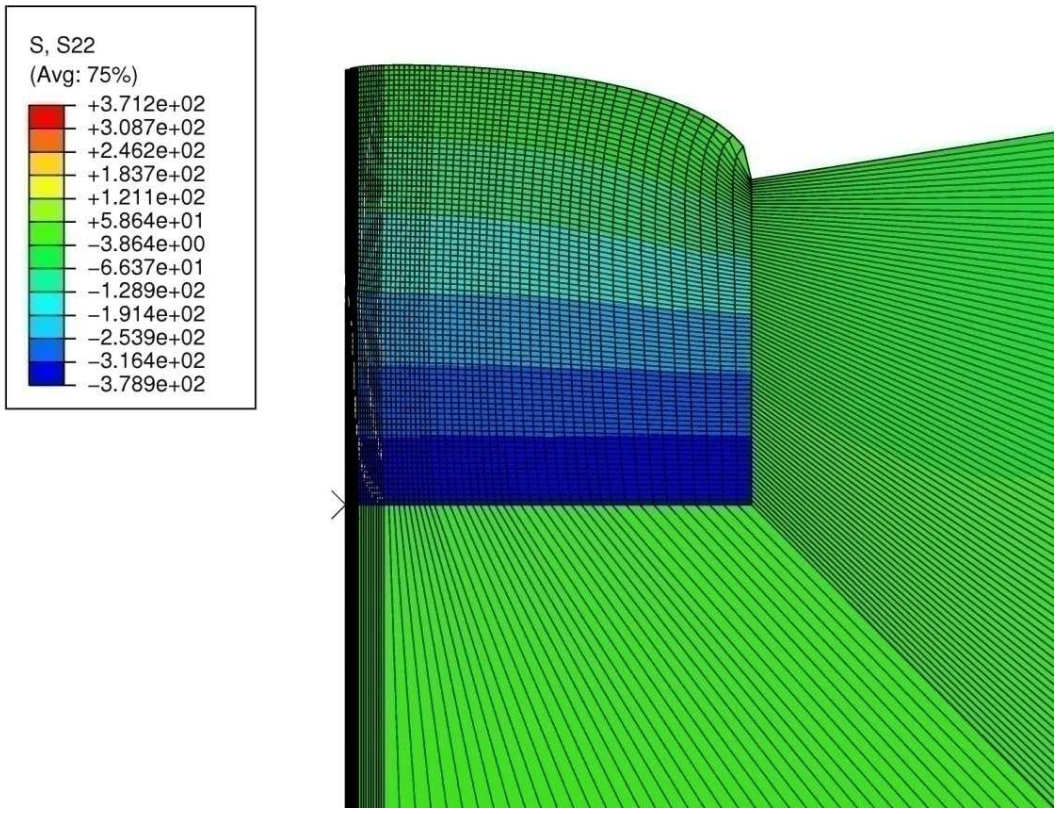

Figure 7.3 The excessive relative displacement of finite elements after geostatic loading.

Another alternative to damp out the excessive vibrations in a finite element model is to define an artificial boundary which damps out the entering waves and acts like a dashpot systems. Such an artificial boundary which was previously introduced in the literature (Liu, et al., 2003) aims to minimize the reflection of stress waves from the far boundary. A modified version of this technique is implemented in our finite element model to avoid the wave-reflection problem. For the implementation, a region in 50 m width is added to the far end of the model. This region is divided into five sections with varying damping ratios as shown in Figure 7.8. The damping ratios are defined as gradually increasing from the first section to the last one. The procedure to determine the damping parameters is as follows:

1. Run the analysis without any artificial boundary condition.
2. Obtain time history of the vertical velocity magnitudes for the furthest node on the surface of the model before entering the artificial boundary.
3. Find velocity magnitudes in the frequency domain using the Fast Fourier Transform (FFT) algorithm. Obtain two frequency values for the motion.
4. Set the damping ratio, ζ=0.7 and ζ=0.8. Find Rayleigh damping factors α and β, substituting the frequency values found in Step 3 into the equation below:

$$\zeta = \frac{1}{2}\left[\frac{\alpha}{\omega} + \beta\omega\right] \text{ with } \omega = 2\pi f$$

where ζ is the damping ratio, α is the mass-proportional Rayleigh damping factor, β is the stiffness-proportional Rayleigh damping factor, ω is the cyclic frequency and f is the frequency of the motion.

5. Define gradually increasing α and β values for each section using the linear interpolation method.

Using this procedure, α and β are chosen for different sections as shown in Table 7.3. To test the artificial boundary, the contour plots of the vertical velocities are plotted

at different times with and without the artificial boundary in Figure 7.4. It is observed that the waves bounce back from the boundary in the regular model. However, in the model with the artificial boundary, the waves dissipate gradually and only a very small portion of waves reflect.

Table 7.1 The Rayleigh damping factors α and β for different sections

Section Name	α (1/s)	β (s)
S1	0.5	5.0×10^{-4}
S2	1.0	5.0×10^{-3}
S3	5.0	5.0×10^{-3}
S4	15	10×10^{-3}
S5	20	20×10^{-3}

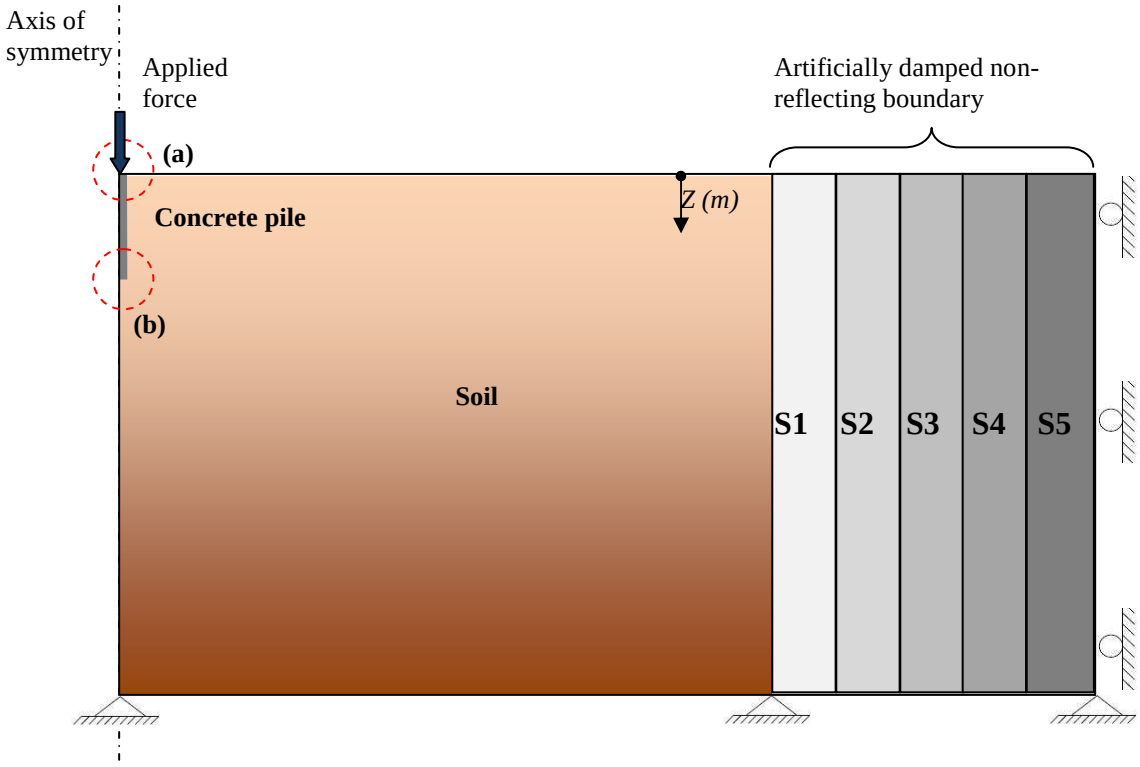

Figure 7.4 Schematics of the finite element model.

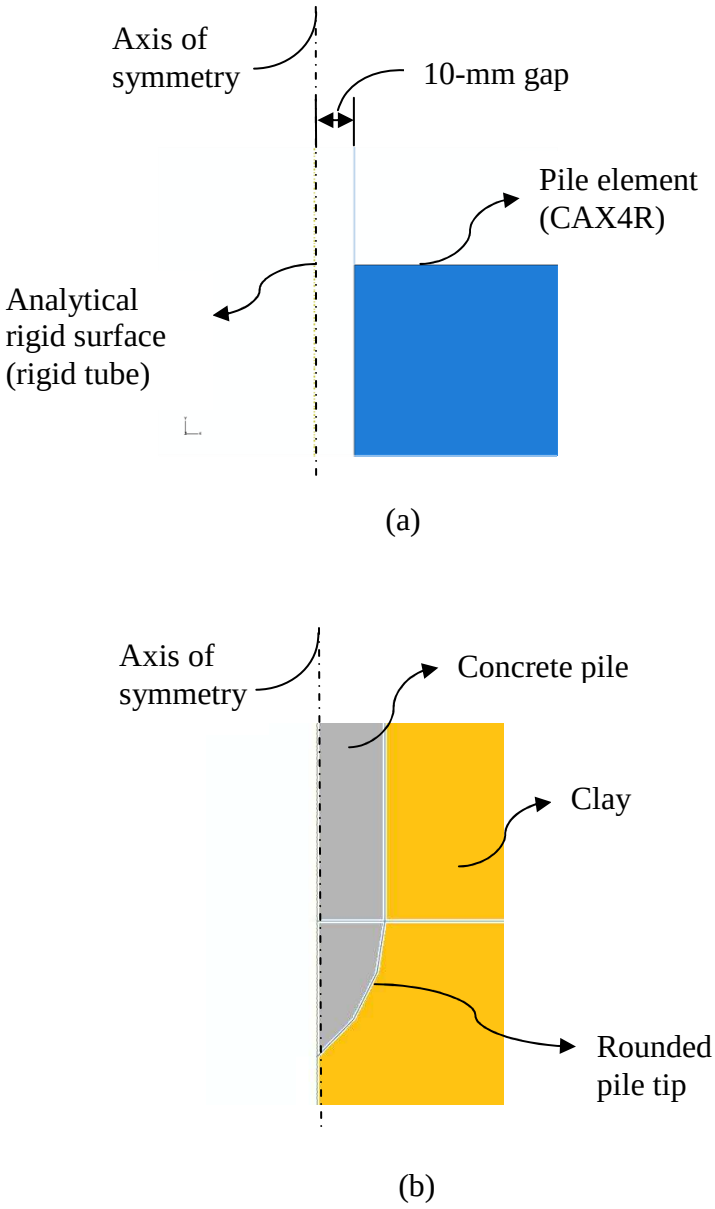

Figure 7.5 The detailed views of (a) the analytical rigid surface and (b) the round pile tip.

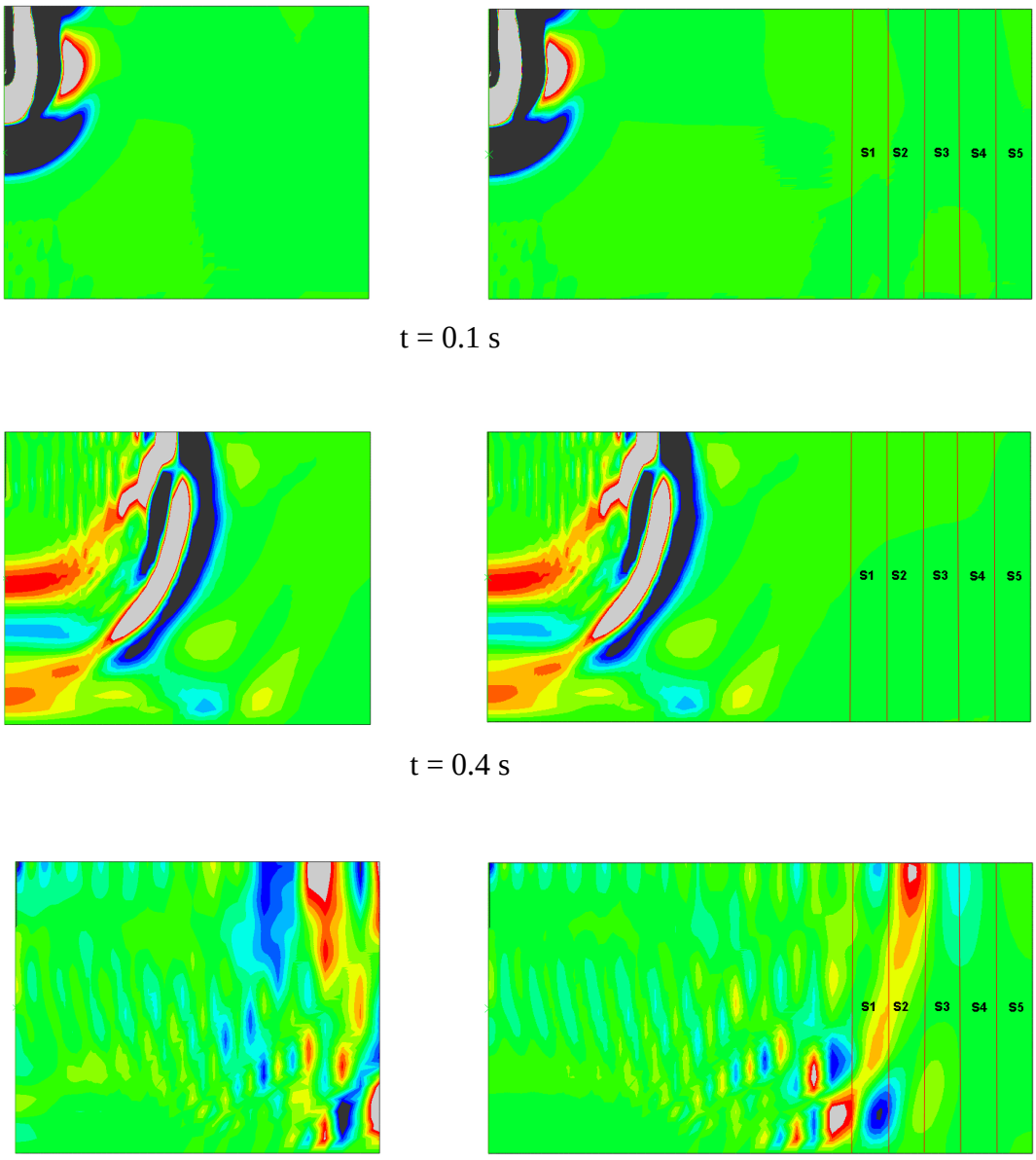

Figure 7.6 The contour plots of vertical velocities in (a) the original model and (b) the model with artificial non-reflecting boundary.

7.3.4 Constitutive Law

A modified version of the Mohr-Coulomb elasto-plastic constitutive model, which is available in ABAQUS is assumed to describe the behavior of soils in this chapter. The Mohr-Coulomb model in ABAQUS is an extension of the classical Mohr-Coulomb failure criterion based on the work of Menétrey and Williams (1995). The detailed description of this model is explained in Chapter 5.

7.3.5 Solution Procedure

The finite element software ABAQUS offers two direct integration methods for the solution of non-linear dynamic problems. These are the implicit and the explicit methods that are used for linear and nonlinear problems. In this study, the implicit time integration method is chosen because the solution of transient analysis of soils in ABAQUS can only be obtained using the implicit method (ABAQUS Manual, 2008). The implicit method uses a fixed or automatic time increment based on the Newton-Raphson iteration scheme for the solution of non-linear problems. The internal element forces before and after each time increment are computed using the dynamic equilibrium. The solution for the nodal accelerations is determined with iteration as opposed to advancing the kinematic state from the previous one in the explicit method.

The general direct-integration method provided in Abaqus/Standard, called the Hilber-Hughes-Taylor operator, is an extension of the trapezoidal rule. The Hilber-Hughes-Taylor operator is implicit which means the integration operator matrix must be inverted, and a set of simultaneous nonlinear dynamic equilibrium equations must be solved at each time increment. This solution is done iteratively using Newton's method. The principal advantage of the Hilber-Hughes-Taylor operator is that it is unconditionally stable for linear systems; there is no mathematical limit on the size of the time increment that can be used to integrate a linear system. An unconditionally stable integration operator is of great value when studying structural systems because a conditionally stable

integration operator can lead to impractically small time steps and, therefore, a computationally expensive analysis.

The implicit time integration procedure uses an automatic increment strategy based on the success rate of a full Newton iterative solution method as follows:

$$\Delta \mathbf{u}_{n+1} = \Delta \mathbf{u}_n + \mathbf{K}_t^{-1} \cdot (\mathbf{F}_n - \mathbf{I}_n) \tag{7.50}$$

where $\mathbf{K}_t$ is the current tangent stiffness matrix, **F** is the applied load vector, **I** is the internal force vector, and $\Delta \mathbf{u}$ is the increment of displacement. The subscripts *n and n*+1 indicate the step orders at time steps t_n and t_{n+1}. For an implicit dynamic procedure, the algorithm is defined as:

$$\mathbf{M}\ddot{\mathbf{u}}_{n+1} + (1+\alpha)\mathbf{K}\mathbf{u}_{n+1} - \alpha \mathbf{K}\mathbf{u}_n = \mathbf{F}_{n+1} \tag{7.51}$$

where **M** is the mass matrix, **K** is the stiffness matrix, **F** is the vector of applied loads and **u** is the displacement vector. The approximations for the displacement and velocity vectors can be written as follows:

$$\mathbf{u}_{n+1} = \mathbf{u}_n + \Delta t \dot{\mathbf{u}}_n + \Delta t^2 \left[\left(\frac{1}{2} - \beta \right) \ddot{\mathbf{u}}_n + \beta \ddot{\mathbf{u}}_{n+1} \right] \tag{7.52}$$

and

$$\dot{\mathbf{u}}_{n+1} = \dot{\mathbf{u}}_n + \Delta t \left[(1-\gamma) \ddot{\mathbf{u}}_n + \gamma \ddot{\mathbf{u}}_{n+1} \right] \tag{7.53}$$

with the parameters

$$\beta = \frac{1}{4}(1-\alpha^2), \quad \gamma = \frac{1}{2} - \alpha, \quad -\frac{1}{3} \le \alpha \le 0 \tag{7.54}$$

where α=-0.05 is chosen by default in ABAQUS as a small damping term to quickly remove the high frequency noise without having a significant effect on the meaningful, lower frequency response.

An automatic incrementing scheme is provided for use with the general implicit dynamic integration method. The scheme uses a half-step residual control to ensure an accurate dynamic solution. The half-step residual is the equilibrium residual error (out-of-

balance forces) halfway through a time increment. This half-step residual check is the basis of the adaptive time incrementing scheme. If the half-step residual is small, it indicates that the accuracy of the solution is high and that the time step can be increased safely. On the other hand, if the half-step residual is large, the time step used in the solution should be reduced.

7.4 Numerical Applications

7.4.1 Pile Driving Problem of Ramshaw et al.

This problem consists of finite element analysis of a dynamically loaded bored-in-situ pile which was tested on a site near Manchester, UK. The original problem has been studied earlier by Ramshaw and her colleagues (1998). The length of the pile is 21 m and diameter is 750 mm. A 2.2 ton hammer was dropped on to the built up instrument head of the piles from a height of 1.2 m. The soil is modeled with pore pressure elements and considered as linear elastic. The subsurface soil consists of two layers. The top soil layer (depth<10.5 m) consists of firm to stiff silty clay. The modulus of elasticity E, Poisson's ratio v and mass density ρ of soil in this layer are 26×10^6 Pa, 0.35 and 1,970 kg/m^3, respectively. The modulus of elasticity E, Poisson's ratio v and mass density ρ of soil in the second layer (depth>10.5 m) are 50×10^6 Pa, 0.35 and 2,100 kg/m^3, respectively. The pile is modeled with solid elements and considered as linear elastic with a modulus of elasticity E=30×10^9Pa, Poisson's ratio υ=0.20 and a bulk unit density of 2,500 kg/m^3. The material properties of the soil layers and the pile are given in Table 7.1.

The finite element mesh shown in Figure 7.5 is generated using *ABAQUS/Standard*. A two-dimensional axisymmetric finite element model consisting of four-noded elements is used for the analysis of the problem. Four-node axisymmetric, quadratic displacement elements (CAX4) are used to model the pile. Four-node axisymmetric biquadratic displacement and bilinear pore pressure elements (CAX4P) elements are used to model the soil. The dimensions of the whole model are selected as a

width of 50 times *D* and a height of 55 times *D*. The boundary conditions consist of restricting both horizontal and vertical movement at the bottom of the mesh, and the horizontal movement at the right side of the mesh. A rigid analytical surface is defined 1.0 mm away from the axis of symmetry. The horizontal and vertical movement of this surface is restricted. Non-reflecting boundary elements consisting of high material damping characteristics are defined for the last five columns of elements at the right hand side of the mesh. The contact pairs for the soil-pile interface are represented by a master-slave algorithm. The impact load which is applied on the top of the pile is defined by a forcing function representing a single hammer blow (Ramshaw, et al., 1998). The forcing function applied on the pile head is shown in Figure 7.6.

The initial stresses are specified for particular nodes or elements, as appropriate. The only initial condition defined in this problem is the initial values of the void ratio, e_o, at the nodes of the soil skeleton. The initial void ratio $e_o = 0.5$ is defined for all nodes. The equilibrium of the initial state requires establishment of the initial stresses. It is important to establish the initial stresses correctly. The applied loads and initial stresses should exactly equilibrate and produce zero deformations. The initial stresses defined for this problem are: (1) the initial pore pressure, *p*, and (2) the initial effective stresses, σ'. The variation of pore pressure and initial effective stress are shown in Figure 7.7.

The reason for choosing this numerical application is to validate the proposed finite element model with published data. Figure 7.8 shows the variation of radial velocity with time at a distance of 5.5 m from the source of vibration. The peak magnitude is calculated as 6.29 mm/s at 0.10 s, whereas the measured peak velocity is approximately 8.0 mm/s. The published data (Ramshaw, et al., 1998) showed a peak radial velocity of approximately 12.0 mm/s. This model did not include the friction between the pile and the soil, and the self-weight of the soil. The difference between the present and the published results can be explained by use of soil-pile interface modeling. Published data shows that at about 0.3 s, the radial velocities almost dissipate, however,

after 0.4 s, the radial velocities increase again. This is not monitored in the measured data. The present work agrees with the measured data. The use of non-reflecting boundary conditions enabled to model the soil elements with high damping ratios in the far field. Hence, the present work shows that the ground vibrations dissipate after 0.4 s agreeing with the measured data. The radial velocities obtained on the ground surface at 16.5 m from the pile are shown in Figure 7.9. The peak radial velocity is computed as 2.3 mm/s at about 0.3 s. The measured data shows that the peak velocity is around 2.0 mm/s which is consistent with the result of the present work. However, the published data computed the peak radial velocities at about 5.0 mm/s. This is due to the use of special non-reflecting artificial boundary conditions in the present model which takes into account the material damping in the soil in the far field. In conclusion, the use of soil-pile interface model and non-reflecting boundary conditions enabled (1) to avoid overestimating the peak radial velocities, (2) to model the ground vibrations with a high precision in the far field.

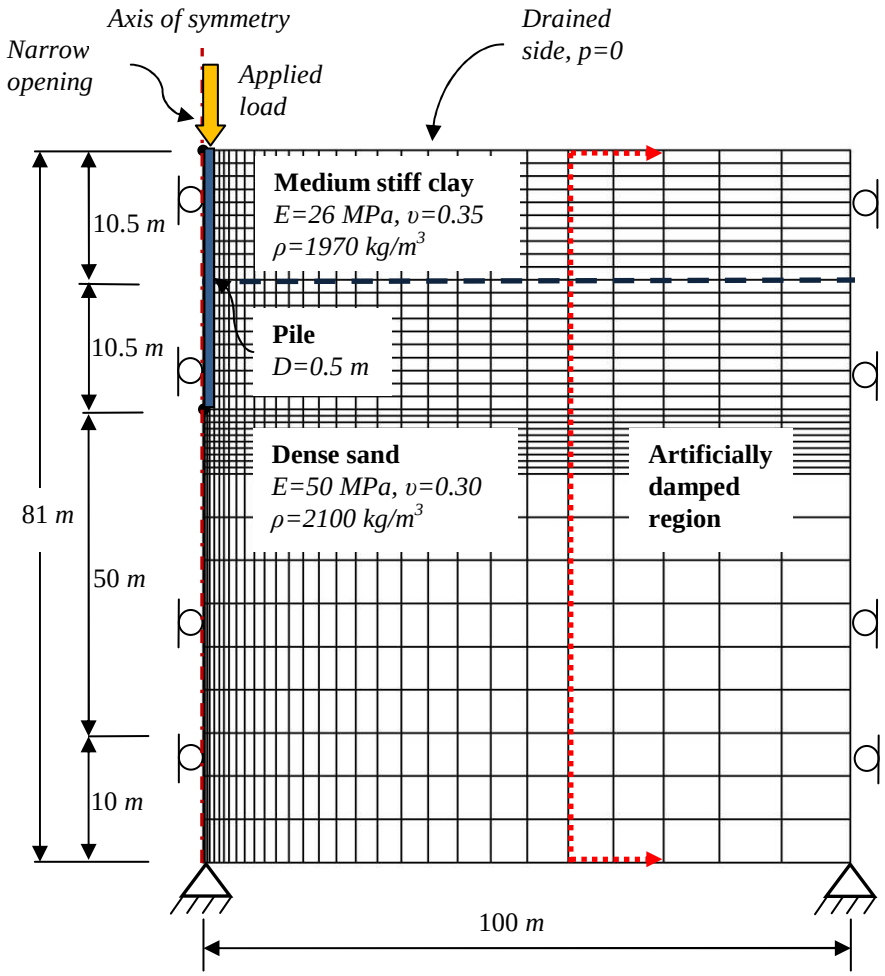

Figure 7.7 The finite element mesh of the model.

Table 7.2 Material properties of the soil and the pile

Material Parameter	Notation	Value	Units
Soil			
Medium Stiff Clay Layer			
Modulus of elasticity	E	26.0×10^3	kN/m^2
Poisson's ratio	v	0.35	-
Dry Density	ρ_{dry}	1970	kg/m^3
Dense Sand Layer			
Modulus of elasticity	E	50.0×10^3	kN/m^2
Poisson's ratio	v	0.30	-
Dry Density	ρ_{dry}	2100	kg/m^3
Pile			
Modulus of elasticity	E	30.0×10^6	kN/m^2
Poisson's ratio	v	0.20	-
Dry Density	ρ_{dry}	2500	kg/m^3

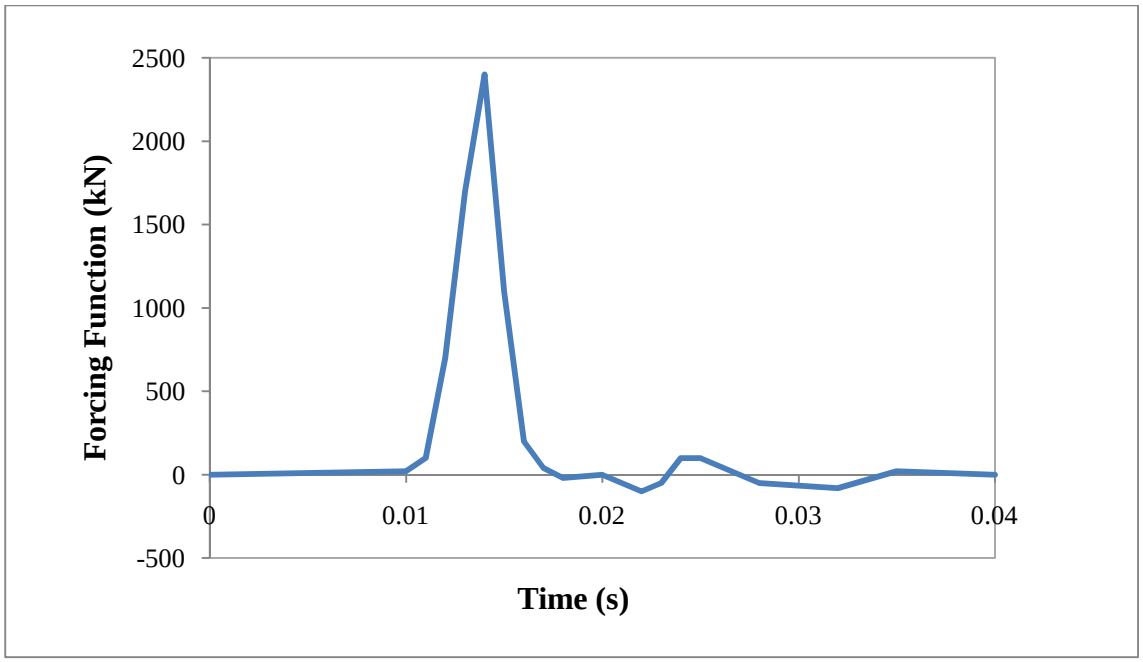

Figure 7.8 The forcing function applied on the pile head.

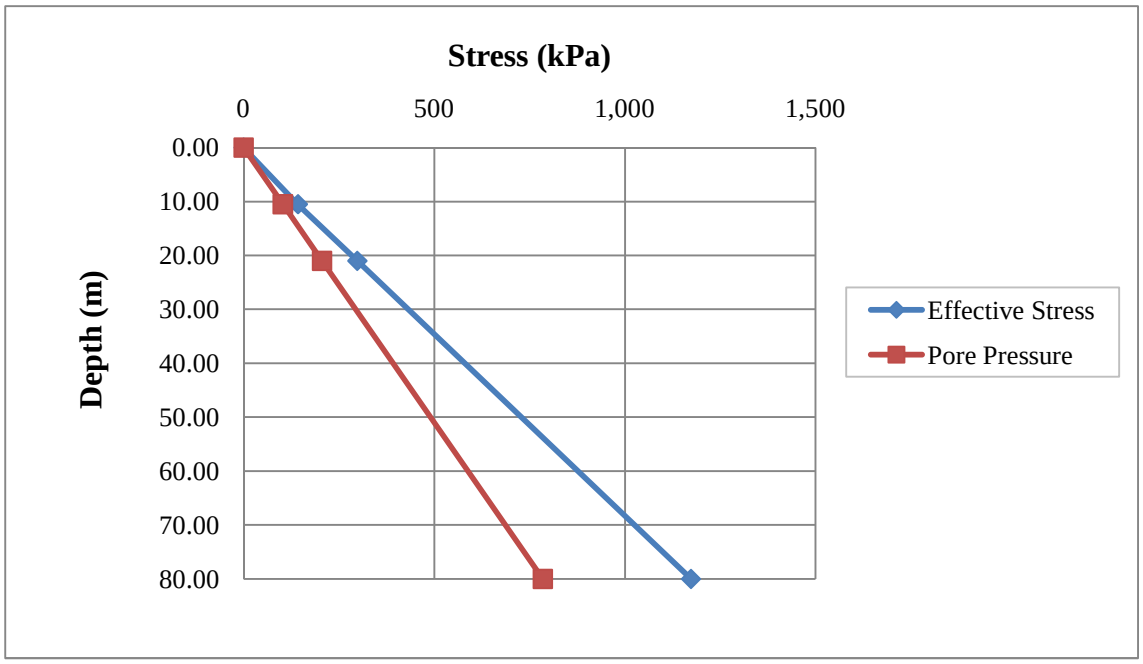

Figure 7.9 The effective stress and pore pressure distribution in soil at initial state.

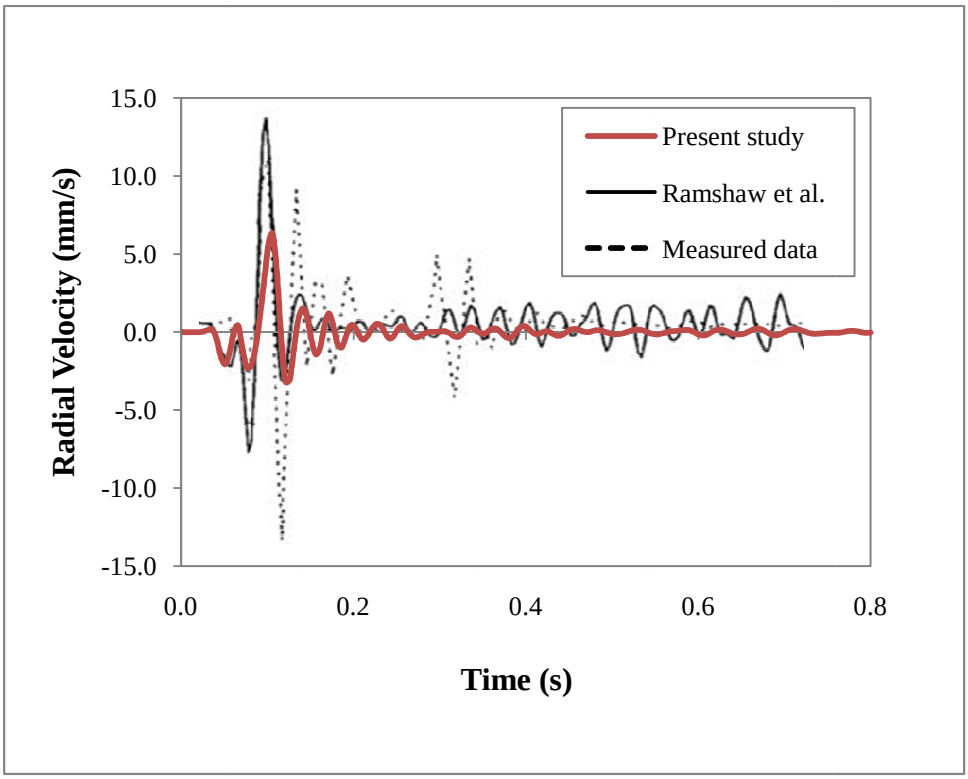

Figure 7.10 Radial velocity at a distance of 5.5 m from the source.

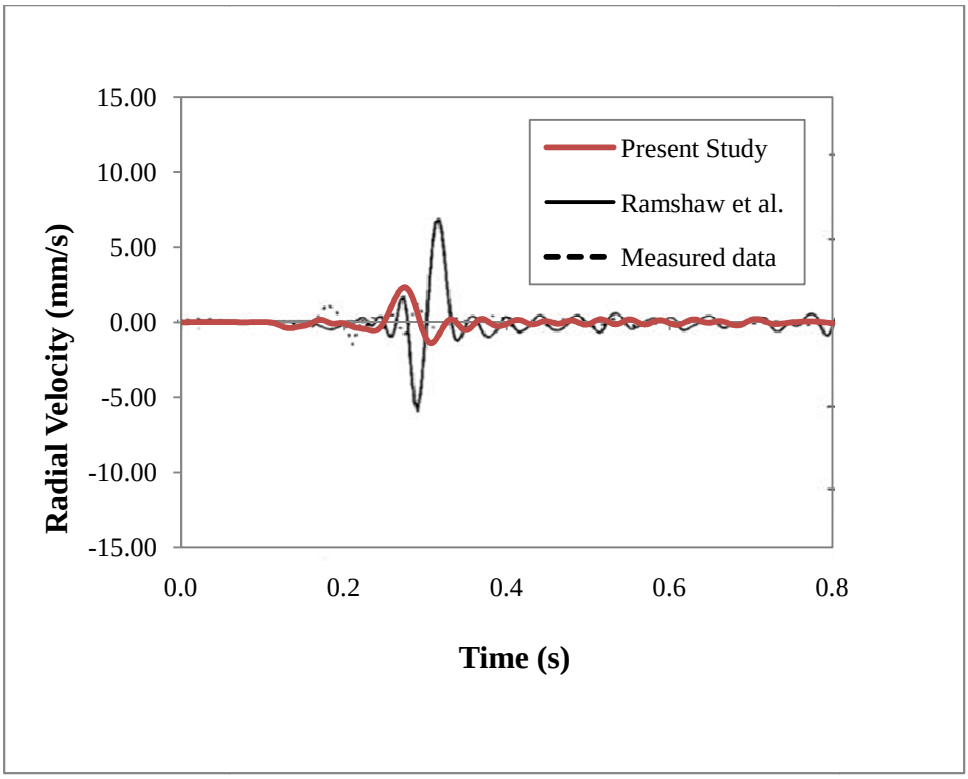

Figure 7.11 Radial velocity at a distance of 16.5 m from the source.

7.4.2 Pile Driving Problem of Mabsout et al.

This problem involves finite element analysis of a pre-bored pile based on the work of from the work of Mabsout et al (1995). The pile is considered as close-end, round, and concrete with a canonical tip. It is driven through undrained, nearly incompressible, normally consolidated clayey soil. The pile is 20 m in length and 0.25 m in diameter. The pre-bored pile is installed at penetration depth of 18 m. The finite element method is used to discretize the pile-soil interaction problem. The mesh consists of four-node axisymmetric bilinear displacement elements with reduced integration (CAX4R) for modeling the pile, and 4-node axisymmetric bilinear displacement/pore-pressure elements with reduced integration (CAX4RP) for modeling the soil. The finite element mesh is shown in Figure 7.10. The tip of the pile is designed as a parabolic shape with the radius to tip height ratio of ½. The modulus of elasticity of the concrete pile is $E_c = 24.8\times10^6$ kPa with a Poisson's ratio of ν=0.2. The density of the concrete is $\rho_c = 2400$ kg/m^3. The soil parameters are chosen to represent normally consolidated clay. The modulus of elasticity of the clay is $E_s = 1060(Z)$ kPa where Z is the depth in meters. The Poisson's ratio is ν=0.2. The dry density of the clay is $\rho_s = 1595$ kg/m^3. The soil and pile parameters are listed on Table 7.2. A forcing function representing a single hammer blow is applied on top of the pile. Figure 7.11 shows the force function applied on the pile head with time.

The boundary conditions consist of restricting the horizontal and vertical movements at the base of the mesh and horizontal movements at the right side of the mesh. An analytical rigid surface is defined 1 mm away from the axis of symmetry to avoid over constraints on the soil elements along the axis of symmetry. The soil-pile interface is modeled using the master-slave algorithm. The initial void ratio is defined as e_o = 0.63 for all nodes. The initial stresses defined for this problem are the initial pore pressure, *p*, and the initial effective stresses, σ'. The variation of pore pressure and initial effective stress are shown in Figure 7.12.

Figure 7.17 shows the displacement at the pile head during a period of 0.10 s. The displacement at the pile top computed as 40 mm which is consistent with the published data (Mabsout, et al., 1995). The variation of vertical velocity at the pile top is shown in Figure 7.18. The peak velocity is calculated as 1900 mm/s. The published data presented a velocity of around 1800 mm/s. The time history of acceleration at the pile top is shown in Figure 7.19. The peak acceleration is calculated as 600×10^3 mm/s^2. The published data showed a peak acceleration of around 600×10^3 mm/s^2. The patterns of the velocity and acceleration graphs are found to be consistent with the present work. This numerical application enabled to validate the proposed nonlinear finite element model, which leads to study ground vibrations with a higher level of confidence in the next sections.

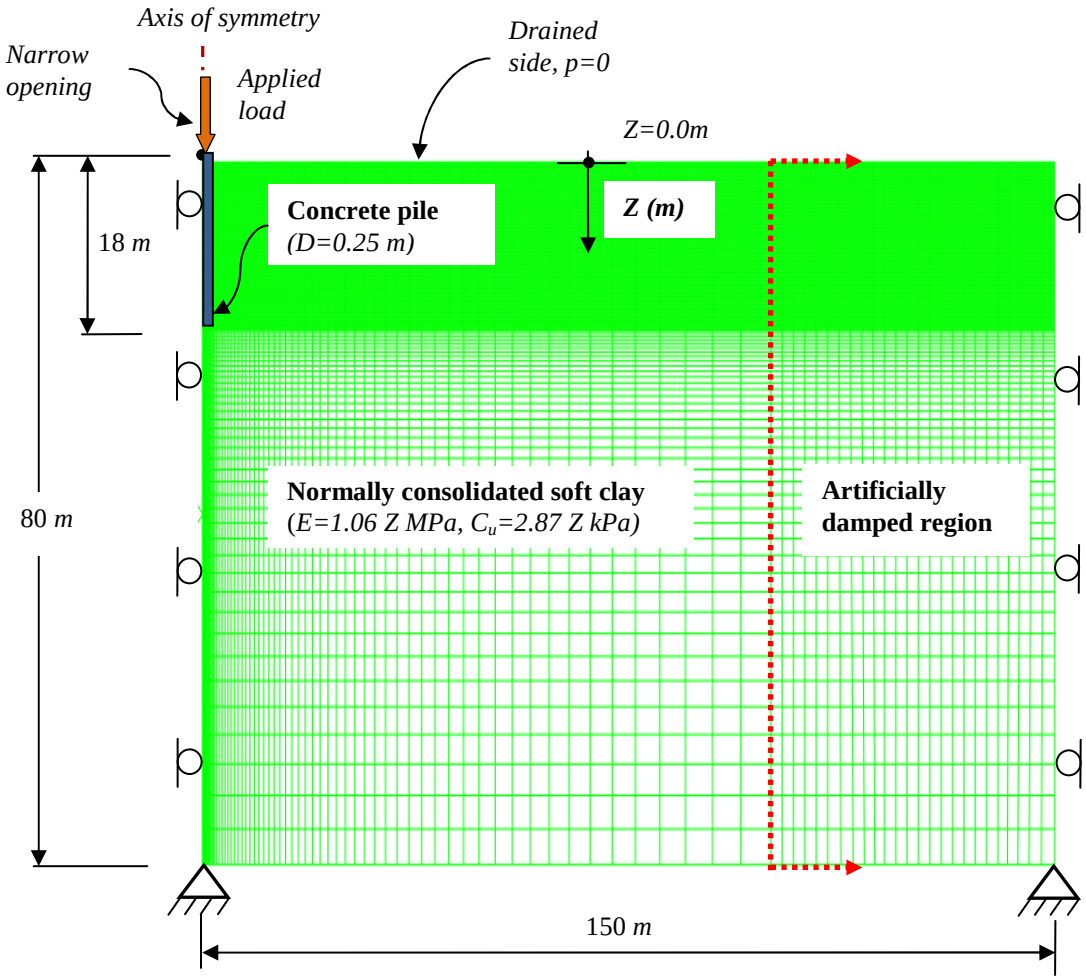

Figure 7.12 The finite element mesh.

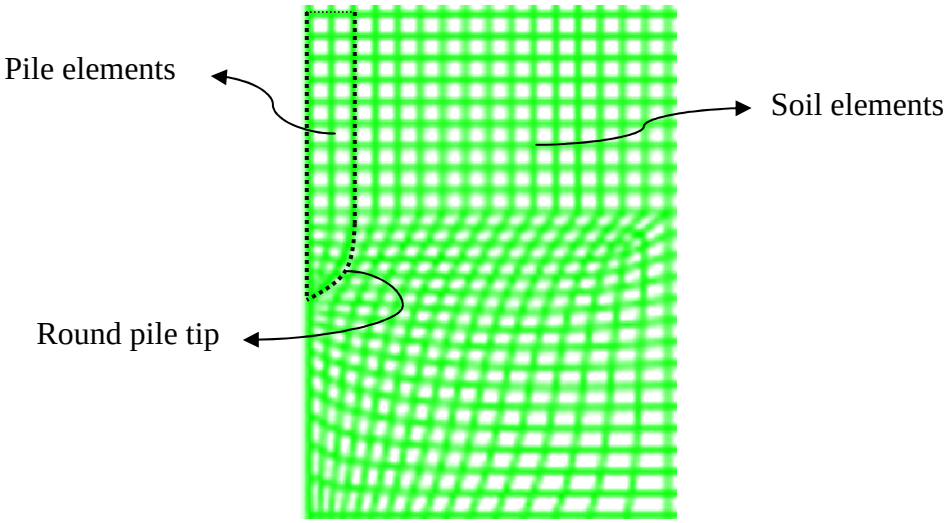

Figure 7.13 The detail view of the pile tip.

Table 7.3 Material properties of the clay and the pile

Material Parameters	Notation	Value	Units
Normally consolidated clay			
Modulus of elasticity	E	1.07×10^{3} Z	kN/m^2
Poisson's ratio	v	0.30	-
Dry Density	ρ_{dry}	1600	kg/m^3
Undrained cohesion	c_u	2.87 Z	kN/m^2
Angle of internal friction	ϕ	6	^{o}
Coefficient of friction	μ	0.10	^{o}
Pile			
Modulus of elasticity	E	24.8×10^{6}	kN/m^2
Poisson's ratio	v	0.20	-
Dry Density	ρ_{dry}	2400	kg/m^3

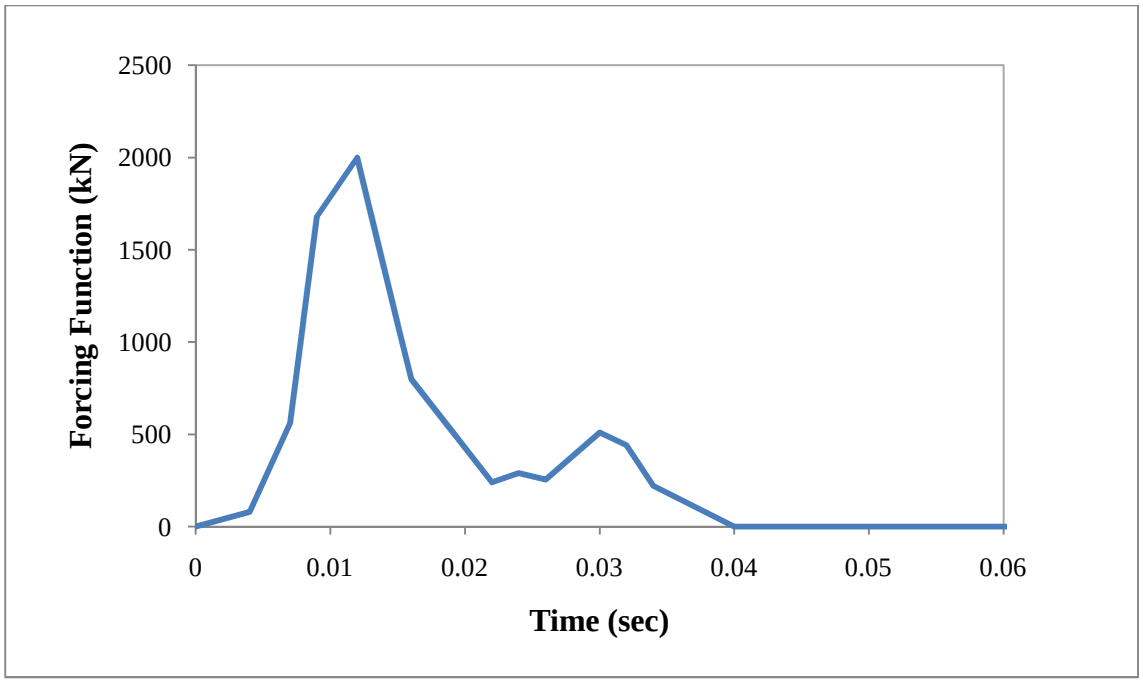

Figure 7.14 The forcing function applied on the pile head.

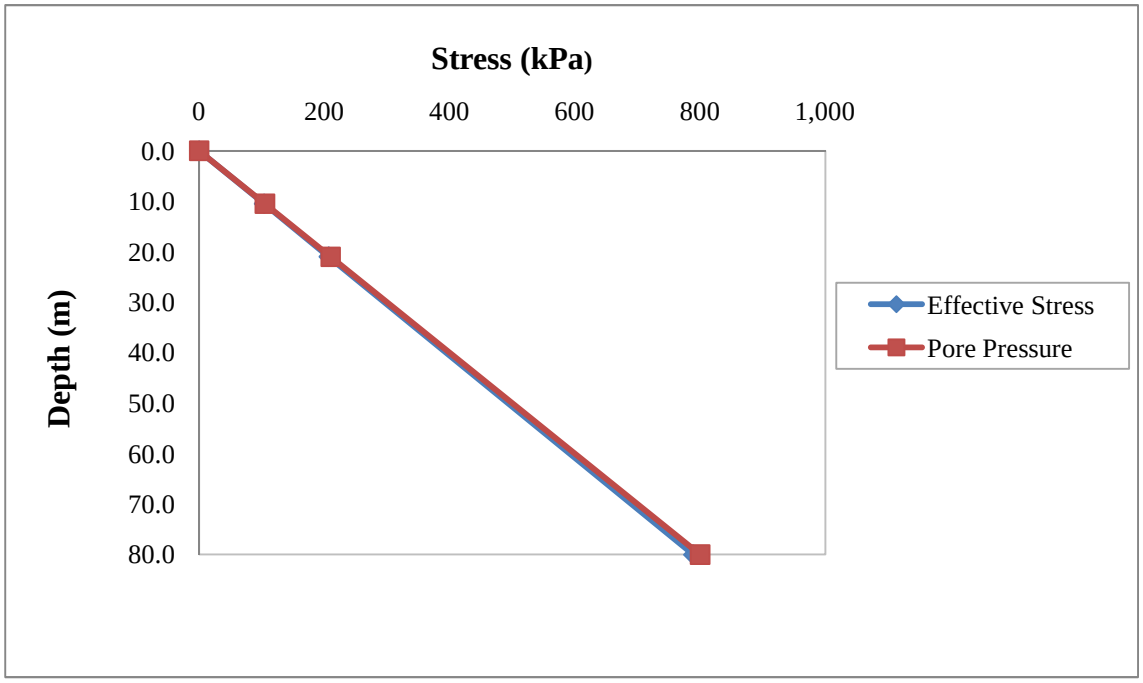

Figure 7.15 The effective stress and pore pressure distribution in soil at initial state.

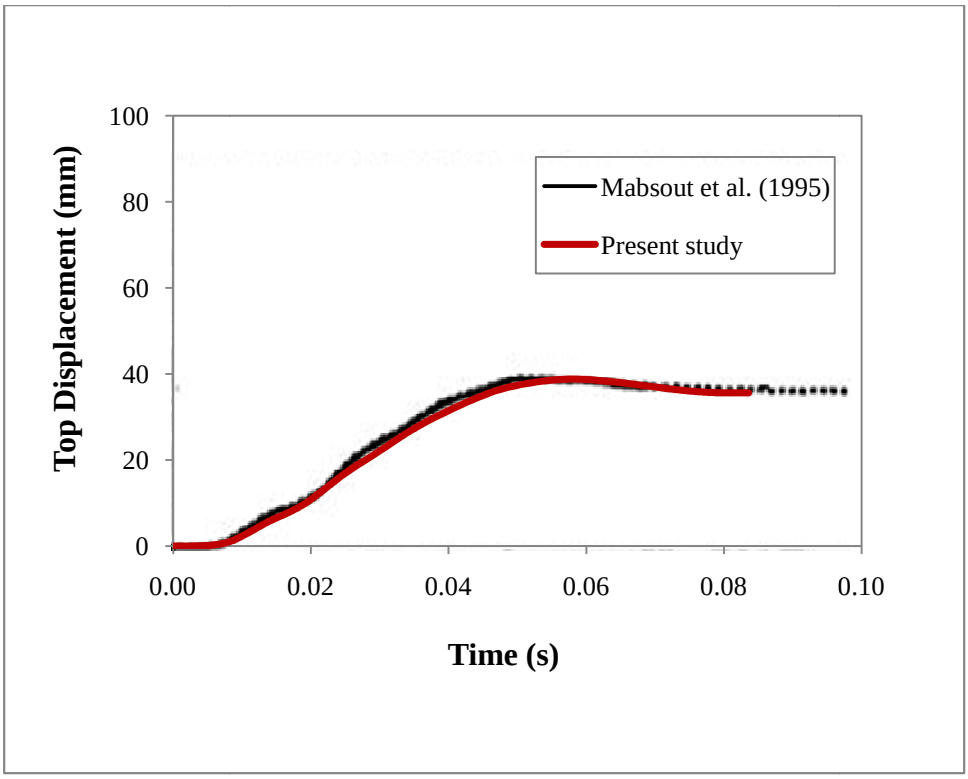

Figure 7.16 Displacement at pile top.

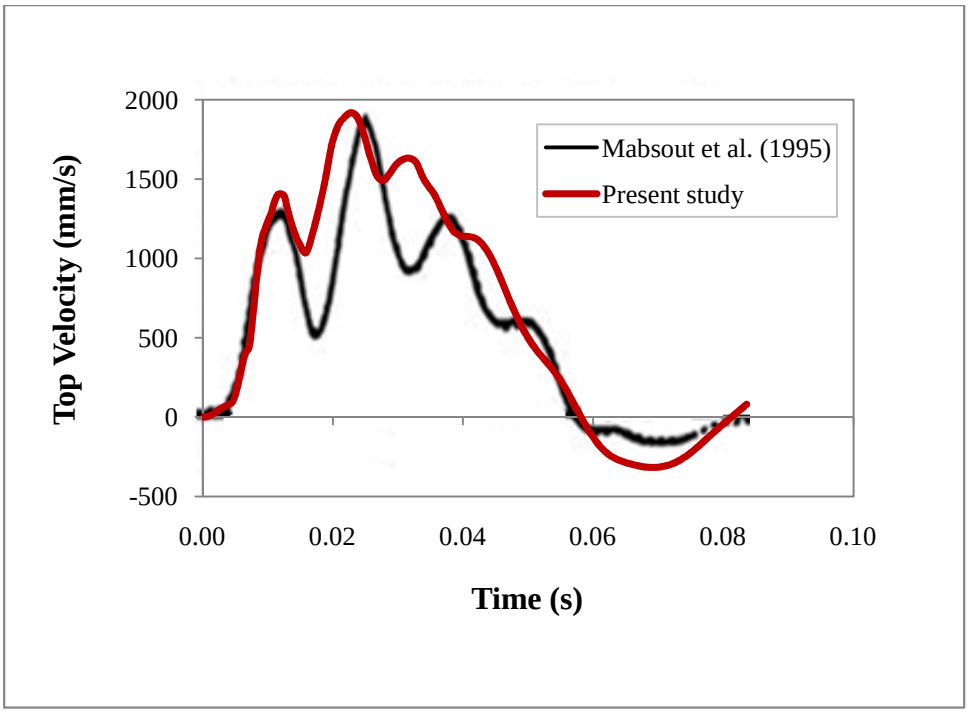

Figure 7.17 Velocity at pile top.

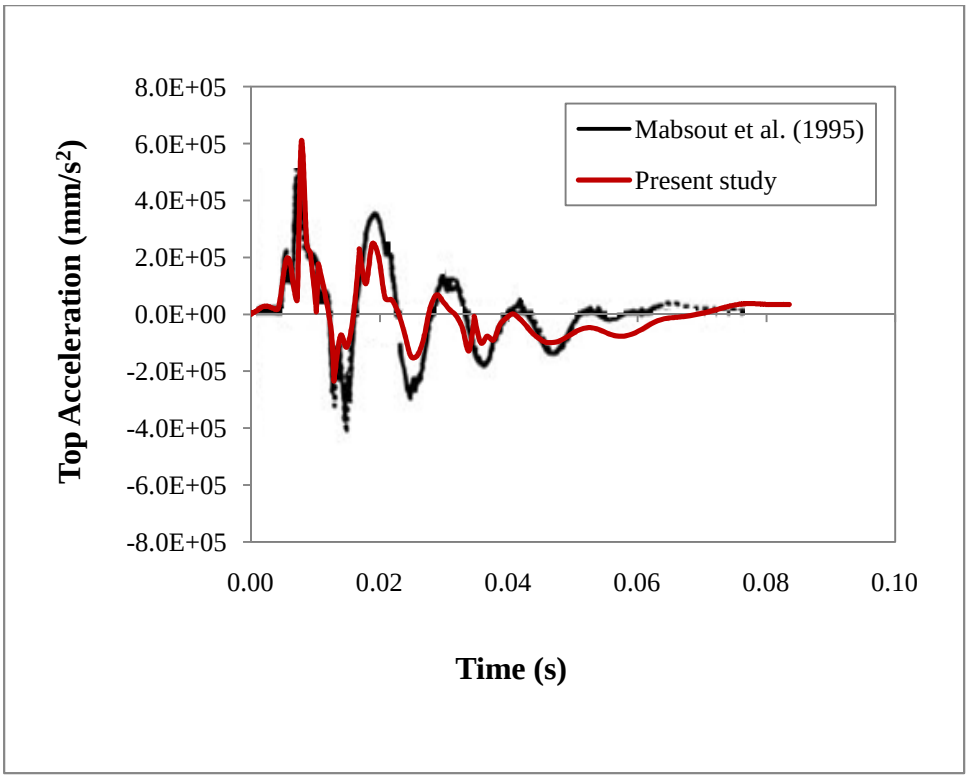

Figure 7.18 Acceleration at pile top.

7.5 Analysis of Ground Vibrations in Soils

The amplitudes of ground vibrations during pile driving are dependent on the soil and source (pile and hammer) parameters. More specifically,(1) the soil type, (2) the pile embedment length and (3) the released hammer energy have significant effects on the transmission of ground vibrations in the soil. The selection of these parameters is the key to the success of a numerical model to predict accurate and reliable vibration records. In this section, the characteristics of the ground vibrations are discussed with numerical applications. The effects of three parameters are explained in the following subsections.

The ground vibrations generated by pile driving are analyzed using the data in the second numerical application (Section 7.4.1). The contour plot of the radial, vertical and resultant velocities in the soil is shown in Figure 7.18. The contour plot for the radial velocities shows spherical wave fronts that are originated from the pile toe. These waves are characterized as P-waves. In the vertical velocities plot, it is noticed that cylindrical wave fronts are transmitted along the pile shaft. These types of waves are characterized as S-waves. The surface waves are also shown in the contour plots.

Following results can be drawn from the finite element results shown by the contour plots: (1) body waves dominate around the pile toe and propagate on a spherical wave front; (2) vertically polarized shear waves dominate around the pile and propagate in a radial path on a cylindrically wave front; and (3) Rayleigh waves propagate on the top surface less rapidly than the shear waves.

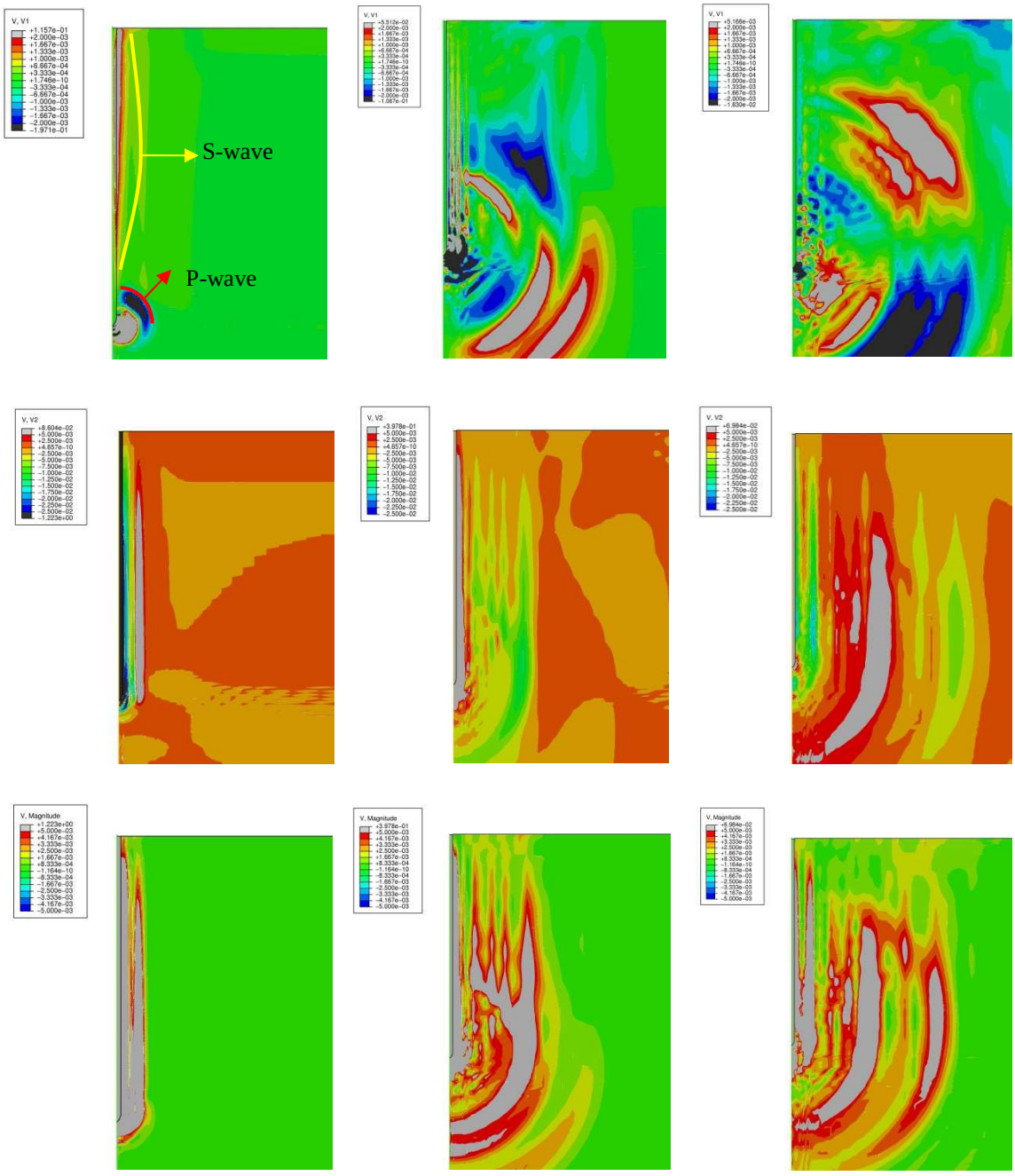

Figure 7.19 The contour plot of radial, vertical and resultant velocities in clay at time steps (a) t = 10 ms, (b) 50 ms, and (c) 100 ms.

7.5.1 Effect of Soil Properties

Five different soil types consisting of loose sand, dense sand, soft clay, medium stiff clay and stiff clay are defined in the finite element model to assess the effect of soil strength on the ground vibrations. The dimensions and pile parameters remain same as in the second numerical example. The modulus of elasticity and the cohesion of the clays defined as increasing with the depth of the soil. The material parameters for different types of sands and clays are shown in Tables 7.4 and 7.5, respectively.

The peak particle velocities (PPVs) versus distance from the pile are plotted for different types of sands –loose and dense- and clays –soft, medium dense and stiff- as shown in Figure 7.20. The loose sand has the greatest PPV with a magnitude of around 11.0 mm/s followed by the dense sand with a PPV of 4.0 mm/s. It can be monitored in Figure 7.20 that the PPVs after 18 m are highest in soft clay, then medium stiff clay and then the stiff clay. In soft clay, the maximum PPV is monitored at a distance of 9 m from the pile as 2.70 mm/s. In medium stiff clay, the maximum PPV is 2.26 mm/s at a distance of 9 m from the pile. In stiff clay, the maximum PPV is 2.73 mm/s at 9 m from the pile.

The radial velocities are higher in the stiff clay compared to the soft clay as shown in Figure 7.21. Although, the stress waves travel faster in the stiff clay, vibrations generated on the ground surface have the highest amplitudes in the soft clay. The reason is in the stiff clay the compression waves, P-waves, encounter the ground surface within a shorter period of time compared to the P-waves in the soft clay. This conclusion can be drawn by analyzing the time history of the radial velocities at 9 m from the pile for soft and stiff clays as shown in Figures 7.22 and 7.23, respectively. In soft clay, the first two peak points represent the shear wave, S-wave, traveling from the shaft, and the third peak point represents the P-wave. In stiff clay, the first peak point represents the S-wave, then the P-wave, which is shown by the following peak points encounter the surface.

The contour plots of radial velocities at t=0.88 s for soft and stiff clays are shown in Figure 7.24. The contour plots clearly show that while P-waves are on the surface in the stiff clay, they are still traveling underground in the soft clay. The S-waves encounter the surface first in the soft clay, and then the P-wave arrives.

The peak particle velocities are compared with the empirical method of Wiss and Jedele (Woods, et al., 1985). In Figure 7.25, the peak particle velocities at 4.5 m, 9 m, 18 m, 27 m, 36 m, 45 m and 54 m are plotted for different types of clays on a scaled distance graph. The red line on the graph shows the envelope for Class II soils that are competent soils as described in Chapter 2. Figure 7.25 illustrates the ground vibrations below the red envelope within first 18 m, which verifies that they are within the safe limits. However, after 18 m, ground vibrations particularly in soft clays considered troublesome to some people.

Table 7.4 Soil parameters for different types of sands

Material Parameters	Notation	Value	Units
Loose sand			
Modulus of elasticity	E	12.0×10^3	kN/m^2
Poisson's ratio	v	0.25	-
Dry Density	ρ_{dry}	1440	kg/m^3
Undrained cohesion	c_u	0.0	kN/m^2
Angle of internal friction	ϕ	30	^{o}
Dense sand			
Modulus of elasticity	E	26.0×10^3	kN/m^2
Poisson's ratio	v	0.40	-
Dry Density	ρ_{dry}	1770	kg/m^3
Undrained cohesion	c_u	0.0	kN/m^2
Angle of internal friction	ϕ	40	^{o}

Table 7.5 Soil parameters for different types of clays

Material Parameters	Notation	Value	Units
Soft clay			
Modulus of elasticity	E	$1.06 \times 10^3\, Z(m)$	kN/m^2
Poisson's ratio	v	0.30	-
Dry Density	ρ_{dry}	1600	kg/m^3
Undrained cohesion	c_u	$2.87\, Z(m)$	kN/m^2
Angle of internal friction	ϕ	6	^{o}
Medium stiff clay			
Modulus of elasticity	E	$2.0 \times 10^3\, Z(m)$	kN/m^2
Poisson's ratio	v	0.30	-
Dry Density	ρ_{dry}	1600	kg/m^3
Undrained cohesion	c_u	$6.0\, Z(m)$	kN/m^2
Angle of internal friction	ϕ	6	^{o}
Stiff clay			
Modulus of elasticity	E	$4.0 \times 10^3\, Z(m)$	kN/m^2
Poisson's ratio	v	0.30	-
Dry Density	ρ_{dry}	1600	kg/m^3
Undrained cohesion	c_u	$12.0\, Z(m)$	kN/m^2
Angle of internal friction	ϕ	6	^{o}

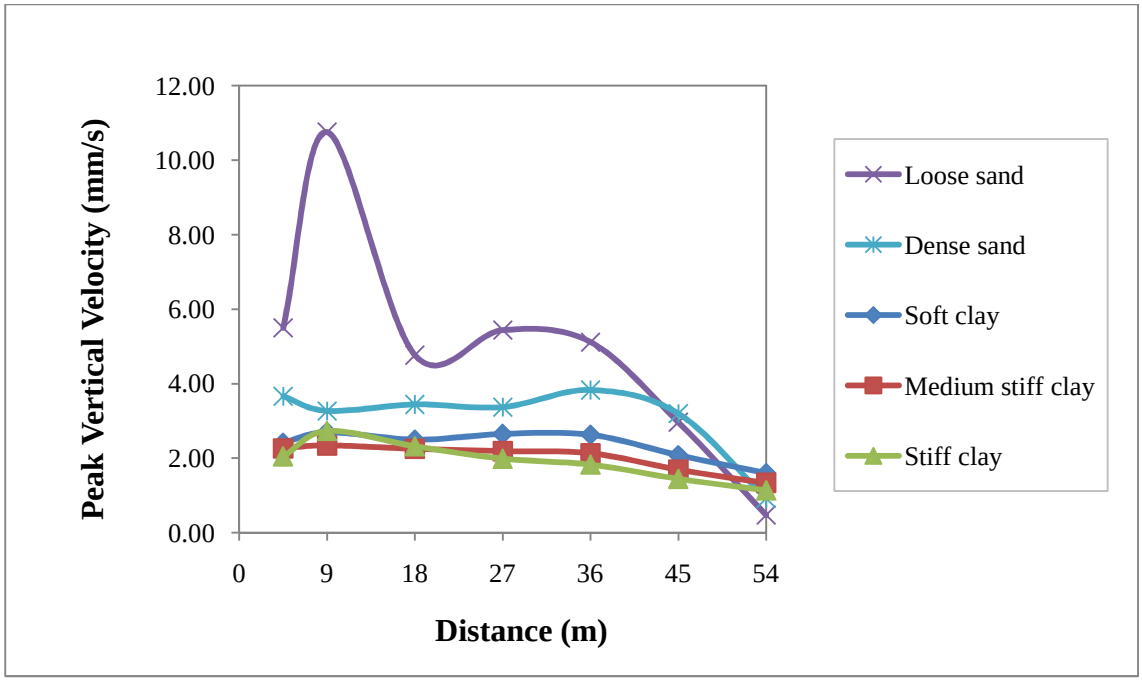

Figure 7.20 Peak particle velocity vs. distance for different types of soils.

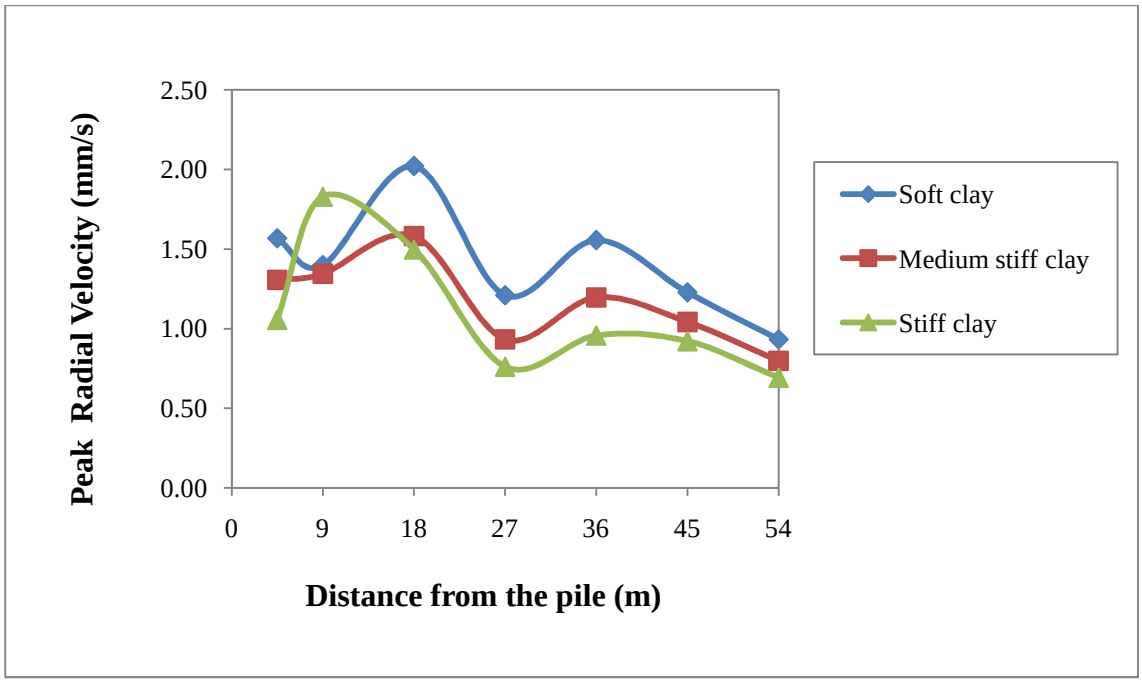

Figure 7.21 Peak radial velocity vs. distance from pile.

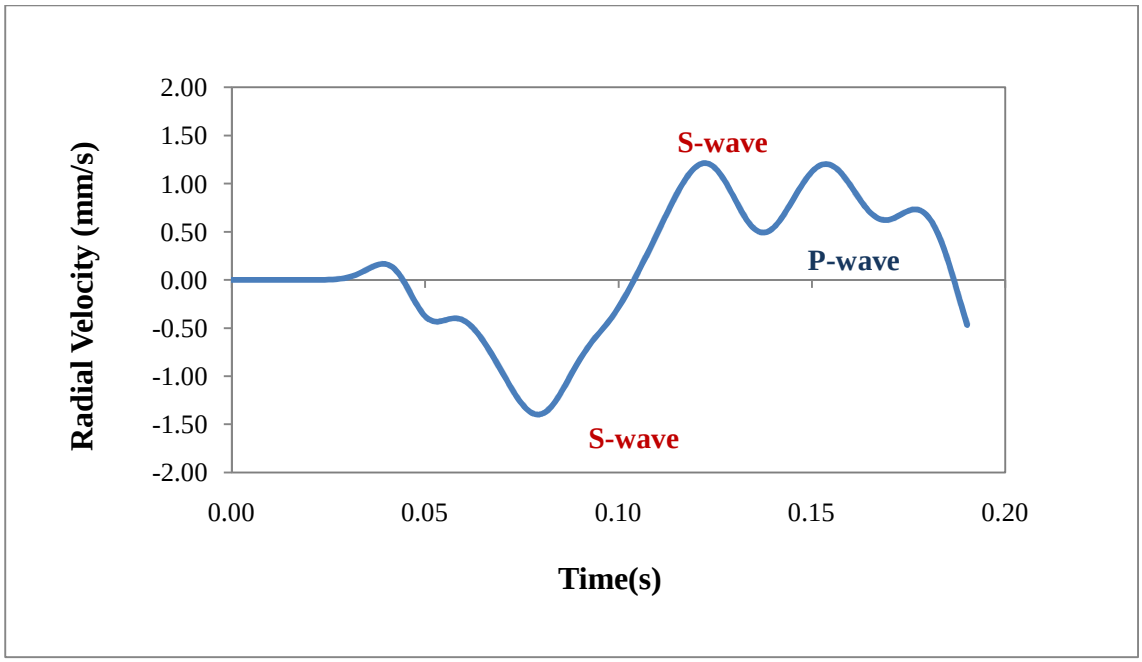

Figure 7.22 Radial velocity vs. time at 9 m from pile for soft clay.

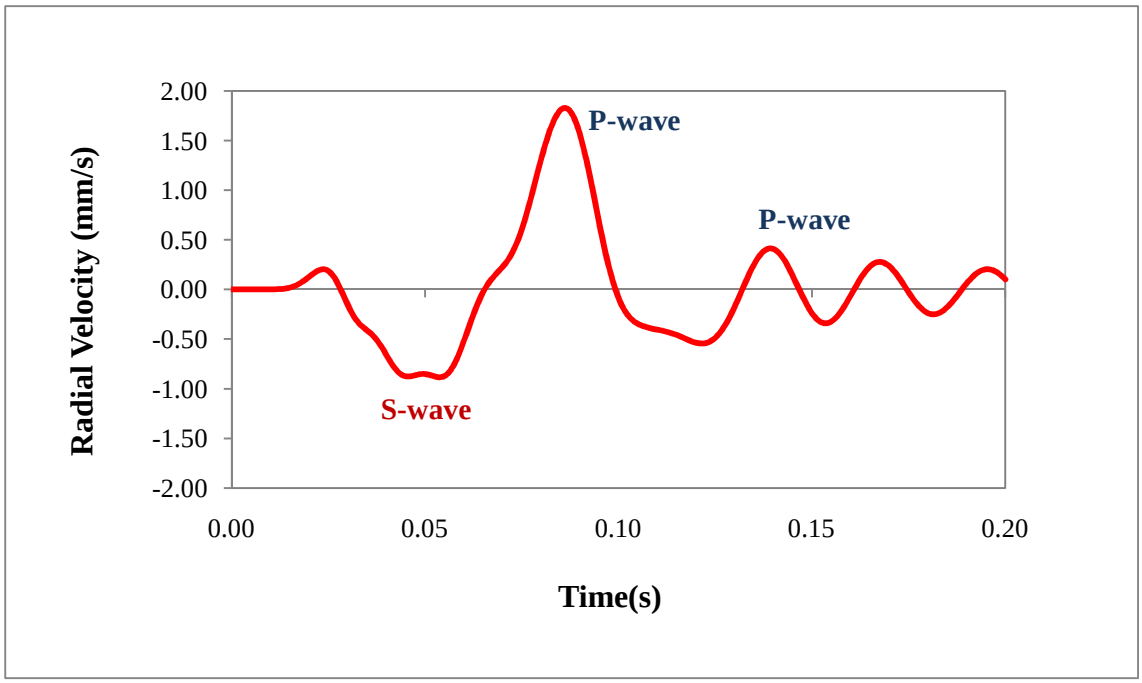

Figure 7.23 Radial velocity vs. time at 9 m from pile for stiff clay.

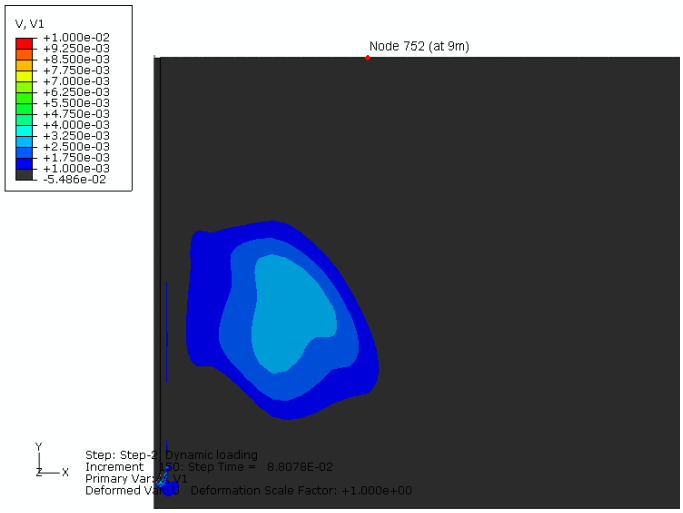

(a)

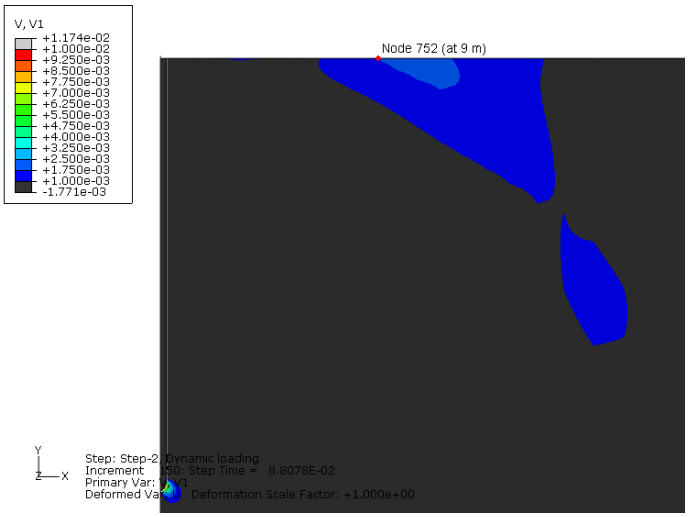

(b)

Figure 7.24 Contour plot of radial velocity at t=0.88 s for (a) soft clay, and (b) stiff clay.

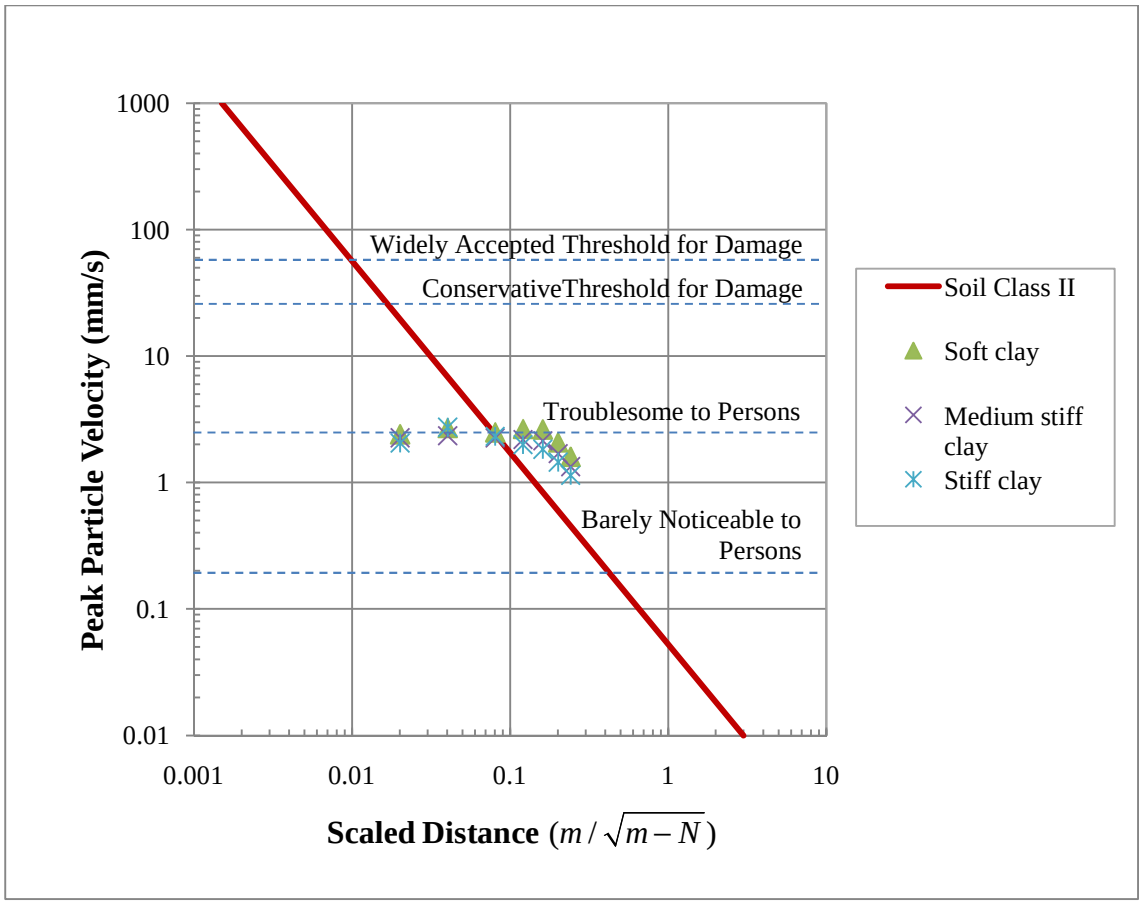

Figure 7.25 Peak particle velocity vs. distance from vibration source for different type of soils.

7.5.2 Effect of Pile Embedment Length

Three different pile embedment lengths are considered for the simulation of pile driving and propagation of ground vibrations. Each simulation has a different pile embedment length consisting of: (1) one pile length, L, embedded, (2) half a pile length, L/2, embedded and (3) quarter of a pile length, L/4, embedded.

As shown in Figure 7.25, the shorter the embedment is the greater the PPVs are on the ground surface. The maximum recorded PPVs for the fully, half, and quarterly embedded piles are 10.5 mm/s, 6.5 mm/s, and 2.5 mm/s, respectively. Although the energy transmitted to the ground is the same for the three different models, the dissipation of the stress waves due to the material damping in the ground causes significant differences in the magnitudes of the vibrations on the ground surface. Less energy is dissipated in the ground as the piles are less embedded. When the pile is quarter-embedded, the PPV at 4.5 m from the pile is two times greater than the PPV at the same point for the half-embedded pile. In addition, when the pile is quarterly embedded, the PPV at 4.5 m from the pile is five times greater than the PPV at the same point for the fully embedded pile. This can be explained by the difference of the arrival times of the P-waves to the ground surface. The P-waves reach the ground surface in a relatively shorter time than the quarterly and half-embedded piles with respect to the arrival time for the fully embedded pile. The contour plots of the resultant velocities are shown in Figure 7.26.

The PPVs for the three cases are plot on the scale distance graph of Woods and Jedele (1985) as shown in Figure 7.27. The PPVs for half and quarterly embedded piles at 18 m and 27 m are found to be troublesome to persons whereas the PPVs for fully embedded piles are found to be barely noticeable to persons.

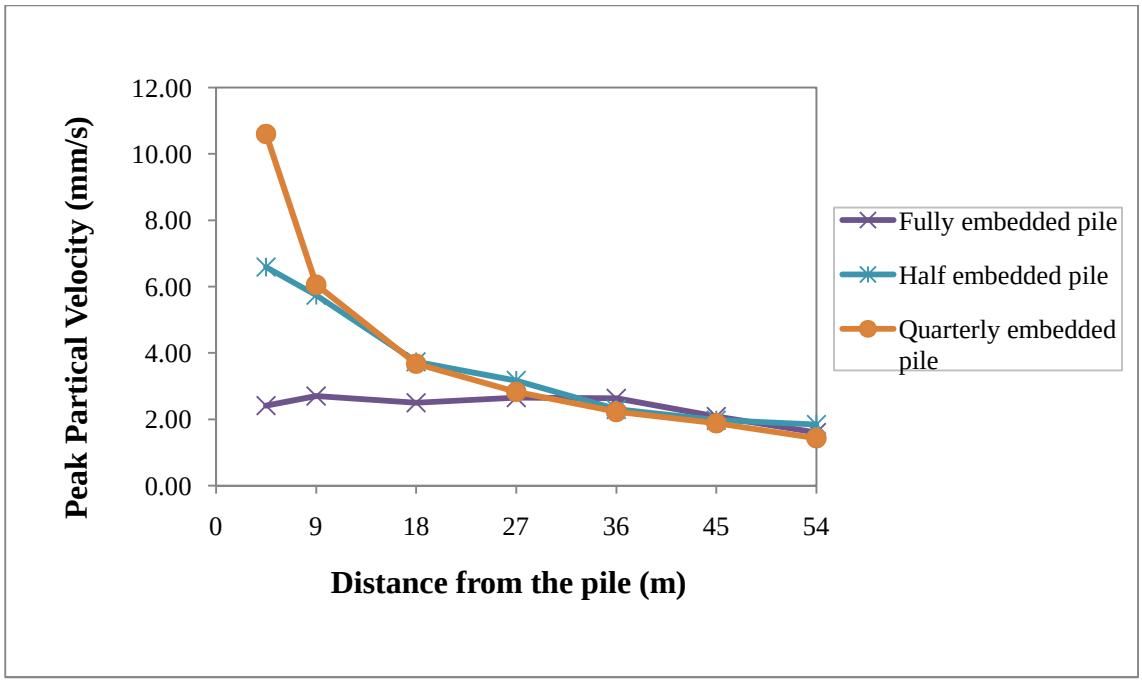

Figure 7.26 Peak particle velocity vs. scaled distance from the pile for different pile embedment lengths.

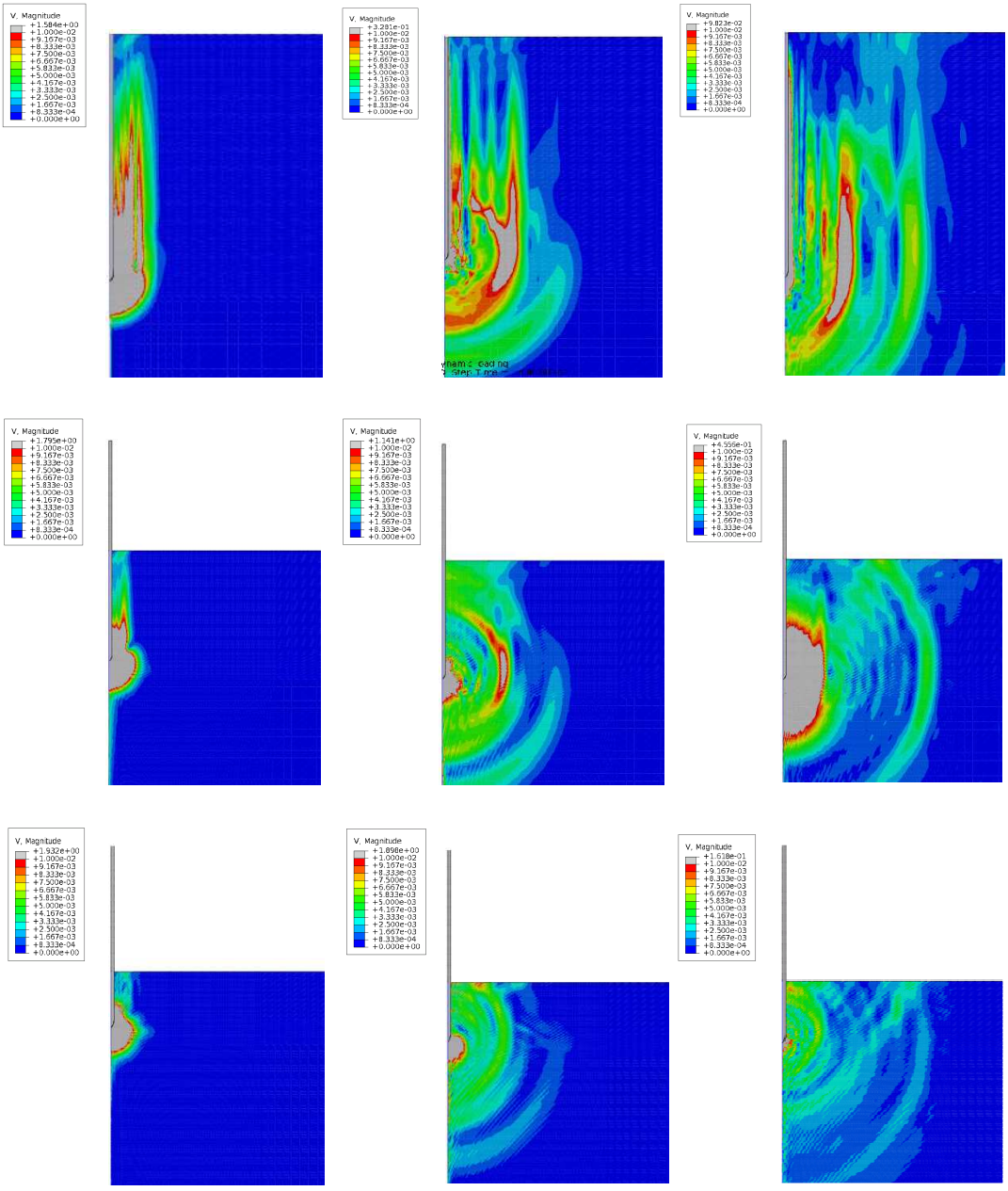

(a) (b) (c)

Figure 7.27 Contour plots of resultant velocities in clayey soil for fully, half and quarter embedded piles at time steps (a) t = 20 ms, (b) 50 ms, and (c) 100 ms.

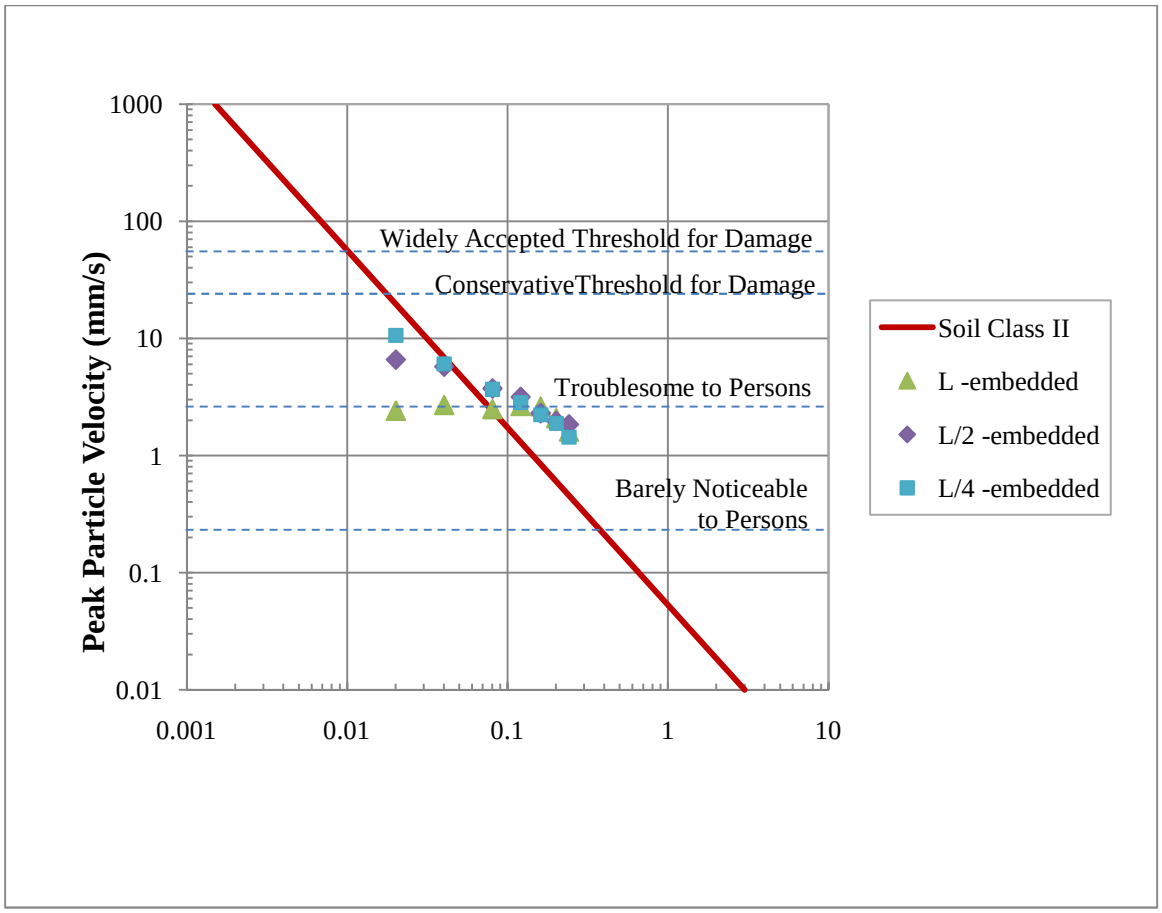

Figure 7.28 Peak particle velocity vs. scaled distance from vibration source for different pile embedment lengths

7.5.3 Effect of Released Hammer Energy

The hammer energies transmitted from the hammer to the pile are compared for three different models. The original forcing function that is shown in Figure 7.13 is used for the analysis. Hammer energies are represented by the peck forces applied on the pile head as F, 3F and 5F. These peak forces are calculated as 2,000 kN, 6,000 kN and 10,000 kN, respectively. The maximum PPVs are computed as 2.0 mm/s, 4.0 mm/s and 7.0 mm/s for peak impact forces of F, 3F and 5F, respectively, as shown in Figure 7.28. The radial (v_1), vertical (v_2) and resultant (v_{norm}) velocities are plotted for 3F and 5F cases as shown in Figures 7.29 and 7.30, respectively. In Figure 7.29, the radial velocities increase up to 9 m then gradually decreases toward the far field. The reason for that is the shear waves dominate in the first 9.0 meters. In Figure 7.30, both radial and vertical velocities gradually decrease in the near and far field. This is because the compression waves dominate on the ground surface. The conclusion can be drawn that the more energy transmitted to the ground the higher the PPVs are on the ground surface.

The results are compared with the empirical method of Woods and Jedele (1985) as shown in Figure 7.31. The PPVs for 3F and 5F are found to be troublesome to persons after a distance of 27 m from the pile.

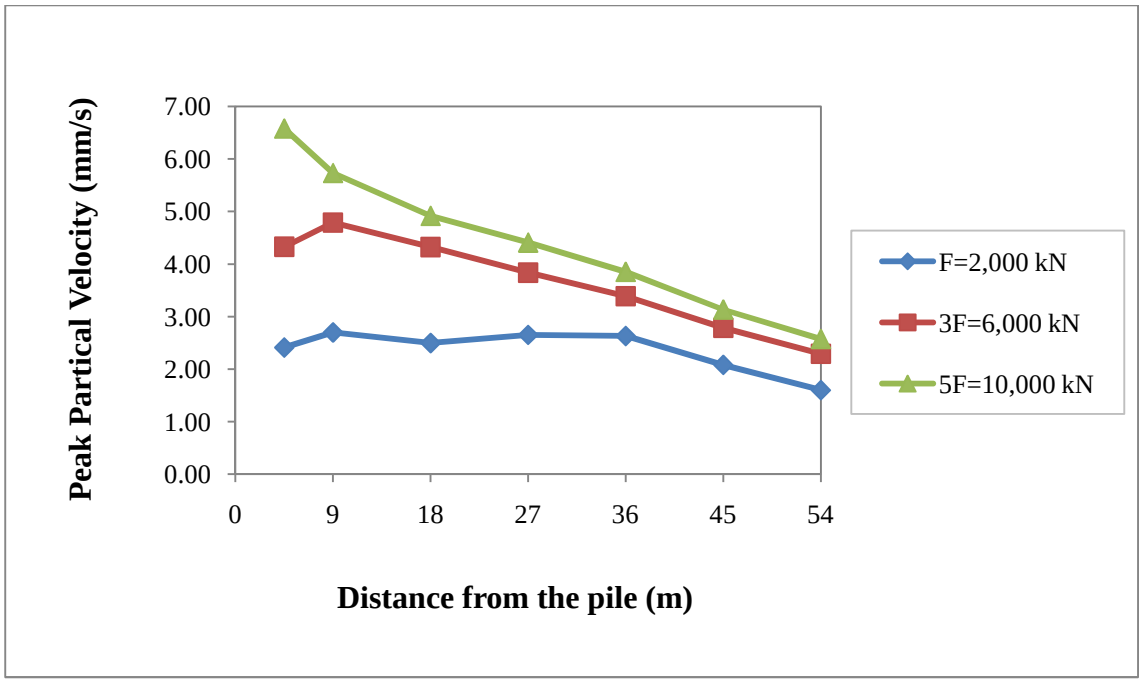

Figure 7.29 Peak particle velocity vs. distance for different hammer energies.

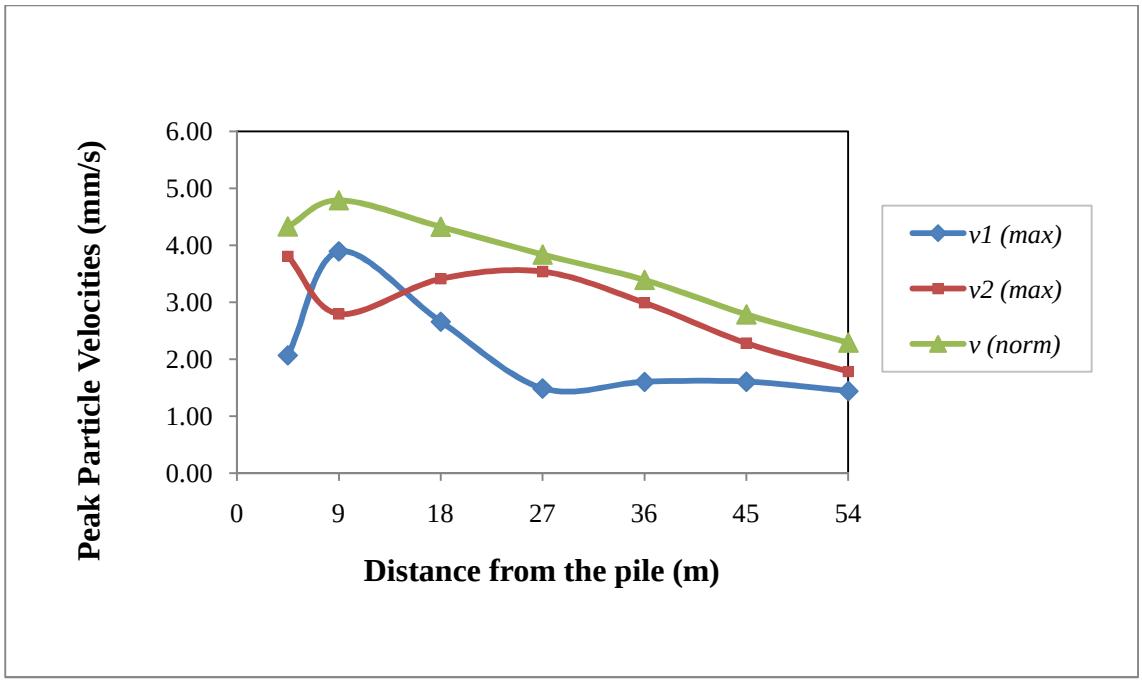

Figure 7.30 Peak particle velocity vs. distance for the peak force of 6,000 kN.

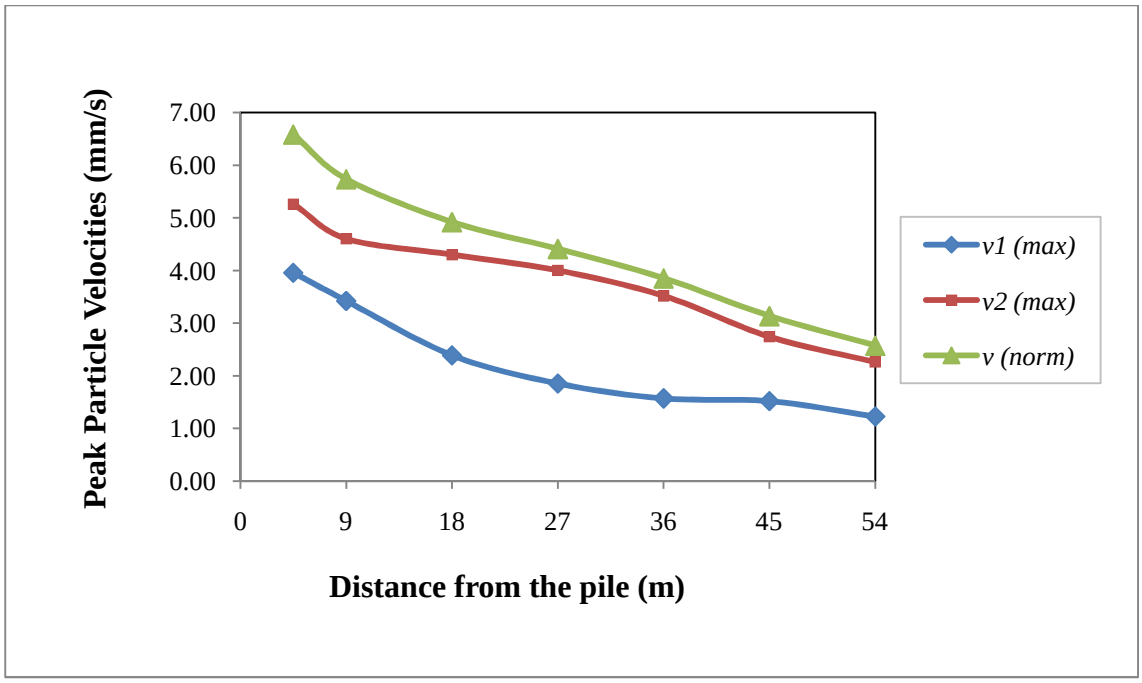

Figure 7.31 Peak particle velocity vs. distance for the peak force of 10,000 kN.

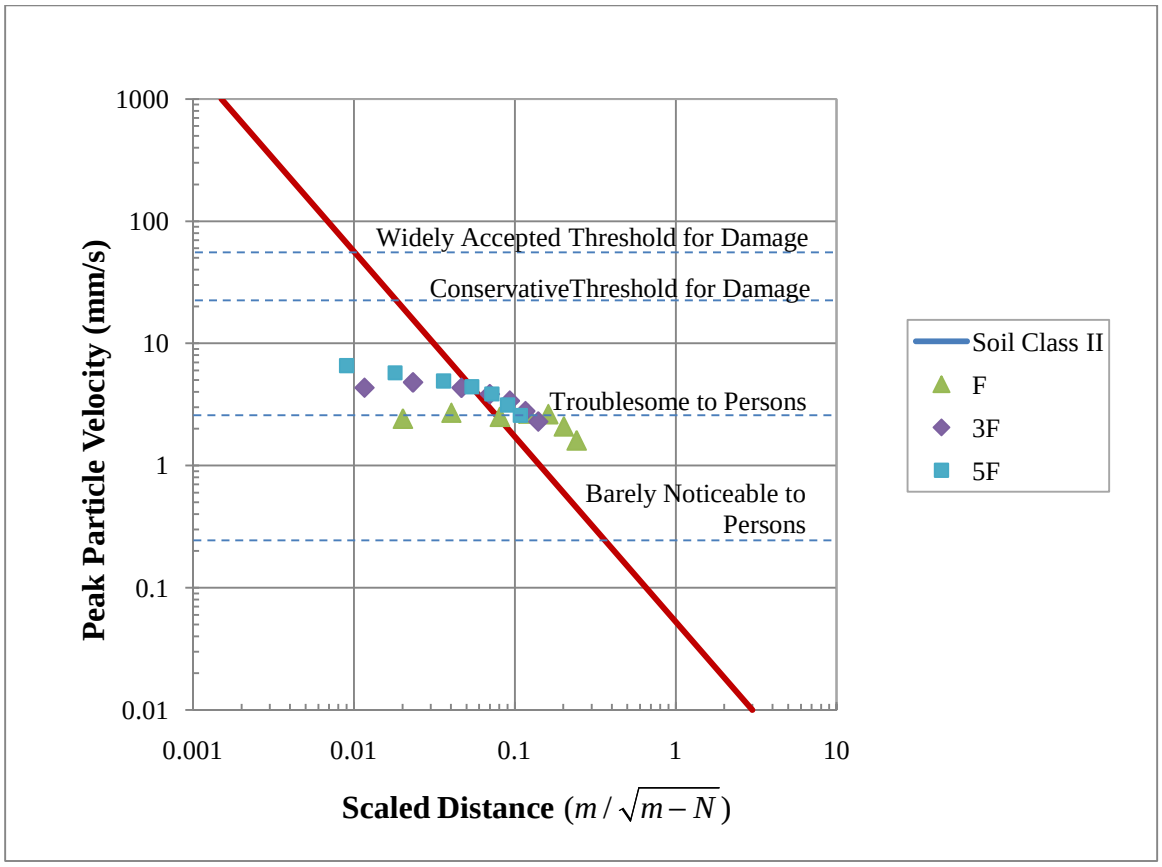

Figure 7.32 Peak particle velocity vs. scaled distance from vibration source for different hammer energies.

7.6 Ground Vibrations at Foundation Levels

Structural damage caused by pile driving induced vibrations are not only caused by stress waves traveling on the ground surface but also caused by the waves below the ground surface. If there are substructures such as subways, pipelines or deep foundations in the near vicinity of a pile driving operation, damage to those substructures can be caused by underground waves. Thus, the damage criterion based on the measurements of the peak particle velocities recorded on the ground surface would be less beneficial.

The radial, vertical and vector sum velocities at the ground surface (Z=0.0) and below the ground surface (Z=4.5 m, Z=9.0 m, Z=18.0 m) are computed for varying distances from the center of the pile as shown in Figures 7.32, 7.33, and 7.34. It can be seen in the figures that the vertical peak velocities are up to 4 times higher than the radial peak velocities on the ground surface. Thus, vertical velocities dominate in the entire field. In Figure 7.34, the resultant peak particle velocities (PPVs) are shown for different depths and distances from the pile. At 18 m below the ground, the PPVs are 10 times, 7.5 times and 3.5 times greater than the PPVs on the ground surface at 2.5 m, 4.5 m and 9 m away from the pile, respectively. This is because the energy transmitted from the pile toe into the ground dissipates when traveling to the ground surface. Thus, the PPVs have a greater magnitude at the depth of the pile toe.

In Figure 7.35, it is shown that the PPVs are between 5 mm/s and 20 mm/s at the depth of the pile toe within 18 m distance from the pile. Hence, the measurement of ground vibrations would be pointless if there are any substructures at the depth of 18 m below the ground surface. The substructures could be adversely affected by the pile driving vibrations from the ground surface to a depth of 18 m.

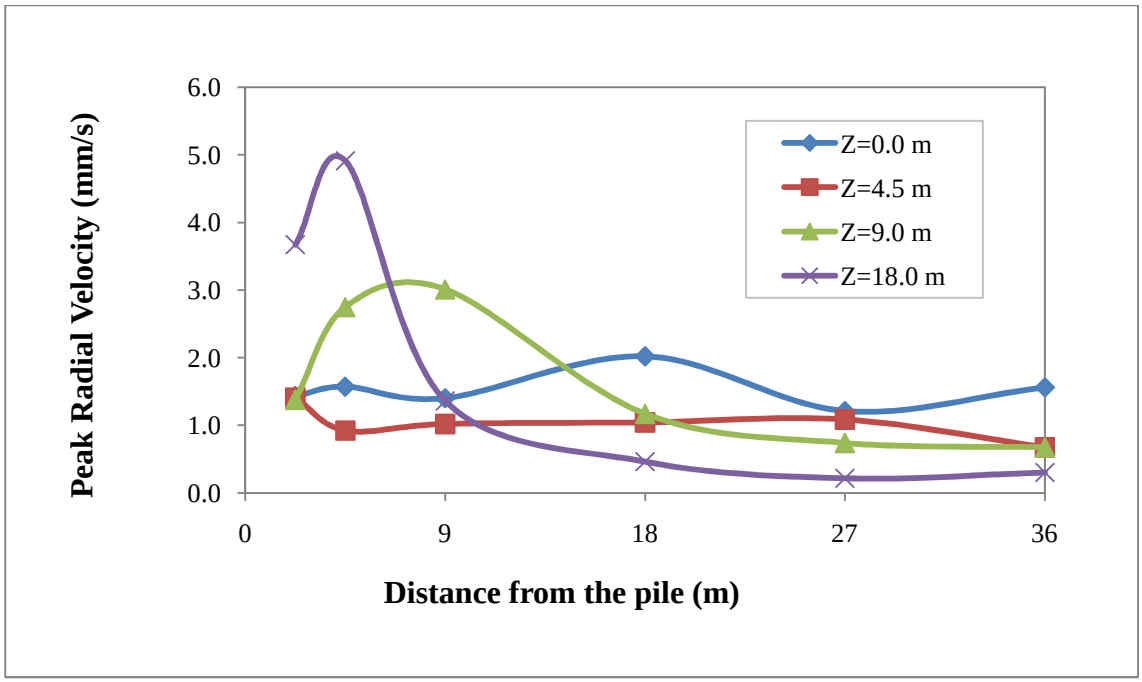

Figure 7.33 Peak radial velocity vs. distance from the pile at different depths.

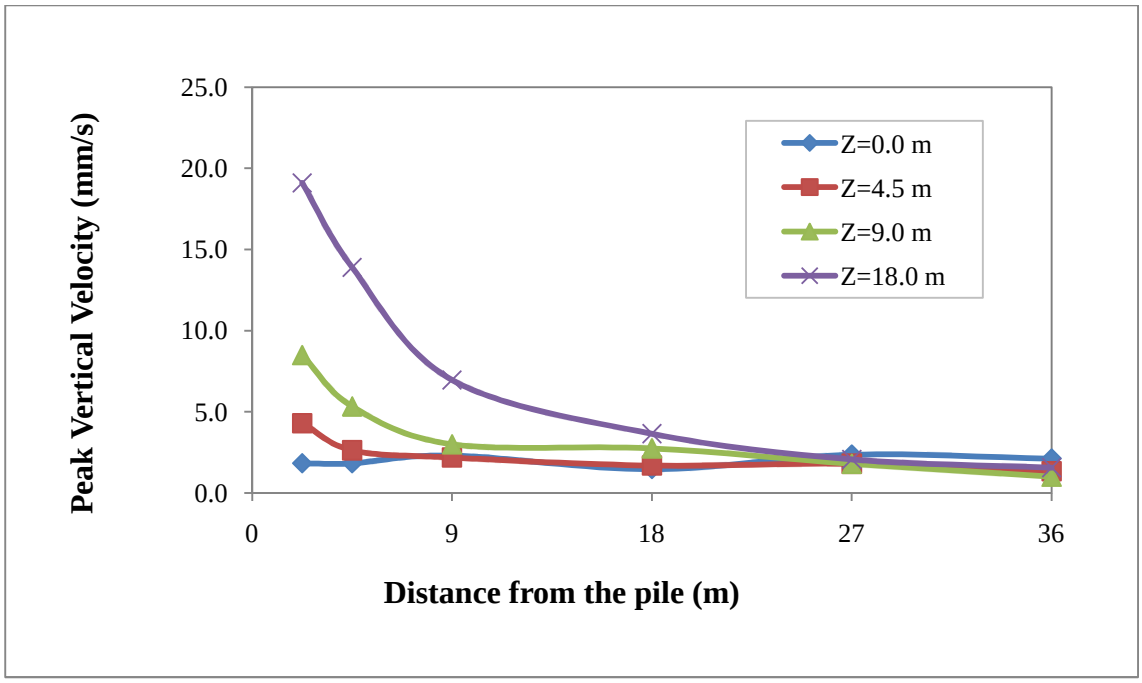

Figure 7.34 Peak vertical velocity vs. distance from the pile at different depths.

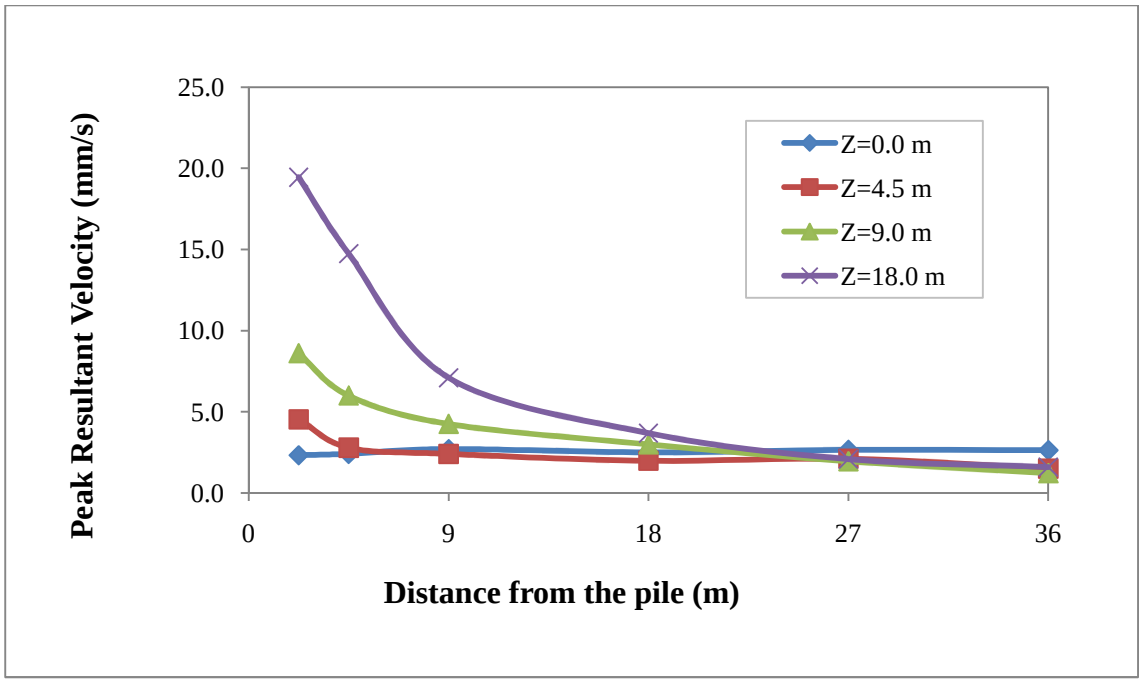

Figure 7.35 Peak resultant velocity vs. distance from the pile at different depths.

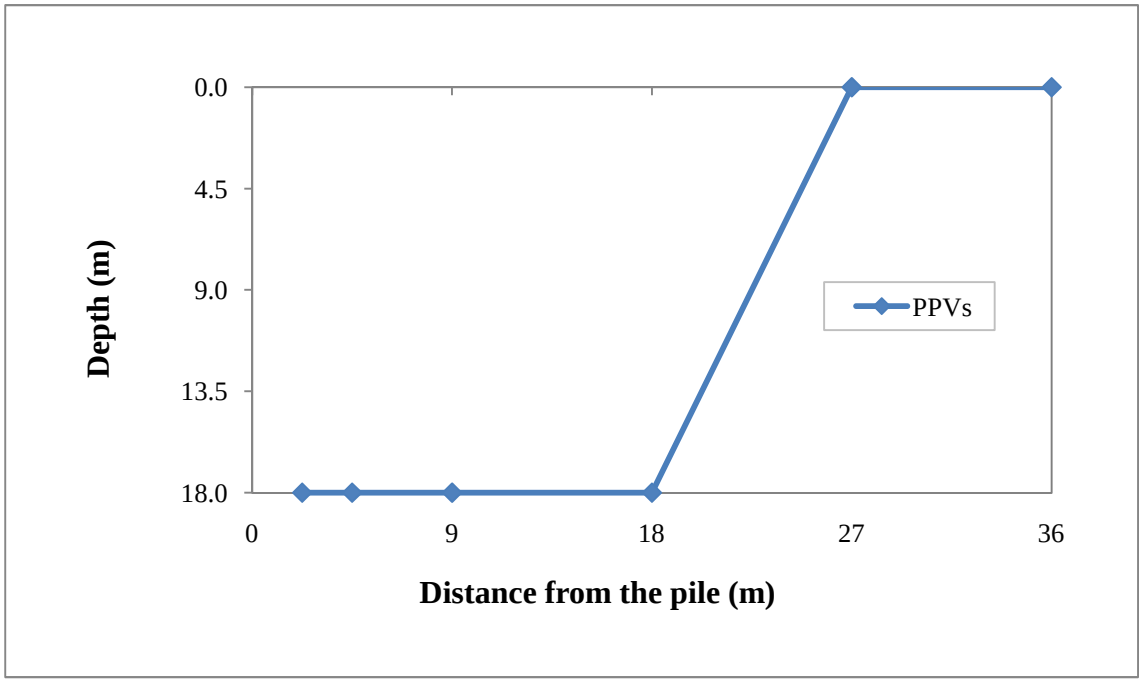

Figure 7.36 Peak particle velocities at different depths vs. distance from the pile.

7.7 Summary and Discussion

This chapter consists of a parametric study on the finite element modeling of ground vibrations caused by impact pile driving. The parameters considered for the assessment if ground vibrations are: (1) the soil strength, (2) the pile embedment length, and (3) the released hammer energy. In addition, the ground vibrations at various depths and distances from pile driving are investigated to illustrate the effect of ground vibrations to buried structures in the vicinity of pile driving.

The first parameter considered is the soil strength. The finite element analysis is run for three different types of soils: (1) soft clay, (2) medium stiff clay, and (3) stiff clay. These soil types are represented by different values of elastic modulus and unconfined compressive strengths. The modules of elasticity are varied from 1.06 MPa to 4 MPa. The unconfined compressive strengths are varied from 2.87 KPa to 12 KPa. The variation of the peak particle velocities (PPVs) on the ground surface is monitored. The following conclusions are drawn from the analyses: (1) the PPVs are higher in stiff clay in the near field, which is 9 m or less away from the pile; (2) the PPVs are higher in soft clay in the far field, which is more than 9 m away from the pile; (3) the shear waves dominate in the soft clay whereas the primary waves dominate in the stiff clay.

The next parameter studied is the pile embedment depth. The analysis is performed for three cases consisting of fully, half, and quarterly embedded piles. The peak particle velocities at different distances from the pile on the ground surface are plotted. The quarterly embedded pile yields greater vibration amplitudes with respect to the half and fully embedded piles. Although the applied energy from the pile hammer remains constant, the magnitude stress waves encountering the ground surface are greater for the less embedded piles.

In the last case, the effect of hammer energy is studied for three cases. In these cases, peak forces of 2,000 kN (F), 6,000 kN (3F) and 10,000 kN (5F) are considered to be applied on top of the pile. The time histories of the peak particle velocities at different

depths are plotted. It is concluded that increase in hammer energy causes increase in the peak particle velocities.

The ground vibrations at various depths are analyzed to investigate the effect of vibrations to the substructures in the vicinity of the pile driving. The vibration amplitudes are recorded at 4.5 m, 9 m, and 18 m below the ground surface. It is shown that the maximum PPV is monitored at a depth of 18 m where the pile toe is located. The PPVs between 0 to 18 m below the ground surface range from four to ten times the magnitude with respect to the PPVs on the ground surface.

CHAPTER 8

SUMMARY AND CONCLUSIONS

This thesis consists of static and dynamic analysis of piles using the finite element method. For the analysis of soil-pile interaction, a coupled displacement/pore pressure element formulation was employed. The governing equations were developed for the transient analysis of soils under static and dynamic loading conditions. These equations are implemented within the finite element framework using the Mathematica software. The ABAQUS/Standard finite element package was used to solve the non-linear axisymmetric static and dynamic equations. The soil was assumed to be normally consolidated. The undrained soil conditions were assumed. The master-slave contact algorithm in ABAQUS was used to model the interaction between the pile and soil. An analytical rigid surface is defined along the axis of symmetry to remove the additional constraints on the soil elements adjacent to the symmetry line to allow slippage of the soil elements. In addition, a non-reflecting artificial boundary is defined to prevent the bounce back of stress waves from the far end of the model. This boundary consisted of soil elements with high damping ratios that are designed to absorb the vibrations.

Two types of problems were solved in this thesis: (1) the static analysis of a pile in which the phenomenon of static consolidation was studied, and (2) the dynamic analysis of a pile in which pile driving and ground vibrations were studied. The results were compared with published data to validate the numerical model.

In the static analysis, the load capacity of a single pile is investigated. The results from the finite element method are compared with and supported by widely recognized theoretical methods. The theoretical methods that are used to estimate the end bearing capacities are as follows: (1) General Formula, (2) Vesic's Method, (3) Janbu's Method, (4) Meyerhof's Method, and (5) Coyle & Castello's Method. The estimation of skin friction resistance, shaft capacity, of single piles is performed using the (1) Alpha

method, (2) Beta method, and (3) Lambda method. Two numerical applications are carried out to estimate the load capacity of single piles in normally consolidated clays. The first numerical application consists of a solid cylindrical concrete pile with a diameter D = 1.0 m and length L= 20 m embedded in a thick homogenous stiff clay layer. It is examined that the model with no slippage at the interface predicts almost twice as much load capacity as the model with interface. In regards with the end bearing capacities, Coyle & Castello's method is found to be most conservative followed by the finite element method, then Janbu's method, then Meyerhof's method, and finally Vesic's method. In respect to skin friction resistance, the finite element is found to be the most conservative method, followed by Beta, then Lambda, and then Alpha. It is concluded that modeling the interaction between the soil and pile (soil pile interface) is vital to obtain accurate pile load capacities.

In the dynamic analysis, the amplitudes of ground vibrations are investigated based on the variation of: (1) the soil type, (2) the pile embedment length and (3) the released hammer energy, all of which have significant effects on the transmission of ground vibrations in the soil.

In the first analysis, five types of soils, loose and dense sands and, soft, medium stiff, and stiff clays, are modeled. It is found that the vibration amplitudes are highest for the loose sand with a PPV of 10.0 mm/s followed by the dense sand with a PPV of around 4.0 mm/s. Among the clay types, the vibrations are higher for the stiffer clay in the near field, which is 9 m, half a pile length, or less away from the pile. In the soft clay, vibration amplitudes are higher in the far field, which is more than 9 m away from the pile. It is concluded that the shear waves dominate in the softer clay whereas the compression waves dominate in the stiff clay.

In the second analysis, three different embedment lengths, full, half, and quarter pile lengths, are modeled. It is found that the quarterly embedded pile produces greater vibration amplitudes with respect to the half and fully embedded piles. The greater

amplitudes of vibrations are encountered on the ground surface for shorter pile embedment lengths. This is due to less energy dissipation in the ground during the transmission of ground vibrations from the pile toe to the ground surface.

In the third analysis, three different impact forces are applied on top of the pile. The peak forces are selected as 2,000 kN (F), 6,000 kN (3F) and 10,000 kN (5F). It is observed that although the increase in hammer energy causes increase in the peak particle velocities, these increments are not linearly proportional with the magnitude of the applied impact force.

The effect of vibrations to the substructures in the proximity of the pile driving was also investigated analyzing the ground vibrations at various depths. The vibration amplitudes were recorded at 4.5 m, 9 m, and 18 m below the ground surface. This analysis showed that the maximum vibrations are monitored at a depth of 18 m where the pile toe is located. The recorded vibrations from the pile toe to the ground surface have shown significant discrepancies with the variation of depths. The vibration amplitudes recorded at the depth of the pile toe where ten times greater than the recorded vibration on the ground surface. It is concluded that to avoid damage to substructures, the ground vibrations must be recorded at various depths in the proximity of the pile driving.

In conclusion, this research was valuable for studying ground vibrations caused by pile driving. The quality of the finite element model was significantly improved by (1) taking into account the friction between pile and soil, (2) considering non-linear behavior of soils, and (3) defining an artificial boundary that minimizes reflection of the waves in the far field. Proper consideration of these factors would be beneficial for developing a safe pile driving strategy to avoid potential structural damage and disturbance in the vicinity of pile driving.

Future work is reserved to develop and implement a suitable constitutive model within the finite element framework to study the settlement of foundation soils in the proximity of repetitive impact pile driving or vibratory pile driving.

REFERENCES

American Petroleum Institute. (1991). *Recommended Practice of Planning, Designing and Construction of Fixed Offshore Platforms.* Washington, D.C.: Report No. API-RP-2A, 19th Ed.

Biot, M. A. (1941). Consolidation under a rectangular load distribution. *Journal of Applied Physics*, 426-430.

Biot, M. A. (1941). General Theory of Three-Dimensional Consolidation. *Journal of Applied Physics, 12*, 155-64.

Biot, M. A. (1955). Theory of Elasticity and Consolidation for a Porous Anisotropic Solid. *J Appl Physics, 28*, 182-185.

Biot, M. A. (1956). Theory of propagation of elastic waves in a fluid-saturated porous solid. II-Higher frequency range. *J Acoust Soc Am, 28*(2), 179-91.

Biot, M. A. (1956). Theory of propagation of elastic waves in a fluid-saturated porous solid. I-Low-frequency range. *28*, 168-191.

Bishop. (1959). The principle of effective stress. *33*, 859-863.

Bolton, M. (1986). The strength and dilatancy of sands. *Geotechnique, 36*, 65-78.

Borja, R. (1986). Finite element formulation for transient pore pressure dissipation: A variational approach. *22*.

Borja, R. (1989). Linearisation of elasto-plastic consolidation equations. *6*, 163-168.

Chang, C. S., & Duncan, J. M. (1983). Consolidation analysis for partly saturated clay by using an elastic-plastic effective stress-strain model. *7*(1), 39-55.

Chen, W. F., & Han, D. J. (1988). Plasticity for Structural Engineers.

Christian, J., & Boehmer, J. (1970). Plain strain consolidation by finite elements. *SM4*.

Coulomb, C. (1773). Essai sur une application des regles des maximis et minimis a quelques problemes de statique relatifs a l'architecture. *mem. pres. par. div. savants, 7*, 343-382.

Craig, R. (1992). *Soil Mechanics.* London: Chapman & Hall.

Cryer, C. (1963). A comparison of the three-dimensional consolidation theories of Biot and Terzaghi. *16*.

Darbkin, S., Lacy, H., & Kim, D. (1996). Estimating settlement of sand caused by construction vibration. *122*, 920–928.

Dowding, C. (1999). *Construction vibrations.* Englewood Cliffs, NJ: Prentice-Hall.

Drucker, D., & Prager, W. (1952). Soil mechanics and plastic analysis for limit design. *Quart. Appl. Math., 10*, 157-165.

Eringen, A. C., & Ingram, C. D. (1965). A continuum theory of chemically reacting media. I (Continuum theory of chemically reacting media) . *Int J Engrg Sci, 3*, 197-212.

Eringen, A., & Suhubi, E. (1964). Nonlinear theory of simple micro-elastic solids-I. *2*, 189-203.

Eringen, C. A., & Ingram, J. D. (1967). A continuum theory of chmically reacting media. II (Constitutive theory for fluid mixtures admitting diffusion and chemical interaction with heat conduction and plane wave propagation). *Int J Engrg Sci, 5*, 289-322.

Ghaboussi, J., & Wilson, E. (1972). Variational formulation of dynamics of fluid-saturated porous elastic solids. *98*, 947-963.

Ghaboussi, J., & Wilson, E. (1973). Flow of compressible fluid in porous elastic media. *5*, 419-442.

Green, A. E., & Naghdi, P. M. (1965). A dynamical theory of interacting continua. *Int J Engrg Sci, 3*, 231-41.

Griffiths, D. (1994). *Coupled analyses in geomechanics. In Visco-plastic Behavior of Geomaterials.* New York: Springer-Verlag, Wien.

Hibbitt, Karlsson, & Sorensen, I. (2008). *ABAQUS User's Manual (version 6.8-1).* Pawtucket, RI.

Huang, M., & Zienkiewicz, O. (1998). New unconditionally stable staggered solution procedures for coupled soil-pore fluid dynamic problems. *43*, 1029-1052.

Hügel, H., Henke, S., & Kinzler, S. (2008). High-performance Abaqus simulations in soil mechanics. *Abaqus Users' Conference.* Newport, RI.

Hwang, C., Morganstern, N., & Murray, D. (1971). On solutions of plane strain consolidation problems by finite elements methods. *8*(109-118).

Janbu, N. (1976). Static bearing capacity of friction piles. *Procedings of the 6th European Conference on Soil Mechanics and Foundation Engineering, 12*(3).

K.Z. Markov, L. (2000). *Heterogeneous Media: Modelling, Mathematical Methods and Simulations.* Boston: Birkhauser.

Katona, M., & Zienkiewicz, O. (1985). A unified set of single step algorithm, Part 3: The Beta-m method, a generalization of the Newmark scheme. *21*, 1345-1359.

Kim, D., & Lee, J. (2000). Propagation and attenuation characteristics of various ground vibrations. *19*, 115–126.

Lewis, R. W., Roberts, G. K., & Zienkiewicz, O. C. (1976). A nonlinear flow and deformation analysis of consolidated problems. *Proceedings of the 2nd International Conference on Numerical Methods in Geomechanics.* New york: ASCE.

Lewis, R., & Schrefler, B. (1987). *The Finite Element Method in the Deformation and Consolidation of Porous Media.* Chichestar: Wiley.

Liu, G., & Quek Jerry, S. (2003). A non-reflecting boundary for analyzing wave propagation using the Finite element method. *Finite Elements in Analysis and Design, 39*, 403-417.

Liyanapathirana, D., Deeks, A., & Randolph, M. (2001). Numerical modelling of the driving response of thin-walled open-ended piles. *25*, 933–53.

Mabsout, M., Reese, L., & Tassoulas, L. (1995). Study of pile driving by finite element method. *121*(7), 535-543.

Mandel, J. (1953). Consolidation des sols (eÂtude mathematique). *3*.

Menétrey, P., & William, K. J. (1995). Triaxial Failure Criterion for Concrete and its Generalization. *92*, 311–18.

Newmark, N. (1959). A method of computation for structural dynamics. *85*, 67-94.

Oka, F., Yashima, A., Shibata, T., Kato, M., & Uzuoka, R. (1994). FEM-FDM Coupled Liquefaction Analysis of a Porous Soil Using an Elasto-Plastic Model. *52*(3).

Potts, D. M., & Zdravkovic, L. (2001). *Finite element analysis in geotechnical engineering: Application.* London: Thomas Telford Publishing.

Poulos, H., & Davis, E. (1980). *Pile Foundation Analysis and Design.* New York: John Wiley and Sons.

Prevost, J. (1982). Nonlinear transient phenomena in saturated porous media. *20*, 3-18.

Provost, J. (1981). Consolidation of an Elastic Porous Media. *107*.

R. W. Lewis, B. A. (1998). *The Finite Element Method in the Static and Dynamic Deformation and Consolidation of Porous Media, 2nd Edition.* New York: Wiley.

R.W. Lewis, B. S. (1998). *The Finite Element Method.* New York: Wiley.

Ramshaw, C., Selby, A., & Bettess, P. (1998). Computation of the transmission of waves from pile driving. *Ground dynamics and man-made processes.* London, UK: Thomas Telford Publishing.

Randolph, M. F., & Murphy, B.J. (1985). Shaft capacity of driven piles in clay. *Proc. Offshore Tech. Conf.* 371-378, Houston, TX.

Reese, L. C., & O'Neill, M. W. (1989). New Design Method for Drilled Shaft from Common Soil and Rock Tests. *2*, 1026-1039.

Rowe, P. (1962). The stress-dilatancy relation for static equilibrium of an assembly of particles in contact. *Proc. R. Soc. A, 267*, 500-527.

Sandhu, R., & Wilson, E. (1969). Finite-element analysis of seepage in elastic media. *95(EM3)*.

Simon, B., Wu, J.-S., Zienkiewicz, O., & Paul, D. (1986). Evaluation of u - w and u - finite element methods for the dynamic response of saturated porous media using one-dimensional models. *10*(5), 461-482.

Skipp, B. (1998). *Ground dynamics and man-made processes.* London, UK: Thomas Telford Services Ltd.

Smith, E. (1960). Pile driving analysis by the wave equation. *86* (EM4), 35–61.

Smith, I. M., & Hobbs, R. (1976). Biot analysis of consolidation beneath embankments. *26*.

Sun, J. S., Lee, K. H., & Lee, H. P. (2000). Comparison of implicit and explicit finite element methods for dynamic problems. *105*(1-2), 110-118.

Terzaghi, K. (1925). *Principle of soil mechanics.* Liepzig: Eng. News Record.

Terzaghi, K. (1943). *Theoritical Soil Mechanics.* New York: Wiley.

Timoshenko, S., & Goodier, J. (1982). *Theory of Elasticity* (Vol. International Edition). Singapore: McGraw-Hill.

U.S. Navy. (1986). *Foundations and Earth Structures Design Manual 7.02.* Philadelphia, PA: Department of Navy, Naval Facilities Engineering Command.

Vijayvergiya, V. N., & Focht, J. A. (1972). A New Way to Predict Capacity of Piles in Clay. *Proceedings, 4th Annual Offshore Technology Conference, Paper No. OTC Paper 1718*.

Wiss, J. (1981). Construction Vibrations: State of the Art. *107* (No. GT2, Proc. Paper. 16030), 167-181.

Woods, R., & Jedele, L. (1985). Energy-attenuation relationships from construction vibrations. *Proceedings of ASCE Symposium on Vibration Problems in Geotechnical Engineering* (pp. 229-246). Detroit, Michigan: American Society of Civil Engineers.

Woods, R., & Sharma, V. (2004). *Dynamic effects of pile installations on adjacent structures.* London, UK: A.A.Balkema.

Yokoo, Y., Yamagata, K., & Nagaoka, H. (1971). Finite element method applied to Biot's consolidation theory. *11(1)*(29-46).

Zienkiewicz. (1980a). Constitutive laws and numerical analysis for soil foundations under static, transient or cyclic loads. *2*(1), 23-31.

Zienkiewicz, O. (1982). Basic formulation of static and dynamic behaviour of soil and other porous material.

Zienkiewicz, O. T. (2005). *The Finite Element Method: Its Basis and Fundamentals* (6th ed.). Burlington, MA, USA: Elsevier Butterworth-Heinemann.

Zienkiewicz, O., & R.L., T. (1985). Coupled problems—a simple time-stepping procedure. *Communications in Applied Numerical Methods, 1*, 233–239.

Zienkiewicz, O., & Shiomi, T. (1984b). Dynamic behaviour of saturated porous media: the generalised Biot formulation and its numerical solution. *8*, 71–96.

Zienkiewicz, O., C.T., C., & Bettess, P. (1980b). Drained, undrained, consolidating and dynamic behaviour assumptionsin soils; limits of validity. *30*, 385-395.

Zienkiewicz, O., Wood, W., Hine, N., & Taylor, R. (1984). A unified set of single step algorithms. Part 1: General formulation and applications. *20*, 1529-1552.